

Aircraft Engineering and Aerospace Technology

13th READ conference and 14th EWADE workshop

Guest Editor: Tomasz Goetzendorf-Grabowski



Guest editorial

Special issue devoted to the 13th READ conference and 14th EWADE workshop

Dear reader,

It is our pleasure to present the special issue of the *Aircraft Engineering and Aerospace Technology Journal*, dedicated to the exceptional event that was a joint *READ&EWADE* conference. The conference was hosted by the Institute of Aerospace Engineering of Brno University of Technology from 7 to 9 of November 2018.

The READ conference – Research and Education in Aircraft Design (former name: RRDPAE – Recent Research and Design Progress in Aeronautical Engineering and its Influence on Education) – was established in 1994 by Professor Zdobyslaw Goraj, who was the chair of the conference for 20 years. The seminar was organized every 2 years as a general forum for the exchange of information about progress in aerospace engineering research. The unique character of the seminar is given by its focus on aircraft engineering education and inclusion of juried student sessions.

Over the years, the seminar has travelled from Warsaw (Poland), through Vilnius (Lithuania), Riga (Latvia) to Tallinn (Estonia), Brno (Czech Republic) and then to Warsaw, Brno, Vilnius, Warsaw, and in 2018 again to Brno (Figure 1).

The European Workshop on Aircraft Design Education (EWADE), which is the education activity of the Technical Committee Aircraft Design under Council of European Aerospace Societies (CEAS) was started in 1994 in Madrid. Next, the workshops were organized every 2 years in Berlin, Bristol, Turin, Linköping, Brno, Toulouse, Hamburg, Samara, Seville and Naples. The next workshop was held in Linköping, together with CEAS Air & Space Conference, and after that, EWADE workshops travelled together with CEAS conferences at Delft and Bucharest. This time EWADE joined the READ conference and arrived at Brno for the second time (Figure 2).

The combined READ&EWADE event strengthened the educational part of the conference and allowed to meet groups of researchers from different parts of Europe. More than 80 participants from 12 countries attended providing a total of 45 presentations. Furthermore, distinguished invited speakers updated the delegates on the newest opportunities for carrying out aeronautics-related research on available research infrastructure and novel research results. I would like to cordially thank the invited speakers, Blanka Lenczowski,

The current issue and full text archive of this journal is available on Emerald Insight at: www.emeraldinsight.com/1748-8842.htm



Aircraft Engineering and Aerospace Technology
91/6 (2019) 805–806
© Emerald Publishing Limited [ISSN 1748-8842]
[DOI 10.1108/AEAT-06-2019-319]

Figure 1 RRDPAE-READ – Travelling Seminar

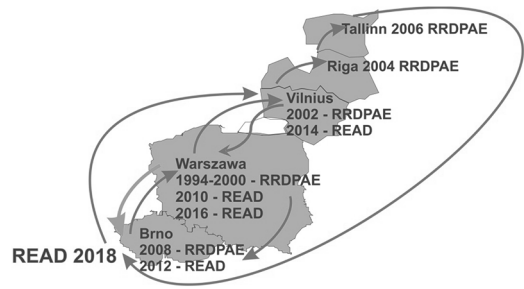
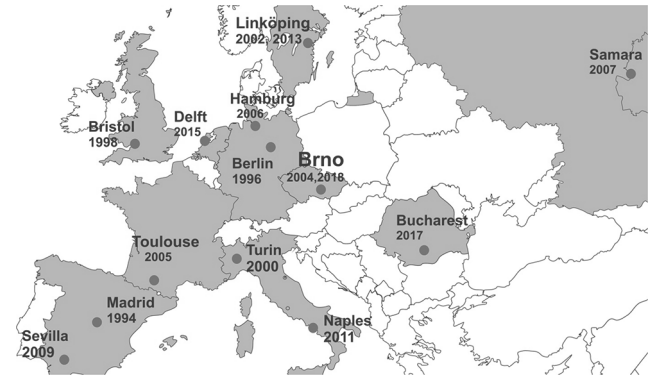


Figure 2 EWADE – Travelling Workshops



Štefan Klein and Milan Šlapák for their interesting presentations.

The following 13 conference papers have been selected for publication in this peer-reviewed special issue:

- 1 Berdnik, Y. and Beskopylny, A., “The approximation method in the problem on a flow of viscous fluid around a thin plate”.
- 2 Goraj, Z.J., Kowalski, M. and Goliszek, B., “Stress, strain and displacement analysis of geodetic and conventional fuselage structure for future passenger aircraft”.
- 3 Masri J., Dala, L. and Huaed, B., “A review of the analytical methods used for seaplanes performance prediction”.
- 4 Šedek, J. and Ruzek, R., “Magna-Lok rivet joint and the stiffness-equivalent FE model”.
- 5 Pobikrowska, K. and Goetzendorf-Grabowski, T., “Stability analysis of the experimental airplane powered by a pulsejet engine”.
- 6 Mieloszyk, J. and Tarnowski, A., “Enhancements in conceptual electric aircraft design”.
- 7 Staack, I., “Establishment of the Swedish Aeronautical Research Center (SARC)”.
- 8 Skawiński, I. and Goetzendorf-Grabowski, T., “FDM 3D printing method utility assessment in small RC aircraft design”.
- 9 Kulhánek, R., “Identification of a degradation of aerodynamic characteristics of a paraglider due to its flexibility from flight test”.
- 10 Kopyt, A., Topczewski, S., Zugaj, M. and Bibik, P., “An automatic system for a helicopter autopilot performance evaluation”.
- 11 Kwiek, A., “Conceptual design of an aircraft for Mars mission”.
- 12 Groth, C., Cella, U., Costa, E. and Biancolini, M.E., “Fast high fidelity CFD/CSM fluid structure interaction using RBF mesh morphing and modal superposition method”.

- 13 Grendysa, W., “Multidisciplinary wing design of a light long endurance UAV”.

The articles deal with different solutions for future aerospace challenges in the areas of novel configuration, aerodynamics, design methods, multidisciplinary optimization, UAV and stress analysis.

With great pleasure, I would like to thank Professor Jaroslav Juračka for his big effort in organization, hosting and co-chairing of the conference. I would also like to thank all authors for writing such excellent technical papers and the reviewers for their insightful critique and suggestions, which

contributed directly to improving the technical content of this Special Issue. Finally, I would like to thank the Editor-in-Chief of the Aircraft Engineering and Aerospace Technology Journal, Dr Askin T. Isikveren, for his agreement and support in making this issue possible.



Tomasz Goetzendorf-Grabowski

*The Faculty of Power and Aeronautical
Engineering, Warsaw University of
Technology, Warsaw, Poland*

The approximation method in the problem on a flow of viscous fluid around a thin plate

Yanina Berdnik

Faculty of Mathematics, Mechanics and Computer Science, Southern Federal University, Rostov-on-Don, Russian Federation, and

Alexey Beskopylny

Don State Technical University, Rostov-on-Don, Russian Federation

Abstract

Purpose – The paper aims to obtain an effective solution to the problem on a flow of viscous fluid around a thin plate using a new approximation method based on the exact Navier–Stokes equations. Also, correction factors are proposed to improve the obtained solution at high Reynolds numbers.

Design/methodology/approach – The paper has opted for a method that is based on an approximation scheme for certain perturbations concerning the velocity of the oncoming unperturbed flow behind a leading edge of the plate as a zero approximation step. The perturbations are assumed to be small, far from the plate when compared to the basic flow to justify the linearization. Numerical methods are used for the integral equations at each approximation step.

Findings – This paper provides the friction force coefficient compared with the classical Blasius solution and the ANSYS results. Also, some diagrams of the velocity distribution in the flow are presented. The first and second approximation steps provide a sufficiently high degree of accuracy.

Research limitations/implications – Because of the chosen research approach, the results may lack accuracy for low and average Reynolds numbers. Thus, researchers are encouraged to improve the proposed method further.

Practical implications – The paper includes implications for the development of an aircraft design or a wind turbine design considering a wing as a thin plate at the first approximation.

Originality/value – This paper provides a new approximation method based on the exact Navier–Stokes equations, in contrast to the known solutions.

Keywords Navier–Stokes equations, Approximation method, Integral equations, Thin rectilinear plate, Viscous fluid

Paper type Research paper

Nomenclature

Symbols

$l = 2a(m)$	= length of the plate;
$U_0(x, y)(m/s)$	= the speed of the oncoming unperturbed flow behind the leading edge of the plate;
Ox	= an axis along the oncoming stream;
Oy	= an axis that is normal to the surface of the plate;
$\rho(kg/m^3)$	= fluid density;
$\nu(m^2/s)$	= kinematic viscosity;
$p(Pa)$	= hydrodynamic pressure;
$v_x(x, y)(m/s)$	= the longitudinal component of the velocity vector;
$v_y(x, y)(m/s)$	= the transverse component of the velocity vector;

$\psi(x, y)(m^2/s)$	= stream function;
$U(x, y)(m/s)$	= the longitudinal component of the main flow velocity;
$V(x, y)(m/s)$	= the transverse component of the main flow velocity;
$v'_x(x, y)(m/s)$	= the longitudinal velocity component of small perturbations that are small, concerning the main flow at the first iteration step;
$v'_y(x, y)(m/s)$	= the transverse velocity component of small perturbations that are small, concerning the main flow at the first iteration step;
$\Psi(x, y)(m^2/s)$	= stream function of the main flow;
$\psi'(x, y)(m^2/s)$	= stream function of the perturbed flow;
$\psi(\alpha, y)(m^2/s)$	= Fourier transform of the function $\psi'(x, y)$;
$\alpha(1/m)$	= Fourier transform parameter;
$\mu(Pa \cdot s)$	= dynamic viscosity;

The current issue and full text archive of this journal is available on Emerald Insight at: www.emeraldinsight.com/1748-8842.htm



Aircraft Engineering and Aerospace Technology
91/6 (2019) 807–813
© Emerald Publishing Limited [ISSN 1748-8842]
[DOI 10.1108/AEAT-07-2018-0196]

Received 5 August 2018
Revised 24 October 2018
Accepted 11 November 2018

$\tau(x)(Pa)$	= general viscous friction function on a plate;
$W_1(N)$	= frictional force on the side of the plate, obtained by the semi-analytical method at the first iteration;
$W_{Blaz}(N)$	= frictional force on the side of the plate, obtained by G. Blasius analytically;
S	= a dimensionless friction coefficient obtained by the semi-analytical method;
S_{Blaz}	= a dimensionless friction coefficient obtained by G. Blasius;
Re	= Reynolds number;
$v'_x(x,y)(m/s)$	= the longitudinal velocity component of small perturbations that are small, concerning the main flow at the second iteration step;
$v''_y(x,y)(m/s)$	= the transverse velocity component of small perturbations that are small, concerning the main flow at the second iteration step;
$\psi''(x,y)(m^2/s)$	= perturbed stream function at the second iteration step;
$\tau'(x)(Pa)$	= viscous friction function obtained at the first iteration step;
$\tau''(x)(Pa)$	= perturbed viscous friction function to the function τ' at the second iteration step;
$b(1/m)$	= an extra parameter;
$K_0\left(\frac{b}{2}\sqrt{\xi^2 + y^2}\right)$	= Macdonald function of the zeroth order;
$K_1\left(\frac{b}{2}\sqrt{\xi^2 + y^2}\right)$	= Macdonald function of the first order;
k, k_1, k_2	= dimensionless correction factors;
S_{ANS}	= a dimensionless parameter whose values are in ANSYS CFX;
S_1	= a dimensionless parameter whose values are calculated at the first iteration by the semi-analytical method; and
S_2	= a dimensionless parameter whose values are calculated at the second iteration by the semi-analytical method.

Definitions, acronyms and abbreviations

HLDE	= homogeneous linear differential equation;
SLE	= system of linear equation; and
LDE	= linear differential equation.

Introduction

The problem of a homogeneous flow of viscous incompressible fluid around a thin rectilinear plate is considered in the present paper. In 1904, Ludwig Prandtl introduced a concept of the boundary layer, which laid the foundation for solving problems of viscous flows around various shapes. Paul Richard Blasius provided a mathematical basis for boundary-layer drag. Thus, the first solution to the problem of laminar flow over a semi-infinite flat plate at zero incidence was obtained by Paul Richard Blasius in the context of boundary layer theory in 1908 (Blasius, 1908). Then, he developed the new results for the problem of laminar flow over a flat plate of finite length at

zero incidence (Loitynskiy, 2003). A few works were published earlier, but they were not fundamental and were not based on adequate theories. That is the reason they are not well known nowadays. Therefore, the problem was mainly considered within the boundary layer theory in the first half of the twentieth century, as Richard von Mises, Walter Tollmien, Hermann Schlichting, Sydney Goldstein and other outstanding scientists thoroughly investigated this theory.

First, the reliability of the theory was confirmed in 1920s. Theodor von Karman verified the Blasius solution and supplemented it with new results for turbulent boundary layers after derived the integral equation across the boundary layer in 1921 (Goldstein, 1930). The experiments were carried out in the 1940s and showed some discrepancies between experimental data and the Blasius solution. As a result, scientists continued researching this problem.

The past few decades have witnessed an increase in interest in the problem owing to improvements in modern technologies in programming and numerical methods (McLachlan, 1991). Researchers are using parallel computing platforms (Kaiyuan *et al.*, 2014) and attractive finite elements software programs, such as ANSYS (Brunschwig and Rondi, 2001), MAPLE, ABAQUS, NASTRAN.

Even though this problem is being solved since the beginning of the twentieth century, it has not been completely solved yet. It is important that nowadays there are no general theories for all Reynolds numbers. However, this task has a wide practical application in aircraft design. Because of these reasons, many researchers from various countries continue to investigate this problem using both semi-analytical and computational methods to solve the Navier–Stokes equations (Feng *et al.*, 2006; Quartapelle, 2012). Currently, the Blasius solution is considered to be a classical solution to the problem for high Reynolds numbers.

Solving the problem

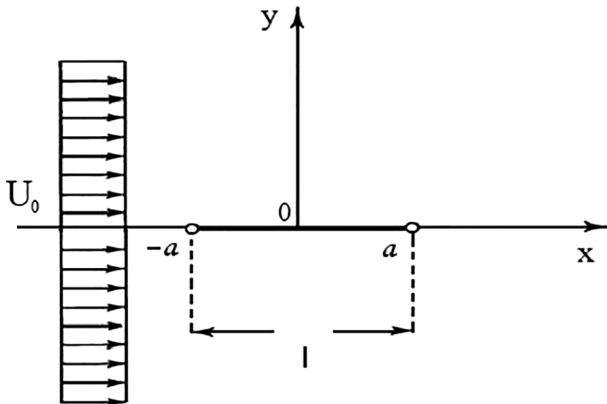
A problem statement and basic hypotheses

In this problem, the infinite uniform flow of an incompressible viscous fluid around an infinitely thin flat plate with length l is carried out. The solving algorithm is considered for a two-dimensional problem. The speed U_0 of the oncoming unperturbed flow behind the leading edge of the plate is constant, and its value is known. While solving the problem, the principal quantity sought is the total frictional force acting on the plate.

Despite the fact that the problem at hand has been considered on several occasions, its investigation is still ongoing; some new results based on boundary layer theory are presented in (Qussai, 2011). In this paper, an approach based on successive approximations concerning velocity perturbations is proposed.

The fluid flow is considered in the Cartesian coordinate system Oxy , where the axis Oy is normal to the surface of the plate and the axis Ox is along the oncoming stream (Figure 1). The origin is located in the middle of the plate $(l/2, 0)$. Taking into account the symmetry of the flow, only the upper half-plane is considered. The fluid flow is assumed to be stationary. Thus, it is described by the continuity equation and the Navier–Stokes equations:

Figure 1 Flow around a flat plate with a length $l = 2a$ of the incoming flow of a viscous liquid at a velocity U_0



$$\begin{cases} \frac{\partial v_x}{\partial x} + \frac{\partial v_y}{\partial y} = 0 \\ v_x \frac{\partial v_x}{\partial x} + v_y \frac{\partial v_x}{\partial y} - \nu \Delta v_x + \frac{1}{\rho} \frac{\partial p}{\partial x} = 0 \\ v_x \frac{\partial v_y}{\partial x} + v_y \frac{\partial v_y}{\partial y} - \nu \Delta v_y + \frac{1}{\rho} \frac{\partial p}{\partial y} = 0 \end{cases} \quad (1)$$

where, ρ represents fluid density, ν represents kinematic viscosity, p represents hydrodynamic pressure and v_x and v_y represent longitudinal and transverse components of the velocity vector, respectively.

The boundary conditions of the problem have the following form:

- the conditions of the fluid adhesion on the plate surface: $v_x = v_y = 0$ for $y = 0, |x| \leq a$;
- symmetry conditions outside the plate: $v_y = 0, \frac{\partial v_x}{\partial y} = 0$ for $y = 0, |x| > a$; and
- conditions for $y \rightarrow +\infty, x \in (-\infty, +\infty)$ at infinity: $v_y \rightarrow 0, v_x \rightarrow U_0$.

Construction of the basic algorithm for solving the problem: the first approximation step

Let us demonstrate the proposed semi-analytical method of successive approximations for the first approximation step. The Navier–Stokes equations should be simplified before solving by numerical methods. In connection with the lack of experimental data in the literature, the solution obtained at each step is compared with the Blasius solution (Schlichting, 1955).

The longitudinal and transverse velocity components are represented as the sum of the main flow velocity and the velocity of small perturbations marked with primes, which are small on its background:

$$\begin{cases} v_x(x, y) = U(x, y) + v'_x(x, y) \\ v_y(x, y) = V(x, y) + v'_y(x, y) \end{cases} \quad (2)$$

Nonetheless, the number of function primes corresponds to the iteration number.

The stream function $\psi = \psi(x, y)$ is introduced by the following relations:

$$v_x = \frac{\partial \psi}{\partial y}, v_y = -\frac{\partial \psi}{\partial x} \quad (3)$$

Thus, the expression of the stream function is similar to the expansion of velocities in equation (2) at the first iteration: $\psi(x, y) = \Psi(y) + \psi'(x, y), \Psi(y) = U_0 y$. Eliminating the pressure from equation (1) and taking into account equations (2) and (3), the resulting equation is linearized concerning small perturbations $\psi'(x, y)$. The form of the determined linear partial differential equation is the same for all approximation steps:

$$\begin{aligned} -U \Delta V + U \frac{\partial \Delta \psi'}{\partial x} - \Delta V \frac{\partial \psi'}{\partial y} + V \Delta U + V \frac{\partial \Delta \psi'}{\partial y} - \Delta U \frac{\partial \psi'}{\partial x} \\ - \nu \Delta^2 \Psi - \nu \Delta^2 \psi' = 0 \end{aligned} \quad (4)$$

When realizing the first approximation of the solution to the problem, it is assumed that a velocity vector coincides with $\{U_0, 0\}$ at the zero step. Thus, at the first approximation step, velocities of small perturbations are considered regarding the constant velocity U_0 ; therefore, there are the following expressions at the first step: $U(x, y) = U_0, V(x, y) = 0$.

While constructing the first iteration, a velocity perturbation near the plate, equaled $\{-U_0, 0\}$ by the adhesion condition, is not small compared to the main stream velocity U_0 . However, in an integral metric over a sufficiently large flow region enclosing the plate, the perturbation will be small in comparison with the same integral value of the velocity U_0 . It will be shown below that full speed has the behavior satisfying all the required conditions, even for the first approximation.

The Fourier transform of x is, therefore, applied to the simplified differential equation (4), considering the assumptions made. The result is a fourth-order homogeneous linear differential equation with constant coefficients solved analytically:

$$\begin{aligned} \nu \frac{d^4 \tilde{\psi}'(\alpha, y)}{dy^4} - (U_0 i \alpha + 2\nu \alpha^2) \frac{d^2 \tilde{\psi}'(\alpha, y)}{dy^2} \\ + (\nu \alpha^4 + U_0 i \alpha^3) \tilde{\psi}'(\alpha, y) = 0 \end{aligned} \quad (5)$$

where, $\tilde{\psi}'(\alpha, y)$ represents Fourier transform of the function $\psi'(x, y)$ and α represents Fourier transform parameter.

The solution to equation (5) bounded in the upper half-plane contains two arbitrary constants. They are found from two relations, one of which is the adhesion boundary condition: $v'_y = 0 \sim \psi' = 0, y = 0, |x| < \infty$, while the second one is a given viscous friction if it is temporarily considered as a known function:

$$\mu \frac{\partial v_x}{\partial y} \Big|_{y=0} = \begin{cases} 0, & |x| > a \\ \tau(x), & |x| \leq a \end{cases} \quad (6)$$

where, μ represents dynamic viscosity and $\tau(x)$ represents viscous friction function on a plate.

Consequently, the first boundary condition of the longitudinal component of the perturbed velocity is presented as follows:

$$v'_x = -U_0 \sim \frac{\partial \psi'}{\partial y} = -U_0, (y = 0, |x| \leq a)$$

and leads to a boundary integral equation regarding a function $\tau(\xi)$:

$$\frac{\nu}{2\pi i \rho U_0} \int_{-a}^a \tau(\xi) d\xi \int_{-\infty}^{+\infty} \frac{|\alpha| - \sqrt{\alpha^2 + \frac{i\alpha U_0}{\nu}}}{\alpha} \cdot e^{i\alpha(\xi-x)} d\alpha = -U_0, |x| \leq a \tag{7}$$

A similar integral equation was derived in 1986 (Alexandrov and Kovalenko, 1986).

It should be noted that the analysis of the integral equation (7) kernel properties has revealed the following properties:

- The kernel is neither even nor odd. Thus, the solution to the integral equation (7) does not have any kind of symmetry.
- The kernel has a standard logarithmic singularity at $x \rightarrow \xi$. Thus, the solution has a root feature at the ends of the plate: when approaching the edges of the plate, the tangential stresses increase indefinitely.

After constructing a numerical solution of the equation (7), the components of the longitudinal and transverse flow velocities are determined explicitly at the first iteration step:

$$v_x(x,y) = U_0 - \frac{1}{2\pi i \rho U_0} \int_{-a}^a \tau(\xi) d\xi \int_{-\infty}^{+\infty} \left(\sqrt{\alpha^2 + \frac{i\alpha U_0}{\nu}} \cdot e^{-\sqrt{\alpha^2 + \frac{i\alpha U_0}{\nu}} y} - |\alpha| e^{-|\alpha| y} \right) e^{i\alpha(\xi-x)} \frac{d\alpha}{\alpha} \tag{8}$$

$$v_y(x,y) = -\frac{1}{2\pi \rho U_0} \int_{-a}^a \tau(\xi) d\xi \int_{-\infty}^{+\infty} \left(e^{-|\alpha| y} - e^{-\sqrt{\alpha^2 + \frac{i\alpha U_0}{\nu}} y} \right) e^{i\alpha(\xi-x)} d\alpha \tag{9}$$

The analytical integral equation (7) obtained is solved numerically at this stage. When using the collocation method, this equation results in solving a system of linear equations regarding a function τ . This system is solved by the Gauss method. The most important numerical calculation results are the values of the frictional force W_1 acting on the plate, but it is also possible to determine the longitudinal and transverse velocity components numerically from equations (8) and (9) at an arbitrary point in the flow.

The following dimensionless quantity is brought into consideration to compare the results received at the first iteration:

$$S_1 = 0.664 W_1 / W_{Blaz} \tag{10}$$

where, W_1 is the frictional force on the side of the plate computed by numerical calculations, $W_{Blaz} = 0.664 U_0^2 \sqrt{\frac{2a\nu}{U_0}}$ is the same quantity of the Blasius solution obtained analytically (Schlichting, 1955). Thus, the value of the dimensionless friction coefficient S_{Blaz} is equal to a constant value of 0.664 for any values of the parameters α, ρ, ν, U_0 , i.e. $S_{Blaz} = 0.664$.

The Blasius solution was received when approximated according to the Prandtl thin boundary layer theory, so it is valid in the case of high Reynolds numbers. The solution obtained in this paper is compared with the Blasius solution for various Reynolds numbers ($Re = \frac{2aU_0}{\nu}$) using the parameters S at each iteration step.

The second approximation step

At the second approximation step, the required small perturbation functions (denoted by two primes) are examined against the background of the first step functions:

$$\begin{cases} v_x(x,y) = U_0 + v'_x(x,y) + v''_x(x,y) = U(x,y) + v''_x(x,y) \\ v_y(x,y) = v'_y(x,y) + v''_y(x,y) = V(x,y) + v''_y(x,y) \end{cases} \tag{11}$$

Whereas, at the second iteration, as the relations from equation (11) show, functions $U(x,y), V(x,y)$ are received from the first iteration and have the following forms: $U(x,y) = U_0 + v'_x(x,y), V(x,y) = v'_y(x,y)$.

Moreover, acting, in the same way, like at the first iteration, the linearized partial differential equation concerning the perturbed stream function $\psi''(x,y)$ is received. The functions $U(x,y)$ and $V(x,y)$ in the resulting partial differential equation are “frozen” by the variable x , the Fourier transform of x is furthermore applied to the equation determined. Therefore, the result of these transformations is a fourth-order non-homogeneous linear differential equation (LDE) with variable coefficients, the solution of which has been obtained using some asymptotic and numerical methods specified in the source (Berdnik, 2014).

However, our numerical experiments show that a calculation can be much more stable and accurate while constructing the second iteration using another method. The method is based on the fact that the length of the intervals of the boundary-layer solution near the ends of the plate is asymptotically small at high Reynolds numbers. The ends, therefore, can be moved to infinity in the first approximation. In this case, the “external” solution outside the boundary layers does not depend on the variable x . Thus, in the simplest case, the second iteration can be constructed assuming that all functions of equation (4) do not depend on the variable x . Therefore, the following boundary value problem for a fourth-order LDE with variable coefficients is at hand:

$$\frac{d^4 \psi''}{dy^4} - \frac{V(y)}{\nu} \frac{d^3 \psi''}{dy^3} + \frac{1}{\nu} \frac{d^2 V(y)}{dy^2} \frac{d\psi''}{dy} = -\frac{U(y)}{\nu} \frac{d^2 V(y)}{dy^2} + \frac{V(y)}{\nu} \frac{d^2 U(y)}{dy^2} - \frac{d^3 U(y)}{dy^3} \tag{12}$$

with the boundary conditions:

$$\frac{d^2 \psi''(y)}{dy^2} \Big|_{y=0} = \frac{\tau''(x)}{\mu}; \psi''(y) \Big|_{y=0} = 0 \tag{13}$$

$$\psi''(y) \Big|_{y \rightarrow +\infty} \rightarrow 0; \frac{d\psi''(y)}{dy} \Big|_{y \rightarrow +\infty} \rightarrow 0 \tag{14}$$

which is solved by the shooting method using the fourth-order Runge–Kutta method (Hafez, 2003). Here, $\tau''(x)$ is the perturbed viscous friction function to the function $\tau'(x)$ constructed in the first approximation.

The coefficients $U(y)$, $\frac{d^2 U}{dy^2}(y)$ are found from the first approximation and have the following forms:

$$U(y) = -\frac{1}{2\pi i \rho U_0} \int_{-a}^a \tau(\xi) d\xi \int_{-\infty}^{+\infty} \left(\sqrt{\alpha^2 + \frac{i\alpha U_0}{\nu}} \cdot e^{-\sqrt{\alpha^2 + \frac{i\alpha U_0}{\nu}} y} - |\alpha| e^{-|\alpha| y} \right) e^{i\alpha \xi} \frac{d\alpha}{\alpha} \tag{15}$$

$$\frac{d^2 U(y)}{dy^2} = -\frac{1}{2\pi i \rho U_0} \int_{-a}^a \tau(\xi) d\xi \int_{-\infty}^{+\infty} \left(\left(\alpha^2 + \frac{i\alpha U_0}{\nu} \right)^{3/2} e^{-\sqrt{\alpha^2 + \frac{i\alpha U_0}{\nu}} y} - |\alpha|^3 e^{-|\alpha| y} \right) e^{i\alpha \xi} \frac{d\alpha}{\alpha} \tag{16}$$

Thus, the integrals over the variable α in equations (15) and (16) are taken analytically through the methods described in Abramowitz and Stegun (1972); Bateman and Erdélyi (1954); and Sumbatyan and Scalia (2005). This greatly facilitates the further problem solution, as the calculation time of functions $U(y)$, $\frac{d^2 U}{dy^2}(y)$ is reduced from several hours while using quadrature formulas to several minutes.

As a result, these functions are represented as follows:

$$U(y) = -\frac{1}{2\pi \rho U_0} \int_{-a}^a \tau(\xi) \left(be^{\frac{b\xi}{2}} \left(\frac{\xi}{\sqrt{\xi^2 + y^2}} K_1 \left(\frac{b}{2} \sqrt{\xi^2 + y^2} \right) + K_0 \left(\frac{b}{2} \sqrt{\xi^2 + y^2} \right) \right) - \frac{2\xi}{\xi^2 + y^2} \right) d\xi \tag{17}$$

$$\frac{d^2 U(y)}{dy^2} = -\frac{1}{2\pi \rho U_0} \int_{-a}^a \tau(\xi) \left(be^{\frac{b\xi}{2}} \frac{d^2}{dy^2} \left(\frac{\xi}{\sqrt{\xi^2 + y^2}} K_1 \left(\frac{b}{2} \sqrt{\xi^2 + y^2} \right) + K_0 \left(\frac{b}{2} \sqrt{\xi^2 + y^2} \right) \right) - \frac{4\xi(3y^2 - \xi^2)}{(\xi^2 + y^2)^3} \right) d\xi \tag{18}$$

where, $K_0 \left(\frac{b}{2} \sqrt{\xi^2 + y^2} \right)$ and $K_1 \left(\frac{b}{2} \sqrt{\xi^2 + y^2} \right)$ represents Macdonald functions of the zeroth and the first order respectively, $b = \frac{U_0}{\nu}$.

Similarly, the functions $V(y)$, $\frac{d^2 V(y)}{dy^2}$ and $\frac{d^3 U(y)}{dy^3}$ have the form:

$$V(y) = -\frac{1}{2\pi \rho U_0} \int_{-a}^a \tau(\xi) \left(\frac{2y}{\xi^2 + y^2} - \frac{e^{\frac{b\xi}{2}} by}{\sqrt{\xi^2 + y^2}} K_1 \left(\frac{b}{2} \sqrt{\xi^2 + y^2} \right) \right) d\xi \tag{19}$$

$$\frac{d^2 V(y)}{dy^2} = -\frac{1}{2\pi \rho U_0} \int_{-a}^a \tau(\xi) \left(\frac{d^2}{dy^2} \left(\frac{e^{\frac{b\xi}{2}} by}{\sqrt{\xi^2 + y^2}} K_1 \left(\frac{b}{2} \sqrt{\xi^2 + y^2} \right) \right) + \frac{4y(y^2 - 3\xi^2)}{(\xi^2 + y^2)^3} \right) d\xi \tag{20}$$

$$\frac{d^3 U(y)}{dy^3} = -\frac{1}{2\pi \rho U_0} \int_{-a}^a \tau(\xi) \left(be^{\frac{b\xi}{2}} \frac{d^3}{dy^3} \left(\frac{\xi}{\sqrt{\xi^2 + y^2}} K_1 \left(\frac{b}{2} \sqrt{\xi^2 + y^2} \right) + K_0 \left(\frac{b}{2} \sqrt{\xi^2 + y^2} \right) \right) + \frac{48\xi y(y^2 - \xi^2)}{(\xi^2 + y^2)^4} \right) d\xi \tag{21}$$

Table I provides the calculations obtained at the first and second approximations. These results are compared with the Blasius solution while S_{ANS} – parameter values calculated in ANSYS CFX, S_1 and S_2 are parameters of S values calculated within the framework of the proposed method at the first and second iterations, respectively.

As shown in the Table I, all dimensionless parameters from the first three columns take much larger values than S_{Blaz} at low Reynolds numbers. The reason is that the Blasius solution is only valid in the case of high Reynolds numbers. All three parameters decrease monotonously with increasing values of Reynolds numbers tending to 0.664. As the results of the second iteration are closer to both the results computed by ANSYS CFX and the Blasius solution for almost all Reynolds numbers, it can be concluded that the second iteration does refine the values obtained at the first iteration.

As the parameters S_1 and S_2 take sustainable values at $Re \geq 1800$, it is possible to introduce correction factors k_1 and k_2 so that the S_1 and S_2 values are close to the Blasius solution at high Reynolds numbers. These correction factors are, therefore, to have the following values: $k_1 = 0.58$, $k_2 = 0.91$. Thus, the relative error of S_1 at $Re \geq 1800$ is within 1 per cent

Table I Dependence of the parameters S_{ANS} , S_1 , S_2 on Reynolds numbers $Re = \frac{2aU_0}{\nu}$: $\rho = 1$ (kg/m³), $\nu = 10^{-3}$ (m²/s), $l = 2a = 1$ (m) with changing values U_0 (m/s)

Re	S_{ANS}	S_1	S_2	S_{Blaz}
100	0.9379	1.2137	1.0014	0.664
150	0.8992	1.2	0.9624	0.664
200	0.8781	1.1915	0.9363	0.664
300	0.8616	1.1818	0.8968	0.664
400	0.8427	1.1762	0.8649	0.664
500	0.8232	1.1724	0.8378	0.664
1000	0.7984	1.1631	0.7580	0.664
1100	0.7746	1.1621	0.7502	0.664
1200	0.7674	1.1611	0.7441	0.664
1300	0.7624	1.16	0.7396	0.664
1400	0.7588	1.1597	0.7364	0.664
1500	0.7559	1.1591	0.7343	0.664
1600	0.7538	1.1585	0.7331	0.664
1700	0.7521	1.1580	0.7327	0.664
1800	0.7512	1.1578	0.7326	0.664

of S_{Blaz} while the relative error S_2 at $Re \geq 1800$ is within 0.4 per cent of S_{Blaz} .

There is also a plot below (Figure 2) representing the longitudinal component distribution of the velocity vector at the first and second approximation steps for the following flow parameters: $\rho = 1 \text{ (kg/m}^3\text{)}$, $\nu = 10^{-3} \text{ (m}^2\text{/s)}$, $l = 2a = 1 \text{ (m)}$. The Reynolds numbers vary according to the selected velocity of the oncoming stream $U_0 \text{ (m/s)}$.

Conclusions

The work has been carried out to find the quantities required both at the first approximation and at the second one. As shown in this paper, there is a semi-analytical method and a numerical one using only ANSYS calculation, which can be used to solve a problem on a laminar flow around a flat plate. Theoretical values of friction force dimensionless S_1 and S_2 parameters have been compared with numerical data of S_{ANS} and those predicted from the Blasius theory given by the S_{Blaz} parameter. The results for both methods provide a sufficiently high degree of accuracy. From the data obtained, it can be concluded that the final results have proved to be very important. Undoubtedly, the approach offered has advantages over numerical realization in ANSYS CFX and the method of G. Blasius. In the first case, the advantage is the small amount of time required to calculate the values (several minutes for one value instead of several hours in the ANSYS CFX environment). Of special importance is the correction factor k_2 , because of which some errors were eliminated at the second iteration for high Reynolds numbers. This approach, therefore, presents more precise results (especially using a correction factor), than ANSYS CFX does. However, the method has some

limitations. The solution obtained is not valid near the edges of the plate, as the edge effects strongly influence the solution of the linear problem. The method is also best suited in evaluating high speeds.

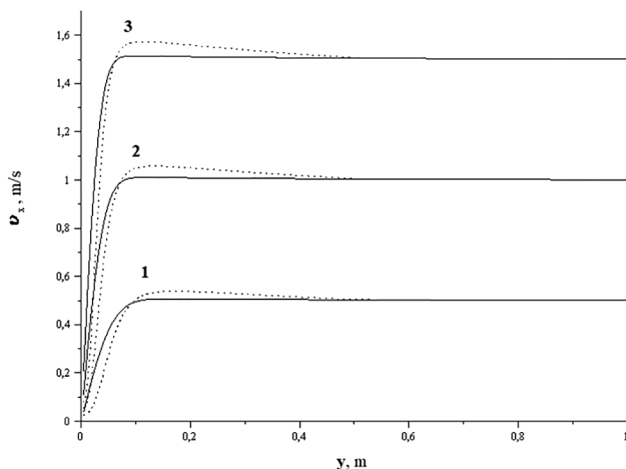
Despite the fact that there is not a good accuracy for the friction force acting on the plate at the first iteration, the good results for the distribution of velocities have been found at both iterations (Figure 2). It has been obtained that the main flow velocity in the longitudinal direction $v_x(x, y)$, satisfying the boundary conditions of adhesion, tends to a constant value. At the second iteration, the velocity curves show higher physical reliability than those at the first iteration as they do not show “peaks” in the range from $y = 0.1 \text{ (m)}$ to $y = 0.5 \text{ (m)}$.

As a result, the approach described lays a foundation for the further development of the semi-analytical method in the problems on flows or gases around plates, as well as around objects of different shapes for various Reynolds numbers.

References

- Abramowitz, M. and Stegun, I. (1972), *Handbook of Mathematical Functions with Formulas, Graphs, and Mathematical Tables*, US Government Printing Office, Dover, New York, NY.
- Alexandrov, V.M. and Kovalenko, E.V. (1986), *Problems with Mixed Boundary Conditions in Continuum Mechanics*, Nauka, Moscow.
- Bateman, H. and Erdélyi, A. (1954), *Tables of Integral Transforms*, McGraw-Hill, New York, NY.
- Berdnik, Y.A. (2014), “The iterative method for the stationary Navier-Stokes equations in the problem on a flow around a linear plate”, *University News: North-Caucasian Region. Social Sciences Series*, Vol. 179 No. 1, pp. 30-34.
- Blasius, H. (1908), “Grenzschichten in flüssigkeiten mit kleiner reibung”, *Zeitschrift Für Angewandte Mathematik Und Physik*, Vol. 56, pp. 1-37.
- Brunschwig, A. and Rondi, C. (2001), “Laminar flow across a flat plate”, *Journal of Numerical Analysis for Engineering*, pp. 1-18.
- Feng, X.F., Tian, Z.F. and Dai, S.Q. (2006), “Numerical solution of the incompressible Navier-Stokes equations with exponential type schemes”, *International Journal of Computer Mathematics*, Vol. 82 No. 9, pp. 1167-1176.
- Goldstein, S. (1930), “Concerning some solutions of the boundary layer equations in hydrodynamics”, *Mathematical Proceedings of the Cambridge Philosophical Society*, Vol. 26 No. 1, pp. 1-30.
- Hafez, M.M. (2003), *Numerical Simulations of Incompressible Flows*, World Scientific, Singapore.
- Kaiyuan, L., Zhaohua, Y. and Qiaohong, L. (2014), “Some experiences of improving the speed of numerical Navier-Stokes solver using CUDA”, *Journal of Algorithms & Computational Technology*, Vol. 8, pp. 287-300.
- Loytysanskiy, L.G. (2003), *Mechanics of Fluid and Gas*, Drofa, Moscow.
- McLachlan, R.I. (1991), “The boundary layer on a finite flat plate”, *Physics of Fluids A*, Vol. 3 No. 2, pp. 341-348.

Figure 2 Distribution of longitudinal velocity v_x at the first and second iterations, depending on the coordinate y at various values of $U_0 \text{ (m/s)}$ ($Re = \frac{2aU_0}{\nu}$): $\rho = 1 \text{ (kg/m}^3\text{)}$, $\nu = 10^{-3} \text{ (m}^2\text{/s)}$, $l = 2a = 1 \text{ (m)}$, $x = 0$



Notes: A dotted line points to the first iteration, a solid line point to the second iteration; lines 1 – $U_0 = 0.5 \text{ m/s}$ ($Re = 500$), lines 2 – $U_0 = 1 \text{ m/s}$ ($Re = 1,000$) and lines 3 – $U_0 = 1.5 \text{ m/s}$ ($Re = 1,500$)

- Quartapelle, L. (2012), *Numerical Solution of the Incompressible Navier-Stokes Equations*, Birkhäuser-Verlag, Basel.
- Qussai, J.A. (2011), "A general velocity profile for a laminar boundary layer over flat plate with zero incidence", *Journal of Engineering*, Vol. 17, pp. 1614-1622.
- Schlichting, H. (1955), *Boundary-layer Theory*, McGraw-Hill, New York, NY.

- Sumbatyan, M.A. and Scalia, A. (2005), *Equations of Mathematical Diffraction Theory*, CRC Press, Boca Raton, FL.

Corresponding author

Yanina Berdnik can be contacted at: yaninaberdnik@mail.ru

Stress, strain and displacement analysis of geodetic and conventional fuselage structure for future passenger aircraft

Zdobyslaw Jan Goraj, Mariusz Kowalski and Bartlomiej Goliszek

Faculty of Power and Aeronautical Engineering, Warsaw University of Technology, Warszawa, Poland

Abstract

Purpose – This paper aims to present the results of calculations that checked how the longerons and frames arrangement affects the stiffness of a conventional structure. The paper focuses only on first stage of research – analysis of small displacement. Main goal was to compare different structures under static loads. These results are also compared with the results obtained for a geodetic structure fuselage model of the same dimensions subjected to the same internal and external loads.

Design/methodology/approach – The finite element method analysis was carried out for a section of the fuselage with a diameter of 6.3 m and a length equal to 10 m. A conventional and lattice structure – known as geodetic – was used.

Findings – Finite element analyses of the fuselage model with conventional and geodetic structures showed that with comparable stiffness, the weight of the geodetic fuselage is almost 20 per cent lower than that of the conventional one.

Research limitations/implications – This analysis is limited to small displacements, as the linear version of finite element method was used. Research and articles planned for the future will focus on nonlinear finite element method (FEM) analysis such as buckling, structure stability and limit cycles.

Practical implications – The increasing maturity of composite structures manufacturing technology offers great opportunities for aircraft designers. The use of carbon fibers with advanced resin systems and application of the geodetic fuselage concept gives the opportunity to obtain advanced structures with excellent mechanical properties and low weight.

Originality/value – This paper presents very efficient method of assessing and comparison of the stiffness and weight of geodetic and conventional fuselage structure. Geodetic fuselage design in combination with advanced composite materials yields an additional fuselage weight reduction of approximately 10 per cent. The additional weight reduction is achieved by reducing the number of rivets needed for joining the elements. A fuselage with a geodetic structure compared to the classic fuselage with the same outer diameter has a larger inner diameter, which gives a larger usable space in the cabin. The approach applied in this paper consisting in analyzing of main parameters of geodetic structure (hoop ribs, helical ribs and angle between the helical ribs) on fuselage stiffness and weight is original.

Keywords Composites, FEM analysis, Geodetic fuselage, Stiffness analysis

Paper type Case study

Introduction

The targets for future aircraft get more demanding every year, and this stimulates the continuous development of aircraft structures and systems. Organizations such as the European Commission or Advisory Council for Aviation Research and Innovation in Europe (ACARE) put a great emphasis on the protection of the natural environment and formulate very demanding requirements [European Commission, 2011; Advisory Council for Aviation Research and Innovation in Europe (ACARE), 2012]. For example, regarding the emission of harmful gases, improvements should be made not only to airplane structures but also to the whole Air Transport System. The increasing maturity of composite structures manufacturing

technology offers great opportunities for aircraft designers. The use of carbon fibers with advanced resin systems gives the opportunity to obtain advanced structures with excellent mechanical properties and low weight (Botelho *et al.*, 2006) (Figure 1).

The geodetic fuselage concept has been known for many years. Such a structure in aluminum was used for the production of a Vickers aircraft during the Second World War (Buttler, 2004).

Currently, much research on such structures, but made of advanced composites, is being carried out. Previous studies have shown that the use of a geodetic structure for fuselages may be beneficial in terms of both weight reduction and structure stiffness, compared to the conventional structure

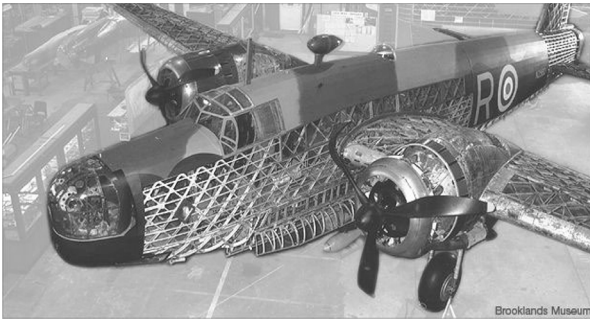
The current issue and full text archive of this journal is available on Emerald Insight at: www.emeraldinsight.com/1748-8842.htm



Aircraft Engineering and Aerospace Technology
91/6 (2019) 814–819
© Emerald Publishing Limited [ISSN 1748-8842]
[DOI 10.1108/AEAT-07-2018-0216]

This paper was written thanks to funding of the project “ConcEpt validation sTudy foR fusElage wake-fillIng propulsioN integration (CENTRELINE)” No 723242 funded from European Union’s Horizon 2020 research and innovation program.

Received 31 July 2018
Revised 24 September 2018
Accepted 9 October 2018

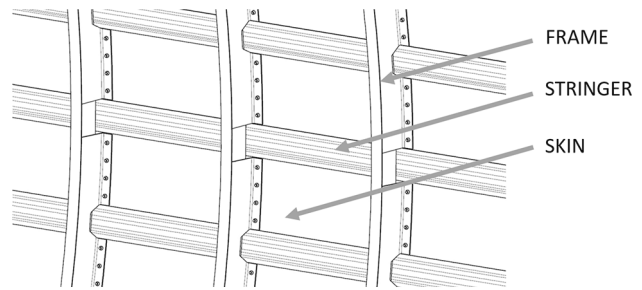
Figure 1 Vickers Wellington, photo courtesy of Brooklands Museum

(Hühne, 2013; Vasiliev *et al.*, 2012). The aim of this paper is to present the results of calculations which checked how the longerons and frames arrangement affects the conventional structure stiffness. These results are also compared to the results obtained for the geodetic structure fuselage model (Goraj *et al.*, 2018) of the same dimensions subjected to the same internal and external loads. This paper focuses only on the first stage of research – analysis of small displacement. Main goal was to compare different structures under static loads. Further research and articles will focus on nonlinear finite element method (FEM) analysis such as buckling, structure stability and limit cycles. However, such an analysis is very complicated and time-consuming, and the result of them will be presented in upcoming papers.

Geodetic and conventional fuselage structure

Conventional (or classic) fuselage structure is an example of a semi-monocoque structure, which has been widely used in commercial aviation for a very long time. This technology was an evolution of the original monocoque structure, which had some disadvantages. However, in monocoque structures of significant size, the problem with strength to mass ratio occurred. A low strength to mass ratio is usually caused by the high weight of the skin, which had to be sufficiently stiff and durable to carry all bending loads. Conventional fuselage structure, like the monocoque structure, consists of frames and skin but has also additional strengthening longerons that extend along the entire length of the fuselage and help to maintain the highest bending loads. Moreover, the longerons prevent the skin from buckling. Frames are used to maintain the shape of the fuselage cross-sections as well as increasing the longerons buckling strength. They also allow the application of concentrated loads to the airframe. All abovementioned elements are connected with rivets, bolts, screws and nuts. Originally, conventional structures were made mainly of aluminum alloys. Nowadays, metal has been replaced by composite materials, but the conventional structure concept remained unchanged. An example of a conventional fuselage structure is presented in Figure 2.

Currently, an old type of design for the airframes, the geodetic structure developed in 1930s, is reconsidered in connection with progress and maturity of composite technology. A geodetic structure made of aluminum was used

Figure 2 Conventional fuselage structure, a generic scheme

Source: Gibson (2016)

for the first time in the construction of the Wellington Mk. X HE239 aircraft. The biggest problem with those structures at that time was the complicated strength calculations (Michalski, 2016).

Geodetic fuselage structures consist of an external shell and ribs grid. The external shell in this structure is responsible mainly for carrying the internal pressure loads. Geodetic grid made of unidirectional carbon fiber composite is responsible mainly for carrying external loads. The load carrying grid consists of hoop and helical ribs that entwine the fuselage. Helical ribs act like diagonals of a rectangular element lying on a cylindrical shell subjected to twisting – one diagonal is extended and the other shortened. Thanks to this principle, the loads acting on the opposite ribs are eliminated. According to research carried out so far, a geodetic fuselage design in combination with advanced composite materials yields an additional fuselage weight reduction of approximately 10 per cent (Hühne, 2013). The additional weight reduction is achieved by reducing the number of rivets needed for joining the elements. A fuselage with a geodetic structure compared to the classic fuselage with the same outer diameter has a larger inner diameter, which gives a larger usable space in the cabin. A fuselage sample with geodetic structure is presented in Figure 3.

Conventional fuselage FEM analysis

The finite element method analysis was carried out for a section of the fuselage with a diameter of 6.3 m and a length equal to 10 m. A conventional structure was used. The purpose of the calculations was to check how the number of longerons and frames affects the rigidity of the structure and to compare the obtained results with those obtained for the geodetic structure. In both cases, the same load pattern was used. The fuselage model was fixed on the one side, with a bending moment applied to the other side of the sample. An internal pressure of 0.0763 MPa (European Aviation Safety Agency, 2007) was applied to the inner surface of the cylindrical section. Loads and constraints are presented in Figure 4 below.

To perform FEM calculations, a surface model was prepared, generated on the basis of a parametric computer aided design model (Goraj *et al.*, 2018). This model made it possible to quickly prepare six different versions of the conventional structure. The influence of three parameters,

Figure 3 Geodetic structure, skin (purple), helical ribs (green) and hoop ribs (yellow)

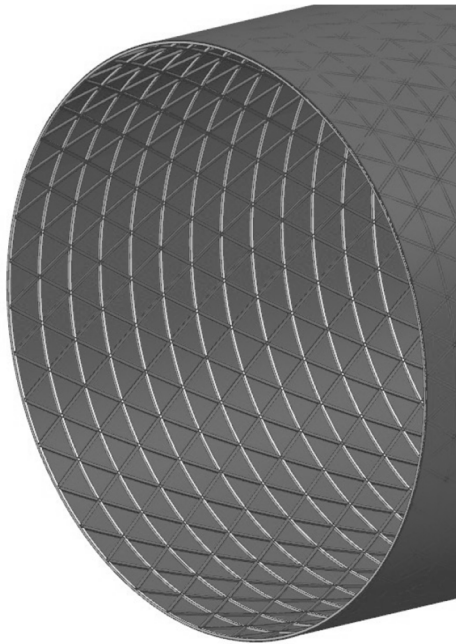
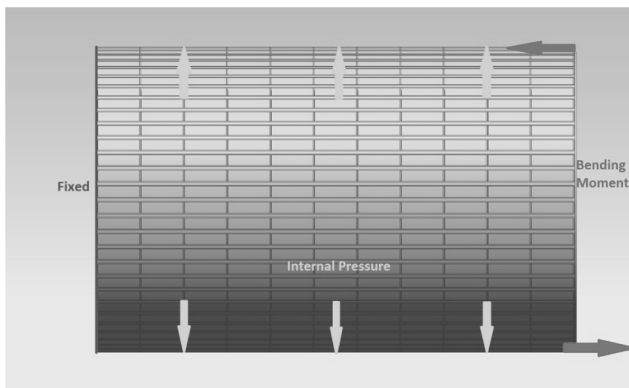


Figure 4 Loads and constraints used for the calculations



including number of longerons, number of frames and thickness of the frame on the state of stress, strain and displacement were investigated. The initial case – a baseline – corresponds to a fuselage with 80 longerons 1 mm thick and 20 frames with a thickness of 2 mm. For all cases, the outer shell consists of four layers of carbon fiber fabric and a 1-mm thick polyurethane core. The total thickness of the external shell is therefore equal to 2.32 mm. Version 1 was treated as a reference case (baseline). In Version 2, the number of longerons has been changed to 60. In Version 3, both the number of longerons and frames were reduced to 60 and 12, respectively. Version 4 was equipped with 80 longerons and 12 frames, the fifth version is analogous to Version 4, but the thickness of the frames was changed to 4 mm, whereas Version 6 is a case similar to 3 but with frames of 4 mm thick. The differences between individual versions are illustrated in Table I.

Table I contains also the information about the total weight for each version. For the baseline, the total weight of the analyzed structure is equal to 786.8 kg. The weight of the external shell is 433 kg, and it is the same for all versions being tested. For the baseline, the skin constitutes 55 per cent of the total weight. In the FEM modeling of the fuselage section, two-dimensional four-node elements were used. The maximum size of the finite elements used in the case of the external shell is 50 mm, whereas for the longerons and frames, it is 30 mm. The layout of the external shell, sizes of the sample and the loads scenario are the same as for the previously analyzed geodetic fuselage (Goraj *et al.*, 2018). Conducted analyses of the conventional structure have shown that for the baseline, the displacement of the “grid” created by the longerons and frames, amounted to 36.04 mm. A contour map of the displacement in the load carrying structure is shown in Figure 5.

The modification introduced in the second version consisted in the reduction of the number of longerons to 60. Owing to this modification, it was possible to achieve both an increase in stiffness and a reduction in the weight of the structure. In Version 2, displacement of frames and longerons decreased to 29.97 mm, which means that the result is improved by 17 per cent compared to the baseline. The weight of the structure has also been reduced by 5.6 per cent compared to the baseline. In this case, the reduction of the number of longerons caused a stiffening of the structure. This effect was achieved probably by increasing the rigidity of frames by limiting the number of cutouts for longerons. In the applied load scenario, the frames are under higher loads than longerons and therefore more responsible for transferring the loads. In the third version, in addition to reducing the number of longerons (to 60 from 80), the number of frames has also been reduced – to 12 from 20. In this case, the displacement of the grid is 32.03 mm, which is 11.1 per cent less than for the baseline. This result is slightly worse than in Version 2, but the weight of the structure has decreased significantly. Compared to the baseline, Version 3 is lighter by almost 15 per cent. In the fourth version, the number of longerons was kept equal to that of baseline, and the number of frames was reduced to 12. In this case, the rigidity of the structure was decreased. Displacement equal to 38.25 mm was recorded which means it is higher by 6.1 per cent than in the case of the baseline. Analysis of this case confirms the conclusions drawn after calculating Version 2. Because the frames are responsible for carrying the loads, so increasing the number of cutouts in frames in Version 4 resulted in a reduction of stiffness. To obtain a better rigidity, the thickness of the frames for Cases 5 and 6 was set to 4 mm, twice as high as in Cases 1–4. In Version 5, in which 80 longerons and 12 frames were used, it was possible to obtain the stiffness 36.4 per cent better, however, with an increase of the total weight of the structure by 4.5 per cent. In the case of Version 6, in which the number of longerons was decreased by 20 (from 80 to 60), the maximum displacement of the load carrying structure was equal to 18.6 mm, which is almost 50 per cent less than in the baseline. This effect was achieved with a simultaneous, slight weight profit. The weight of the Version 6 is about 1 per cent lower than the weight of the baseline. The comparison of results obtained for all versions is presented in Table II.

In Table 2, there are shown also the displacements of the outer shell for all six versions. It can be observed that the

Table I Specification of the calculated versions of the conventional fuselage

Version	No. of stringers	No. of frames	Frame thickness [mm]	Weight [kg]	± Weight %
1	80	20	2	786.79	0
2	60	20	2	742.79	-5.6
3	60	12	2	671.30	-14.7
4	80	12	2	715.30	-9
5	80	12	4	822.53	+4.5
6	60	12	4	778.54	-1

Figure 5 Displacement of load-carrying structure of the conventional fuselage (Version 1)

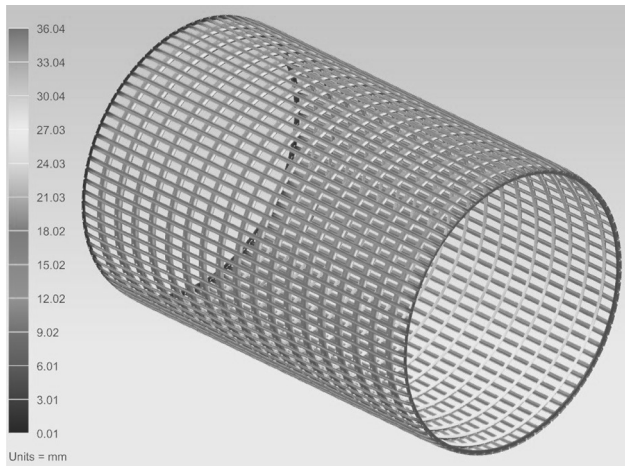
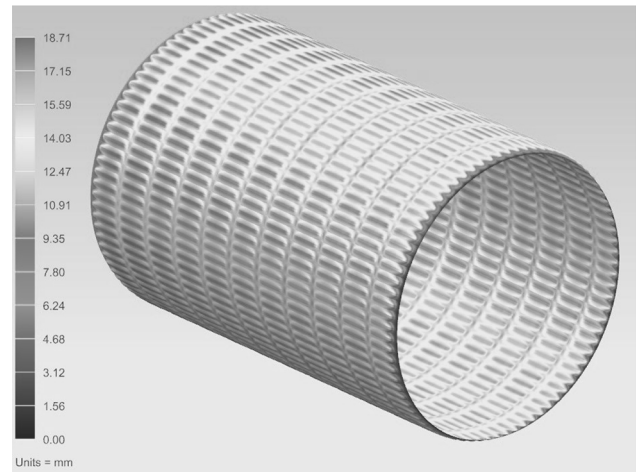


Figure 6 External shell displacements in the conventional fuselage (Version 5)



displacements depend mostly on the number of longerons. For Cases 2, 3 and 6, where the number of longerons is 60, the displacements of the outer shell are between 24.5 and 25.1 mm, whereas for the remaining cases, where the number of longerons is equal to 80, the displacement values are between 18.7 and 19.7 mm. These displacements are dependent on the space between the longerons and frames, through which the shell is subject to the internal pressure. The smallest value of the displacement in the outer shell is obtained in Version 5. The contour map of the outer shell displacement in Version 5 is shown in Figure 6.

Table II Comparison of displacements of the conventional fuselage in each calculated version

Version	Shell displacement [mm]	"Grid" displacement [mm]	± % (grid displacement)
1	18.95	36.04	0
2	25.09	29.97	-16.8
3	24.59	32.03	-11.1
4	19.69	38.25	-6.1
5	18.71	22.91	-36.4
6	24.54	18.60	-48.4

Conventional and geodetic fuselage stiffness comparison

In previous research (Goraj *et al.*, 2018), an analysis of the impact of the arrangement of hoop and helical ribs on the stiffness of the geodetic fuselage was provided. FEM calculations were performed for a sample of the same dimensions, with the same composite layup on the outer shell and being subjected to the same loads. In the case of a geodetic fuselage, six versions were also analyzed, changing the number of helical ribs, the number of hoop ribs and the angle between the helical ribs. The differences of each geodetic version are presented in the Table III.

The comparison of results obtained for a fuselage with geodetic and conventional structure is presented in Table IV.

In the geodetic version of the fuselage, the best results in terms of the stiffness to mass ratio are obtained in Version 6, similar to the conventional fuselage case. Comparing the results obtained in these cases, it can be observed that the fuselage in the conventional version is almost 14 per cent heavier while having almost 17 per cent worse stiffness. Comparing the versions in which similar displacement values were noted (geodetic Version 4 with conventional Version 5, and geodetic Version 5 with Conventional Version 6), it may be observed that with comparable

Table III Specification of the calculated versions of the geodetic fuselage

Version	No. of helical ribs	No. of hoop ribs	Angle between helical ribs [deg]	Weight [kg]	± Weight %
1	80	24	60	658.54	0
2	100	24	60	695.52	+5.6
3	80	41	60	712.93	-8.2
4	80	24	90	690.83	-4.9
5	80	24	50	651.98	-1
6	80	37	50	684.38	+4

Table IV Comparison between geodetic and conventional structure displacement

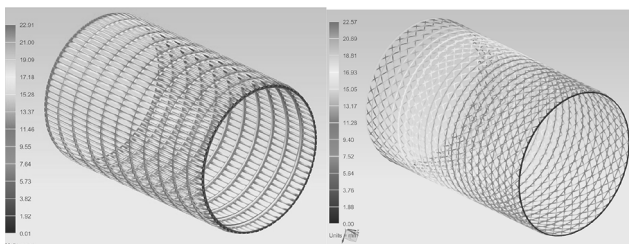
Version	Geodetic		Version	Conventional	
	Frame displacement [mm]	Weight [kg]		"Grid" displacement [mm]	Weight [kg]
1	21.13	658.54	1	36.04	786.79
2	19.07	695.52	2	29.97	742.79
3	14.89	712.93	3	32.03	671.3
4	22.57	690.83	4	38.25	715.3
5	18.17	651.98	5	22.91	822.53
6	15.95	684.38	6	18.6	778.54

stiffness, the weight of the fuselage in the conventional version is about 19 per cent higher than in the geodetic fuselage. The comparison of the displacement of load carrying structures (Version 5 geodetic and Version 4 conventional) is presented in Figure 7.

Conclusion

The calculations have proved once again that the concept of the geodetic fuselage is worth attention. Finite element analysis of the fuselage model with a conventional structure showed that with comparable stiffness, the weight of the geodetic fuselage is almost 20 per cent lower than the conventional fuselage weight. For the structure being analyzed, a very significant increase in stiffness can be observed. Displacements of the load-carrying structure in Version 6 were almost 50 per cent lower than in the baseline. Despite significant improvement, it was not possible to achieve the stiffness level that was obtained for a fuselage with a geodetic structure. For the applied load scenario, the geodetic structure was much better, both in terms of stiffness and the total weight of the structure.

Figure 7 Displacement of conventional fuselage load-carrying structure (Version 4) and geodetic grid (Version 5)



However, the conventional structure has also many advantages. For example the thickness of individual frames or stringers can be varied and adapted to the specific load schemes. The conventional structure is also much easier to manufacture; in addition, the state of knowledge about the mechanics of conventional structures is much more advanced. The geodetic structure is also difficult to apply for noncylindrical cross sections of the fuselage. However, this study shows that the geodetic fuselage structure is worth investigating, to find optimal rib arrangement for specific load cases. At the same time, research is needed to find optimal methods for manufacturing geodetic structures for aviation applications.

References

- Advisory Council for Aviation Research and Innovation in Europe (ACARE) (2012), Strategic Research and Innovation Agenda (SRIA) – Volume 1.
- Botelho, E.C., Silva, R.A., Pardini, L.C. and Rezende, M.C. (2006), “A review on the development and properties of continuous fiber/Epoxy/Aluminium hybrid composites for aircraft structures”, *Materials Research*, Vol. 9 No. 3, pp. 247-256.
- Buttler, T. (2004), *British Secret Projects: Fighters & Bombers 1935-1950*, Hinckley.
- European Aviation Safety Agency (2007), *Certification Specifications for Large Aeroplanes CS-25*.
- European Commission (2011), *Flightpath 2050 Europe’s Vision for Aviation – Report of the High Level Group on Aviation Research*.
- Goraj, Z., Goliszek, B., Kowalski, M., Seitz, A., Peter, F. and Meller, F. (2018), “Strategy and implementation of a parametric CAD model for R2035 aircraft structure and

- external configuration”, *31st International Congress of the Aeronautical Sciences (ICAS)*, Belo Horizonte.
- Hühne, C. (2013), *Advanced Lattice Structures for Composite Airframes – Project Final Report*, Grant Agreement number: 265881.
- Michalski, K. (2016), *Concept and preliminary strength analysis of composite geodetic structure under compression*, Autobusy 12/2016.

- Vasiliev, V.V., Barynin, V.A. and Razin, A.F. (2012), “Anisogrid composite lattice structures – development and aerospace applications”, *Composite Structures*, Vol. 94 No. 3, pp. 1117-1127.

Corresponding author

Zdobyslaw Jan Goraj can be contacted at: goraj@meil.pw.edu.pl

A review of the analytical methods used for seaplanes' performance prediction

Jafar Masri and Laurent Dala

Department of Mechanical and Construction Engineering, Northumbria University, Newcastle upon Tyne, UK, and

Benoit Huard

Department of Mathematics, Physics and Electrical Engineering, Northumbria University, Newcastle upon Tyne, UK

Abstract

Purpose – This paper aims to investigate the different analytical methods used to predict the performance of seaplanes to define the weaknesses in each method and be able to extend the analytical approach to include the nonlinear terms (unsteadiness).

Design/methodology/approach – First, the elemental hydrodynamic characteristics of seaplanes are discussed. Second, five different analytical methods are reviewed. The advantages and disadvantages of each method are stated. After that, the heave and pitch equations of seaplane motion are illustrated. The procedure of obtaining the solution of the heave and pitch equations of seaplane motion is explained. Finally, the results obtained from the most common methods are compared.

Findings – The results show that the methods are based on different assumptions and considerations. As a result, no method is optimal for all types of seaplanes. Moreover, some of the analytical methods do not study the stability of the seaplane, which is a major issue in the design of seaplanes. In addition, all methods consider the motion as steady and linear. The objective is to extend the work to include the nonlinear effects.

Originality/value – This paper presents some of the analytical methods used in describing the performance of seaplanes and explains how can they be applied. Moreover, it summarises the advantages and disadvantages of each method.

Keywords Prediction, Seaplane, Analytical, Ekranoplan, Planing, Savitsky

Paper type General review

Nomenclature

g	= Acceleration of gravity (m/s^2);
V	= Velocity (m/s);
V_m	= Mean velocity (m/s);
b	= Seaplane beam (m);
S	= Wetted surface area (m^2);
A	= Aspect ratio = $\frac{b^2}{S}$;
t	= Time (s);
Δ or m	= Seaplane mass (kg);
∇	= Static volume of displacement (m^3);
C_v	= Speed coefficient = $\frac{V}{\sqrt{gb}}$;
$C_{L\beta}$	= Lift coefficient, dead-rise surface;
C_{L0}	= Lift coefficient, zero dead-rise;
λ	= Wetted length-beam ratio;
λ_y	= Dimensionless distance between stagnation point and transom;
L_w	= Wetted length (m);
L_k	= Keel length (m);
L_m	= Mean wetted length (m);
L_c	= Chine length (m);
C_f	= Friction drag coefficient;
C_p	= Centre of dynamic pressure (m);

ε	= Inclination of thrust line relative to keel line ($^\circ$);
ρ	= Density of fluid (kg/m^3);
F_n	= Froude Number = $\frac{V}{\sqrt{gb}}$;
$F_{n\nabla}$	= Volumetric Froude Number = $\frac{V}{\sqrt{g\nabla}}$;
R_e	= Reynold's number = $\frac{V_m \lambda b}{\nu}$;
\emptyset	= Roll angle ($^\circ$);
β	= Dead-rise angle ($^\circ$);
τ	= Trim angle ($^\circ$);
D_f	= Fluid friction drag (N);
ν	= Kinematic viscosity of fluid (m^2/s);
P_{max}	= Maximum pressure at stagnation point (Pa);
q	= Pressure along the keel line (Pa);
P_L	= Pressure behind the stagnation point (Pa);
P_T	= Pressure at the transom (Pa);
M	= Moment (N.m);
η	= Displacement coordinate vector;
$\dot{\eta}$	= Velocity coordinate vector;
$\ddot{\eta}$	= Acceleration coordinate vector;
F_3	= Amplitude of the exciting force (heave);
F_5	= Amplitude of the exciting moment (pitch);
I_{55}	= Mass moment of inertia (kg.m^2); and
ω	= Circular frequency of the encounter (rad/sec).

The current issue and full text archive of this journal is available on Emerald Insight at: www.emeraldinsight.com/1748-8842.htm



Aircraft Engineering and Aerospace Technology
91/6 (2019) 820–833
© Emerald Publishing Limited [ISSN 1748-8842]
[DOI 10.1108/AEAT-07-2018-0186]

1. Introduction

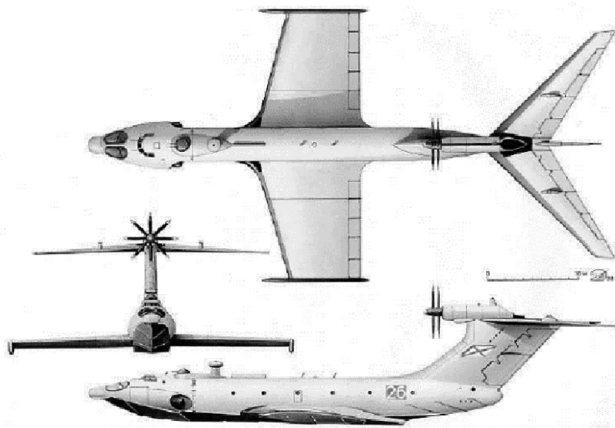
The seaplane concept was initially developed in the Soviet Union by the Central Hydrofoil Design Bureau under the

Received 10 July 2018
Revised 27 August 2018
Accepted 12 September 2018

guidance of the soviet engineer R.E. Alekseev. It is also known as Ekranoplan. The first seaplanes produced were the Orlyonok and Lun types shown in Figures 1 and 2, respectively (Rozhdestvensky, 2006).

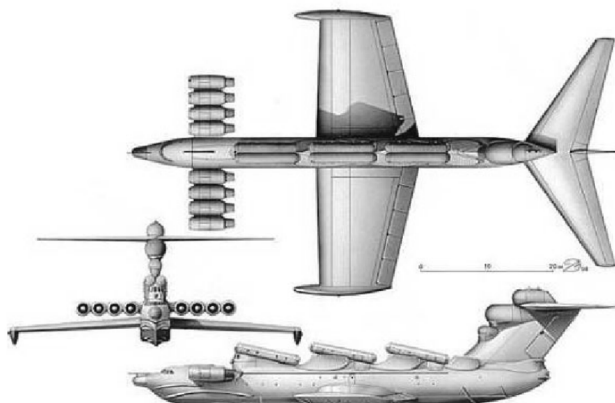
The performance of seaplanes has been widely investigated in the past century. The first studies in the development of seaplanes were taken on high-speed planing hulls which have similar performance characteristics as seaplanes as they are designed to glide on top of water and take advantage of the positive dynamic lift produced by their motion. Seaplanes have the ability to fly close to water surface and use the wing-in-ground (WIG) effect phenomenon to create more lift force and use less power to fly. According to Yun *et al.* (2010), WIG effect can be defined as the enhanced lift force acting on a craft that is flying close to water or ground surface. The enhanced lift force is produced by the higher pressure increase on the under-surface of the craft due to higher deceleration of the air trapped between the surface and the craft. Figure 3 shows the airflow lines around the hull and wings of a seaplane and explains how the ground effect phenomenon is experienced.

Figure 1 Orlyonok Ekranoplan



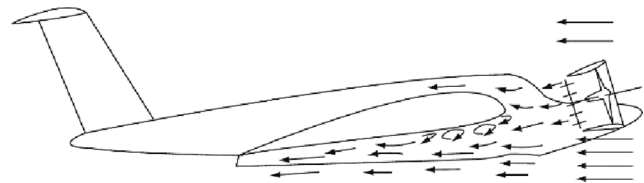
Source: Collu (2008)

Figure 2 Lun Ekranoplan



Source: Collu (2008)

Figure 3 WIG effect on a seaplane

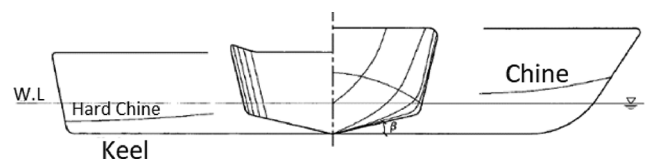


Source: Yun *et al.* (2010)

In the recent years, the need for a fast watercraft has increased sharply in the different areas of civil or military applications. One of the prerequisites of a successful seaplane design is the appropriate hydrodynamic stability prediction (Dala, 2015). Hydro-planing hulls have a unique instability phenomenon known as porpoising defined as a periodic, bounded, vertical motion that a craft might show at certain speeds (Faltinsen, 2010). This behaviour is a function of craft speed and can happen even in calm water. Porpoising can lead to structural damage or diving when the motions are very severe that the craft hull is thrown out of water and subsequently impacts the water surface (Faltinsen, 2010). In 1964, Savitsky published a research on the hydrodynamics of prismatic planing hulls and presented a mathematical approach to study the dynamics of planing surfaces. Savitsky's work suggested a set of empirical equations that allow the performance of prismatic planing hulls to be studied in the design stage. This analytical approach is still being used as the main analytical approach in speedboat design. Prismatic bodies have constant cross section and straight buttocks through the length of the craft. Figure 4 shows a typical high speed planing hull. The parameters commonly used in the analytical performance prediction are speed, weight, length, beam, dead-rise angle (β) and longitudinal centre of gravity. These parameters define the basic geometry of the craft (Almeter, 1993).

The purpose of this paper is to review the analytical methods used in the prediction of the performance of seaplanes. As the seaplane is a WIG craft that has intermediate configuration between ships and aircraft, the main issue in the design of the seaplane is the stability during take-off and landing. In the region, the hydrodynamic and aerodynamic forces are coupled and very important to consider; otherwise, the craft cannot take-off. First, the hydrodynamic characteristics of seaplanes will be illustrated. Second, the performance prediction methods will be briefly discussed. Third, the analytical methods available in the open literature will be explained in details and compared to each other. After that, seaplanes motion will be reviewed in which the linear equations of

Figure 4 Typical planing hull



Source: Faltinsen (2010)

seaplane motion will be presented. Furthermore, the results obtained by Savitsky will be compared to results obtained by other methods.

2. Hydrodynamic characteristics of prismatic planing surfaces

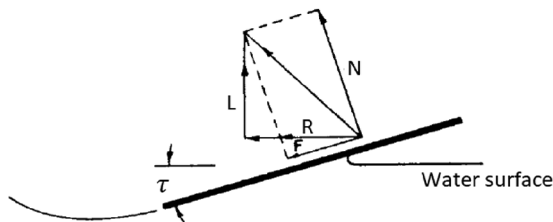
It is critical to study the hydrodynamic characteristics of planing surfaces before undertaking the design of a seaplane. Planing starts when the centre of gravity of the hull is lifted above its normal still-floatation height. A planing surface is designed to be supported by the dynamic reaction between the body and the water. There are two different types of pressure forces acting on the hull of a WIG craft. The first one is the hydrostatic force (buoyancy force). According to Archimedes principle, the hydrostatic force acting on a body that is fully or partially submerged in water equals the weight of the water that the body displaces. The buoyancy force is always in the upward direction and passes through the centre of mass of the body. The second force is the hydrodynamic force, which depends on the fluid flow around the hull and proportional to the speed square. The total hydrodynamic pressure drag of seaplanes is composed of two different types. The first one is the pressure drag developed by water pressure acting normal to the inclined hull. The second one is the viscous drag acting tangential to the bottom of the hull and is the result of fluid friction (Murray, 1950). Figure 5 shows the different forces acting on a planing surface in viscous water.

Seaplanes have different operating modes depending on speed and position. Figure 6 explains the different operating modes of a seaplane.

The operating modes can be explained as follows (Yun *et al.*, 2010):

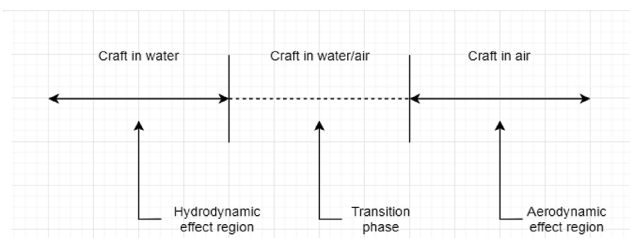
- At low Froude number $F_n < 0.4$, the seaplane travels in water and can be considered as a displacement hull (moving through water by pushing the water aside). In this

Figure 5 Forces acting on a planing surface



Source: Murray (1950)

Figure 6 Seaplane operating regions



region, the craft is affected by hydrodynamic and hydrostatic forces. The hydrostatic force (restoring force) is dominant in this region relative to the hydrodynamic forces (added mass and damping).

- At higher Froude number ($0.4 < F_n < 1.0$), the seaplane enters the planing mode where it starts to rise up and glide on the top of water surface. In this case, the craft is affected by both hydrodynamic and hydrostatic forces in which the hydrostatic force is less dominant. Moreover, the craft is also affected by aerodynamic forces.
- When Froude number $F_n > 1.0$, the seaplane gets out of water and becomes completely in air in which it only encounters aerodynamic forces.

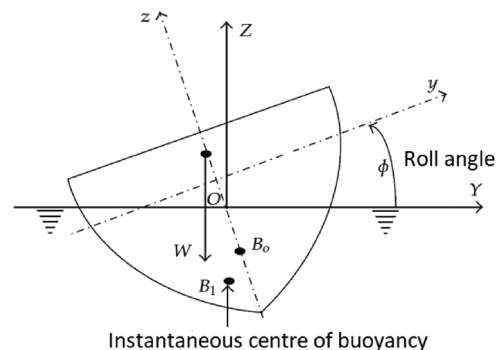
According to Almeter (1993), the basic speed regimes that the planing hull can operate in can be defined with respect to the volumetric Froude number ($F_{n\nabla}$) as follows:

- *Pre-planing*: It is also called displacement mode. It is the hydrodynamic effect region and can be experienced up to $F_{n\nabla} = 2.5$. Most of the weight of the hull is supported by hydrostatic forces (buoyancy).
- *Semi-planing*: It is also known as semi-displacement mode. It is the transition phase and can be experienced in the range of $2.5 < F_{n\nabla} < 4.0$. In this case, the weight of the hull is supported by both hydrostatic (buoyancy) and hydrodynamic forces. As the speed increases, the contribution of hydrodynamic forces in lifting the weight of the craft increases while the hydrostatic forces contribution decreases.
- *Fully-planing*: It is the aerodynamic effect region. It can be experienced when $F_{n\nabla} \geq 4.0$. At higher speeds, the weight of the hull is supported by aerodynamic forces only.

It can be understood from Almeter's study that when the seaplane is hydroplaning, the pressure forces acting on the surface of the hull are buoyancy and dynamic pressure. Each of the forces has a different centre of pressure. The buoyancy force has a centre of hydrostatic pressure, while dynamic forces have a centre of hydrodynamic pressure as shown in Figure 7.

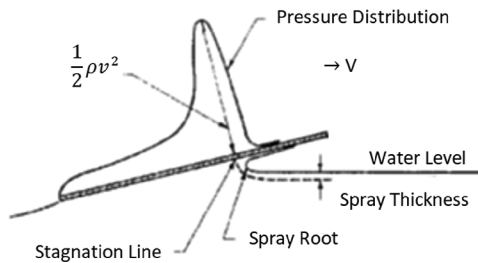
Savitsky (1964) claims that the horizontal centre of buoyancy is 33 per cent of the wetted length forward of the transom. The latter goes on to claim that the horizontal centre of dynamic pressure is 75 per cent forward of the transom in case of a small angle of attack. The pressure distribution on a planing surface is presented in Figure 8. The figure shows that the centre of

Figure 7 The centre of hydrodynamic and hydrostatic pressures



Source: Ibrahim and Grace (2010)

Figure 8 Pressure distribution on a planing surface



Source: Almeter (1993)

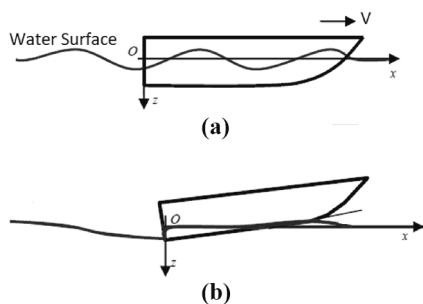
dynamic pressure is approximately at a point 75 per cent forward of the transom. As the speed increases, the forces start to change from hydrostatic to hydrodynamic. This means that at higher speeds, the buoyancy force can be neglected, and the centre of pressure moves from the centre of buoyancy to the centre of dynamic pressure (Savitsky, 1964).

The basic hull design of seaplanes demonstrates a hull that assists in lifting off the craft in the water. Priyanto *et al.* (2012) suggests that when a hull is in the planing mode, there is a tendency that it trims at a certain angle. This means that the front of the hull will lift out of water and the rear part of the hull will immerse partially in water. Figure 9 explains the difference between a hull in the planing and pre-planing (displacement) modes. The hydrodynamic lift and resistance will be encountered at the rear part of the hull where the front will be affected by aerodynamic forces (Priyanto *et al.*, 2012).

3. Performance prediction methods

In the past century, fundamental research on the hydrodynamics of water-based aircraft has been carried out. The first experimental research on planing surfaces was conducted by Baker (1912). This is followed by wider investigations carried by Sottorf (1932). After that, more examinations on the topic were carried out by Shoemaker (1934); Sambraus (1938); Sedov (1947); Locke (1948); Korvin-Kroukovsky *et al.* (1949) and Murray (1950). Subsequently, in 1964, Savitsky discussed the hydrodynamic characteristics of planing surfaces and presented a method to predict the performance of prismatic planing surfaces (Almeter, 1993).

Figure 9 (a) Displacement hull; (b) planing hull



Notes: (a) Displacement mode; (b) planing mode

Source: Priyanto *et al.* (2012)

As previously stated, the performance of planing hulls is predicted by studying the relations between different variables such as speed, displacement, longitudinal length, beam length, trim angle, dead-rise angle and longitudinal centre of gravity. These variables are called the basic dimensions (geometry) and loading of the planing hull. The shape of the hull can be concave, convex or straight and can have high warp or high beam taper. Resistance prediction methods can generally be classified into the following categories (Almeter, 1993):

- analytical methods (also called empirical prediction methods);
- graphical prediction methods;
- planing hull series prediction methods;
- numerical methods;
- statistical methods; and
- experimental methods.

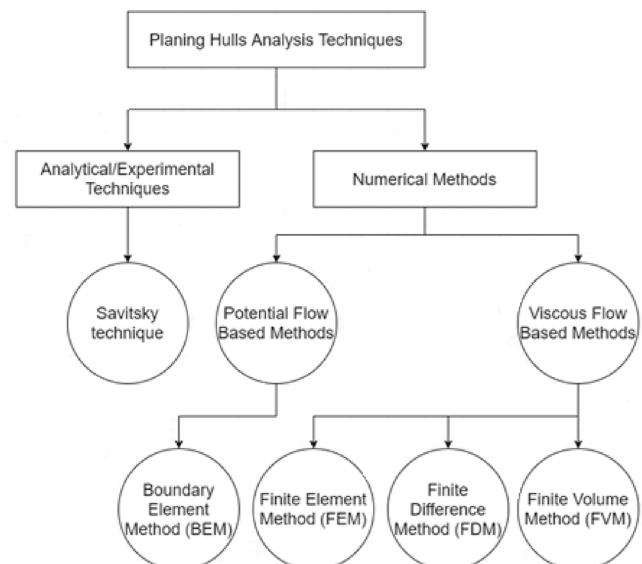
It is important in the design stage to choose the most applicable performance prediction method that conforms with the shape and geometry of the planing hull. This is because if the method is not applicable to the examined hull, it might over or under-predict the performance of the hull (Almeter, 1993). The hydrodynamic analysis techniques for seaplanes available in the open literature are summarised in Figure 10.

In this paper, attention will be given only to the analytical methods, especially Savitsky's method. In the next subsections, the analytical methods available in the open literature will be discussed.

3.1 Savitsky's method

The equations developed by Savitsky (1964) describe the wetted area, lift force, drag force, centre of pressure and the porpoising stability limits of hard chine prismatic planing plate in terms of its dead-rise angle, trim angle, speed and weight. This method is based on the dynamic lift equations first developed by Sedov (1947). Once the shape and geometry of

Figure 10 Performance prediction methods



Source: Yousefi *et al.* (2013)

the hull are defined, it becomes easier to predict its performance. Figure 11 shows the basic terms that describe a planing hull according to Savitsky (1964).

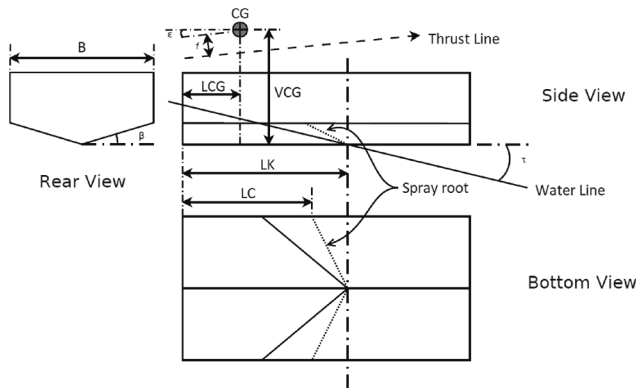
The figure demonstrates that the intersection of the bottom surface with the undisturbed water surface is along the two sloping lines (O-C) between the keel and chines. It can be observed from Figure 11 that for a V-shaped planing hull, there is no noticeable evidence of water pile-up at the keel line. When the hull starts to rise and have a larger trim angle, the water will pile-up at the keel. Also, along the spray root line (O-B), there is a tendency of the water surface to rise before the initial point of contact with water. Savitsky (1964) argues that the spray root line is slightly convex. However, as the curvature is relatively small, it is considered straight. As a result, the mean wetted length of a dead-rise planing surface can be defined as the average of the keel length and chine length calculated from the back of the hull (transom) to the point of intersection with spray root line (O-B).

As shown in Figure 12, the total hydrodynamic drag on a planing hull has two components:

- 1 the fluid friction drag D_f ; and
- 2 the pressure drag $\frac{D_p}{\cos \tau}$.

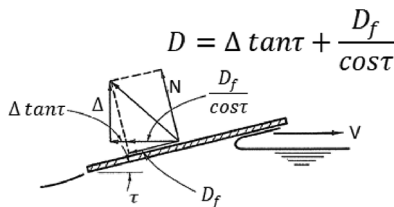
To develop his equations, Savitsky (1964) studied the equilibrium of the planing craft. First, he assumed that the planing hull is moving in a constant speed with no acceleration in any direction. Second, the planing hull is considered to have a constant dead-rise angle (β), a constant equilibrium trim angle (τ_e) and a constant beam length (b) for the whole wetted planing area. Nevertheless, Savitsky's theory only investigates

Figure 11 Planing hull characteristics



Source: Savitsky (1964)

Figure 12 Hydrodynamic drag components



Source: Savitsky (1964)

the hydrodynamic conditions. This means that the weight of the hull is balanced only by the hydrodynamic lift forces. According to Savitsky (1964), equilibrium is achieved when the following conditions apply:

- The summation of forces in the vertical direction is 0.
- The summation of forces in the horizontal direction is 0.
- The summation of moments about the centre of gravity CG is 0 (pitching moment equilibrium).

Figure 13 shows the different forces and parameters Savitsky (1964) has used in the development of his method.

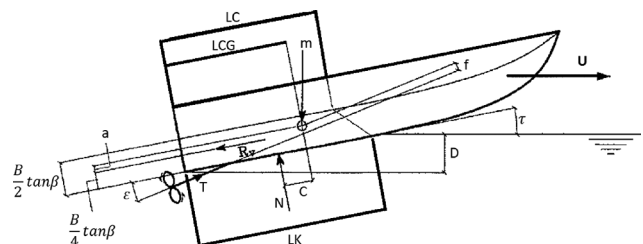
It is worth mentioning that in his analysis, Savitsky (1964) considered the beam to be more important than the length of the hull because the wetted length of the hull does not remain constant. It varies with trim angle, loading and speed, while the wetted beam generally remains constant. Moreover, the latter points out that at high speeds, it is possible to change the wetted length of the planing hull without changing its hydrodynamic characteristics. In addition, Savitsky (1964) used Froude law of similitude to produce the planing coefficients and symbols in his analysis. It can be noted that these analysis can be applied to study the performance of water-based aircraft.

By applying the equilibrium principle, the equilibrium trim angle (τ_e) can be calculated. After that, the performance characteristics of the planing hull can be predicted. The procedure of Savitsky's method is explained as follows:

- 1 The geometry of the hull is defined, in which the following variables are specified:
 - The total mass of the boat m (or can be expressed as Δ).
 - The beam length b .
 - The longitudinal distance of centre of gravity measured from the transom LCG.
 - The vertical distance of centre of gravity measured from the keel VCG.
 - The dead-rise angle β .
 - The trim angle τ .
 - The velocity of the craft V .
 - The inclination of thrust line relative to keel line ϵ .
- 2 Then a few variables are calculated in the same order as follows:
 - The speed coefficient (which is the beam Froude number):

$$C_v = \frac{V}{\sqrt{gb}} \quad (1)$$

Figure 13 Analysed planing hull



Source: Savitsky (1964)

- The lift coefficient of dead-rise planing surface:

$$C_{L\beta} = \frac{mg}{\frac{1}{2}V^2 b^2 \rho} \quad (2)$$

- The lift coefficient of an equivalent flat plate C_{Lo} , which is calculated using the following equation:

$$C_{Lo} = C_{L\beta} + 0.0065\beta C_{Lo}^{0.6} \quad (3)$$

- The wetted length-beam ratio λ , which is calculated from the following equation:

$$C_{Lo} = \tau^{1.1} \left[0.012\lambda^{0.5} + \frac{0.0055\lambda^{2.5}}{C_v^2} \right] \quad (4)$$

Then the wetted length is calculated as: $L_w = \lambda b$

- The mean velocity over bottom of planing surface:

$$V_m = V \left[1 - \frac{0.012\lambda^{0.5}\tau^{1.1} - 0.0065\beta(0.012\lambda^{0.5}\tau^{1.1})^{0.6}}{\lambda \cos(\tau)} \right]^{0.5} \quad (5)$$

- The friction drag coefficient:

$$C_f = \frac{0.075}{(\log_{10}(R_e) - 2)^2} \quad (6)$$

where R_e is Reynold's number and can be calculated as:

$$R_e = \frac{V_m \lambda b}{\nu} \quad (7)$$

- The water friction drag D_f :

$$D_f = \frac{1}{2} \frac{\rho V_m^2 \lambda b^2}{\cos(\beta)} (C_f + \Delta C_f) \quad (8)$$

where ΔC_f is ATTC standard roughness = 0.0004

- Then, the total hydrodynamic drag, which can be calculated as follows:

$$D = mg \tan(\tau) + \frac{D_f}{\cos(\tau)} \quad (9)$$

- The centre of dynamic pressure, which is found from:

$$C_p = 0.75 - \frac{1}{\frac{5.21C_v^2}{\lambda} + 2.39} \quad (10)$$

- Then the two distances a and c shown in Figure 13, which are calculated from:

$$c = LCG - C_p \lambda b \quad (11)$$

$$a = VCG - \frac{b}{4} \tan(\beta) \quad (12)$$

- The equation of equilibrium of pitching moment, which is then solved:

$$M_{tot} = mg \left[\frac{c}{\cos(\tau)} (1 - \sin(\tau)\sin(\tau + \varepsilon)) - f \sin(\tau) \right] + D_f(a - f) \quad (13)$$

If the equation satisfies the equilibrium (sum of moments = 0), then the wetted length of keel L_k and the vertical depth of trailing edge of craft below level of water d are found from:

$$L_k = \lambda e b + \frac{b \tan(\beta)}{2\pi \tan(\tau_e)} \quad (14)$$

$$d = L_k \sin(\tau_e) \quad (15)$$

If the equation of equilibrium does not equal to zero, a different trim angle (τ) must be assumed and the procedure is repeated till two different values of moment are found (negative and positive) and then by interpolation the equilibrium trim angle (τ_e), D_f and λ can be found (Savitsky, 1964).

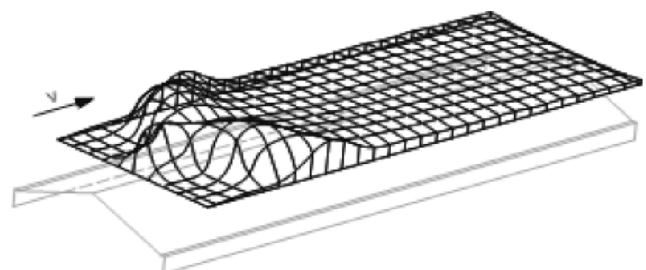
3.2 Morabito's method

This method claims that the pressure at the stagnation point is far greater than the pressure at the other parts of the hull. Therefore, the problem becomes very complex, and direct calculation methods cannot be applied to calculate the pressure distribution along the hull surface. As a result, the pressure can be calculated in length-wise and breadth-wise directions independently. It could then be extended to a three-dimensional distribution over the hull. Figure 14 shows the three-dimensional pressure distribution over the bottom of a planing surface (Morabito, 2010).

Iacono (2015) studied Morabito's method and states that the dynamic pressure along the planing hull exhibits a maximum at the stagnation point. Eventually, the pressure deteriorates and reaches atmospheric pressure at the end of the hull. As explained in Figure 15, Morabito's method focuses on the pressure distribution along the longitudinal keel line at the bottom of the hull. Also, it calculates the pressure at the transom and the longitudinal pressure distribution over other sections (Iacono, 2015).

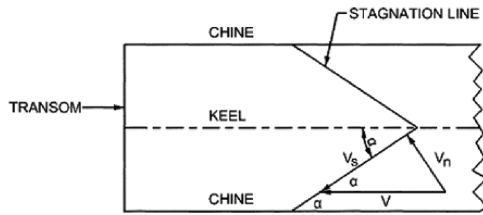
In the case of the keel line, Morabito (2010) introduced the following equation to calculate the maximum pressure at the stagnation point:

Figure 14 3D pressure distribution over the bottom of a planing hull



Source: Iacono (2015)

Figure 15 Components of planing hull explained by Morabito



Source: Iacono (2015)

$$\frac{P_{max}}{q} = \sin^2 \alpha \quad (16)$$

where:

α = the angle between the stagnation line and keel line shown in the next figure; and

q = the pressure along the line = $\frac{1}{2} \rho V^2$.

The pressure gradually decreases along the keel line till it becomes almost zero at the transom. The pressure reduction along the line can be calculated using the following equation:

$$\frac{P_L}{q} = 0.006 \frac{\tau^{1/3}}{X^{2/3}} \quad (17)$$

P_L is the pressure behind the stagnation point and X is the dimensionless distance from the stagnation and can be calculated from:

$$X = \frac{x}{b} \quad (18)$$

where b is the breadth of the hull.

Then, Morabito modified the equation of reduced pressure along the keel line as:

$$\frac{P}{q} = \frac{0.006\tau^{1/3}X^{1/3}}{\left(X + \frac{(0.006\tau^{1/3})^{1.5}}{2.588(\frac{P_{max}}{q})^{1.5}} \right)} \quad (19)$$

Morabito calculated the pressure at the transom by introducing the following equation:

$$P_T = \frac{(\lambda_y - X)^{1.4}}{(\lambda_y - X)^{1.4} + 0.05} \quad (20)$$

where λ_y is the dimensionless distance between the transom and the stagnation line as each longitudinal section and can be calculated from:

$$\lambda_y = \lambda - \frac{(Y - 0.25)}{\tan(\alpha)} \quad (21)$$

where $Y = \frac{y}{b}$ is the dimensionless transverse distance from the longitudinal symmetry (keel) line (the same as the previously defined X but in the transverse direction).

The previous equations of Morabito only measure the pressure distribution at the transom, at the stagnation point and

along the symmetry line in between them. Morabito claims that the pressure declines along the stagnation line, and consequently, at each longitudinal section, the maximum pressure is less than that on the longitudinal symmetry (keel) line. The latter has used the swept wing theory to calculate the pressure reduction along the other sections (Morabito, 2010).

As previously presented in Figure 15; Morabito (2010) suggests that the fluid velocity is a combination of two components, velocity along the stagnation line and velocity normal to it. Using the normal component of velocity and resulting pressure, the ratio of transverse pressure along the stagnation line is found as follows:

$$\frac{P_{YStag}}{P_R} = [1.02 - 0.25Y^{1.4}] \frac{0.5 - Y}{0.51 - Y} \quad (22)$$

By multiplying the previous equation by maximum pressure, the pressure over the stagnation line at a desired longitudinal section is found as:

$$\frac{P_{max}}{q} = \frac{P_{YStag}}{P_R} \sin^2(\alpha) \quad (23)$$

Morabito's method is not able to define many terms needed in predicting the hydrodynamic performance of planing hulls. For example, it cannot define the porpoising stability limit. As a result, it cannot be used as the staple method for boat design.

3.3 The Central Aero-Hydrodynamic Institute (CAHI) method

The CAHI method was proposed by Almeter (1993). This method is used to predict the performance of prismatic planing hulls. It is also known as Lyubomirov method or TSAGI method from the Central Aero-hydrodynamic Institute in Moscow. The CAHI method was initially developed by Perelmutter (1938), who investigated the take-off characteristics of seaplanes (Alourdas, 2016).

Almeter (1993) developed this method based on the same dynamic lift equations prepared by Sedov (1947) that Savitsky (1964) used to develop his method. In Savitsky's method, the trim angle is corrected based on the constant dead-rise, while in the CAHI method, the wetted area increases with dead-rise.

CAHI method supports the claim of Chambliss and Boyd (1953), who investigated the planing characteristics of two v-shaped hulls of different dead-rise angles. CAHI method agrees with Chambliss and Boyd's (1953) method that in theory for a given lift coefficient, any increase in the dead-rise angle will increase the trim angle and wetted length of a planing hull. This means that the hydrodynamic resistance will increase (Chambliss and Boyd, 1953). The procedure of CAHI method can be summarised as follows:

- The same variables as Savitsky's method should be defined and then the equation of moment should be solved to obtain the mean wetted length-beam ratio λ . Once an acceptable λ is obtained (almost 0.75^*LCG), the trim angle τ and the dead-rise lift coefficient can be calculated. The equations for the mentioned variables are as follows:

$$M = \frac{\frac{0.7\pi\lambda}{1+1.4\lambda} \left[0.75 + 0.08 \frac{\lambda^{0.865}}{\sqrt{C_v}} \right] + \frac{(\lambda - 0.8)\lambda^2}{(3\lambda + 1.2)C_v^2}}{\frac{0.7\pi}{1+1.4\lambda} + \frac{(\lambda - 0.4)\lambda}{(\lambda + 0.4)C_v^2}} \quad (24)$$

$$C_{L\beta} = \frac{\Delta}{0.5\rho V^2 b^2} \quad (25)$$

$$\frac{C_{L\beta}}{\tau} = \frac{0.7\pi\lambda}{1+1.4\lambda} + \frac{(\lambda - 0.4)\lambda^2}{(\lambda + 0.4)C_v^2} \quad (26)$$

- The mean wetted length-beam ratio and the trim angle can now be calculated for a dead-rise planing hull from the following:

$$\lambda_\beta = \frac{\lambda^{0.8}}{\cos(\beta)} \left[1 - 0.29(\sin(\beta))^{0.28} \right] \cdot \left[1 + 1.35(\sin(\beta))^{0.44} \cdot \frac{M}{\sqrt{C_v}} \right] \quad (27)$$

$$\tau_\beta = \tau + \frac{0.15(\sin(\beta))^{0.8}}{C_v^{0.3}} \cdot \frac{1 - 0.17\sqrt{\lambda_\beta \cos(\beta)}}{\sqrt{\lambda_\beta \cos(\beta)}} \quad (28)$$

- After that, the wetted surface S , the average bottom velocity V_m and the drag of prismatic hull are calculated as follows:

$$S = \frac{b^2 \lambda_\beta}{\cos(\beta)} \quad (29)$$

$$V_m = V \left[1 - \frac{\tau}{1 + \lambda} \right] \quad (30)$$

$$D = \Delta \tan(\tau_\beta) + \frac{0.5C_f \rho S V_m^2}{\cos(\tau_\beta)} \quad (31)$$

- C_f can be calculated from the same equation proposed by Savitsky:

$$C_f = \frac{0.075}{(\log R_e - 2)^2} \quad (32)$$

- Finally, the wetted keel length and the wetted chine length are calculated as follows:

$$\lambda_\beta = \frac{L_m}{b} \quad (33)$$

$$L_m = \frac{L_k + L_c}{2} \quad (34)$$

$$L_k - L_c = \frac{b \tan(\beta)}{\pi \tan(\tau)} \quad (35)$$

3.4 Payne's method

In 1995, Payne studied the planing theory. The latter has discussed the difference in empirical equations used to predict

the performance of flat and v-shaped planing hulls available at that time. As a result, a method to predict the resistance of planing hulls was proposed.

In his study, Payne (1995) points out that Savitsky's equations are the most accurate equations developed in the past century for describing the total hydrodynamic drag and lift forces acting on a planing hull. Therefore, he compared his method to Savitsky's method. Figure 16 presents a comparison between Payne's and Savitsky's results. The figure shows the lift produced by a planing hull versus the wetted length/beam ratio. It can be observed that when the wetted length/beam ratio is low, Payne's method overestimated the lift force. As the length/beam ratio increases, Payne's method gives lower lift force estimations.

It is worth mentioning that Payne (1995) claims that the hydrostatic pressure acting on a planing hull is less than Archimedes force.

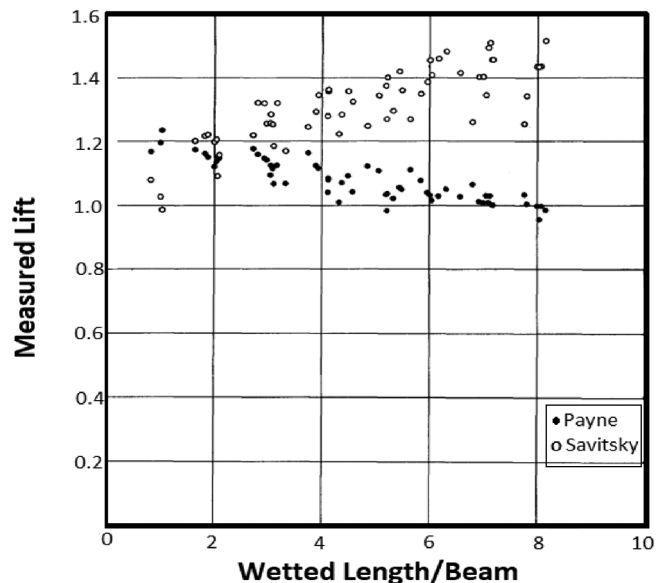
Table I summarises the different empirical equations of hydrodynamic lift of planing plates developed previously as provided by Payne (1995).

Payne's theory is based on two-dimensional flow analyses of a flat plate. It can be seen as an improved version of the resistance prediction methods available at its time. The latter modified the coefficients developed previously. Furthermore, Payne (1995) made different assumptions based on the revision of the experimental data available. He states that the modifications are made to the coefficients used in the "added mass" equations for planing forces predicted formerly.

3.5 Shuford's method

This method was developed to predict the performance of deep-V planing hulls operating at high-speed regime where the buoyancy force is negligible. It does not discuss the effects of spray drag. It discusses the effects of the vertical spray rails on

Figure 16 Comparison between Payne and Savitsky Methods



Source: Payne (1995)

Table I Equations of hydrodynamic lift of planing plates

Author/Year	Equation	Geometrical specifications
Perring and Johnston (1935)	$C_L = 0.9\tau A^{0.42}$	$\beta = 0^\circ$
Sottorf (1937)	$C_L = 0.845\tau A^{0.5}$	$\tau \leq 10^\circ$
Perelmutter (1938)	$C_L = \frac{2A\tau}{(1+A)}$	$5^\circ \leq \tau \leq 8^\circ$
Sedov (1947)	$C_L = \frac{0.7\pi A\tau}{(1.4+A)}$	$\tau \leq 4^\circ$
Siler (1949)	$C_L = \frac{\pi A \sin\tau \cos\tau}{(4+A)} + 0.88 \sin^2\tau \cos\tau$	$\beta = 0^\circ$
Korvin-Kroukovsky <i>et al.</i> (1949)	$C_L = 0.012\tau^{1.1}A^{0.5}$	$\tau \leq 4^\circ$
Locke (1948)	$C_L = \frac{k}{2}\tau^n$	$\beta = 0^\circ$ $\beta = 0^\circ$
	k and n are given in the reference as functions of the aspect ratio A	
Korvin-Kroukovsky (1950)	$C_L = \frac{0.73\pi A\tau}{(2+A)} + 0.88\tau^2$	$0.25^\circ \leq \tau \leq 10^\circ$
Schnitzer (1953)	$C_L = \varphi \left(\frac{\pi^3 A}{16} \sin\tau \cos^2\tau + 0.88\sin^2\tau \cos\tau \right)$ $\varphi = \frac{1}{\sqrt{1+\lambda^2}} \left(1 - \frac{0.485}{1+\frac{1}{\lambda}} \right)$	$0^\circ \leq \tau \leq 45^\circ$ $\beta = 0^\circ$ $\beta = 30^\circ$
Shuford (1954)	$C_L = \frac{\frac{\pi}{2}A\tau}{(1+A)} \cos^2\tau + \sin^2\tau \cos\tau$	$\tau \leq 16^\circ$ $\beta = 0^\circ$
Brown (1954)	$C_L = \frac{2\pi}{\cot\frac{\tau}{2} + \pi + \left(2\cot\frac{\tau}{2} - \pi \right) \frac{1}{A}}$	$A > 1$
Brown (1954)	$C_L = (1.67\sin\tau + 0.09) \cdot (1-A)\sin\tau \cos\tau + \frac{2\pi A}{3\cot\frac{\tau}{2}}$	$A < 1$
Farshing (1955)	$C^3 + [(2.293 - 1.571A)\tau - 2.379 - A]C^3$ $+ [2A + 4 + (6.283A - 4.584)\tau]C$ $- 6.283A\tau = 0$	$18^\circ \leq \tau \leq 30^\circ$
	$C_L = \xi C$ $\xi = 1.359 - \tanh\left(\frac{1+A}{8A}\right)$ $+ \left(\frac{\tau^\circ - 18^\circ}{90.53}\right) \tanh\frac{1}{A^2}$	
Farshing (1955)	$C^3 + [(2.293 - 1.571A)\tau - 2.379 - A]C^3$ $+ [2A + 4 + (6.283A - 4.584)\tau]C$ $- 6.283A\tau = 0$	$2^\circ \leq \tau \leq 18^\circ$
	$C_L = \xi C$ $\xi = 1.359 - \tanh\left(\frac{1+A}{8A}\right)$	
Shuford (1958)	$C_L = \frac{\frac{\pi}{2}A\tau}{(1+A)} \cos^2\tau + \frac{4}{3}\sin^2\tau \cos^3\tau$	$8^\circ \leq \tau \leq 18^\circ$ $\beta = 0^\circ$ $\beta = 20^\circ$ $\beta = 40^\circ$

the performance of planing hulls. It has been modified several times to produce improved performance prediction methods. Brown (1971) produced a version of this method that takes in consideration the buoyancy force, which makes his method applicable to lower speeds (lower Froude number). This modified version is based on the same basis as Savitsky's method (Brown, 1971). The equations and procedure of this method have been explained in literature (Shuford, 1958).

3.6 Summary of the methods discussed

The specifications of each analytical method discussed previously are listed in the Table II. The advantages and disadvantages of each method along with its validation method are summarised in the table.

4. Heave and pitch equations of seaplane motion

The equations of motion of a seaplane advancing at a constant forward velocity with arbitrary heading in regular sinusoidal sea waves are presented in this section. To compare the results of Savitsky's method with the results of these equations, the oscillatory motions are assumed to be linear and harmonic.

A seaplane can experience motions in six directions. Hence, the performance of seaplanes is presented by six-degrees-of-freedom system. The six motions are a set of independent displacements and rotations that completely define the displaced position and orientation of the seaplane (Fossen, 2011). Therefore, seaplane motion can be considered to be made of three translational (linear) components (surge, sway and heave) and three rotational (angular) components (roll,

Table II Methods specifications

Method/Author	Advantages	Disadvantages	Validated with
Savitsky	It can predict the porpoising stability limit It can predict the performance of hulls with pure planing conditions which have similar performance characteristics as seaplanes It is the most common method used in speedboat design	Applicable to steady state conditions only Only hydrodynamic investigations. No other forces are considered Only applicable to trim angle $\tau < 4^\circ$. At higher trim angle, the results starts to deviate from the results of the experiments The centre of dynamic pressure is assumed to be at 75% of the mean wetted length forward of the transom which is not accurate when analysing seaplanes It assumes that the thrust is always parallel to the axis thruster (prime mover axis) which may not be always true Spray drag (whisker spray) is not included or taken into account It start to behave irrationally when the dead-rise angle (β) is higher than 50° or when the dead-rise angle is not constant along the hull	Previous analytical methods
Morabito	It can be used to predict the performance of displacement and planing hulls Very simple and easy to use	It does not define the porpoising stability limit of planing hulls It is not applicable for high coefficient of speed C_v It only investigates the pressure distribution along the keel line and stagnation line of the planing hull It does not explain the relations between the different design variables of the planing hull (dead-rise and trim angles) It cannot be mathematical combined with the aerodynamic effect because it only explains the hydrodynamic pressure on the hull It does not investigate the contribution of the hydrostatic force (Buoyancy) Spray drag (whisker spray) is also not included or taken into account	CFD and experiments
CAHI	Was initially developed to predict the characteristics of seaplanes. Thus, it can be modified to give more accurate results under different conditions	This method is based on Savitsky's method. As a result, it has the same limitations It does not define the porpoising stability limit of planing hulls Only applicable to a certain hull geometry Only applicable under the same conditions and assumptions it is based on	Experiments
Payne	It can be used to predict the performance of displacement hulls Very simple and easy to use	It does not define the porpoising stability limit of planing hulls It is not applicable for high coefficient of speed C_v It only discusses the hydrodynamics of flat plates with no dead-rise angle It lacks the investigations of the aerodynamic forces acting on planing hulls	Experiments and previous analytical methods
Shuford	It can be applied to high speed-regime ($F_n > 1.0$) Applicable to high trim angle $8^\circ \leq \tau \leq 18^\circ$ Different dead-rise angles were tested in the development of this method	It is based on the same basis as Savitsky's method Pure hydrodynamic conditions	Experiments

pitch and yaw). Figure 17 shows the sign convention of the six motions of a planing hull (Lewis, 1989).

It can be observed from Figure 17 that the linear displacements about the x -, y - and z -axes are η_1 (*surge*), η_2 (*sway*) and η_3 (*heave*), respectively. In addition, the angular displacements about the x -, y - and z -axes are η_4 (*roll*), η_5 (*pitch*) and η_6 (*yaw*), respectively (Lewis, 1989).

By taking into consideration that the responses are linear and harmonic, the six linear equations of motion can be written using subscript notation as follows (Ogilvie, 1969):

$$\sum_{k=1}^6 [(M_{jk} + A_{jk}) \ddot{\eta}_k + B_{jk} \dot{\eta}_k + C_{jk} \eta_k] = F_j e^{i\omega t} \quad (36)$$

where:

$$j = 1 - 6;$$

M_{jk} = the component of the generalised mass matrix of the craft in the j th direction due to k th motion;

A_{jk} = the added-mass coefficient in the j th direction due to k th motion;

B_{jk} = the damping coefficient in the j th direction due to k th motion;

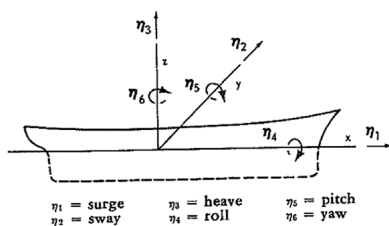
C_{jk} = the hydrostatic restoring force coefficient in the j th direction due to k th motion; and

F_j = the complex amplitudes of the exciting forces and moments in the j th direction. ($F_j e^{i\omega t}$ are forces and moments given by the real part).

For a planing hull with lateral symmetry, the six coupled equations of motion are reduced to two sets of equations, connecting the heave, pitch and surge, and the sway, roll and yaw. This means that the linear equations are not coupled with the angular equations. Moreover, as long as the planing hull is assumed to be a slender body, the hydrodynamic forces associated with the surge motion are much smaller than the forces associated with the other five equations of motion. As a result, the motion of the craft can be described by the two coupled equations of heave and pitch motions (Salvesen *et al.*, 1970).

A heaving and pitching system of seaplane motions behaves like a two-degree-of-freedom spring-mass system. According to Ogilvie (1969), this assumption is clear when a craft model is given heave or pitch displacements from its equilibrium position. It will rapidly oscillate several times before it comes to rest. Therefore, the resulting equations of heave and pitch of seaplanes are expressed as follows:

Figure 17 The six motions of a planing hull



Source: Salvesen *et al.* (1970)

$$(m + A_{33}) \ddot{\eta}_3 + A_{35} \ddot{\eta}_5 + B_{33} \dot{\eta}_3 + B_{35} \dot{\eta}_5 + C_{33} \eta_3 + C_{35} \eta_5 = F_3 e^{i\omega t} \quad (37)$$

$$A_{53} \ddot{\eta}_3 + (A_{55} + I_{55}) \ddot{\eta}_5 + B_{53} \dot{\eta}_3 + B_{55} \dot{\eta}_5 + C_{53} \eta_3 + C_{55} \eta_5 = F_5 e^{i\omega t} \quad (38)$$

The determination of the coefficients and exciting force and moment is a major problem in the motion prediction. To simply this problem, the craft can be divided into transverse strips or segments. The coefficients are then calculated by applying a strip theory (Brown, 1971). The added mass and damping coefficients are calculated using a two-dimensional hydrodynamic theory.

The general solution for each of the two previous equations has two components: the homogenous solution and the particular integral. The homogenous solution is obtained when the system is considered under no external excitation forces or moments. On the other hand, the particular integral is obtained when the external excitation forces and moments are considered.

To obtain the homogenous solution, the equations of heave and pitch can be written as follows:

$$(m + A_{33}) \ddot{\eta}_3 + A_{35} \ddot{\eta}_5 + B_{33} \dot{\eta}_3 + B_{35} \dot{\eta}_5 + C_{33} \eta_3 + C_{35} \eta_5 = 0 \quad (39)$$

$$A_{53} \ddot{\eta}_3 + (A_{55} + I_{55}) \ddot{\eta}_5 + B_{53} \dot{\eta}_3 + B_{55} \dot{\eta}_5 + C_{53} \eta_3 + C_{55} \eta_5 = 0 \quad (40)$$

If a steady-state solution is assumed, then heave and pitch can have the following form:

$$\eta_3 = Z_0 e^{\lambda t} \quad (41)$$

$$\eta_5 = \theta_0 e^{\lambda t} \quad (42)$$

If equations (41) and (42) are substituted in equations (39) and (40), the following equations will be obtained:

$$(m + A_{33}) \lambda^2 Z_0 + A_{35} \theta_0 \lambda^2 + B_{33} \lambda Z_0 + B_{35} \lambda \theta_0 + C_{33} Z_0 + C_{35} \theta_0 = 0 \quad (43)$$

$$A_{53} \lambda^2 Z_0 + (A_{55} + I_{55}) \lambda^2 \theta_0 + B_{53} \lambda Z_0 + B_{55} \lambda \theta_0 + C_{53} Z_0 + C_{55} \theta_0 = 0 \quad (44)$$

These two equations can be written in the form of a matrix as follows:

$$\begin{bmatrix} (m + A_{33}) \lambda^2 + B_{33} \lambda + C_{33} & A_{35} \lambda^2 + B_{35} \lambda + C_{35} \\ A_{53} \lambda^2 + B_{53} \lambda + C_{53} & (A_{55} + I_{55}) \lambda^2 + B_{55} \lambda + C_{55} \end{bmatrix} \begin{bmatrix} Z_0 \\ \theta_0 \end{bmatrix} = \begin{bmatrix} 0 \\ 0 \end{bmatrix} \quad (45)$$

For non-trivial solutions of Z_0 and θ_0 , the determinant of equation (45) is set to be 0. As a result, the characteristic equation can be written in the following form:

$$a\lambda^4 + b\lambda^3 + c\lambda^2 + d\lambda + e = 0 \quad (46)$$

where:

$$a = [(m + A_{33})(A_{55} + I_{55}) - A_{35}A_{53}] \quad (47)$$

$$b = [(m + A_{33})B_{55} + B_{33}(A_{55} + I_{55}) - A_{35}B_{53} - B_{35}A_{53}] \quad (48)$$

$$c = [(m + A_{33})C_{55} + B_{33}B_{55} + C_{33}(A_{55} + I_{55}) - A_{35}C_{53} - B_{35}B_{53} - C_{35}A_{53}] \quad (49)$$

$$d = [B_{33}C_{55} + C_{33}B_{55} - B_{35}C_{53} - C_{35}B_{53}] \quad (50)$$

$$e = [C_{33}C_{55} - C_{35}C_{53}] \quad (51)$$

Equation (46) is a fourth-order characteristic equation of the system. This equation is solved to obtain four roots. The characteristics of motion of the seaplane will depend on the nature of the roots of this equation. Assuming that all roots are pairwise distinct, the solution has three possible cases, described as follows:

- If the equation has four real roots, then the general solution of the two equations of heave and pitch [equations (43) and (44)] can be given by:

$$\eta_{3h} = Z_{01}e^{\lambda_1 t} + Z_{02}e^{\lambda_2 t} + Z_{03}e^{\lambda_3 t} + Z_{04}e^{\lambda_4 t} \quad (52)$$

$$\eta_{5h} = \theta_{01}e^{\lambda_1 t} + \theta_{02}e^{\lambda_2 t} + \theta_{03}e^{\lambda_3 t} + \theta_{04}e^{\lambda_4 t} \quad (53)$$

where Z_{0i} and θ_{0i} are constants and can be determined from the initial conditions by substituting the values of λ_i ($i = 1, 2, 3, 4$) into equation (45).

- In the case of two real roots and two complex conjugate roots, the general solution of the two equations is in the following form:

$$\eta_{3h} = Z_{01}e^{\lambda_1 t} + Z_{02}e^{\lambda_2 t} + e^{\alpha t}(Z_{03}e^{i\omega_1 t} + Z_{04}e^{-i\omega_1 t}) \quad (54)$$

$$\eta_{5h} = \theta_{01}e^{\lambda_1 t} + \theta_{02}e^{\lambda_2 t} + e^{\alpha t}(\theta_{03}e^{i\omega_1 t} + \theta_{04}e^{-i\omega_1 t}) \quad (55)$$

The constants in this case can also be determined using equation (45) by substituting the values of λ_1, λ_2 and $\alpha \pm i\omega_1$. The system in this case will oscillate with only one natural frequency ω_1 of damped oscillations.

- If the solution gives a pair of two complex conjugate roots, then the homogenous solution can be expressed as follows:

$$\eta_{3h} = e^{\alpha t}(Z_{01}e^{i\omega_1 t} + Z_{02}e^{-i\omega_1 t}) + e^{\varphi t}(Z_{03}e^{i\omega_2 t} + Z_{04}e^{-i\omega_2 t}) \quad (56)$$

$$\eta_{5h} = e^{\alpha t}(\theta_{01}e^{i\omega_1 t} + \theta_{02}e^{-i\omega_1 t}) + e^{\varphi t}(\theta_{03}e^{i\omega_2 t} + \theta_{04}e^{-i\omega_2 t}) \quad (57)$$

where ω_1 and ω_2 are the two natural frequencies of damped oscillations.

These three possible cases of damped vibrations discussed above depend on the values of the constants a, b, c, d and e . In the case of repeated roots, the corresponding eigenmodes must be multiplied by t^k , where k is the algebraic multiplicity of the root.

When the excitation forces and moments of equations (37) and (38) are considered, then the particular integrals of the two equations have the following form:

$$\eta_{3p} = P_1 \cos(\omega_1 t) + P_2 \sin(\omega_1 t) \quad (58)$$

$$\eta_{5p} = P_3 \cos(\omega_1 t) + P_4 \sin(\omega_1 t) \quad (59)$$

Then the general solution of the heave and pitch equations of motion will be the summation of the homogenous solution and the particular integral. It can be written in the following form:

$$\begin{bmatrix} \eta_3 \\ \eta_5 \end{bmatrix} = \begin{bmatrix} \eta_{3h} \\ \eta_{5h} \end{bmatrix} + \begin{bmatrix} P_1 \\ P_3 \end{bmatrix} \cos(\omega_1 t) + \begin{bmatrix} P_2 \\ P_4 \end{bmatrix} \sin(\omega_1 t) \quad (60)$$

5. Comparison of results

In this section, Savitsky's method results will be compared to results obtained using CAHI method. Moreover, the porpoising stability limit obtained by the heave and pitch equations of motion will be compared to the limit obtained by Savitsky.

As discussed before, the CAHI method is based on the same basis as Savitsky's method. The results obtained by both methods are in good agreement, as shown in Figures 18 and 19.

The higher drag obtained using the CAHI method is because this method assumes that the wetted area increases with the increase in the dead-rise angle. As a result, higher drag force will be obtained using the CAHI method. In addition, Savitsky assumes that the trim angle is corrected in constant dead-rise angle hulls. On the other hand, CAHI assumes that the trim angle increases with the dead-rise angle. These assumptions justify the higher trim angle obtained by Savitsky.

Figure 20 shows the porpoising stability line obtained by heave and pitch equations of motion and Savitsky method for a constant dead-rise angle of 10°. For a given dead-rise angle, if

Figure 18 Trim angle predicted by Savitsky and CAHI

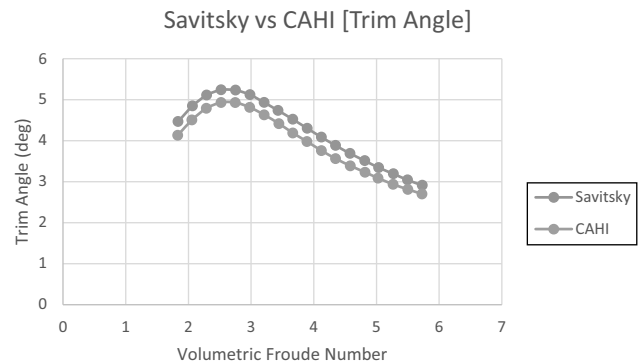
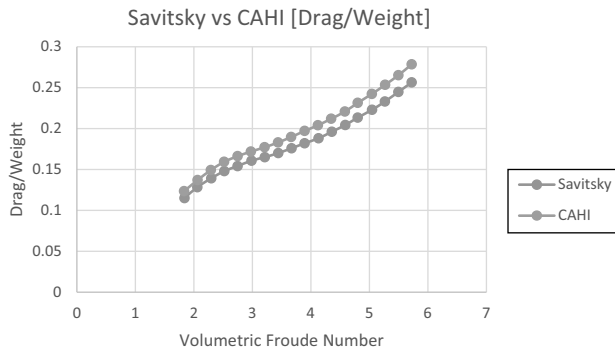
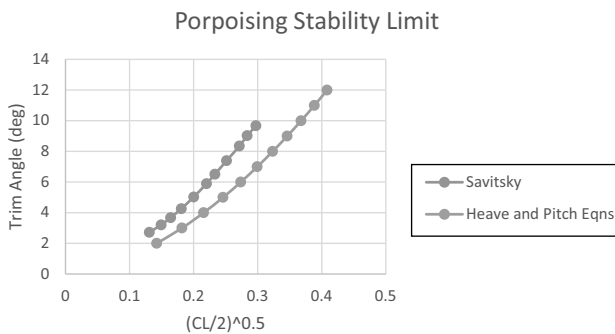


Figure 19 Drag/weight ratio predicted by Savitsky and CAHI**Figure 20** Porpoising stability limit obtained by heave and pitch equations and Savitsky

the combination of the lift coefficient and the trim angle is above the line, then the hull will tend to porpoise. It can be noted that the higher the dead-rise angle, the more stable the planing hull. A higher dead-rise angle will allow a higher trim angle to be reached without inducing porpoising behaviour.

The porpoising line obtained by heave and pitch equations allows for higher speed characteristic prediction. The results obtained are for higher coefficient of lift as well. Savitsky's method can obtain results for lower speed regime and lower coefficient of lift. It can be concluded that this method can be extended to allow for more accurate prediction than Savitsky under various conditions.

6. Conclusion

The prediction of the performance of seaplanes is very important, especially in the design stage. It allows the designer to produce enhanced seaplanes that could fly comfortably under different conditions. Moreover, seaplanes can reduce the environmental harm of air transport as they take advantage of the high lift force in the WIG effect region. The performance characteristics of seaplanes have been discussed. In addition, several analytical methods used for seaplane performance prediction have been explained. The methods have been compared with each other along with their validation methods. It can be noted that the main issue with seaplanes is the take-off and landing stability in which the craft experiences nonlinear and unsteady hydrodynamic and sea water wave characteristics. The available analytical methods lack the ability of predicting

the stability limits of the craft. Moreover, most of the methods discussed are valid under certain geometry and conditions. For example, Savitsky's method can predict the performance up to a trim angle of 4°. Also, it can be used for a dead-rise angle of 50° or less. Nevertheless, it is valid for steady-state conditions only. Therefore, no analytical method is good for all types of seaplanes. The prediction depends on the geometry of the hull and the operation conditions.

Heave and pitch equations of motion have the ability to predict the performance of seaplanes for higher speed regime than other methods. Also, this approach can be modified to produce results for a wider geometry range than Savitsky's method. It also can be expanded to allow for nonlinear performance prediction.

References

- Almeter, J. (1993), "Resistance prediction of planing hulls: state of the art", *Marine Technology*, Vol. 30 No. 4, pp. 297-307.
- Alourdas, P. (2016), *Planing Hull Resistance Calculation: The CAHI Method [PowerPoint Presentation]*, SNAME Greek Section, Greece.
- Baker, G. (1912), *Some Experiments in Connection with the Design of Floats for Hydro-Aeroplanes*, ARC R&M.
- Brown, P. (1954), "An empirical analysis of the planing characteristics of rectangular flat-plates and wedges", *Hydrodynamic Notes*, Short Bros & Harland, Belfast.
- Brown, P. (1971), *An Experimental and Theoretical Study of Planing Surfaces with Trim Flaps*, Stevens Institute of Technology, Report SIT-DL-71-1462, Hoboken, NJ.
- Chambliss, D. and Boyd, G. (1953), *The Planing Characteristics of Two V-Shaped Prismatic Surfaces Having Angles of Deadrise of 20 and 40 Degrees*, National Advisory Committee for Aeronautics, Washington, DC.
- Collu, M. (2008), "Dynamics of marine vehicles with aerodynamic surfaces", PhD, Cranfield University, Cranfield.
- Dala, L. (2015), "Dynamic stability of a seaplane in takeoff", *Journal of Aircraft*, Vol. 52 No. 3, pp. 964-971.
- Faltinsen, O. (2010), *Hydrodynamics of High-Speed Marine Vehicles*, Cambridge University Press, Leiden, p. 344.
- Farshing, D. (1955), "The lift coefficient of flat planing surfaces", MSc, Stevens Institute of Technology.
- Fossen, T. (2011), *Handbook of Marine Craft Hydrodynamics and Motion Control*, 1st ed., John Wiley & Sons, Chichester, West Sussex.
- Iacono, M. (2015), "Hydrodynamics of planing hulls by CFD", MSc, University of Naples, Naples.
- Ibrahim, R. and Grace, I. (2010), "Modeling of ship roll dynamics and its coupling with heave and pitch", *Mathematical Problems in Engineering*, Vol. 2010, pp. 1-32.
- Korvin-Kroukovsky, B. (1950), "Lift of planing surfaces", *Journal of the Aeronautical Sciences*, Vol. 17 No. 9, pp. 597-599.
- Korvin-Kroukovsky, B. Savitsky, D. and Lehman, W. (1949), "Wetted area and center of pressure of planing surfaces", Stevens Institute of Technology, Davidson Laboratory Report No. 360.
- Lewis, E. (1989), *Principles of Naval Architecture*, Society of Naval Architects and Marine Engineers, Jersey City, NJ.

- Locke, F. (1948), "Tests of a flat bottom planing surface to determine the inception of planning", US Navy Department, BUAER, Research Division Report No 1096.
- Morabito, M. (2010), "On the spray and bottom pressures of planing surfaces", PhD, Stevens Institute of Technology.
- Murray, A.B. (1950), "The hydrodynamic of planing hulls", New England SNAME Meeting 1950, SNAME, Jersey City, NJ.
- Ogilvie, T. (1969), *The Development of Ship-Motion Theory*, Department of Naval Architecture and Marine Engineering, College of Engineering, The University of MI, Ann Arbor, MI.
- Payne, P. (1995), "Contributions to planing theory", *Ocean Engineering*, Vol. 22 No. 7, pp. 699-729.
- Perelmuter, A. (1938), "On the determination of the take-off characteristics of a seaplane", NACA Technical Memorandum No 863.
- Perring, W. and Johnston, L. (1935), "Hydrodynamic forces and moments on a simple planing surface and on a flying boat hull", R&M No. 1646 British A.R.C.
- Priyanto, A., Maimun, A., Noverdo, S., Saeed, J., Faizal, A. and Waqiyuddin, M. (2012), "A study on estimation of propulsive power for Wing in Ground Effect (WIG) craft to take-off", *Jurnal Teknologi*, Vol. 59 No. 1.
- Rozhdestvensky, K. (2006), "Wing-in-ground effect vehicles", *Progress in Aerospace Sciences*, Vol. 42 No. 3, pp. 211-283.
- Salvesen, N., Tuck, E. and Faltinsen, O. (1970), *Ship Motions and Sea Loads*, The Society of Naval Architects and Marine Engineers, Jersey City, NJ.
- Sambrus, A. (1938), "Planing surfaces tests at large froude numbers – airfoil comparison", NACA TM 509.
- Savitsky, D. (1964), "Hydrodynamic design of planing hulls", *Marine Technology*, Vol. 1 No. 1, pp. 71-95.
- Schnitzer, E. (1953), "Theory and procedure for determining loads and motions in chine-immersed hydrodynamic impacts of prismatic bodies", NACA Report, Washington, DC, p. 1152.
- Sedov, L. (1947), "Scale effect and optimum relation for sea surface planning", NACA TM 1097.

- Shoemaker, J. (1934), "Tanks tests of flat and Vee-bottom planing surfaces", NACA TM 848.
- Shuford, C. (1954), *A Review of Planing Theory and Experiment with a Theoretical Study of Pure-Planing Lift of Rectangular Flat Plates*, NACA TN 3233, Washington, DC.
- Shuford, C. (1958), "A theoretical and experimental study of planing surfaces including effects of cross section and plan form", National Advisory Committee for Aeronautics Report p. 1355.
- Siler, W. (1949), "Lift and moment of flat rectangular low aspect ratio lifting surfaces", MSc, Stevens Institute of Technology TM No. 96.
- Sottorf, W. (1932), "Experiments with planing surfaces", NACA TM 661 and NACA TM 739.
- Sottorf, W. (1937), *Analysis of Experimental Investigations of the Planing Process of the Surface of Water*, NASA, NACA-TM-1061, Washington, DC.
- Yousefi, R., Shafaghat, R. and Shakeri, M. (2013), "Hydrodynamic analysis techniques for high-speed planing hulls", *Applied Ocean Research*, Vol. 42, pp. 105-113.
- Yun, L., Bliault, A. and Doo, J. (2010), *WIG Craft and Ekranoplan*, Springer, New York, NY.

Further reading

- Fossen, T. (1994), *Guidance and Control of Ocean Vehicles*, John Wiley & Sons, West Sussex.
- Korvin-Kroukovsky, B. (1955), *Investigation of Ship Motions in Regular Waves*, The Society of Naval Architects and Marine Engineers, Jersey City, NJ.

Corresponding author

Jafar Masri can be contacted at: jafar.masri@northumbria.ac.uk

Magna-Lok rivet joint and the stiffness-equivalent FE model

Jakub Šedek and Roman Růžek

Czech Aerospace Research Centre, Prague, Czech Republic

Abstract

Purpose – The purpose of this paper is to present a methodology for the determination of the stiffness when using simplified substitutive model of the joint. The usage of detailed finite element (FE) model of the joint in complex assemblies is not convenient; therefore, the substitutive model of the joint is used in FE models.

Design/methodology/approach – The detailed and simplified FE model of the joint is created in ABAQUS software and the analysis as well. The results of displacements are used for the determination of the stiffness of connecting element in simplified substitutive FE model. The approach is presented based on the general view on the different regions in the joint.

Findings – A simple FE modelling approach for the joint including the equivalent stiffness is presented. The particular solution is performed for Magna-Lok type of the rivet. The results show the same displacement for the detailed and simplified FE models. The analytical formula for stiffness determination in the load case with minimal secondary bending is introduced.

Practical implications – The approach for stiffness determination is straightforward and so no stiffness “tuning” is necessary in the simplified FE model.

Originality/value – The new approach for definition of simple FE model of the joint is introduced. It is not necessary to model a complex structure with detailed joints. The equivalent stiffness can be determined by presented procedure for every joint without limitation of the type.

Keywords Modelling, FE, Joint

Paper type Research paper

Nomenclature

Symbols

- A = Area of cross section (mm^2);
- d = Diameter (mm);
- D = Region of the joint;
- E = Young's modulus;
- K = Stiffness (N/mm);
- l = Length (mm);
- P = Load (N);
- t = Thickness (mm);
- δ = Deformation (mm);
- $\Delta\delta$ = Difference of deformation (mm); and
- ν = Poisson's number.

Introduction

In transportation, there are several types of joints used. Riveting is very common fastener non-dismantlable technology. Originally, it was widely used in steel constructions of bridges, halls and pressure vessels also mounted to trains. Army ships and tanks were riveted mostly till the Second World War when riveting was replaced by welding and bolts. Despite that reduction, the modern types of rivets are used till now.

Moreover, riveting is the most common way of connecting parts together in the aircraft industry (Fárek, 2010; Kaniowski *et al.*, 2009). The usage in aerospace is very wide. The primary or secondary structures are being traditionally connected by rivets. One of the modern types is the Magna-Lok rivet (see Figure 1). It is a new versatile, one-side and hole-filling fastener that can be installed with conventional installation tools. It has a unique circle-lock feature, which means a simple visual inspection to ensure it is installed properly (Arconic, 2017).

Generally, rivets are designed to transfer shear loading primarily. Some longitudinal load can be applied as well, but the contribution to the whole load transfer should be small. The connection of construction parts is therefore realized in such a way that the shear loading is introduced by rivets and longitudinal load by contact of connected bodies. Fasteners are also commonly grouped into the fields, but the stiffness is better to investigate individually. The multiple joints eliminate secondary bending caused by the offset of connected plates.

Finite element model (FEM) is an excellent method to analyse the structure from the point of stress, strain and deformations. The stiffness definition is crucial for the structure response. The FE representation of the joint can be realized by several ways:

- full model of the joint (Fárek, 2010; Kaniowski *et al.*, 2009; Langrand and Patronelli, 2002; Liu *et al.*, 1999; de

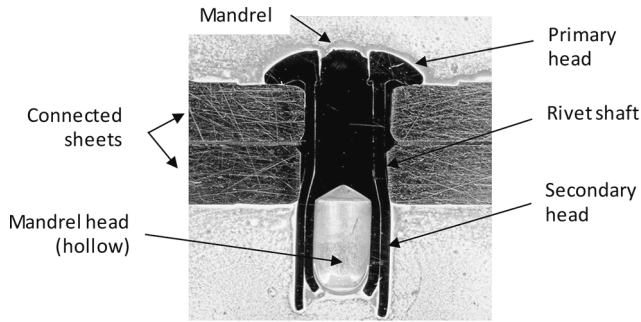
The current issue and full text archive of this journal is available on Emerald Insight at: www.emeraldinsight.com/1748-8842.htm



Aircraft Engineering and Aerospace Technology
91/6 (2019) 834–842
© Emerald Publishing Limited [ISSN 1748-8842]
[DOI 10.1108/AEAT-07-2018-0188]

This work was funded by the Technological agency of the Czech Republic under project number TE01020038.

Received 12 July 2018
Revised 14 August 2018
16 October 2018
Accepted 8 November 2018

Figure 1 Metallographic cross-section of the Magna-Lok rivet joint

Koning *et al.*, 1998; Atre and Johnson, 2006; Liao *et al.*, 2001);

- joint substitution by simplified connecting element (con. el.) (Bedair and Eastaugh, 2007; Langrand and Patronelli, 2002); and
- joint substitution by continuous layer of finite element (FE) elements with locally changed characteristics (Adamík, 2009).

The full model of the joint requires the detail representation of the connecting element and the neighbourhood. The technological operations when plastic deformations occur during manufacturing should be included in the analyses as well (Fárek, 2010; Kaniowski *et al.*, 2009). The analysis cost is high if several joints in the assembly are analysed at once. The material characteristics are also crucial. Only single joints are therefore analysed.

In complex structures, individual parts are being discretised by FEs, but it cannot be performed for joints. The joints in the complex model are usually under the level of resolution capability, because their dimensions are smaller than the minimal mesh size. Nevertheless, joints are important from the point of load transfer, and their stiffness should be covered well. The joint substitution by simplified connecting FE element reduces the analysis cost. The subcomponents representation is also simplified, so for example the metal sheets are modelled by planes and meshed by shell elements. The geometry of the joint can be kept (Bedair and Eastaugh, 2007), or the simplified connection can be used (Šedek, 2011). The substitutive FE element is connected to the surrounding mesh, but its stiffness differs in comparison with the real joint. To ensure the same load transfer through the substitutive FE element, its stiffness must be set accordingly. The strains near the joint are not simulated well, but in the wider neighbourhood, the strains are covered sufficiently as shown in the analysis of the fuselage panel presented in Langrand and Patronelli (2002). The approach with simplified connecting FE element is used primarily for modelling the assemblies containing several tens or hundreds of joints.

The joint substitution by continuous layer of FE elements with locally changed characteristics is covered in the literature very rare partly from the reason of several dependencies on the geometry, material, etc. The simplicity can be advanced when analysing structures where the local deformations are not relevant.

The stiffness of the joint K can be generally described as the relation between the load P and deformation δ as:

$$K = \frac{P}{\delta} \text{ (N/mm)} \quad (1)$$

The shear stiffness is expressed as the shear load versus tangential displacement of connected parts.

The joint stiffness can change because of service conditions as the type of loading, environment or chemical and electrochemical reactions. All elements determining rivet stated above can influence the shear stiffness as well. Test of joints are being mainly performed for the strength capabilities of the joint. The stiffness can be evaluated as the slope of the stress–strain curve, but the dependency on the load history occurs. The evaluation is then carried out after several cycles when the stiffness stabilizes (Kadlec and Kucharský, 2016).

In analytical stiffness determination, the basic approach of assuming only geometrical characteristics, static load and material characteristics is widely used. The shear stiffness of the joint can be expressed in the general form as:

$$K = K(P, d, t_1, t_2, E_1, E_2, E_s) \quad (2)$$

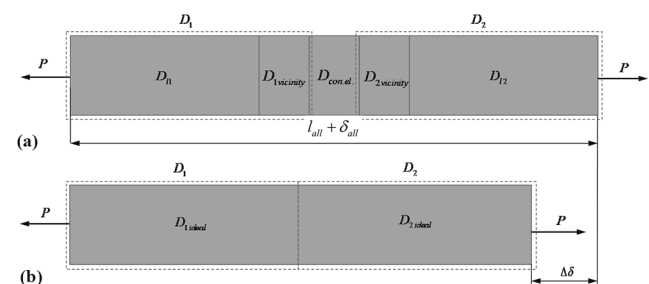
where d denotes rivet diameter, t_i is the thickness of connected part, E_i is its Young's modulus and E_s is the Young's modulus of the rivet.

Based on the experiments and analytical analyses of different types of joints, several analytical formulas for shear stiffness determination were introduced (Vogt, 1947; Swift, 1974; Barrois, 1978; Huth, 1984). These formulas differ mostly in possibility of using different connected materials and the joint geometry. Analytical formulas have been used mainly in specialized companies for typical applications on which they were verified. The validity depends on technology as well and the generalization can be difficult.

Definition of shear stiffness of a joint

The deformation during loading P occurs not only in the rivet but also in its neighbourhood. The connected parts are also deformed and influence the stiffness in analysed region. The stiffness of the joint is therefore composed of the stiffness of the rivet and certain regions D in connected parts as schematically shown in Figure 2(a). D_i denotes the region of part i , δ_{all} is the deformation of connected parts with length l_{all} , $D_{con.el.}$ is the rivet itself, $D_{1\text{ vicinity}}$ is the vicinity of the rivet in the part i and $D_{i\text{ rest}}$ is the rest of part i contributing to the stiffness.

The whole deformation of connected parts can be described as:

Figure 2 (a) Schematic representation of deformation of connected parts and (b) the relation to the parts without joint

$$\delta_{all} = \delta_1 + \delta_{con.el.} + \delta_2 \quad (3)$$

where δ_1 and δ_2 denote the deformation of connected part D_{1i} and D_{2i} , and $\delta_{con.el.}$ is the deformation of the connecting element. By expanding equation (3), the whole deformation of the connected parts can be written as:

$$\delta_{all} = \delta_{i1} + \delta_{1vicinity} + \delta_{con.el.} + \delta_{i2} + \delta_{2vicinity} \quad (4)$$

In this formula, δ_{ii} denotes the deformation of the part not influenced by the rivet and hole, and $\delta_{i\text{vicinity}}$ is the deformation of the vicinity of part i .

In a real joint, the border between regions D_{ii} and $D_{i\text{vicinity}}$ is not strict, but it is vague. In the engineering approach, it is necessary to choose the border so that the influence of the connecting element is not severe. In the analytical approach, the regions are analysed individually (Swift, 1974), or together, and the influence is evaluated by correction factor.

The deformation of connected parts is being commonly evaluated according to the deformation without joint as $\Delta\delta$, which is schematically shown in Figure 2(b). $D_{i\text{ideal}}$ denotes the region of the part if no deformation occurs in the vicinity of the connecting element.

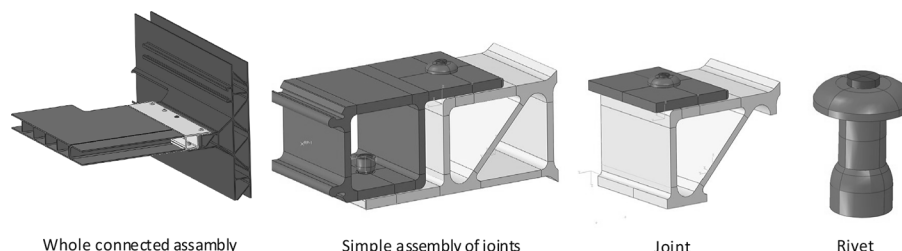
Structure definition

The representation of the connection in design stage of the structure can be divided into several levels according to building block approach. It enables to investigate the connection at several levels. In the assembly level, the joint itself is not assumed in detail, and only the stiffness and strength characteristics are mostly in interest. In lower levels, the joint should be not understood only the fastener itself but also the near neighbourhood included. At the lowest levels, the connection can be represented by the fastener (rivet).

The secondary structure joint connecting the floor and the wall in transportation vehicle was chosen as the demonstrator for the analysis of rivet connection in this work. The assembly is divided into down-level components for stiffness investigation as shown in Figure 3.

The joint is determined by several elements, e.g. the connected bodies, the hole with its diameter and tolerance, technology of assembling remaining residual stresses, roughness of contact surfaces determining friction and also the rivet itself with its geometry differing especially in the head shape. All these elements influence the joint behaviour. The joint representation in the analysis should cover all determining elements, but it is difficult to ensure. The stiffness is one of the primary characteristics of the joint. It can be determined analytically

Figure 3 Building block approach



mostly based on the empirical formulas, numerically using FEM or experimentally.

FE stiffness-equivalent model

From the point of numerical modelling by FEM, it is not possible to represent the joint in detail. For practical use, the joint is necessary to replace by the simple representation; however, the same load transfer must be ensured. The simplification result is therefore the stiffness-equivalent joint (Doubrava, 2015).

Let us assume the whole deformation of connected parts determined by the detailed numerical analysis, by experimental evaluation or by analytical formula δ_{all} . Then let us define the substitutive numerical model of the joint, which can be used in assembly with a lot of joints. This work includes definition of a mesh size, element types, boundary conditions, connecting element and material characteristics as well.

To avoid secondary bending, the simple assembly with upper and lower joint is analysed. The model (see Figure 4) represents the connection of two aluminium alloys by Magna-Lok type of the rivet. To characterize this connection in global FE model, the substitutive local model was created. In this work, the ABAQUS 2017 FE software was used. The parts were modelled by shell elements with reduced integration, and the connection was realized by ABAQUS BUSH-type element, which connects two nodes and enables setting the stiffness of relative translations and rotations in individual directions separately. No hole was created in connected parts, but the mesh was adapted to represent the rivet shank and rivet head by two circles with corresponding diameters. The boundary conditions are obvious from Figure 4.

Loading of connecting points is redistributed via “continuum distributing coupling” similar to RBE3 element in NASTRAN software. It is not necessary to use only this type of connection, but the mesh in this region and the connecting element must be the same for all joints in a global model.

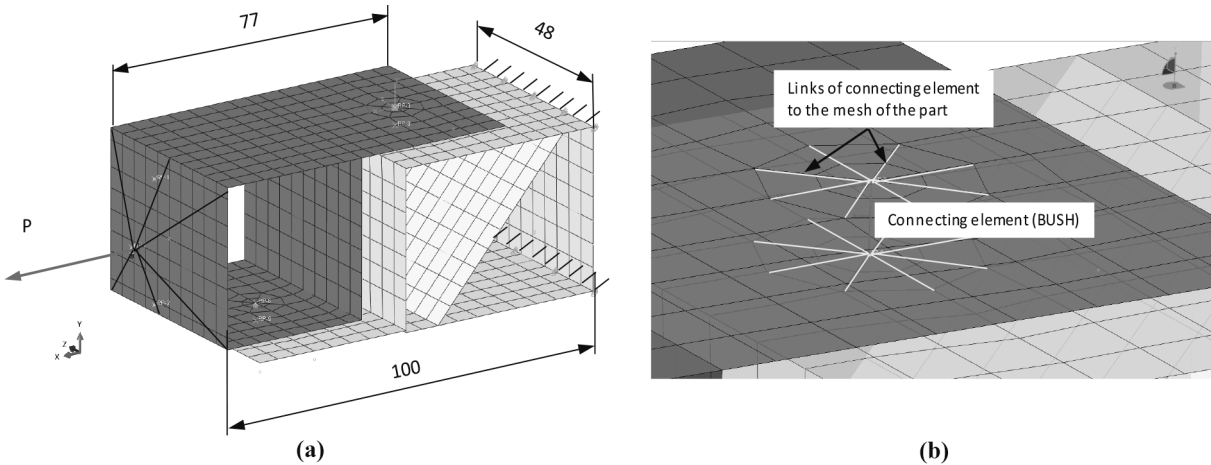
Shear stiffness of the finite element model of a joint

In numerical models, it is necessary to take into account, especially, the shear stiffness of the joint. The whole deformation of the joint δ_{all} with the load transfer P is the sum of the deformations of individual regions δ_i . The deformation of connecting element $\delta_{con.el.}$ can be determined as:

$$\delta_{con.el.} = \delta_{all} - \delta_1 - \delta_2 \quad (5)$$

The stiffness of connecting element $K_{con.el.}$ is then:

Figure 4 Substitutive model of analysed basic assembly with rivet joints Magna-Lok (mesh shown)



Notes: (a) The overall view; (b) the connecting element and links to connected parts

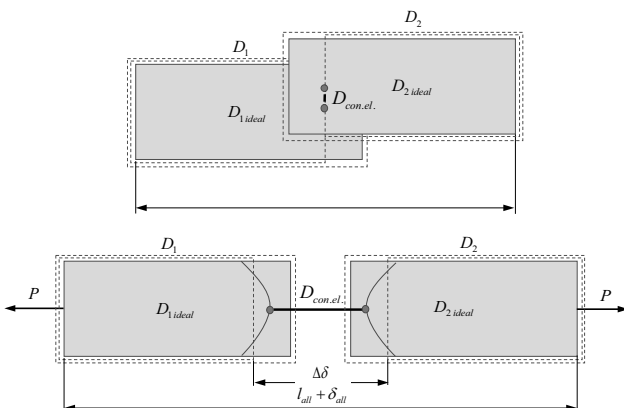
$$K_{con.el.} = \frac{P}{\delta_{con.el.}} \quad (6)$$

The stiffness of the connecting element $K_{con.el.}$ is not sufficient to provide a stiffness-equivalent FE joint. The dependency on the mesh and the link of the connected element to the mesh appears. The situation for two connected sheets is shown schematically in Figure 5, where D denotes the regions of the joint. In the vicinity of the connecting element, the sheets will be deformed. On the other hand, if the load is regularly distributed in the cross section, no such local deformation will occur. In the FE model, the local deformation will be very dependent on the mesh and the type of the link of the connecting element to the mesh. In case of the link to a single node, the singularity will occur and by refining the mesh, the deformation will increase.

The deformation of the joint $\Delta\delta$ is generally done by the difference of total deformation δ_{all} and ideal deformation of sheets (no local deformation) ($\delta_{1ideal} + \delta_{2ideal}$):

$$\Delta\delta = \delta_{all} - \delta_{1ideal} - \delta_{2ideal} \quad (7)$$

Figure 5 The regions of two connected sheets (schematically shown)



The total deformation of connected parts can be expressed as:

$$\delta_{all} = \delta_{1ideal} + \delta_{1vicinity}^* + \delta_{con.el.} + \delta_{2vicinity}^* + \delta_{2ideal} \quad (8)$$

where, $\delta_{i\ vicinity}^*$ represents the difference between the deformation of the ideal region $\delta_{i\ ideal}$ and the real one δ_i :

$$\delta_{i\ vicinity}^* = \delta_i - \delta_{i\ ideal} \quad (9)$$

In case of sheets, the deformation δ_i ideal can be simply expressed analytically as:

$$\delta_{i\ ideal} = \frac{Pl_i}{EA} \quad (10)$$

where A represents the cross section of the sheet, and l_i is the length of the connected region measured from the connecting element.

The stiffness of the joint can be expressed in accordance with Figure 5 and previous equations as:

$$K_{joint} = \frac{P}{\Delta\delta} \quad (11)$$

In the form of stiffnesses, we can write:

$$K_{joint} = \frac{K_{1\ vicinity}^* K_{2\ vicinity}^* K_{joint}}{K_{1\ vicinity}^* K_{2\ vicinity}^* - K_{joint} (K_{1\ vicinity}^* + K_{2\ vicinity}^*)} \quad (12)$$

with condition

$$\frac{K_{joint} (K_{1\ vicinity}^* + K_{2\ vicinity}^*)}{K_{1\ vicinity}^* K_{2\ vicinity}^*} \leq 1 \quad (13)$$

The condition limits the deformation of the joint $\Delta\delta$ to be greater or the same as the sum of deformations δ_{1ideal} and δ_{2ideal} . If the condition is not fulfilled, the deformation decreases with increasing load (unreal in common engineering materials):

$$\Delta\delta \geq \delta_{1ideal} + \delta_{2ideal} \quad (14)$$

Secondary bending of connected parts

Pure shear loading does not occur in the real connection. Owing to the offset of neutral planes of connected parts, the secondary bending appears and the rotation of the connecting element as well. The rotation causes the displacement in the direction of the load, and it decreases the shear stiffness of the joint.

The value of joint deformation caused by the rotation $\delta_{all\ rotation}$ can be determined as the subtraction of the deformation in pure shear mode $\delta_{all\ shear}$ from the deformation including tangential and rotation displacements $\delta_{all\ shear+rotation}$:

$$\delta_{all\ rotation} = \delta_{all\ shear+rotation} - \delta_{all\ shear} \quad (15)$$

The deformation of connection element $\delta_{con.el.}$ for determination of its stiffness $K_{con.el.}$ can be obtained as:

$$\delta_{con.el.} = \delta_{defined} - \delta_{all\ rotation} - \delta_{all\ shear} \quad (16)$$

where $\delta_{defined}$ denotes the deformation of the joint determined by the detailed FE analysis, the test or analytical formula. The corresponding stiffness is then expressed according to Equation (6).

Detailed analysis of the joint with Magna-Lok rivet

One of the approaches to determine the stiffness of the joint is the detail FE analysis. The three-dimensional model of the joint using Magna-Lok rivet was created in more general assembly. Two rivets were included to prevent excessive secondary bending of connected parts. The model is shown in Figure 6.

In the model, there are represented both connected profiles and two rivets. The geometry of the rivet is in the shape after riveting. The geometrical tolerances are not taken into account, the diameter of the hole and the rivet are the same. The residual stresses caused by manufacturing technology are not taken into account as well for simplicity; however, the preload in the rivet with magnitude of 2,200 N is applied to represent the tension in the rivet. In the model, the hexahedral elements with reduced integration were used (C3D8R in Abaqus). The characteristic size of the element was 2 mm, but six elements with the

thickness of 0.67 mm were created through the thickness of profile wall in the location of the rivet. In the rest of the model, only three elements were used through the thickness. The rivet was meshed similarly, but the element size was smaller of about 0.3–1 mm (see Figure 6b).

The connected profiles are made from aluminium alloy EN AW 6005A/T6, which is represented by isotropic material model with the Young's modulus $E = 72$ GPa and Poisson's ratio $\nu = 0.33$. The Magna-Lok rivet is MGLP-U8-6 type (Magna-Lok, 2017) made from stainless steel. Material characteristics with $E = 210$ GPa and $\nu = 0.3$ were used for the rivet in the model. The assembly is loaded by the force $P = 20,900$ N, which is the double of the maximum load prescribed by the manufacturer (Magna-Lok, 2017). The penalty contact between the surfaces is applied with the friction coefficient of 0.15.

The results of the detailed finite element model

The analysis of the joint assembly is carried out using linear characteristics of materials, but the nonlinearity is present because of the contact of surfaces. The deformation of the model was in the interest to determine the stiffness.

The load causes the displacements mainly in the direction of the load and the rotation of the rivets (see Figure 7). The rotation is caused mainly because of free ends of the rivet, where only lower part of the head is in contact with the surface of the profile. The other reason is the deformation of the rivet hole. In reality, the plastic deformation would occur during riveting in the hole, and the rivet and the residual stresses will prevent these displacements. The displacements can be therefore expected smaller than in the model. From the displacement field, the deformations of the connected parts can be determined. In Figure 8, the regions according to the general approach as described before are shown and in Table 1, and the determined values are stated. The stiffness is evaluated in upper and lower rivet individually and in the centre and surface location for each rivet as well.

The deformations in the square profile are little lower than in triangular profile, but the load transfer is little higher. In consequence, the stiffnesses are almost the same for upper and lower rivet. The stiffness determined at the outer surface is approximately twice lower in comparison with the stiffness in the middle of the profile wall. The reason is the rotation of the

Figure 6 (a) detailed FE model of the joint assembly and (b) detail of the mesh of Magna-Lok rivet

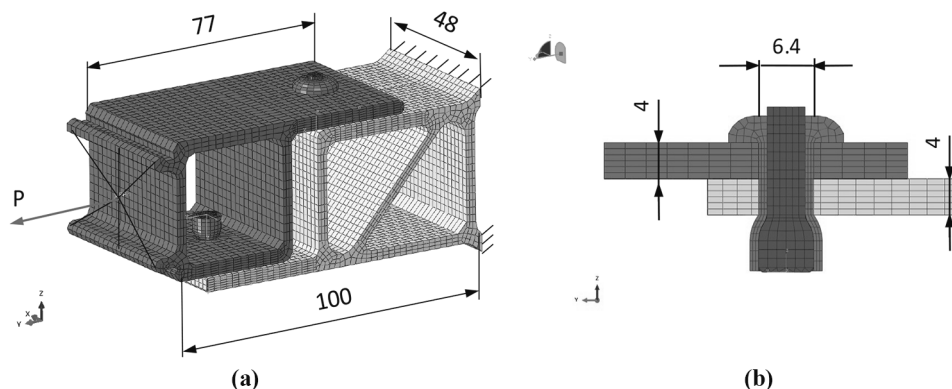
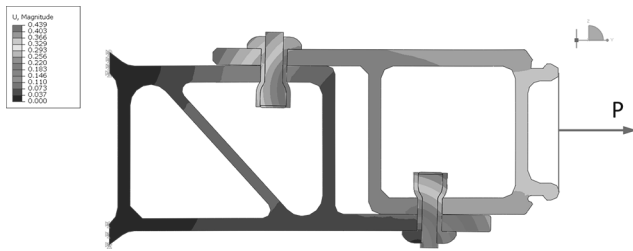


Figure 7 Total displacements of the model of rivets assembly, $P = 20,900$ N



rivet and the twice greater displacement at the end of the rivet than in the centre. Therefore, the attention should be paid to the stiffness determination. The location according to the stiffness measurement should be always noted. The stiffness in Table 2 corresponds only to the rivet, and the deformation of profiles in the vicinity is not covered. The displacement of the loaded point was determined $\delta_{all} = 0.31$ mm. This value should be obtained in substitutive simplified FE model using equivalent stiffness approach as well and so the stiffness of the connecting element should be determined.

Definition of the connecting element stiffness in substitutive model of the assembly with Magna-Lok rivets

The substitutive model of the simplified assembly with Magna-Lok rivets was created as described in chapters above. Two variants with fine mesh (V1) and coarse mesh (V2) were chosen for the demonstration of the approach. The variant V1 was discretized by shell elements with the characteristic size of 2 mm and the variant V2 with the size of 10 mm. The quad-shaped elements with reduced integration scheme were used, and in the connecting point, the triangular elements were only used (see Figure 9). Refining the mesh near the connecting point causes increase of the deformation in this

area and vice versa (Šedek, 2011); therefore, the mesh size should be set appropriately. Connection of both parts was realized by the spring element (BUSH type) with six independent stiffnesses in displacements and rotations. The axial stiffness was determined assuming circular tube representing the rivet shank. The rotation stiffnesses were set as rigid with $K = 10^9$ N/mm except rotation around the bolt axis which was not assumed. The shear stiffness was determined according to the general description of joint regions described above. For this purpose, the pure shear and shear plus bending load cases were analysed. The values determined on the simple substitutive models for the upper and lower joint under the load of 20 900 N are stated in Table 2. The stiffness of connecting element in the coarse variant (V2) is little higher than in the variant with fine mesh (V1). Figure 9 shows the displacement and deformation fields for the detailed model and for the simplified substitutive models using determined shear stiffnesses for the connecting element. It is seen that the response of the simplified models and the detailed one on the load is almost the same, and only in the vicinity of the connection element, some slight differences appear. The displacement of the point with load applied is the same for the detail and the substitutive FE models.

Comparing the stiffnesses of the connecting element determined from the detailed FE model (K_{rivet}) and from the substitutive simplified FE model ($K_{con.el.}$), the very close values between the one determined for outer surface and the other for substitutive models are obvious. This result should not be generalized, and it is probably the result only for the analysed configuration.

Using the equivalent joint stiffness approach in the analysis of a wing spar

Presented approach of equivalent joint stiffness can be used in any FE model containing joints to decrease the complexity of the model and to increase the representativeness. For

Figure 8 Detail of the displacements of joint at the assembly load $P = 20,900$ N

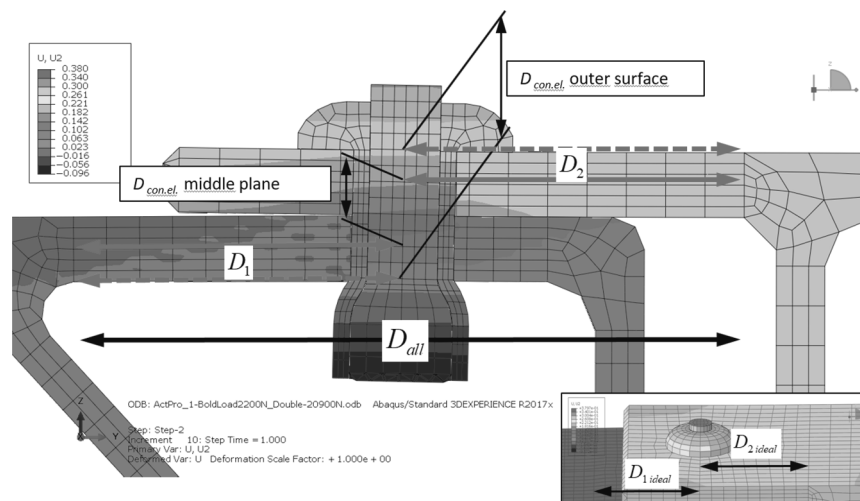


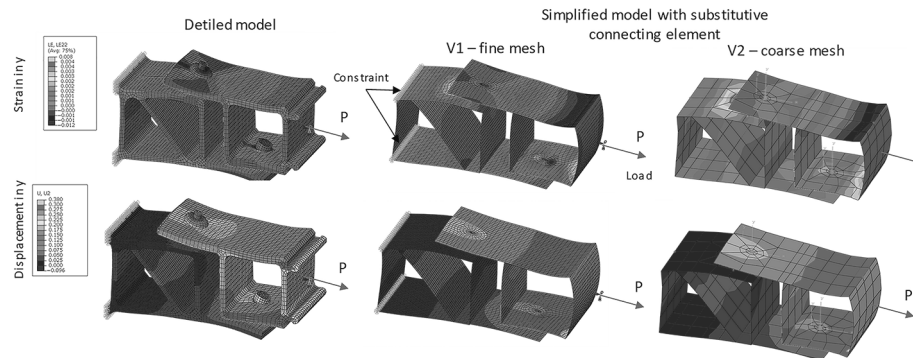
Table I The Values of substitutive FE model of the joint assembly

Pure shear	$\delta_{1 ideal}$ [mm]	δ_1 [mm]	$\delta_{1 vicinity}^s$ [mm]	$K^*_{1 vicinity}$ [N/mm]	$\delta_{2 ideal}$ [mm]	δ_2 [mm]	$\delta_{2 vicinity}^s$ [mm]	$K^*_{2 vicinity}$ [N/mm]	$\delta_{all rigid con.el.}$ [mm]
V1 upper rivet	2.54E-02	3.61E-02	1.07E-02	9.72E+05	4.51E-02	5.65E-02	1.14E-02	9.17E+05	9.26E-02
V1 lower rivet	6.41E-02	7.56E-02	1.15E-02	9.07E+05	1.56E-02	2.44E-02	8.82E-03	1.18E+06	1.00E-01
V2 upper rivet	2.53E-02	3.57E-02	1.03E-02	1.01E+06	4.53E-02	5.60E-02	1.06E-02	9.83E+05	9.16E-02
V2 lower rivet	6.41E-02	7.46E-02	1.04E-02	1.00E+06	1.55E-02	2.35E-02	7.96E-03	1.31E+06	9.81E-02
Shear + Bending	δ_1 [mm]	δ_2 [mm]	$\delta_{all rigid con.el.}$ [mm]	Rotation = shear + rotation	$\delta_{all rigid con.el.}$ [mm]	Shear stiffness of compliant con. el. (BUSH element)	$\delta_{con.el.}$ [mm]	$K_{con.el.}$ [N/mm]	$\delta_{all compliant con.el.}$ [mm]
V1 upper rivet	3.66E-02	5.68E-02	1.24E-01	pure shear	3.10E-02	(BUSH element)	1.83E-01	5.70E+04	3.07E-01
V1 lower rivet	7.64E-02	2.50E-02	1.27E-01	rotation	2.70E-02		1.80E-01	5.81E+04	3.07E-01
V2 upper rivet	3.67E-02	5.62E-02	1.31E-01		3.90E-02		1.76E-01	5.92E+04	3.07E-01
V2 lower rivet	7.60E-02	2.44E-02	1.30E-01		3.23E-02		1.77E-01	5.92E+04	3.07E-01

Note: Model load P = 20,900 N

Table II The values of detailed FE model of the joint at the assembly load $P = 20,900$ N

Position	P_{rivet} [N]	δ_{rivet} middle [mm]	δ_{rivet} outer surface [mm]	K_{rivet} middle [N/mm]	K_{rivet} outer surface [N/mm]
Upper rivet	1.03E+04	0.102	0.188	1.02E+05	5.50E+04
Lower rivet	1.06E+04	0.099	0.180	1.08E+05	5.87E+04

Figure 9 Connection of two profiles using Magna-Lok rivets; FE analysis of detailed model and the shell models (V1 and V2), including connecting element with equivalent stiffness

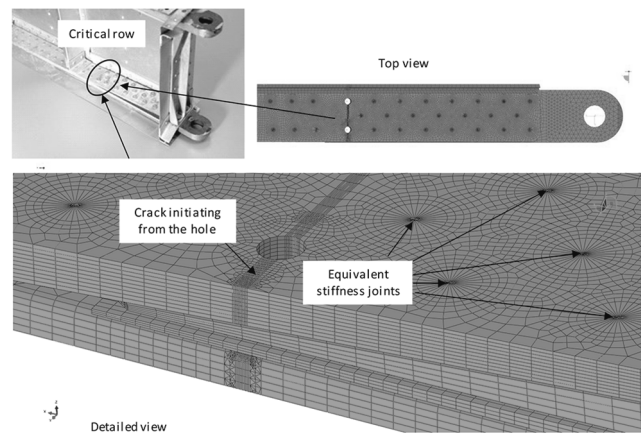
example, the analysis of lower root spar assembly of a sailplane was performed employing presented approach (Šedek *et al.*, 2015). The crack growth in the flange was analysed to obtain the fatigue life and to assess the load level which were close to the critical load of the structure. The crack initiated from the rivet hole in the flange. The FE model of critical location was created to determine parameters of fracture mechanics of included crack as shown in Figure 10. To correctly represent the stress and strain fields around the crack tip, it was necessary to model the stiffness of surrounding rivets. The representative stiffness of connecting element was determined accordingly to presented approach. The results of computed crack growth increments caused by overloads were very close to those determined by fractographic analysis.

Conclusion

Based on the general view on the regions of the joint and their contribution to the joint stiffness, the technique for the determination of the stiffness characteristic of the connecting element into the substitutive FE model is introduced. The approach can be summarized into the following steps:

- definition of the base geometry of the joint and its characteristics;
- definition of the stiffness of the joint – analytical formula, test and FE analysis;
- definition of the parameters of the substitutive joint – FE mesh, stiffness of the connecting element, etc.;
- implementation of the joint into the global FE model; and
- analysis and evaluation of results.

These steps are straightforward, and therefore, it is not necessary to “tune” the stiffness of connecting element by iterative approach. If the shear loading is dominant and the secondary bending is minimal, the stiffness of the connecting element can be determined directly from equation (12).

Figure 10 Critical location and the FE model of analysed region

The equivalent stiffness of the joint in the global model is reached by the same FE mesh as applied at the individual substitutive model. The change of the mesh does not need to be significant in the case of small mesh size differences as shown by two analysed variants of simplified model with different mesh. The values of the stiffness of connecting element are very close. On the contrary, the type of the link of the connected element to the mesh is crucial. The principal of similarity of the joint model in substitutive and global model must be satisfied. For example, if the boundary conditions applied close to the joint differ, the stiffness variability should be checked.

Presented approach for stiffness determination of substitutive element was used in the works dealing with the crack propagation. The stiffness of the joints close to the crack influences the crack opening displacement and the crack growth rate; therefore, the representative stiffness must be ensured.

References

- Adamík, P. (2009), “Experimental analysis of rivet joint stiffness and its modeling in finite element analysis, PhD. thesis”, Brno University of Technology, Faculty of Mechanical Engineering, p. 132, available at: www.vutbr.cz/www_base/zav_prace_soubor_verejne.php?file_id=58792
- Atre, A.P. and Johnson, W.S. (2006), “Analysis of the effects of riveting process parameters on the fatigue of aircraft fuselage lap joints”, *9th Joint FAA/DoD/NASA Aging Aircraft Conference*.
- Arconic (2017), “Magna-Lok”, available at: www.afshuck.net/us/en/Products/Fasteners/Blind_Fasteners/Magna-Lok.html
- Barrois, W. (1978), “Stress and displacement due to load transfer by fasteners in structural assemblies”, *Engineering Fracture Mechanics*, Pergamon Press, Vol. 10.
- Bedair, O.K. and Eastaugh, G.F. (2007), “A numerical model for analysis of riveted splice joints accounting for secondary bending and plates/rivet interaction”, *Thin-Walled Structures*, Vol. 45 No. 3, pp. 251-258.
- Doubrava, R. (2015), “Effect of mechanical properties of fasteners on stress state and fatigue behaviour of aircraft structures as determined by damage tolerance analyses”, *Procedia Engineering*, Vol. 101, pp. 135-142, doi: 10.1016/j.proeng.2015.02.018.
- Fárek, J. (2010), “FE-Modelling methodology of riveted joints”, *Czech Aerospace Proceedings*, No. 2/2010, Prague, pp. 12-16.
- Huth, H. (1984), “Zum einfluss der nietnachgiebigkeit mehrreihiger nietverbindungen auf die lastübertragungs- und lebensdauervorhersage, dissertation thesis”, Darmstadt, Fraunhofer - Institut für Betriebsfestigkeit (LBF).
- Kadlec, V. and Kucharský, P. (2016), “Fastener stiffness measurement methodology”, in Plánička, F. and Krystek J. (Eds), *54th International Conference on Experimental Stress Analysis, EAN 2016; May 30 – June 2, Srní*.
- Kaniowski, J., Wronicz, W., Jachimowicz, J. and Szymczyk, E. (2009), “Methods for FEM analysis of riveted joints of Thin-Walled aircraft structures within the IMPERJA project”, *ICAF 2009, Bridging the Gap between Theory and Operational Practice, Part 6*, pp. 939-967, doi: 10.1007/978-90-481-2746-7_52.
- de Koning, A.U., ten Hoeve, H.J., Grooteman, F.P. and Lof, C.J. (1998), “Advances in the modelling of cracks in space structures”, *European Conference of Spacecraft Structures, Brunschweig*, NLR-TP-98423.
- Langrand, B. and Patronelli, L. (2002), “An alternative numerical approach for full scale characterisation for riveted joint design”, *Aerospace Science and Technology*, Vol. 6 No. 5, pp. 343-354.
- Liao, M., Shi, G. and Xiong, Y. (2001), “Analytical methodology for predicting fatigue life distribution of fuselage splices”, *International Journal of Fatigue*, Vol. 23, pp. 177-185.
- Liu, J.Y., Flach, D.D., Ross, R.J. and Lichtenberg, G.J. (1999), “An improved shear test fixture using the iosipescu specimen”, *Mechanics of Cellulosic Materials*, AMD-Vol. 231, MD Vol. 85, The American Society of Mechanical Engineers, pp. 139-147.
- Magna-Lok (2017), “Structural rivets – list of specification”, available at: www.kvt-fastening.cz.
- Swift, T. (1974), “Development of the fail-safe design features of the DC- 10, ASTM STP 486”.
- Šedek, J. (2011), “FE - modeling of stiffness equivalent riveted joints”, In Fuis, V. (Ed.) *Proceedings of 17th International Conference Engineering Mechanics 2011: May 9-12, 2011, Svatka, Czech Republic*, 1st ed., Institute of Thermomechanics, Academy of Science of the Czech Republic, Prague, v.v.i., pp. 591-594.
- Šedek, J., Běhal, J. and Siegl, J. (2015), “Structure overloading evaluation based on the identification of subcritical crack increments”, *Engineering Failure Analysis*, Vol. 56, pp. 265-274.
- Vogt, F. (1947), *The Load Distribution in Bolted or Riveted Joints in Light-Alloy Structures*.

Corresponding author

Jakub Šedek can be contacted at: sedek@vzlu.cz

Stability analysis of the experimental airplane powered by a pulsejet engine

Katarzyna Pobikrowska and Tomasz Goetzendorf-Grabowski

Faculty of Power and Aeronautical Engineering, Warsaw University of Technology, Warsaw, Poland

Abstract

Purpose – This paper aims to present stability analysis of a small pulsejet-powered airplane. This analysis is a part of a student project dedicated to designing an airplane to test valved pulsejet engine in flight conditions.

Design/methodology/approach – The panel method was chosen to compute the airplane's aerodynamic coefficients and derivatives for various geometry configurations, as it provides accurate results in a short computational time. Also, the program (PANUKL) that was used allows frequent and easy changes of the geometry. The evaluation of dynamic stability was done using another program (SDSA) equipped with means to formulate and solve eigenvalue problem for various flight speeds.

Findings – As a result of calculations, some geometry corrections were established, such as an increase of the vertical stabilizer's size and a new wing position. Resulting geometry provides satisfactory dynamic and static stability characteristics for all flight speeds. This conclusion was based on criteria given by MIL-F-8785C specifications. This paper presents the results of the first and the final configuration.

Practical implications – The results shown in this paper are necessary for the continuation of the project. The aircraft's structure was being designed in the same time as the calculations described in this paper proceeded. With a few modifications to make up for the changes of external geometry, the structure will be ready to be built.

Originality/value – The idea to design an airplane specifically to test a pulsejet in flight is a unique one. Most RC pulsejet-powered constructions that can be heard of are modified versions of already existing models. What adds more to the value of the project is that it is being developed only by students. This allows them to learn various aspects of aircraft design and construction on a soon-to-be real object.

Keywords UAV, Stability, Aircraft design, Pulsejet

Paper type Case study

Introduction

The history of a pulsejet engine starts in 1906, when Russian engineer V.V. Karavodin patented the first working pulsejet. Next the French inventor G. Marconnet patented valveless pulsejet engine in 1908. The first pulsejet-powered aircraft however did not show up until the Second World War period. Most constructions were used either as missiles or aircraft for suicidal missions. This has its reasons. By nature, the pulsejet is a very lightweight, easy to build and low-cost combustion engine, making it perfect for a one-time use. Moreover, it has high fuel consumption, and some of its variants have parts that wear very quickly. The most popular pulsejet-powered aircraft to be found in history is the German V-1 bomb. It was propelled by the Argus As-014 engine. Its valves could only stand a time of one flight (around 1 h).

After the Second World War, the development of more efficient pulsejets continued. The most promising result is the pulse detonation engine (PDE) which has been proven to have the lowest fuel consumption and the highest specific impulse of all jet engines for up to 5 Mach. Today, companies such as

NASA, P&W and GE work on the development of PDE both for subsonic and supersonic aircraft.

A conventional pulsejet however has more drawbacks, i.e. a high dependence of flight speed on thrust, large noise and vibration, and low fuel efficiency. Nonetheless, it has a very simple design and operation principle, making it possible to build even by amateurs.

Worth mentioning pulsejet-powered constructions from history are as follows:

- XH-26 Jet Jeep (1952), JK-1 Trzmiel (1957) – tip jet helicopters with pulsejet engines used to spin the rotor;
- SZD-9 Bocian Puls (1955) – a motor glider powered by four valveless pulsejets; and
- Borealis (2008) – the first PDE-powered aircraft; a modified Rutan Long-EZ.

Recently, the topic of aircraft powered by pulsejet engines has surfaced in the remote-controlled aircraft world. The pulsejet is a cheaper and easier in operation alternative to jet engines for use in fast flying models or flying targets. Inspired by this trend, a group of students from Warsaw University of Technology started a project dedicated to designing a RC airplane for an already-built valved pulsejet engine (Pobikrowska, 2018), shown in Figure 1.

The name of this airplane will be *Numinosum*, which refers to an experience that is equally fascinating and frightening.

The current issue and full text archive of this journal is available on Emerald Insight at: www.emeraldinsight.com/1748-8842.htm



Aircraft Engineering and Aerospace Technology
91/6 (2019) 843–850
© Emerald Publishing Limited [ISSN 1748-8842]
[DOI 10.1108/AEAT-07-2018-0184]

Received 9 July 2018
Accepted 2 August 2018

Figure 1 The pulsejet engine to be mounted on Numinosum airplane.

Idea

Project requirements

The aim to build the airplane is to test an engine during flight. To accomplish that, the airplane must be able to fly for a set amount of time propelled by the pulsejet. During the flight, it will change altitude and flight speed. The impact on the engine work parameters will be measured. Next step, in the future, is to include more complicated manoeuvres to the test.

Numinosum is not a competitive aircraft – it is a kind of flying testing platform, so it does not need to be fast or to have a high endurance. The time of flight is based only on the time of engine performance. A pulsejet is a type of engine that consumes relatively big amounts of fuel, so the time of flight must have been set to ensure that the fuel tank can be fitted in airplane's fuselage. For liquid fuel (kerosene), this resulted in a time of flight of around 3 min.

Liquid fuels are easy to store and lighter than gaseous for they do not require a pressurized tank, but a fuel pump and a more sophisticated injector are necessary. The gaseous fuels on the other hand are more reliable, as the safety is guaranteed by the tank valve. Also, in contrast to liquid fuels, there is no problem with the fuel moving around during manoeuvres. Our engine has so far been tested only on propane-butane mixture. The choice of fuel type is still open for discussion.

Our engine is unpredictable and has not yet been tested in flight. The pulsejet can die during a manoeuvre, when the fuel tank empties or in any other difficult to predict case. For this reason, there will be an additional electric engine mounted on the airplane to assist during start and landing. The pulsejet will be started either on the ground or in the air. The second option seems more reliable, as the engine might need forced airflow to start.

The airplane must be protected from hot exhaust gases and heat radiation from the combustion chamber. It should also be immune to the engine's vibration. Moreover, the airplane's geometry and structure must be simple, so that it is easy to build.

The airplane must be safe for people on the ground and for itself. The first can be achieved by satisfying good flying qualities, which does mean good stability of the airplane, the

second by securing the structure from high temperatures and flame. This will be achieved by installing a switch to remotely stop the fuel flow in case of an emergency. Top of the fuselage and parts of the aerodynamic surfaces closest to the engine will be covered with aluminium heat shield to protect them from radiation.

Airplane description

Numinosum is a high-wing, unmanned aircraft with a conventional horizontal stabilizer and two vertical stabilizers. This configuration ensures that the tail surfaces are protected from hot exhaust gases. Airplane's specifications are listed in Table I. The airplane will be controlled by a pilot on the ground. In later phases of the project, an autopilot may be implemented.

One of the problems that arose during the design was to properly balance the airplane. The initial conception was to place the engine so that its exhaust pipe reaches behind the tail. This configuration would prevent hot exhaust gases from hitting the empennage. Unfortunately, it could not be applied due to the large weight of the pulsejet (Table II). The engine therefore will be installed closer to the front. However, this will still need to be compensated by placing all the RC equipment in the very front part of the fuselage.

The aircraft's structure will be composed of Styrofoam, light wood and fiberglass. The numerical model is presented in Figure 2. The Figure 3 presents the sideview and the main dimensions.

Pulsejet engines

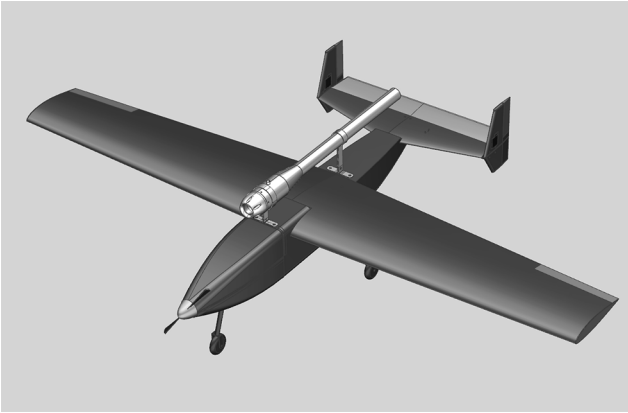
A pulsejet engine is a very simple engine, most often consisting of no moving parts. The engine can be split into three parts: inlet, a conical combustion chamber with fuel injectors and a spark plug and a cylindrical exhaust pipe. Pulsejets vary in combustion chamber size, length of the outlet pipe and the type of inlet.

Table I Basic airplane specifications

Wing area	S	0.55	m ²
Mean aerodynamic chord	ca	0.28	m
Wingspan	b	1.94	m
Aspect ratio		7	
Estimated take-off weight		8.7	kg
Thrust of pulsejet engine		35	N
Power of electric motor		2000	W
Cruising speed		45	m/s
Landing speed		15	m/s

Table II Weight data (estimated)

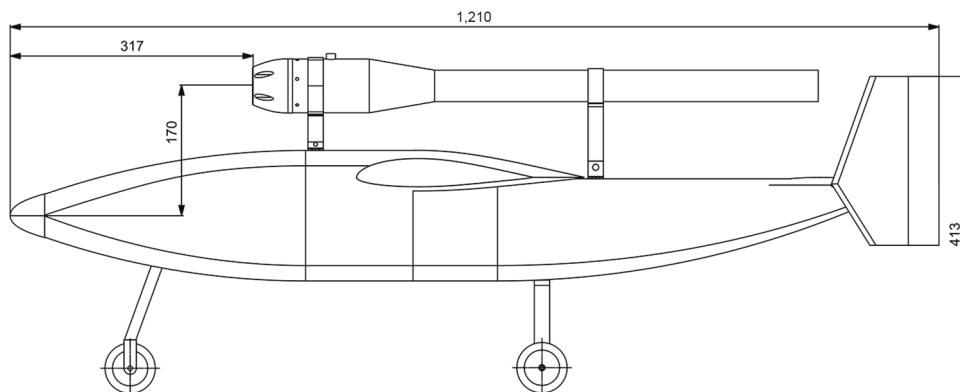
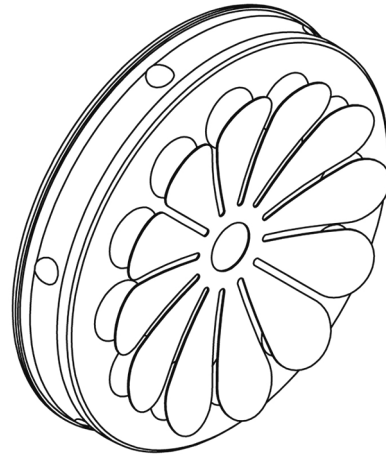
Empty frame	3.6	kg
Fuel (liquid)	1.4	kg
Pulsejet engine	1.8	kg
Components	1.9	kg
Take-off weight	8.7	kg

Figure 2 Numerical model of Numinosum airplane

There are two kinds of pulsejet engines, valved and valveless (Wójcicki, 1962). For a valved version, airflow is controlled by deflection of a valve (shown in Figure 4). For the valve to work effectively, the engine's frequency must correspond to the natural frequency of a valve. The valve must be thin, so that the air pressure can overcome its stiffness, but not so thin as to prolong its lifespan. Valve deflection is caused by the difference in pressure across the valve. During the combustion, the pressure increases thus closing the valve. This prevents air from going back to the valve and forces it to expand through the exhaust pipe. From this point, a pressure drop follows. The valve opens, and new air flows into the engine.

The pulsejet requires three things to start: fuel, a spark from a spark plug and airflow, either from a fan or airspeed. Once started, the combustion continues by ignition from the flame that remained in the burning chamber and the airflow is forced by pressure changes.

The way the pulsejet acts is very dependent on external conditions, such as air speed and direction and so there is a reduced capability of changing parameters during operation. One important parameter, called the supercharge, determines the amount of air that is being sucked into the engine through the exhaust pipe. This value changes with the airspeed. That is one of the reasons for a dependence between engine thrust and flight velocity. This is an interesting effect, worth testing during flight.

Figure 3 Sideview of Numinosum airplane**Figure 4** Illustration of a deflected valve

However, due to simplicity and lack of moving parts of the pulsejet, most working parameters, such as thrust and efficiency, are mostly dependent on engine's geometry and cannot be changed during operation. This is visibly in opposition to standards for engines of today's world. Modern engines can change many parameters to ensure the most efficient work and reduce the engine's fuel consumption.

The reason why pulsejets recently gained popularity among students, amateur modellers and designers of small fast UAVs was that it is way easier and cheaper to design and build a working pulsejet engine than a turbine or piston engine. Also, the pulsejet can start on its own only with the use of a fuel pump and a spark and can be tested on the ground as well as in flight.

Calculations

The main objective of the calculations was to assess flying qualities and indicate the necessary corrections. Dynamic stability analysis requires aerodynamic characteristics including stability derivatives as well as mass and inertia data. The aerodynamic characteristics were computed using 3D panel method (Katz and Plotkin, 2001) implemented in PANUKL software (Goetzendorf-Grabowski T., 2012). PANUKL is a

home-built code developed in the Warsaw University of Technology and well linked with other software modules (Goetzendorf-Grabowski and Mieloszyk, 2017). The stability analysis was performed using SDSA package (Simulation and Dynamic Stability Analysis, Goetzendorf-Grabowski T. *et al.*, 2011), which was developed within the SimSAC project (Rizzi, 2011) and is included in CEASIOM environment (CEASIOM, 2016).

Calculations proceeded along the following path. First, the geometry for the initial configuration was prepared. Then aerodynamic characteristics were calculated by PANUKL and input files for SDSA were created. The stability analysis results were analysed upon MIL-F-8785C specifications. If they were not acceptable, geometry was changed, and calculations repeated until the criteria were met.

Aerodynamics

Calculations of all aerodynamic coefficients and derivatives were performed in PANUKL. The geometry consisted of around 5,000 panels. Whole airplane's geometry was created, along with control surfaces. Pulsejet engine was modelled as a closed, axisymmetric body (Mieloszyk *et al.*, 2016). Fuselage was modelled in CAD system (Figure 5) and exported to PANUKL using a specially written Python script. Figure 6 shows the mesh of the final configuration.

Figure 5 Export of fuselage geometry from CAD to PANUKL

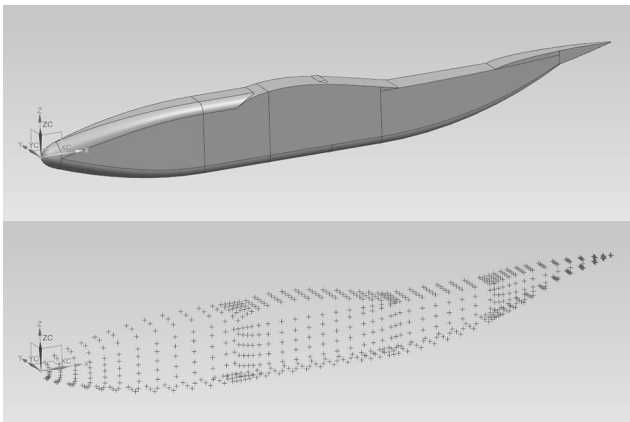
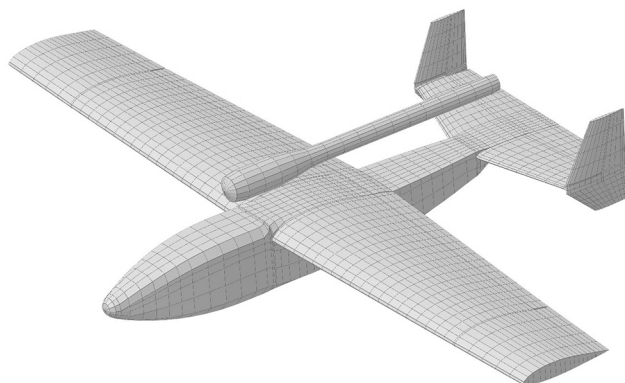


Figure 6 Panel mesh of the final configuration



All aerodynamic moments were calculated with respect to the origin located in 25 per cent of mean aerodynamic chord. Range of angle of attack was from -5 to 15 degrees.

The mesh is split into two symmetrical parts, and consists of the following pieces: fuselage, wing, horizontal stabilizer, vertical stabilizer and pulsejet engine. Every aerodynamic surface is combined of a fixed part, a separator and a moving part (control surface). Every control surface was modelled as a deflected airfoil.

Stability

Calculations of dynamic stability were made using SDSA package, mentioned above. The program uses classical model of motion with 6 DoF and its linearized form, which is usable to create the state matrix and compute the eigenvalues for various flight conditions (airspeed, altitude). Next the frequency and damping characteristics are analysed upon the flight quality criteria (MIL-F-8785C, 1980).

The influence of the pulsejet thrust on stability and longitudinal control was also taken into consideration. The vertical distance between the engine and the centre of gravity is 0.18 m. The centre of gravity was in all cases slightly ahead of 25 per cent of mean aerodynamic chord. Table III contains mass and inertia data. Presented moments of inertia were calculated with respect to the gravity centre.

Results

Calculations were performed for a few configurations along the way. Below are shown results only for the initial and final geometry in a form of a comparison.

To improve the airplane's behaviour was a game of compromises. Changing parameters in one direction bettered some characteristics but worsened others. Table IV contains parameters that were considered during the process and summary of their limiting factors. Moreover, change in horizontal stabilizer size was also considered, but within realistic limits, it did not bring any improvements. Moving the wing had the biggest impact on both the longitudinal and lateral stability.

In result, the initial and final configurations differ by wing position and vertical stabilizer's size. The wing has been moved by 10 cm to the front and stabilizer's height increased from 0.18 to 0.22 m. Moreover, horizontal stabilizer's incidence angle was changed from -3 to 0 degrees to simplify geometry. The comparison of these two geometries is shown in Figure 7.

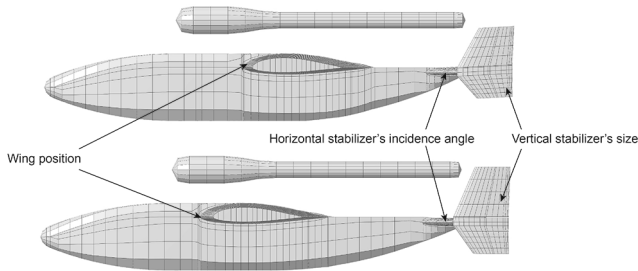
Table III Mass and inertia data

Weight	m	8.7	kg
Moments of inertia	lx	0.669	kg*m ²
	ly	0.699	
	lz	1.252	
Products of inertia	lxy	0.000	
	lxz	0.037	
	lyz	0.000	

Table IV Limiting factors of parameters considered during geometry changes

Stability	Parameter	Limits
Longitudinal	Wing position	Moving wing forward increased maximum value of elevator deflection on low angles of attack The centre of gravity position moved with the wing and had to be kept in realistic values Static stability improved with the wing moving forward
	Engine position	The engine could not be too low to protect the fuselage from heat radiation from the combustion chamber Moving the engine higher increased maximum value of elevator deflection and worsened phugoid characteristics
Lateral	Front shape of the fuselage	Front part of the fuselage had to be big enough to provide sufficient space for the RC installation, but small enough so that the Dutch roll characteristics are satisfactory
	Vertical stabilizer size	The size large enough to provide good Dutch roll characteristics

Figure 7 Comparison of the initial and final configuration



Aerodynamic coefficients

In this paragraph, basic aerodynamic coefficients are presented, namely, drag coefficient (Figure 9), lift coefficient (Figure 10) and pitching moment coefficient (Figure 11). The difference between the two configurations is mostly visible in the pitching moment coefficient. Moving the wing to the front decreased the slope of the graph, and therefore improved static stability of the airplane. As for drag and lift coefficients, they show only a slight change.

Worth noting here is that PANUKL is a program based on the potential flow method, so it does not consider the effects of fluid viscosity, which are important for parasite drag estimation, especially for low Reynolds number. Taking this into account, the drag coefficient obtained from PANUKL is corrected by adding the estimated (Raymer, 2012) friction drag coefficient, which is calculated as:

$$C_{Df} = C_{fe} \frac{S_{wet}}{S} \tag{1}$$

Figure 8 Comparison of the drag coefficient acquired with PANUKL and ANSYS Fluent (Ranachowski, 2017)

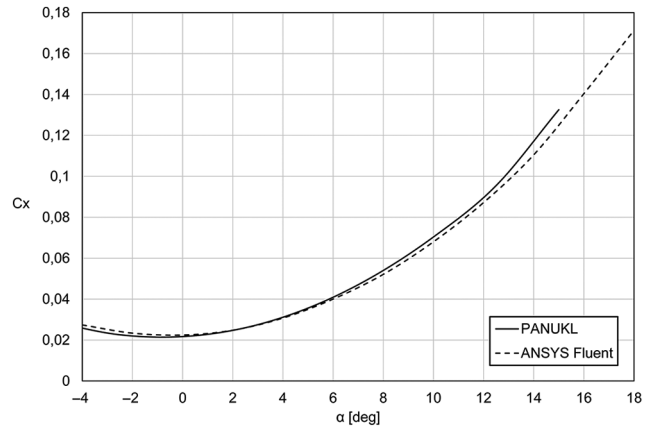


Figure 9 Drag coefficient for both configurations

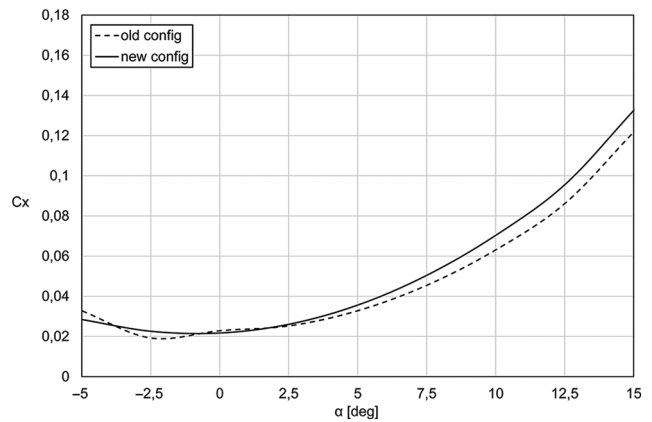
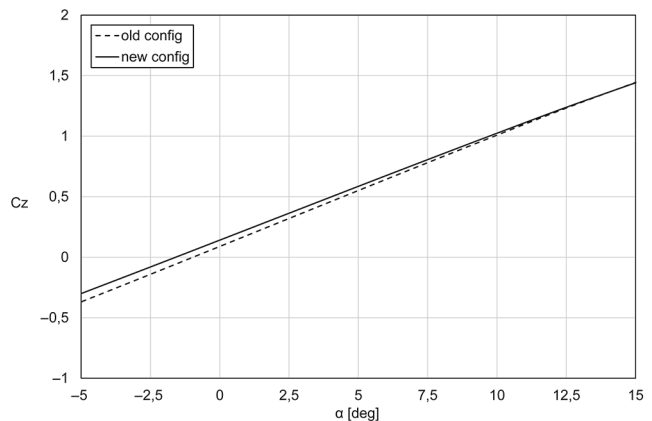


Figure 10 Lift coefficient for both configurations



where C_{fe} represents the minimal friction coefficient, assumed as 0.004 and S_{wet} is the airplane's wetted surface, calculated by PANUKL as 1.92 m². The resulting drag coefficient is consistent with the one acquired from ANSYS Fluent for the same geometry (ANSYS, 2016) – Figure 8.

Figure 11 Pitching moment coefficient for both configurations

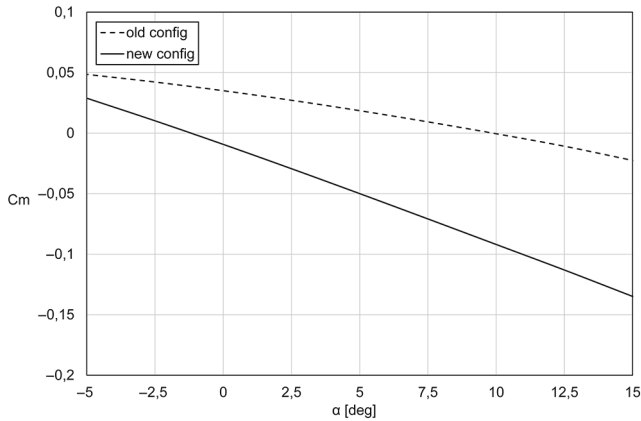
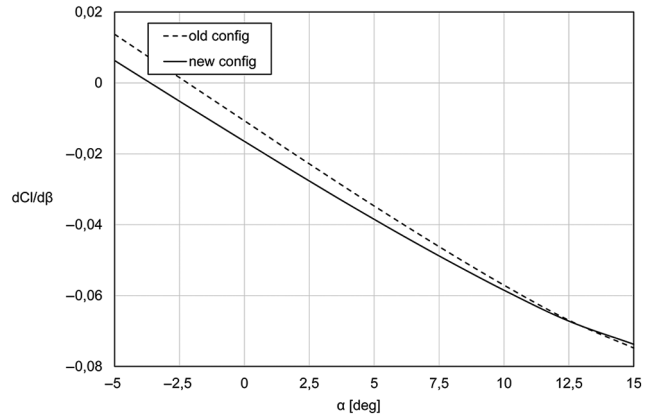


Figure 13 Rolling moment derivative with respect to sideslip angle



Aerodynamic derivatives

Below are shown derivatives of aerodynamic moments. Pitching moment derivative with respect to angle of attack presented in Figure 12 is a measure of static longitudinal stability, and it has to be negative. Lateral static stability is determined by rolling moment derivative with respect to sideslip angle (Figure 13 – it should be negative), and directional static stability is determined by yawing moment derivative (Figure 14 – it must be positive). After modifications of the geometry, the rolling and pitching moment derivatives decreased, and the yawing moment derivative increased. This provides an improvement in both the longitudinal and lateral static stability.

Static stability

The static margin of the airplane was analysed as shown on Figure 15. It is the distance from the aerodynamic moments’ calculation pivot for which the airplane remains statically stable. On graph, it is shown as a percentage of the mean aerodynamic chord. As can be seen, for the new configuration, it reaches around 10 per cent, which means that the centre of gravity of the airplane must be no farther than 35 per cent of mean aerodynamic chord. However, the centre of gravity position is limited by other factors, such as elevator deflection and dynamic stability, and so the recommended gravity centre

Figure 14 Yawing moment derivative with respect to sideslip angle

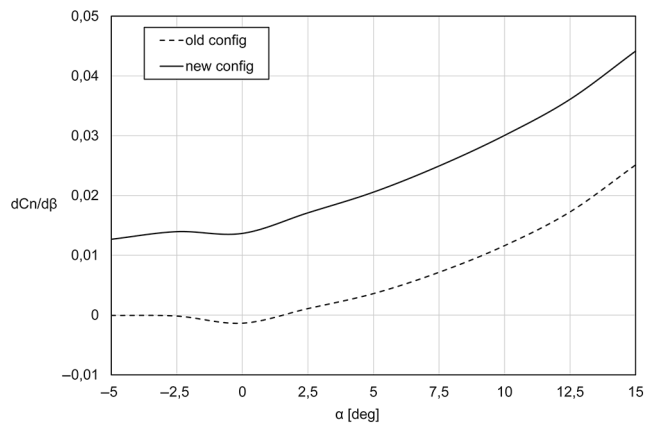


Figure 12 Pitching moment derivative with respect to angle of attack

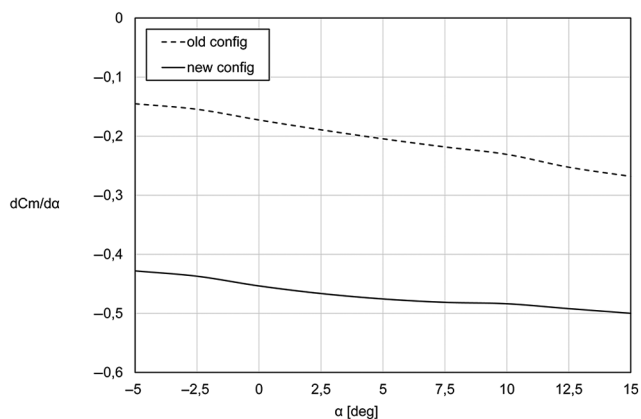
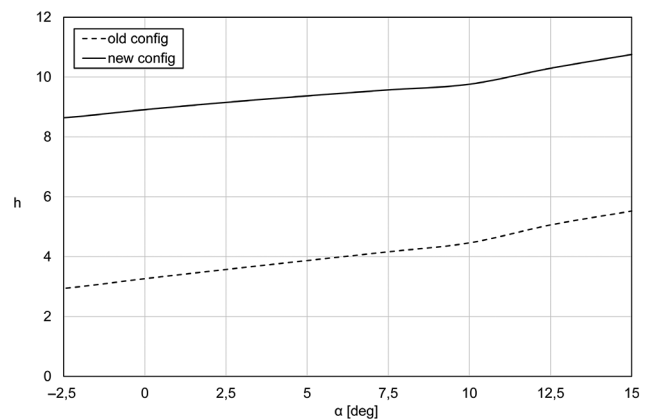


Figure 15 Static margin



position remains in about 25 per cent of mean aerodynamic chord.

Elevator deflection

After geometry modifications the elevator effectiveness increased. The derivative $dC_m/d\delta_H$ changed from -0.824

to -1.074 . To properly estimate the elevator deflection, the impact of the pulsejet engine must have been considered. The engine's thrust placed in a distance from the gravity centre generates an additional pitching moment. To preserve straight line flight for all flight speeds, this effect must be compensated by a larger elevator deflection. Figure 16 shows a comparison of the needed deflection for cases of the engine turned on or off. The graph shows only the value for the final configuration of the airplane. From the graph, one more information can be acquired, that is the elevator deflection for the cruising speed. For most airplanes, this value is set to zero by placing the horizontal stabilizer at an incidence angle. In the case of Numinosum, it was decided to set this angle to zero to simplify geometry.

Dynamic stability

SDSA identified all classic modes of motion, namely, phugoid, short period, Dutch roll, spiral and roll. For the new configuration, all modes of motion except phugoid are stable for all flight speeds. Phugoid gets unstable around 16.5 m/s. Nevertheless, this mode is easy to control for the pilot, so such result does not cause worry. All modes after geometry changes meet the criteria given by CS-23 (EASA, 2012) and MIL-8785C (1980) specifications for all but low speeds.

CS-23 specifications states that the Dutch roll amplitude must dampen to one-tenth of initial value in less than seven cycles. This criterion is shown in Figure 17. Modification of the geometry significantly improved the Dutch roll characteristics. The new geometry meets the requirements for speeds above 16 m/s. As for the MIL-8785C criterion, shown on Figure 18, Dutch roll falls in the second acceptability level. Figure 19 shows phugoid's time to half amplitude. It can be observed from this graph that the flight speed for which the phugoid changes from stable to unstable was around 35 m/s for the old configuration. After geometry modifications, this mode improved, being unstable only for low flight speeds. Figure 20 shows the requirements for short period. This mode did not cause any trouble for either configuration.

Figure 16 Elevator deflection (final configuration)

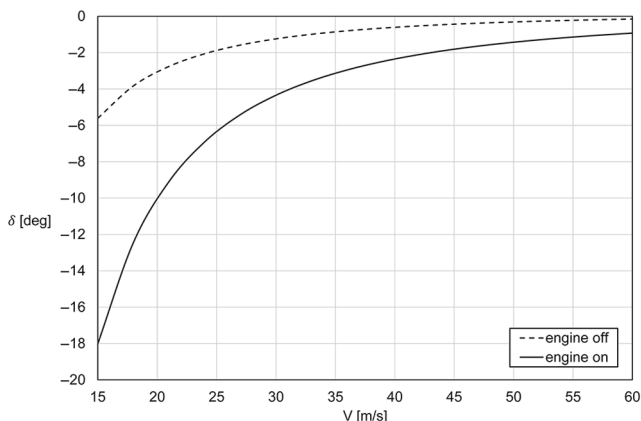


Figure 17 Dutch roll characteristics against the background CS-23 requirements

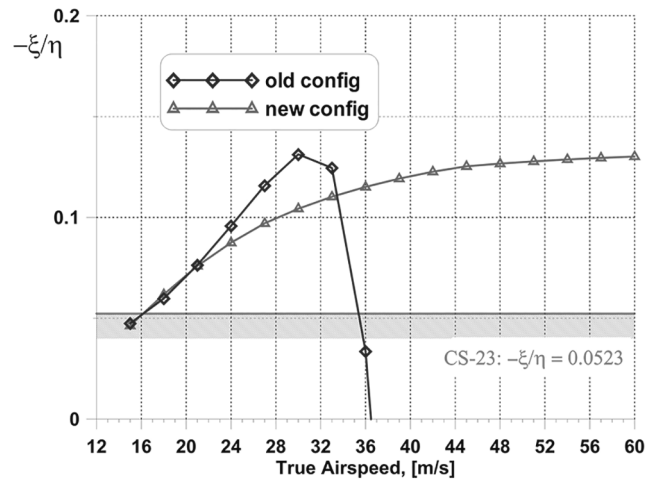
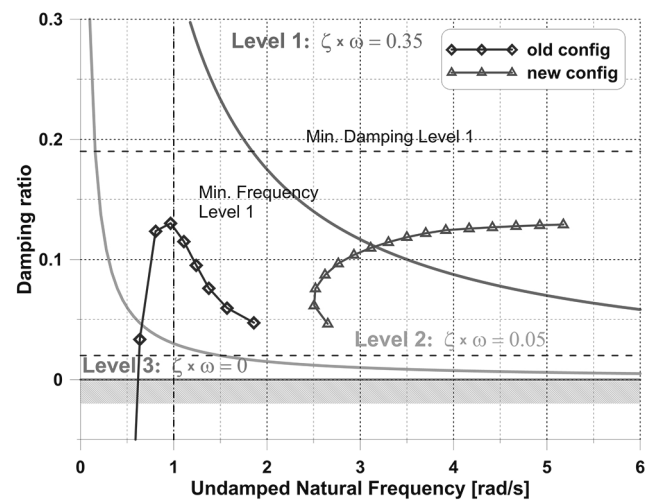


Figure 18 Dutch roll characteristics against the background of MIL-8785C criteria



Conclusion

The aim of calculations presented in this paper was to enhance the static and dynamic stability of a small airplane powered by a pulsejet engine. This was achieved by modification of the initial geometry to satisfy the criteria given by MIL-F-8785C specifications. The influence of engine thrust on elevator deflection was also investigated. The resulting geometry provides good stability characteristics for almost whole airspeed range. Flying slowly could simply require more attention from the pilot due to phugoid characteristics. In the future, it is possible that an autopilot will be added to compensate for this problem.

Further work

Following calculations presented in this paper, it is planned to finish the build of the model, taking into account all modifications presented above. The process of assembling has

Figure 19 Phugoid time to half amplitude

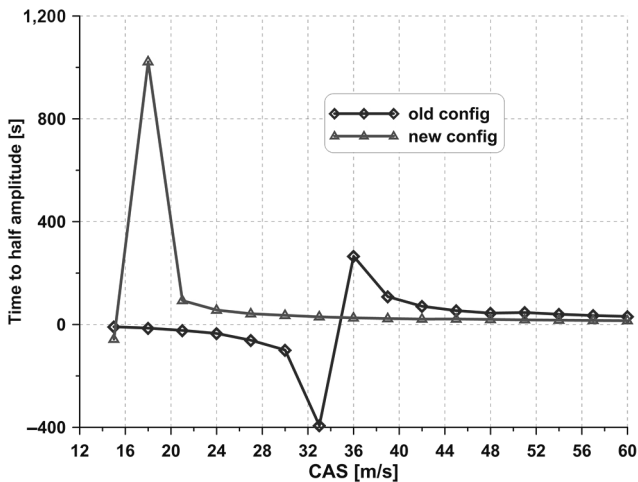
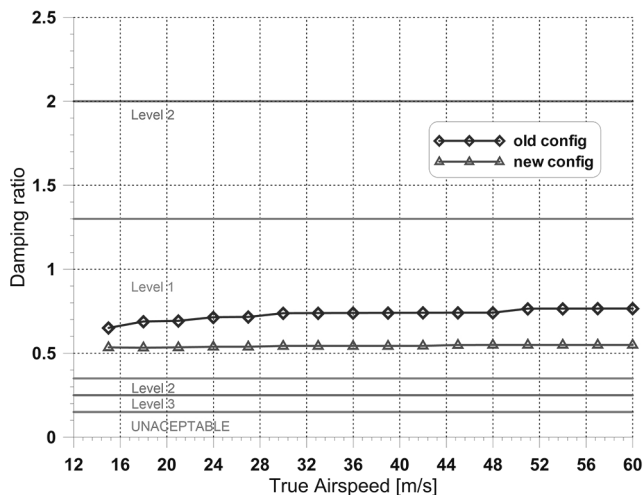


Figure 20 Short period damping ratio against the background of MIL-8785C criteria



been started. After it is finished flight test will start. First flights will be performed with an electric engine. The pulsejet will also be mounted on the fuselage to ensure proper center of gravity position, but it will be turned off for those first tests. Next, stationary tests with the pulsejet might be conducted, to make sure the hot parts of the engine do not threaten the structure. After these are complete, the pulsejet and the airplane will be equipped with various sensors, and actual tests will be performed.

References

- ANSYS (2016), ANSYS Workbench – Integrated Simulation Platform available at: www.ansys.com/Products/Platform
- CEASIOM (2016), CEASIOM – Computerised environment for aircraft synthesis and integrated optimisation methods, available at: www.ceasiom.com
- European Aviation Safety Agency (2012), Certification Specifications for Normal, Utility, Aerobatic, and Commuter Category Aeroplanes – CS-23, Amendment 3.
- Goetzendorf-Grabowski, T. and Mieloszyk, J. (2017), “Common computational model for coupling panel method with finite element method”, *Aircraft Engineering and Aerospace Technology*, Vol. 89 No. 5, pp. 654-662, doi: 10.1108/AEAT-01-2017-0044.
- Goetzendorf-Grabowski, T. (2012), *PANUKL Potential Solver*, Software package, Warsaw University of Technology, available at: www.meil.pw.edu.pl/add/ADD/Teaching/Software/PANUKL
- Goetzendorf-Grabowski, T., Mieszalski, D. and Marcinkiewicz, E. (2011), “Stability analysis using SDSA tool”, *Progress in Aerospace Sciences*, Vol. 47 No. 8, pp. 636-646, doi: 10.1016/j.paerosci.2011.08.007, November 2011.
- Katz, J. and Plotkin, A. (2001), *Low-Speed Aerodynamics*, 2nd ed., Cambridge University Press.
- Mieloszyk, J., Goetzendorf-Grabowski, T. and Mieszalski, D. (2016), “Rapid geometry definition for multidisciplinary design and analysis of an aircraft”, *Aviation*, Vol. 20 No. 2, pp. 60-64, doi: 10.3846/16487788.2016.1195066.
- MIL-F-8785C. (1980), “Military specification flying qualities of piloted airplanes”, (accessed 5 November 1980).
- Pobikrowska, K. (2018), “Stability analysis of experimental aircraft with pulsejet engine”, BSc. Thesis (in Polish), Warsaw University of Technology.
- Ranachowski, M. (2017), *Numerical Model of Small Pulsejet UAV-ANSYS-FLUENT Analysis, Intermediate Project (in Polish)*, Warsaw University of Technology.
- Raymer, D. (2012), *Aircraft Design – A Conceptual Approach*, AIAA Education Series.
- Rizzi, A. (2011), “Modeling and simulating aircraft stability and control – the simSAC project”, *Progress in Aerospace Sciences*, Vol. 47 No. 8, pp. 573-588, doi: 10.1016/j.paerosci.2011.08.004, November 2011.
- Wójcicki, S. (1962), *Pulsejet, ramjet and Rocket Engines (in Polish: Silniki Pulsacyjne, strumieniowe i Rakietowe)*, Wydawnictwo Ministerstwa Obrony Narodowej, Warszawa.

Corresponding author

Katarzyna Pobikrowska can be contacted at: kasia.pobikrowska@gmail.com

For instructions on how to order reprints of this article, please visit our website:

www.emeraldgroupublishing.com/licensing/reprints.htm

Or contact us for further details: permissions@emeraldinsight.com

Enhancements in conceptual electric aircraft design

Jacek Mieloszyk

Institute of Aeronautics and Applied Mechanics, Warsaw University of Technology, Warsaw, Poland, and

Andrzej Tarnowski

Politechnika Warszawska Wydział Mechaniczny Energetyki i Lotnictwa, Warszawa, Poland

Abstract

Purpose – This paper aims to describe the enhancement of the numerical method for conceptual phase of electric aircraft design.

Design/methodology/approach – The algorithm provides a balance between lift force and weight of the aircraft, together with drag and thrust force equilibrium, while modifying design variables. Wing geometry adjustment, mass correction and performance estimation are performed in an iterative process.

Findings – Aircraft numerical model, which is most often very simplified, has a number of new improvements. This enables to make more accurate analyses and to show relationships between design parameters and aircraft performance.

Practical implications – The presented approach can improve design results.

Originality/value – The new methodology, which includes enhanced numerical models for conceptual design, has not been presented before.

Keywords Conceptual design, Electric propulsion, Low Re drag model

Paper type Research paper

Nomenclature

Symbols

b	= wing span;
AR	= wing aspect ratio;
V	= flight velocity;
S	= wing reference area;
CL	= lift aerodynamic coefficient;
CD	= drag aerodynamic coefficient;
Re	= Reynolds number;
mpay	= mass of payload;
mbatt	= mass of batteries;
mpropulsion	= mass of propulsion system;
mstruct	= mass of aircraft structure;
m	= total mass of aircraft;
g	= gravity acceleration;
ρ	= air density;
T	= thrust;
Pflight	= power needed for flight;
Ptotal	= total power consumed;
Pavio	= power needed for avionics and steering;
Ppayload	= power needed for payload equipment;
η_{esc}	= efficiency of electric speed controller;
η_{mot}	= efficiency of electric motor;
η_{grb}	= efficiency of gearbox;
η_{prop}	= efficiency of propeller;

η_{bec}	= efficiency of battery eliminator circuit;
η_{dchrg}	= efficiency of discharge process;
Es	= energy density of battery (specific energy) [kg/W];
kpropulsion	= mass to power ratio of propulsion system [kg/W];
t	= endurance;
A	= constant of minimum drag mathematical model;
B	= constant of minimum drag mathematical model; and
C	= constant of minimum drag mathematical model.

Introduction

New strategies for air transport are investigated (Holmes *et al.*, 2017; Lukasiak and Wisniowski, 2017; Moore, 2015; Piwek and Wiśniowski, 2016) with special attention to electric aircrafts, which are considered as environment-friendly future type of propulsion.

Conceptual phase of aircraft design is very important because of very few constraints on aircraft configuration, compared to more advanced stages of design. This leaves much space for the design decisions, and almost any configuration of an aircraft is possible. Conceptual design needs efficient tools for computations but can perform with less complexity and with basic aircraft physical model. However, the physical model should describe the reality as close as possible. Many researchers are working on this subject (Baalbergen *et al.*, 2017; Goetzendorf-Grabowski and Mieloszyk, 2017; Immer and Juretzko, 2018; Iwaniuk and Wiśniowski, 2017;

The current issue and full text archive of this journal is available on Emerald Insight at: www.emeraldinsight.com/1748-8842.htm



Aircraft Engineering and Aerospace Technology
91/6 (2019) 851–856
© Emerald Publishing Limited [ISSN 1748-8842]
[DOI 10.1108/AEAT-07-2018-0192]

Received 13 July 2018
Revised 22 September 2018
Accepted 5 November 2018

Trifari *et al.*, 2017). The developed algorithm is an enhancement of a method introduced by Noth (2008) for design of solar-powered aircrafts. The method is applicable for aircrafts with solar panels and electric propulsion system. However, in this paper, solar panels and solar irradiance effects are not included.

The basic algorithm

Considering only electric propulsion system in this work, the algorithm core equations state that vertical forces, lift and weight of an aircraft, and horizontal forces, drag and thrust, should be equal. Equation (2) can be also considered in terms of power balance. After derivation of flight velocity from equation (1), it can be inserted into equation (4) for power balance. Power consumption of onboard electronics together with efficiency coefficients have to be incorporated into equation (5) to make the numerical model closer to real flight conditions:

$$m \cdot g = \frac{1}{2} \cdot \rho \cdot V^2 \cdot C_L \cdot S \quad (1)$$

$$T = \frac{1}{2} \cdot \rho \cdot V^2 \cdot C_D \cdot S \quad (2)$$

$$V = \sqrt{\frac{2 \cdot m \cdot g}{\rho \cdot C_L \cdot S}} \quad (3)$$

$$P_{flight} = T \cdot V = T \cdot \sqrt{\frac{2 \cdot m \cdot g}{\rho \cdot C_L \cdot S}} \quad (4)$$

$$P_{total} = \frac{P_{flight}}{\eta_{esc} \cdot \eta_{mot} \cdot \eta_{grb} \cdot \eta_{prop}} + \frac{P_{avio} + P_{payload}}{\eta_{bec}} \quad (5)$$

More power needed for flight and larger flight endurance means bigger mass of battery pack [equation (6)]. Increased mass of batteries results in heavier aircraft structure and propulsion system. The mass of the structure can be approximated with good accuracy by equation (7), derived earlier (Noth, 2008), which depends on wingspan *b* and wing aspect ratio *AR*. Mass of propulsion system depends mainly from power needed for flight and can be approximated by equation (8):

$$m_{bat} = \frac{P_{total} \cdot t}{\eta_{dchrg} \cdot E_S} \quad (6)$$

$$m_{struct} = 0.44 \cdot b^{3.1} \cdot AR^{-0.25} \quad (7)$$

$$m_{propulsion} = k_{propulsion} \cdot P_{flight} \quad (8)$$

The system of equations has to be solved in an iterative process to converge to a solution. This algorithm contains simplifying assumptions for single constant flight condition. Authors of this work present the method how to take into account different flight conditions of flight mission stages. The second

improvement is making the friction drag a function of changing Reynolds numbers. Friction drag changes significantly especially for low Reynolds numbers, approximately below *Re* 500,000, which is often the case of small electric UAV aircrafts. The last enhancement is to reject simplification for small climb angles, which is often untrue for small electric aircrafts with proportionally big motors.

Multiple flight conditions

The basic algorithm proposed by Noth (2008) lacks possibility of mission definition, which includes different flight conditions. This shortcoming was improved in the new algorithm. Figure 1 shows simple example of mission that is common for small electric UAV. After immediate takeoff, the aircraft starts to climb and then cruises to the observation area, where the UAV loiters while observing the object of interest. After the observation plane comes back and then descends to land.

Descend phase of the mission can be completed without propulsion, so the energy consumption is negligible. Cruise to the observation point and back can be considered as one part of the mission, as without fuel consumption, mass of the aircraft will not change. Mission phases with flight parameters are summed up in Table I. Every phase of the mission has been given duration and cruise speed. The angle of climb θ has significant influence on power consumption and ceiling that the aircraft can reach. Efficiency of the propeller can vary in different phases of the mission, because of varying flight speeds and altitude. Finally, density and viscosity of the air will change with altitude.

Vertical forces equilibrium and power needed for flight are calculated for every phase of the mission. The procedures are nested in the basic iterative algorithm and visualized in Figure 2.

Thrust method for high angles of attack

To calculate the performance characteristics, very often, a widespread power method is used. The method is fairly simple and efficient but can be only used for aircrafts with low thrust to weight ratio and Mach numbers below 0.7. This assumptions comes from more detailed constrains:

Figure 1 Example of aircraft flight mission

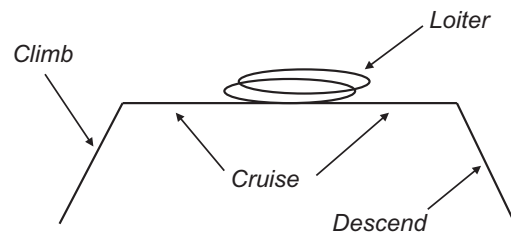
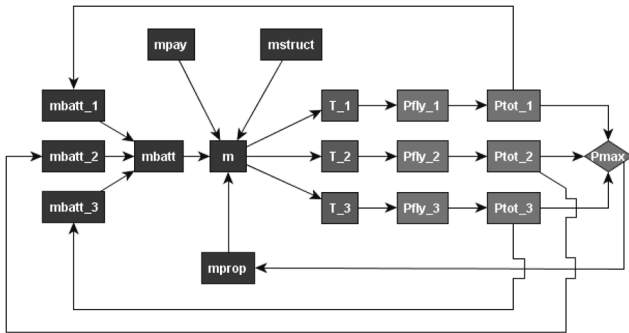


Table I Mission parameters

Mission phase	t[h]	V[m/s]	θ [°]	η_{prop} [-]	ρ [kg/m ³]	ν [m ² /s]
Climb	0.07	15	6	0.45	1.225	1.51e-005
Cruise	0.083	20	0	0.5	1.225	1.51e-005
Loiter	1.15	15	0	0.6	1.225	1.51e-005

Figure 2 Improved algorithm with multiple flight conditions



- Flight angle has to be small, where $\sin(\theta) \sim 0$, $\cos(\theta) \sim 1$.
- Angle between flight direction and thrust vector is negligibly small.
- The weight of the aircraft is constant.
- There are no moments around center of gravity.
- It is a sustained flight.

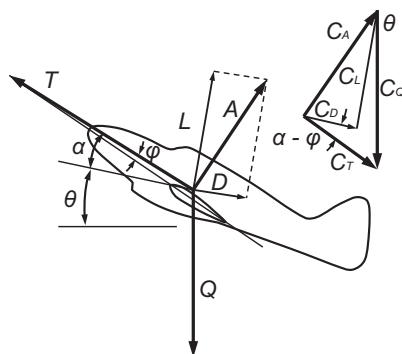
However, this is untrue for small electric aircrafts (Mieloszyk and Tarnowski, 2015), which are light, but have powerful motors. In that cases thrust method is better, which does not assume small climb angles simplification. In the presented method, three main forces are considered: aerodynamic, gravity and thrust forces (Figure 3). Considering the three forces vectors, equation for power needed to fly can be written down as equation (9). Equation (9) should be used instead of simplified equation (4):

$$P_{fly} = \frac{T \cdot V}{\cos(\alpha - \phi_{mot})} = \frac{(\frac{1}{2} \rho \cdot V^2 \cdot S \cdot C_D + m \cdot g \cdot \sin(\theta)) \cdot V}{\cos(\alpha - \phi_{mot})} \quad (9)$$

Low Reynolds number friction drag correction

Friction drag can change significantly for small Reynolds numbers. This phenomenon is shown on an example of MH45 airfoil aerodynamic characteristics (Figure 4), designed for small Reynolds numbers. More sophisticated mathematical model of airfoil drag dependent on lift coefficient and Reynolds number was developed in this work. Aerodynamic polars for different Reynolds numbers can be approximated with

Figure 3 Aerodynamic, gravity and thrust forces acting on an aircraft



quadratic equation (10). The coefficients A, B and C depend on Reynolds number and are shown in Figure 5. The relationship of the coefficients from Reynolds number can be approximated by exponential equations (11)-(13). Constants for the equations were obtained by best fit and least squares method and are gathered in Table II:

$$C_{D_{profile}}(C_L, Re) = A_{(Re)^2} \cdot C_L + B_{(Re)} \cdot C_L + C_{(Re)} \quad (10)$$

$$A = A_{const} \cdot Re^{A_{exp}} + A_{shift} \quad (11)$$

$$B = B_{const} \cdot Re^{B_{exp}} + B_{shift} \quad (12)$$

$$C = C_{const} \cdot Re^{C_{exp}} + C_{shift} \quad (13)$$

Calculated data with usage of Xfoil software (Drela, 1989) and approximated polars are compared in Figure 6. Mathematical model fits well with data for high Reynolds numbers almost to the maximum lift coefficient. For lower Reynolds numbers, the approximation is getting worse for higher lift coefficients, but still should be acceptable for conceptual phase of design. The mathematical model gets rather crude for very low Reynolds numbers.

Design and optimization procedure

This example shows results obtained for small electric UAV. Computations were done for five different payload masses and three levels of minimum speeds, essential for safe landing. Mission graph has been already shown in Figure 1, and mission parameters are shown in Table I. The design goal was to reach maximum flight endurance and reconnaissance observation time, while fulfilling all design constrains to make the aircraft construction feasible. Design variables were span and aspect ratio of the wing, which have high impact on aerodynamic performance and mass of the aircraft. The design and optimization task can be written in standard form as:

Maximize:

$$t_{max}(X) = \frac{m_{batt} \cdot \eta_{dchrg} \cdot ES}{P_{total}}$$

With respect to:

$$X = \{b, AR, m_{pay}\}$$

Subject to:

$$b_{min} < b < b_{max}$$

$$AR_{min} < AR < AR_{max}$$

$$V_{min} > V_{min_defined}$$

Type of battery with given number of cells, energy density and discharge efficiency is defined as constant. Depending on the design variables, total power consumed and mass of batteries can change. The design has to balance between aerodynamic

Figure 4 Aerodynamic polars for airfoil MH45 for different Reynolds numbers

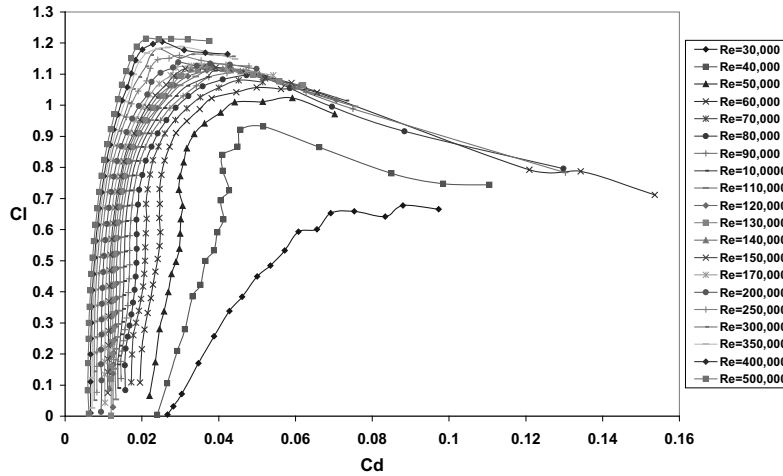


Figure 5 A, B and C coefficients for drag mathematical model dependent on Reynolds number

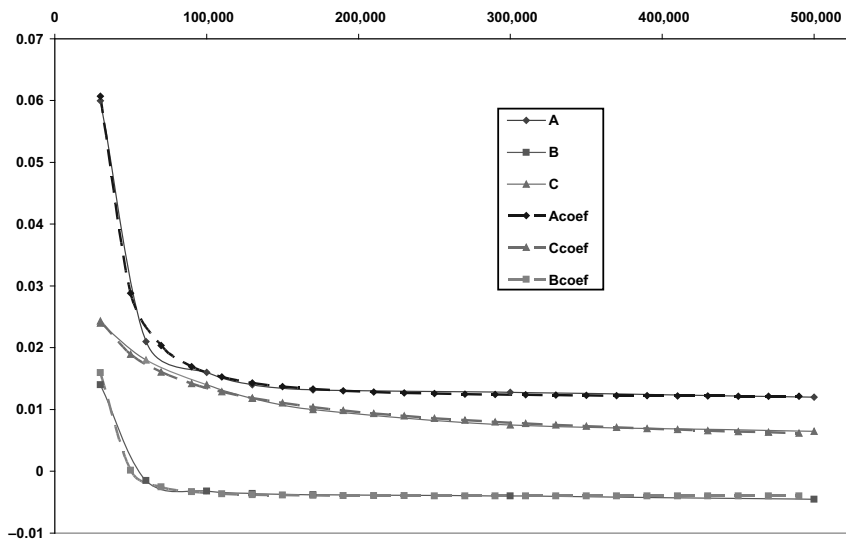


Table II Constants for the drag mathematical model

Coefficients	A	B	C
Const	1.00E+08	1E+12	3.8
Exp	-2.08	-3.06	-0.49
Shift	0.012	-0.004	0

performance and proportions between masses to achieve optimum configuration. The consolidated results for five different payloads and three minimum speeds are shown in Table III.

Figure 7 shows dependency of loiter time and power needed for flight from mass of payload with different minimum speed constrains. Time of loiter is decreased and power for flight is increased when mass of payload is increased, which is expected.

It is also clear that mass of payload had a higher impact on loiter time than constrain for minimum speed, although influence of minimum speed constrain is also noticeable especially for power required to fly.

Figure 8 shows how the design variables, wing span and aspect ratio and minimum speed constrain, change depending on the amount of payload. With increasing amount of payload, wing span increases and aspect ratio decreases. For the given mass of payload, wing span will be almost the same for different minimum speeds. In contradiction, aspect ratio and wing span will change significantly for the same mass of payload, but with different values of minimum speed.

Similar sensitivity analyze was done for time of loiter (Figure 9). With increasing time of loiter, wing span decreases and aspect ratio increases. Once again, aspect ratio and dependent wing area are more sensitive to the minimum speed constrain than wing span.

Figure 6 Comparison of computed polars and approximated with mathematical model

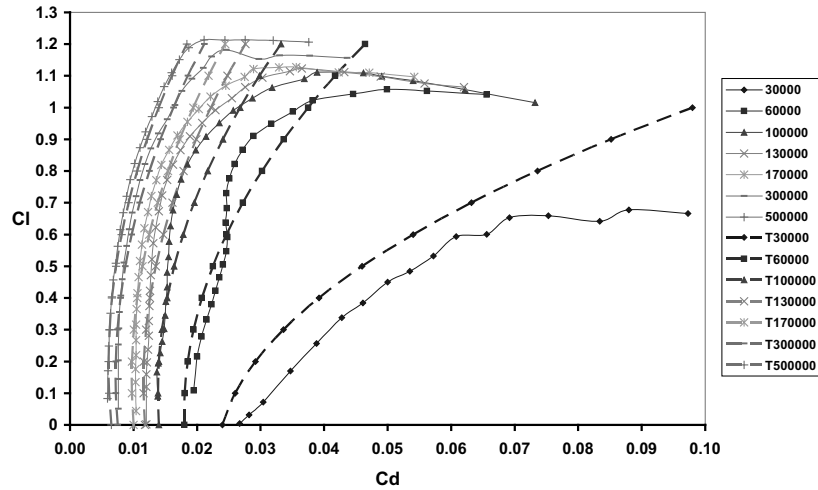


Table III UAV parameters after design

$m_{\text{payload}}[\text{kg}]$	$t_{\text{loiter}}[\text{min}]$	$b[\text{m}]$	$AR[-]$	$V_{\text{min}}[\text{m/s}]$	$P_{\text{total}}[\text{W}]$
0.2	67.2	1.11	3	8	110.4
0.5	49.9	1.41	2.29	8	284.8
1	37.1	1.66	1.71	8	669.5
1.5	30.2	1.89	1.46	8	1,186.5
2	25.7	2.03	1.29	8	1,730.6
0.2	69.3	1.13	3.60	9	120.2
0.5	51.6	1.42	2.71	9	325.5
1	38.6	1.70	2.16	9	723.8
1.5	31.6	1.93	1.87	9	1,215.6
2	26.97	2.07	1.64	9	1,795.3
0.2	70.5	1.16	4.03	10	163.5
0.5	52.8	1.45	3.26	10	374.0
1	39.7	1.74	2.57	10	833.0
1.5	32.6	1.96	2.23	10	1,374.8
2	27.9	2.11	1.97	10	2,028.9

Figure 7 Time of loiter and power required for flight as function of mass of payload and minimum speed

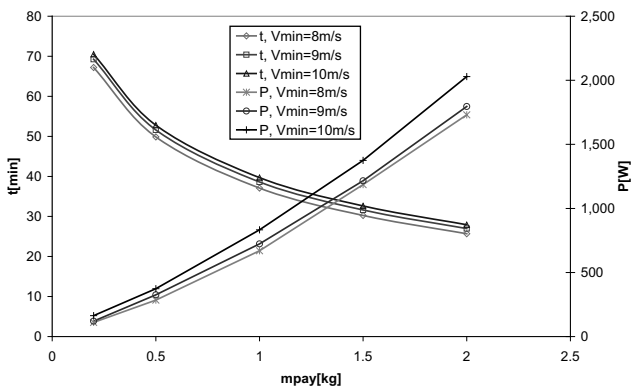


Figure 8 Wing span and wing aspect ratio as function of mass of payload and minimum speed

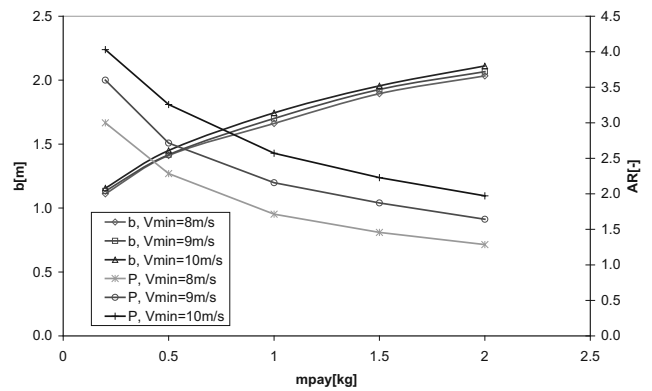
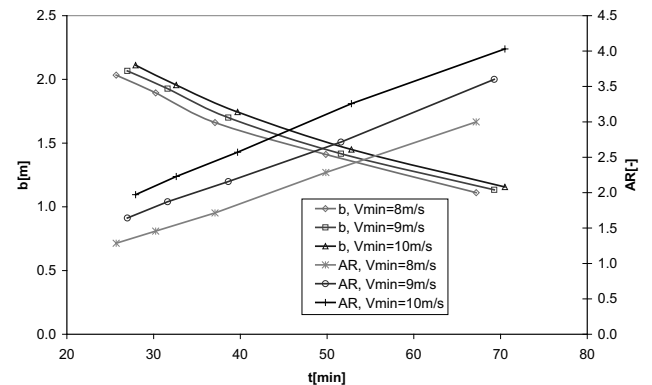


Figure 9 Wing span and wing aspect ratio as function of time of loiter and minimum speed



Wing span and aspect ratio can be chosen depending on the time of loiter and mass of payload desired for the mission. Other issues also can be considered; for example, more maneuverable aircraft will require smaller aspect ratio.

Table IV Aircraft mass brake down

Mass	Config A	Config B	Config C
m_{pay}	0.20	1.0	2.0
m_{struct}	0.46	1.85	3.73
m_{batt}	1.16	4.14	7.94
m_{prop}	0.15	0.72	1.71
m_{total}	1.97	7.72	15.38

Figure 10 Mass break down for three payloads configurations

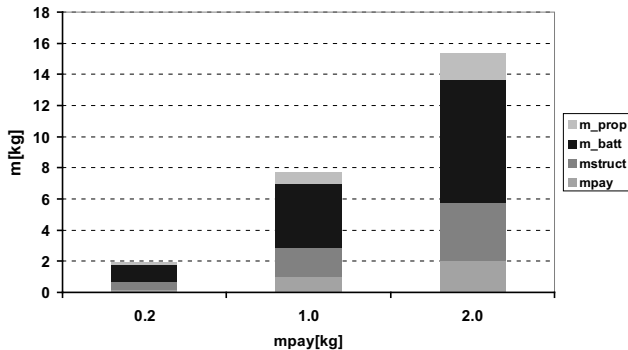


Table IV shows aircraft mass break down for three chosen payloads configuration and minimum speed equal to 8 m/s. While the total mass of an aircraft differs significantly between configurations, percentage of mass break down is almost constant (Figure 10).

Conclusion

The process of iterative conceptual electric aircraft design was presented. The method included various flight conditions for different phases of aircraft mission. Mathematical model of aircraft was improved by utilizing thrust method for power required to fly and enhancing friction drag model as a function of small Reynolds numbers. These improvements give more reliable analysis model for conceptual design. Finally, example results were computed and discussed for small electric UAV aircraft.

Presented methodology facilitates balanced and optimal aircraft design for specific mission phase. It is an improved tool for designers, which gives them opportunity to create more challenging, efficient and competitive aircraft structures.

References

Baalbergen, E., Moerland, E., Lammen, W. and Ciampa, P.D. (2017), "Methods supporting the efficient collaborative

design of future aircraft", Paper 844, 6th CEAS Air & Space Conference Aerospace Europe, Bucharest.

Drela, M. (1989), "XFOIL: an analysis and design system for low Reynolds number airfoils", in Mueller, T.J. (Ed.), *Low Reynolds Number Aerodynamics*, Lecture Notes in Eng. 54.

Goetzendorf-Grabowski, T. and Mieloszyk, J. (2017), "Common computational model for coupling panel method with finite element method", *Aircraft Engineering and Aerospace Technology* 08/2017, Vol. 89 No. 7, doi: 10.1108/AEAT-01-2017-0044.

Holmes, B.J., Parker, R.A., Stanley, D., McHugh, P., Garrow, L., Masson, P.M. and Olcott, J. (2017), *NASA Strategic Framework for on-Demand Air Mobility*, National Institute of Aerospace, Hampton, VA.

Immer, M. and Juretzko, P.G. (2018), "Advanced aircraft performance analysis", *Aircraft Engineering and Aerospace Technology*, Vol. 90 No. 4, pp. 627–638, available at: <https://doi.org/10.1108/AEAT-11-2016-0205>

Iwaniuk, A. and Wiśniowski, W. (2017), "Optimization of small aircraft parameters in the initial phase of the project", *Proceedings of the Institution of Mechanical Engineers, Part G: Journal of Aerospace Engineering*, Vol. 231 No. 12, pp. 2248–2258.

Lukasik, B. and Wisniowski, W. (2017), "All-electric propulsion for future business jet aircraft: a feasibility study", *Proceedings of the Institution of Mechanical Engineers, Part G: Journal of Aerospace Engineering*, Vol. 231 No. 12, pp. 2203–2213.

Mieloszyk, J. and Tarnowski, A. (2015), "Mass, Time and cost reduction in MAV manufacturing", *Transactions of the Institute of Aviation 03 Aviation*, Vol. 238 No. 1, pp. 22–34, doi: 10.5604/05096669.1151306.

Moore, M. (2015), "Electric propulsion (EP) Example roadmap decomposition", *Joint NASA-FAA On-Demand Mobility and Emerging Technology Workshop*, KS City, MO, 21–22 October, KS City, MO.

Noth, A. (2008), "Design of solar powered airplanes for continuous flight", Doctoral thesis ETH Zurich

Piwek, K. and Wiśniowski, W. (2016), "Small air transport aircraft entry requirements evoked by FlightPath 2050", *Aircraft Engineering and Aerospace Technology*, Vol. 88 No. 2, pp. 341–347.

Trifari, V., Ruocco, M., Cusati, V., Nicolosi, F. and De Marco, A. (2017), "Java framework for parametric aircraft design – ground performance", *Aircraft Engineering and Aerospace Technology*, Vol. 89 No. 4, pp. 599–608, available at: <https://doi.org/10.1108/AEAT-11-2016-0209>

Corresponding author

Jacek Mieloszyk can be contacted at: jmieloszyk@meil.pw.edu.pl

For instructions on how to order reprints of this article, please visit our website:

www.emeraldgroupublishing.com/licensing/reprints.htm

Or contact us for further details: permissions@emeraldinsight.com

Establishment of the Swedish Aeronautical Research Center (SARC)

Ingo Staack

Department of Management and Engineering, Linköping University, Linköping, Sweden

Abstract

Purpose – This paper aims to present the newly founded Swedish Aeronautical Research Center (SARC), based on the triple helix theory, to foster the seamless Swedish aerospace research interplay between academia, research organizations and industry.

Design/methodology/approach – The paper is a technical paper, mainly relating and explaining sources and concepts for research planning and organization. Used concepts are the triple helix approach (for socioeconomic effects), the role of academia and industry interplay for education and the technology readiness level (TRL) concept for strategic research planning. Focusing on the establishment of a graduate school, lessons learned from previous national research schools are also presented.

Findings – The paper gives an overview of and explains the interplay between politics, social welfare and industrial R&D needs, with the academic viewpoint of aeronautical research and education. Shortcomings in both the use of TRL for research program planning and the Swedish competence cluster system are identified and remedies suggested. The main findings are suggestions for future actions to be conducted by SARC in the fields of research and education.

Practical implications – The paper includes implications for the seamless interplay between academia, research organizations and industry.

Originality/value – So far, no publication about the newly founded SARC has been made yet. It is unique in the way that it makes substantial use of national technical documents so that this information becomes available for non-Swedish speakers. Additionally, the perhaps-unique system of industrial competence clusters is presented.

Keywords Triple helix, Academia–industry interplay, PhD academy, Research and education, Technology readiness level (TRL)

Paper type Technical paper

Introduction

Aerospace is – alongside communication technologies – bringing the world together. The result is a never-before-seen increase in traveling and worldwide flow of goods, with positive social and economic effects, and significant negative environmental impacts. However, aerospace is not only “joining the world,” but also representing an international business with a worldwide supply chain for both civil and military systems that can act as a key driver of a country’s growth and international competitiveness (Hartley, 2014). Sweden, with a population of ca. ten million and a GDP of \$601bn, is one of the smallest countries with an intact/complete (military) aviation industry, including a broad national aviation research strategy, to maintain the competitiveness and expertise of its main industrial actors. The largest industrial actors are Saab AB (aircraft and complete defense systems) and GKN (propulsion and jet engine technologies), formerly, Volvo Flygmotor.

The enhanced technical complexity of nowadays (aerospace) products, systems and operations render it hardly manageable by one country alone. This obviously has an influence on research and education, too. With the recent establishment of

the Swedish Aeronautical Research Center (SARC) in June 2018 (SARC, 2018), these two topics – research and education, among others – are expected to be strengthened by a careful interplay conducted by SARC among industry, universities and government agencies, based on a concept of strategic research clusters. This paper presents two topics, each presenting future challenges facing the aerospace sector, with the boundary condition of Sweden as a small country with limited resources and a strategic, complete expertise in aviation technologies:

- 1 Part 1: TRL-based research and the slanted wave: research complexity and the need for academic collaboration; and
- 2 Part 2: The establishment of SARC as a catalyst for collaboration in research and education

Swedish Aeronautical Research Center background: TRL-related strategic research collaborations and the triple helix

Research and education are both topics based on and blossomed out by collaboration, the sharing of knowledge and information,

The current issue and full text archive of this journal is available on Emerald Insight at: www.emeraldinsight.com/1748-8842.htm



Aircraft Engineering and Aerospace Technology
91/6 (2019) 857–864
© Emerald Publishing Limited [ISSN 1748-8842]
[DOI 10.1108/AEAT-07-2018-0201]

The author would like to give credit to the founder and driving persons of the SARC initiative, namely, Anders Blom (Director, INNOVAIR), Prof Dan Henningson (KTH), Prof Petter Krus (LiU) and Prof Tomas Grönstedt (Chalmers).

Received 28 August 2018
Revised 24 October 2018
Accepted 26 October 2018

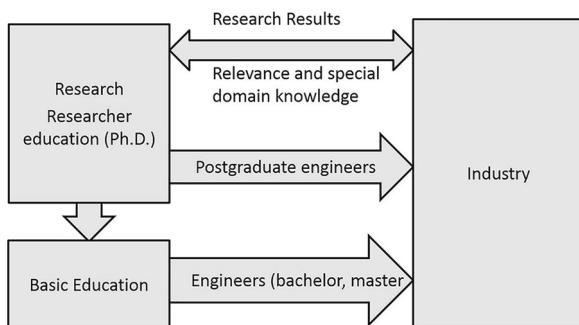
communication and discussion. It is also recognized that a very important reason for universities to have research – rather than to place research solely at separate establishments – is to provide a research overhead to education, which after all is the prime objective of universities (Fung *et al.*, 2017). University-based education includes postgraduate students, who are more directly involved in research projects, and graduate or undergraduate students, as indicated in Figure 1. With the presence of industrial research collaboration, university staff as well as students learn the application and relevance of different research topics, which leads to a more relevant, better and up-to-date education.

The SARC's vision is to be a national forum and contact for aeronautical research, to promote research continuity and to give input for a national long-term research strategy. Those topics foster a sound research overhead for education. Furthermore, it directly benefits the aeronautical industry, which is more short-/medium-term focused and runs short on long-term, low TRL level research project financing.

The aerospace industry is for various reasons prone to large, international consortia for research, product development, production and operation. There are many reasons for this trend: system complexity, high reliability demand, multi-domain characteristic, extremely long life cycles, valuable products and scale effects (small number of produced products and fleet design), to name only a few. In addition, aeronautical products are often not only complex products but also represent so-called system of systems (SoS) (for a definition, see Maier, 1998), which have to be dealt with in a different way, within both research and product development (Staack *et al.*, 2018). The high risks to be taken, the high reliability requirements and the long lead times and extremely long life-cycle times of aeronautical products/systems render the aerospace industry rather conservative – with some exceptions[1]. A useful measure introducing new technologies from an engineering/technical point of view, introduced by NASA for the space industry in the late 1990s, is the technology readiness level (TRL) (NASA, 2007). The TRL index of a technology can be used as a rough estimate of:

- cost needed to conduct the required actions to reach the next TRL level;
- time to market;
- risks taken; and

Figure 1 The interaction between academia and industry, including straddlers/industrial teachers and industrial PhD students (not shown: government agencies and society)



Source: Krus (2018)

- uncertainty/lack of knowledge regarding the technology use/application and implications.

While time-to-market shrinks with increasing TRL level, the costs within each step expand. At very low TRL, the long-term development to be performed, the vast amount of money needed and the uncertainty/absence of knowledge as to where and how to implement it (on which product and how) make it hard for (short-/medium-term profit-oriented) companies to motivate research at low TRL levels. On the other hand, high TRL level development within the aerospace sector requires large enterprises, workload and infrastructure (for manufacturing and testing/operation) that it is unfeasible to be reached by universities. With Sweden as an example, high-level TRL research is so large and costly for most enterprises that such research has to be conducted by bi-/multi-lateral (usually EU-funded) projects such as Horizon 2020.

Figure 2 shows the so called slanted wave behavior of the technology-maturing process, indicated by the TRL level in the example of Swedish National Aeronautical Research Programs (NFFPs) (NFFP, 2018). Lead times from national low TRL research until a product appears on the market typically vary from 10 to 20 years (Olsson, 2018). While Figure 2 shows only civil applications, the NFFP-financed (low TRL level) research focuses on dual use (military and civil) or triple use (additional innovation/technology spread to other sectors) (Blom, 2018).

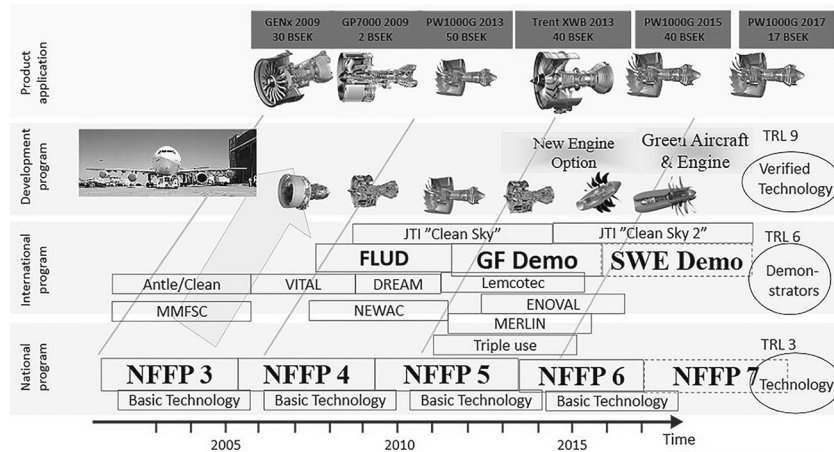
An important aspect of the research financing within the strategic innovation programs (SIPs) financed by the Swedish Governmental Agency for Innovation Systems (VINNOVA) is socioeconomic effects (measures) (for instance, the return on public investment in the C/D version Gripen program beyond the 2.6-fold social return on public investment [Tillvaxtanlys, 2016]). Eliasson (2010) identified three main areas of the technology contribution of Sweden's aeronautical sector:

- 1 technology transfer of a high TRL level/operational-focused technologies – industry acting as a university, providing research, education and training to other firms and sectors;
- 2 spillovers to other domains, such as software engineering, systems engineering, lightweight structures and medicine; and
- 3 maintaining of a (defense) industry, capable of developing complete military aircraft-combat systems and associated systems.

Sweden's military aviation industry's capability is based on spillover effects from the Gripen and its predecessors' projects, routines and systems-engineering capabilities. This becomes apparent in the example of the pace of recent maiden flights, with significant contributions from Saab AB: December 20, 2017 – Trainer Boeing T-X[2]; June 15, 2017 – Gripen NG; March 14, 2018 – GlobalEye Airborne Early Warning and Control Aircraft; and September 26, 2017 – the civil Airbus A340 BLADE.

The above-mentioned triple (or dual) use NFFP research approach should not be confused with the triple helix approach by Henry Etzkowitz (2008). The latter focuses on the interplay between universities, industry and government within modern societies. Sweden, with a high educational level and a high innovation capacity, seems made to match Etzkowitz's view. In the context of the SARC establishment, it is useful to have

Figure 2 The slanted-wave TRL-based technology spread on an example of civil (GKN) engine technologies



Source: Olsson (2018)

knowledge and understanding of the triple helix axiom to be able to establish an as-good-as-possible collaboration of the research-centered part of the triple helix, including university research centers, science parks, technology transfer offices and incubators.

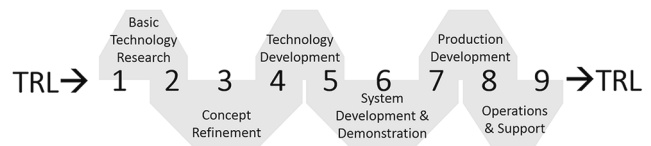
More on readiness level measures

The use of the TRL as a metric of time-to-market and development cost, as explained in the section above, is a crude estimation that can easily be refined with limited effort. Various shortcomings and limitations of the TRL metric have to be kept in mind when using this index. The US Government Accountability Office (GAO) lists the most prominent of them (GAO, 2016). Alongside the widely used and established TRL, other complementary indices with slightly different foci exist, such as:

- manufacturing readiness level, a measure of the maturity of the manufacturing readiness of an object of technology related to TRL;
- business readiness level, a measure of the success or failure risk of a technology transition based on business considerations (circumstances);
- integration readiness level (IRL), a measure of the interfacing of compatible interactions of different technologies and the maturity of integration between them; and
- system readiness level (SRL), a measure of the “individual TRLs in a system and their subsequent integration points with other technologies, the Integration Readiness Level (IRL)” (Sausser *et al.*, 2006).

Figure 3 shows the difference between product-focused development phases (top) and technology-related TRL evolution (bottom). Lead times from national low TRL research until a product appears on the market typically vary from 10 to 20 years (Olsson, 2018). Sausser *et al.* (2006) show that a technology-individual TRL assessment (also denoted as a TRA) has certain shortcomings when applied to a “[...]system context, which may involve interplay between multiple technologies” that can be overcome by extending the assessment by means of some of the

Figure 3 The parallel but different phased phases of product development and technology evolution alongside the TRL scale



Source: Adapted from Sausser *et al.* (2006)

above-mentioned maturity indexes. These concerns are highly relevant for most aerospace applications, which often not only represent complex systems with a number of different domains and (new, unproven) technologies but also may represent so called SoSs that suffer or benefit even more strongly from the interplay between the entities (component or systems).

Consequently, the TRL-based research assessment is applicable to rough estimations (such as shown in Figure 2), but for detailed research or product development planning, more complex assessment criteria have to be applied.

Focusing on SoS engineering, SRL- or IRL-focused methods might be more relevant than the TRL index. The IRL addresses three stages of integration maturity that have to be completed until the integration of a new technology can be assessed as proven: semantic, syntactic and pragmatic (Sausser *et al.*, 2009). Each of these topics consists of three subsets, leading to nine steps in total, similar to the TRL index. The use of IRL enables the identification of integration maturity risks or incompatibility at very early stages on the semantic levels 1-3 (comparable to TRL 1-3). Higher IRL levels can therefore be considered unnecessary if the focus is on conceptual (SoS) design only.

To conclude, it can be said that the TRL index is a reasonable and sufficient measure with respect to the SARC stakeholder needs – research-focused project and high-level research management on mainly low (up to medium-low) TRL levels. However, it falls short in the industrial aspects of product/system development, with its slightly different foci. A

more complex approach (e.g. using IRL and similar indexes mentioned above) should therefore be considered to attain a good match between the academic research and the industries' R&D needs (and timelines) for future products. This topic seems especially important for Saab's military branch, with a product portfolio of individual customer-adapted (defense) SoSs with high integrational risks.

Establishment of the Swedish Aeronautical Research Center (SARC)

The SARC was inaugurated in 2018 at Linköping University (LiU) and serves as the host after several years of planning activities (SARC, 2018). Founding members are LiU and Chalmers University of Technology (Chalmers) only, but a dialog is maintained with several academic players within aeronautics to shape SARC into a national entity. Expectations of SARC are high and differ slightly between the various stakeholders. Three to four[3] main areas of activity have been identified:

- research collaborations and alliances (national);
- international research collaborations; and
- education of graduate (PhD academy) and undergraduate students.

Motivation for the center's establishment

As mentioned earlier, the SARC's stakeholders have slightly different motives, but all have common main reasons for its establishment. The central point is to ensure and enhance the competitiveness of the Swedish aeronautical sector, which inevitably includes both industry and academia (Figure 1, Chapter 2). One relevant NFFP socioeconomic effect measure is the education of graduate students (PhDs), who to a large extent continue within the Swedish aviation industry after achieving the doctoral diploma (Åström *et al.*, 2008). From the center's funders' point of view (the Swedish Strategic Innovation Programme for Aeronautics (INNOVAIR, 2018 and VINNOVA), SARC should act for the following purposes (Blom, 2018):

- structure and further improve the academic system in aeronautics and its relations with the other actors in the innovation system;
- guarantee long-term supply of skilled workforce within prioritized technical fields of relevance for aeronautics;
- guarantee long-term (low-level TRL) research of national/international (socioeconomic) interests such as e.g. "green flight" for the national zero CO₂ transportation target[4];
- act as a lobby group for academic/aeronautical interests; and
- strengthen the national university/agency-conducted research by better alignment and closer collaboration (instead of segregation and competition).

All SARC research studies should contribute to lower environmental impact and improve social welfare by contributing to attain the European Commission goals (ACARE, 2011).

Swedish Aeronautical Research Center–industry collaboration

The dialog between industry and academia should be strengthened by a tight integration of the competence clusters

that were established at GKN and Saab together within the NFFP/INNOVAIR program in 2014. Each cluster – represented by a responsible (industrial) cluster lead (Swedish: klusterledare) – represents one key technology of the company. Table I lists these 15 strategic technology clusters.

Within NFFP, an education program was offered for the cluster leads. In addition to seminar series, workshops and courses in R&D and academic processes, the focus had been put on a detailed insight into the various clusters' topics to create an active, closely collaborating network among the cluster leads. Figure 4 shows the comprehensive, anticipated interactions between universities, research agencies and industries as an effect-chain from the first idea to research financing to industrial realization, conducted by the cluster lead (Alfredson and Jouannet, 2017). According to a evaluation of (international) research projects with contributions from GKN by Vallhagen (2016), the following targets had been reached with the cluster setup already in 2016:

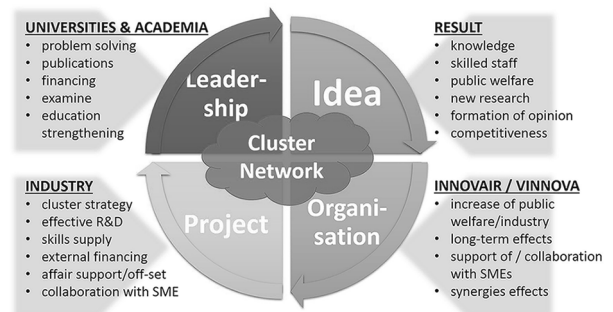
- enhanced holistic project lead and better inter-project organization (focus alignment, synergy effects, collaboration);
- exchange of experiences (inner/inter-enterprise) during the cluster lead training program; and
- finding of synergy effects and better-aligned research of high industrial relevance.

Table I European and US city-pairs selected for this investigation

Saab AB	GKN
Avionic platform technology	
Operation and maintenance	Engine systems and installation
Aeronautical engineering	Turbomachinery
HMI and decision support	Value-driven development
Concept and SoS methods	Advanced materials (metallic)
Cooperating systems	Production systems and processing
Sensors – system and functions	Composite components
Structures and manufacturing technology	Lifting

Note: HMI = Human-machine interaction

Figure 4 The interplay of academia and industry with the help of the cluster lead acting as a central hub



Source: Adapted from Alfredson and Jouannet (2017)

Early cluster lead activities focused mainly on industrial needs. While it worked out well for the industry (Vallhagen, 2016), no such tightly interconnected network existed on the academic side. Instead, collaboration and information exchange was arranged by extended use of so called straddlers (Swedish: gränsångare) – people who are employed part-time in industry and academia – enabling, among other things, an active engagement at university research centers and contact with PhD students and undergraduate student projects. A less strictly controlled academic environment made it easier for these people to spend more time on academic publications and enabled more flexibility and collaboration with international researchers (Vallhagen, 2016). This system worked well on an individual/group level, but a central administration and inter-project/disciplinary and strategic, national long-term perspective from an academic viewpoint were lacking. This lack of an academic counterpart to the well-working (industrial) cluster leads will be taken up by SARC in the future.

Swedish Aeronautical Research Center research academy

One important topic in the industry human resource supply is graduate engineers (Figure 1). To render aeronautical engineering more attractive, enhance the quality and increase the proportion of foreign PhDs with doctorates from Sweden who stay in the country, SARC will build a national aeronautical PhD academy. Approximately half of the SARC budget is designated to drive this graduate school.

The SARC PhD academy picks up lessons learned from the former *SSF Endrea* (1997 to ca. 2002, research on engineering design) and the *ProViking* (2002-2012, research on product realization) (ProViking, 2013) graduate schools. Both graduate schools were introduced together within research programs, with some similarities to the NFFP. Especially, the *Endrea* PhD academy was successful, with many former PhD candidates nowadays in leading academic and industrial positions within engineering design. Quality assessment (and assurance) was performed by a scientific advisory board of international experts within the field of study, who reviewed each student's research performance (and relevance) once a year. A positive side effect of this advisory board was not only ensuring high quality among the students but also bringing the spotlight on the supervising professors. Additional quality-assurance arrangements were implemented, following the graduate school quality-assessment criteria and recommendations stated by the Swedish National Agency for Higher Education (Hogskoleverket, 2008). In addition to the metrics for course/program evaluation, this also includes the candidate-recruitment process, the quality of the doctoral thesis, the individual researcher competence achieved (e.g. self-reliance), gender equality, international relations and support for mobility/traveling.

In addition to the education of PhD students, other important success factors had been common publications among the students (from different fields). An important lesson learned from the *Endrea/ProViking* graduate program is that there is an optimum number of school activities to avoid distraction and too high workload.

Too frequent activities distract the PhD candidates from their research and may result in too high workloads, whereas too few activities fall short as regards their feelings associated with the graduate school and do not lead to a sound research network among the students (e.g. evaluable through the number of collaborative publications). A fine balance between credit-giving courses, social activities/networking, quality assessment and aligned feedback is necessary. The planned types of courses within the SARC PhD academy can be classified as follows[5]:

- shared *soft skills courses* (such as academic writing, research methods, research ethics, media training);
- common *basic/fundamental courses*, creating a common sense and understanding among the students (within aeronautics. e.g. aircraft design); and
- *specialist courses* close to the topics of the PhD candidates' research field(s).

At *Endrea* – and similar planned for SARC – courses were mainly given by members/professors of the contributing universities and research organizations. In addition, renowned international experts were invited to hold courses. The latter had two positive side effects: firstly, ensuring a high-level education program with attractive courses and secondly, encouraging the establishment of links and networks between lecturers, students and the involved staff at the universities. This could (and should) result in new collaboration and research program applications.

Swedish Aeronautical Research Center's future education ambitions

While the previous chapters are based on the analysis and explanation of facts and planned and founded SARC activities, the following section gives a future scenario and interpretation, based on the author's expected changes within university-based education. So far, SARC's educational activities focused solely on graduate students. This is a rather shortsighted approach with the well-aligned academia–industry interplay at hand (cf. Figure 1). To be well prepared for future scenarios, SARC is considering extending its activities to two additional topics: undergraduate education and work/job-accompanying courses. Several trends and possible game-changers may strongly influence and change higher education in the future:

- trends within the industry and the whole of society toward life-long learning;
- higher university graduation rate alongside a change in students' learning attitude;
- maturation of information and communication technologies and availability of digital teaching tools, along with worldwide Web access;
- internationalization and consequently a widespread availability of English education (material); and
- increased demand for shorter education programs.

It has to be highlighted that the above-mentioned topics should not be interpreted as threads by universities but as chance and possible game-changers for future academic education profiles. There will be a rising demand for short/block courses, perhaps partly or completely remotely given via the internet or as 24/7 available material, such as the edX platform founded by MIT (edX, 2018). The European

Bologna Bachelor-Master reform (Bologna reform, 1999, in Sweden established since 2007) – driven by industrial needs – paved the way for shorter educational (bachelor and master) programs, which replaced the usual five-year national university education degree (Swedish: *civilingenjör*), comparable with a master certificate.

In engineering education in particular, tremendous enhancements and cost/effort optimizations can be made possible, e.g. by virtual labs (Budhu, 2002) or virtual reality technology instead of hardware components and physical test benches. The availability of high-quality online courses – partly offered free-of-charge and from high-ranked universities – may change the education and certification system dramatically in the future (e.g. the edX platform founded by MIT [edX, 2018]). Will traditional university education, especially at smaller universities, survive? Should academia in future open up for non-academic education programs or courses and act more as an educational think tank where interested people/students can stay for shorter periods and then return directly to their affiliation? From the SARC stakeholders' points of view, with the goal of strengthening national aeronautical education and industry, collaboration on undergraduate and extension studies for persons with work experience should be established in the future. While the author has no idea how this will look, inspiration can be taken from the research side. Given Sweden's limited size, research focus and competence are – as explained in Section 3.2 – already split into strategic collaborations between industry and universities, with the help of the cluster leads. As an example, the aeronautical research focus at the three largest academic actors, Royal Institute of Technology in Stockholm, LiU and Chalmers, is related to certain competence domains (Table II). Consequently, would it not be possible to form a national aeronautical master education program where every actor contributes its main competence? With the tight industry-academia coupling at hand, namely, with the original equipment manufacturer (OEMs) GKN in Gothenburg and Saab in Linköping, Sweden has the chance to shape a national aeronautical education program (probably including practical internships) of a unique kind, with a never-before-seen attraction that could beat top-ranked universities and attract students from all over the world to study aeronautics in Sweden.

International collaborations and strategic partner countries

The globalization and consolidation of the aviation market is also affecting Sweden. With the limited population size at hand, acting as an export-oriented nation, international relations are natural for independent Sweden. While not being part of North Atlantic Treaty Organization, close collaboration within aeronautics has been established since World War II and the

Table II Overview of strategic industry–university collaboration fields within aeronautics

University	Main/strategic competence domain
KTH	Aerodynamics, CFD and structure
LiU	Aircraft design and control
Chalmers	Propulsion system and material

Note: CFD = Computational fluid dynamics

Cold War with Central Europe, the UK and the USA. Since signing a large export contract for the Gripen aircraft with Brazil, a significant knowledge transfer and strategic collaboration with Brazil – both on academia and industry levels – are being established, e.g. through the bilateral Swedish Demonstrator Project (VINNOVA, 2015).

Referring to the TRL-based slanted technology wave (Figure 2) and the arguments in Chapter 2, demonstrator programs are of a bi- or multi-lateral nature to handle the high complexity, size and costs. Recent examples with Swedish industrial participation include the BLADE project (Airbus, 2017) and the unmanned combat aerial vehicle/international UCAS project lead by France program, both with a significant contribution from Saab. While the main Swedish aeronautical OEMs are large enough to apply for such large and complex long-term projects, most of the academia actors are not large enough to do so. SARC's ambition here is to form larger national alliances among the academia actors, with significant expertise and size that are able to apply for larger EU-funded calls such as the Clean Sky 2 (Horizon 2020) program.

Conclusion

A national center for research and education has been established in Sweden. The main motives are to promote long-term competence development and to strengthen aviation technologies (VINNOVA, 2018a), one of the 17 SIPs in Sweden (VINNOVA, 2018b). Focusing on the academic part within the overall socioeconomic and R&D interplay, SARC represents a long-awaited missing link toward the strategic (industrial) research clusters established about five years ago. With SARC in place, beneficial triple helix effects are also expected through a stronger aeronautics policy influencing weight by this joint researcher forum.

While the TRL index is extensively used to plan, organize and review actions by INNOVAIR, it has been shown (in Chapter 2) that a more distinct approach using system-specific and system-integration-related indices should be preferred to enable a more concise planning and arrangement between the academia researcher's and the industry's R&D viewpoints. This is in particular the case when shifting the focus from complex product development toward SoS engineering. In this respect, SARC limits its own funded research to low-level TRLs.

What is expected of SARC is to foster collaboration between all actors, enhancing the efficiency and coordination of research projects. SARC's own financing is limited; the major part will be used to drive the PhD school, e.g. finance courses and award scholarships or travel grants for the PhD students. A small part of the money can be used to finance long-term low-level research, e.g. to support important societal topics such as energy saving and environmental pollution, backing the European Commission's air mobility Flightpath 2015 agenda (ACARE, 2011). The first funded research project will be a joint PhD student research project to lay the foundation for assessing the environmental impact of technologies applied in the civil air transportation sector. Backed with domain-specific courses, this should result in interdisciplinary publications and widen the (researchers') horizon of the involved PhD students.

SARC's financing is secured only for the next three years. Further continuation will only be possible if a new funder is found by 2021. The continuation will largely depend on whether SARC manages to form a joint national entity (without leaving any aeronautical research actor outside) and whether the stated goals are reached and can withstand a detailed assessment after that timeframe. However, first impressions and the feedback from both Swedish and international (Brazilian) researchers are positive and give hope for a long-lasting SARC.

Notes

- 1 Exceptions are usually start-ups/newcomers such as SpaceX in the aerospace market, with its vertical landing rockets, the UAV market with uncountable actors and the emerging electric flying taxi market with start-ups such as Lilium.
- 2 With a significant work share and system responsibility performed by Saab.
- 3 Depending on the way of counting sub-graduate and post-graduate as one or two topics.
- 4 The year 2020 climate targets set by the Swedish Government, see (Naturvårdsverket, 2017).
- 5 For examples of such a course setup, see the *ProViking* course program (ProViking, 2012).

References

- ACARE (2011), *Flightpath 2050 – Europe's Vision for Aviation: Report of the High Level Group on Aviation Research*, Advisory Council for Aviation Research and innovation in Europe (ACARE), European Commission, doi: 10.2777/50266 EUR 098 EN.
- AIRBUS (2017), "BLADE press backgrounder: the breakthrough laminar aircraft demonstrator in Europe", *Technical Report*, Airbus, September 2017.
- Alfredson, J. and Jouannet, C. (2017), "Saab – en klusterledares funktion och uppgifter", presented at the Seminarium för utlysning av NFFP7, INNOVAIR.
- Åström, T., Jansson, T., Mattsson, P., Segerpalm, H. and Faugert, S. (2008), "Evaluation of the Swedish national aeronautics research programme – NFFP", Report VR 2008:05 2006-00665, VINNOVA – Verket för Innovationssystem.
- Blom, A. (2018), "INNOVAIRs SARC vision", presented at the SARC Kickoff Workshop, Linköping, 6 June 2018, Swedish Aeronautical Research Center, LiU.
- Budhu, B. (2002), "Virtual laboratories for engineering education", *Proceedings of the International Conference on Engineering Education, International Network for Engineering Education and Research (iNEER)*, Manchester.
- edX (2018), "edX: the online learning destination and MOOC", available at www.edx.org/learn/education (accessed 6 July 2018).
- Eliasson, G. (2010), *Advanced Public Procurement as Industrial Policy: The Aircraft Industry as a Technical University*, Springer, New York, NY.
- Etzkowitz, H. (2008), *The Triple Helix: University-Industry-Government Innovation in Action*, Routledge, New York, NY and London.
- Fung, D., Besters-Dilger, J. and Van der Vaart, R. (2017), *Excellent Education in Research-Rich Universities*, League of European Research Universities (LERU), Leuven.
- GAO (2016), "Technology readiness assessment guide", *GAO Reports GAO-16-410G*, US Government, Accountability Office (GAO).
- Hartley, K. (2014), *The Political Economy of Aerospace Industries: A Key Driver of Growth and International Competitiveness*, Edward Elgar Publishing, Cheltenham.
- Hogskoleverket (2008), *Utvärdering av 16 Nationella Forskarskolor, Report 2008:16*, The Swedish National Agency for Higher Education (Högskoleverket), ISSN 1400-948X.
- INNOVAIR (2018), "National aeronautical research programme for aeronautics (INNOVAIR): the Swedish strategic innovation program", available at: <http://innovair.org/en/> (accessed 29 June 2018).
- Krus, P. (2018), "SARC.academy: national graduate school for aeronautics", presented at the SARC Kickoff Workshop, Linköping, 6 June 2018, *Swedish Aeronautical Research Center, LiU*.
- Maier, M.W. (1998), "Architecting principles for systems-of-systems", *Systems Engineering*, Vol. 1 No. 4, pp. 267-284.
- NASA (2007), *Systems Engineering Handbook, NASA/sp-2007-6105 rev1*, National Aeronautics and Space Administration (NASA), Washington, DC.
- Naturvårdsverket (2017), "Sweden's seventh national communication on climate change", Technical Report, Government Offices of Sweden, Ministry of the Environment and Energy (Naturvårdsverket), ISSN 0282-7298.
- NFFP (2018), "NFFP - the Swedish national aeronautical research program", available at: <https://innovair.org/international-forskningsprogram/nffp/> (accessed 29 June 2018).
- Olsson, M.-O. (2018), "NFFP: the Swedish national aeronautical research program", presented at the SARC Kickoff Workshop, Linköping, 6 June 2018, *Swedish Aeronautical Research Center, LiU*.
- ProViking (2012), "ProViking course program", available at: www.chalmers.se/ppd/provikingforsarskola-sv/kursprogram (accessed 2 July 2018).
- ProViking (2013), "ProViking – en satsning på svensk industri", available at: <http://innovair.org/en/> (accessed 2 July 2018).
- SARC (2018), "The Swedish aeronautical research center (SARC)", available at: www.sarc.center/ (accessed 29 June 2018).
- Sausser, B., Forbes, E., Long, M. and McGrory, S.E. (2009), "Defining an integration readiness level for defense acquisition", *International Symposium of the International Council on Systems, INCOSE*.
- Sausser, B., Ramirez-Marquez, J., Verma, D. and Gove, R. (2006), "From TRL to SRL: the concept of systems readiness levels", *Conference on Systems Engineering Research 2006, INCOSE, Los Angeles*.
- Staack, I., Amadori, C. and Jouannet, C. (2018), "A holistic engineering approach for aeronautical product development",

31st Congress of the International Council of the Aeronautical Sciences, 9-14 September 2018, ICAS, Belo Horizonte.

Tillväxtanalys (2016), "Nurturing spillover from the industrial partnership between Sweden and Brazil: a case study of the Gripen project", *Technical Report*, The Swedish Agency for Growth Policy Analysis (Tillväxtanalys), Östersund.

Vallhagen, J. (2016), "Tekniska kluster- lessons learned", *Innovais Årsmöte, Trollhättan*, September 2016.

VINNOVA (2015), "SWE DEMO utlysning", Verket för Innovationssystem – Swedish Governmental Agency for Innovation Systems.

VINNOVA (2018a), "SARC projekt: beslut om bidrag", Technical Report nr. 2018-00063, Verket för Innovationssystem – Swedish Governmental Agency for Innovation Systems.

VINNOVA (2018b), "The strategic innovation programmes, VINNOVA: verket för Innovationssystem – Swedish governmental agency for innovation systems", available at www.vinnova.se/en/m/strategic-innovation-programmes/ (accessed 3 July 2018).

Corresponding author

Ingo Staack can be contacted at: ingo.staack@liu.se

FDM 3D printing method utility assessment in small RC aircraft design

Igor Skawiński and Tomasz Goetzendorf-Grabowski

Faculty of Power and Aeronautical Engineering, Warsaw University of Technology, Warsaw, Poland

Abstract

Purpose – The purpose of this paper is to investigate the possibility of manufacturing fused deposition modelling (FDM) 3D printed structures such as wings or fuselages for small remote control (RC) aircraft and mini unmanned aerial vehicles (UAVs).

Design/methodology/approach – Material tests, design assumptions and calculations were verified by designing and manufacturing a small radio-controlled motor-glider using as many printed parts as possible and performing test flights.

Findings – It is possible to create an aircraft with good flight characteristics using FDM 3D printed parts. Current level of technology allows for reasonably fast manufacturing of 3D printed aircraft with good reliability and high success ratio of prints; however, only some of the materials are suitable for printing thin wall structures such as wings.

Practical implications – The paper proves that apart from currently popular small RC aircraft structural materials such as composites, wood and foam, there is also printed plastic. Moreover, 3D printing is highly competitive in some aspects such as first unit production time or production cost.

Originality/value – The presented manufacturing technique can be useful for quick and cost-effective creating scale prototypes of the aircraft for performing test flights.

Keywords FDM, Aircraft design, Optimization, Material, 3D print, RC plane

Paper type Research paper

Introduction

In today's remote control (RC) model aircraft or small unmanned aerial vehicle (UAV) design, a variety of materials are used to form the structure of the aircraft, such as fibre Reinforced Polymers, injection molded foam or wood. During the past decade, a new technique of 3D printing has been developed and popularized (Banke, 2018). There are several types of 3D printers; however, fused deposition modeling (FDM) type has been the most popular among the 3D printing community because of low machine and material cost and reasonably high print speed and quality. Professional selective laser sintering 3D printers are being used in commercial aviation to produce complex nylon, steel or titanium parts with shapes that would be impossible to produce using traditional methods. Unfortunately, these machines are expensive and available only for industry leaders. The demonstrator of this technology was developed by Airbus (Julien, 2016). Most structure parts were made with additive technology.

The concept of 3D printable RC aircraft was born a couple of years ago, but there have been just a few designs from one company – 3Dlab Print (2015) from Czech Republic. The company provides ready to print 3D models or pre-sliced G-codes along with instructions on how to print and assemble the aircraft.

There aren't any comprehensive studies on 3D printing thin-wall structures such as wings or fuselages, determining advantages and disadvantages of 3D printing in comparison to other manufacturing methods. There are some articles related to joints, e.g. wing-fuselage joint (Ferro *et al.*, 2017) or on manufacturing small details, e.g. fittings (Mieloszyk *et al.*, 2018) but there is very difficult to find article on entire structure manufactured using 3D printing.

The purpose of this paper is to investigate the possibilities of creating a 3D printed aircraft, determine the design limitations imposed by the FDM method and discover the advantages and disadvantages of 3D printing in comparison to other manufacturing methods. The results have been tested in real life by building and flight testing a small RC aircraft.

Fused deposition modelling technology overview

FDM, also known as fused filament fabrication is a process of 3D printing that uses a continuous roll of a thermoplastic material called filament. Filament is fed to extruder block, where it is heated and pushed through a nozzle into the printing area. Extruder block is moved to create a demanded shape. After completing extrusion of one layer, extruder block moves upwards and begins printing another layer.

FDM was first developed in 1980s by S. Scott Crump and commercialized in 1990s by Stratasys (2018). After the expiry of the US patent protecting the technology, it became popular in the DIY (Do It Yourself) community. Nowadays, there is a variety of FDM printers available on the market

The current issue and full text archive of this journal is available on Emerald Insight at: www.emeraldinsight.com/1748-8842.htm



Aircraft Engineering and Aerospace Technology
91/6 (2019) 865–872
© Emerald Publishing Limited [ISSN 1748-8842]
[DOI 10.1108/AEAT-07-2018-0189]

Received 12 July 2018
Revised 31 August 2018
Accepted 24 September 2018

with prices ranging from \$200 for the DIY kits to \$10,000 for the professional machines. Range of available materials is wide, from typical thermoplastics like ABS or PET to elastic filament, fluorescent filament or filament containing wood powder to resemble real wood.

Material overview

There is a variety of materials available for FDM printers, each providing different mechanical and thermal properties. The following materials were taken into consideration:

- polylactic acid (PLA);
- acrylonitrile butadiene styrene (ABS);
- polyethylene terephthalate (PET);
- nylon PA12; and
- polycarbonate (PC).

Material tests

Table I shows different properties of each material according to their tech data sheets. Comparison of mechanical parameters does not specify a superior material. Further tests needed to be performed in order to specify the one that performs best in a thin wall structure. A small sample of the thin-wall wing with the chord of 100 mm and span of 50 mm was printed with each of the selected materials in order to compare results and choose the optimal material.

The following factors were carefully checked:

- surface quality;
- layer adhesion;
- deformation and shrinkage; and
- strength and stiffness.

Tests showed that:

- PLA print results in the best surface quality – the thickness of the wall is consistent, structure is watertight, which is a proof that there are no gaps in the thin walls. No blobs of air are visible inside the structure and there are no print inconsistencies in places where the retraction of the material occurs. PLA also provides good mechanical properties and layer adhesion. However, PLA print is very rigid and allows almost no flex before failure; therefore, the durability is low. Another negative property of PLA is its low glass- transition temperature of 60°C, which may result in print losing its shape when left in a car during summer.
- ABS print results in good surface quality as well as mechanical properties and layer adhesion. It is also more flexible and durable than PLA. However, it is difficult to print large thin-wall ABS structures without ability to use a heated print chamber. High shrinkage results in a print

detaching from a print surface and sometimes cracking between the layers during the process of printing.

- PET prints with good surface quality and good mechanical properties, however it is more flexible than PLA and ABS, and thin wall can be easily deformed under small load. Material does not shrink during the print and has good layer adhesion; therefore, prints with PET are usually successful.
- PA12 nylon turned out to be difficult to print with. It did not adhere to the print bed properly, and layer adhesion was average. Nylon is also the most flexible of the materials tested and would require thicker walls to obtain the necessary stiffness.
- PC showed big shrinkage during the print which resulted in cracks between the layers and print failures. Out of five test prints, none succeeded. Because of that further tests of PC were dropped.

Tests showed that Nylon and PC are not suitable for this application. PLA has also been rejected because of its poor temperature resistance. PET is the optimal choice because of its ease of printing and mechanical properties. ABS also performs well, but gives slightly less consistent results than PET. Generally, low shrinkage materials are the best choice for printing thin wall structures as they eliminate all the typical problems, such as deformation, print cracking, warping, bed adhesion.

Technical disadvantages of using fused deposition modelling technology in aircraft design

- One of the biggest challenges in the FDM technology is poor layer adhesion. It not only leads to cracks during the print, but also affects strength of the part. 3D printed parts have anisotropic properties, with reasonably good mechanical strength in two dimensions along the layers and noticeably worse mechanical strength in a dimension across the layers. Moreover, layers are a source of crack propagation, so if the part fails locally, there is a high chance that it will be fully damaged.
- Another challenge is material shrinkage during cooldown. It leads to part losing its initial shape, print warping from the print bed and cracks between layers. Using a printer with a heated build chamber helps a lot, but such machines are expensive and not popular on the consumer market. This is one of the reasons why materials with high shrinkage such as ABS are becoming less popular.
- FDM technology implies use of support structures if printing a horizontal plane in the air. Support structures are a waste of material. The amount of support structures

Table I Comparison of properties of materials according to F3D filament TDS

Material	PLA	ABS	PET	Nylon PA12	PC
Density [g/cm ³]	1,24	1.05	1.27	1.25	1.2
Water absorption [%]	–	0.85	0.13	1.1	0.35
Elastic modulus [MPa]	3,310	2,500	2,100	1,900	2,300
Tensile strength [MPa]	110	–	50	42	60
Print temperature [°C]	190	245	225	255	285

varies between the designs – some of them do not need support structures at all, but in some cases, support structures may weigh more than the actual part. Support structures also extend printing time and post-processing time, as they need to be removed manually.

- Outer surface quality is also an issue, as connecting layers do not form a single smooth wall. Instead, wall surface is rough in the direction perpendicular to the layers. This is clearly shown in the Figure 1. There is a possibility to increase layer quality, e.g. grinding and painting or acetone vapour smoothing if a material is acetone soluble like ABS. However, these methods are not applicable for thin wall structures.
- Another limiting factor is poor mechanical properties of the materials. The best ones available on the market have a tensile strength of 110 MPa, which is very low compared to 500 MPa of PA9 aluminum.

Design limitations of fused deposition modelling technology in printing an RC aircraft

One of the most important aspects when printing a wing or empennage with integrated covering is minimal wall thickness. To determine this parameter, further tests needed to be performed.

Most of the 3D printer slicing software do not allow single extrusion thin wall. Therefore, the minimal layer thickness achievable is equal to twice the diameter of the nozzle.

Test was performed by printing a thin-wall tube of 50 mm diameter and 50 mm height as shown in Figure 2. Three samples were printed: 0.8 mm thick using 0.4 mm nozzle, 0.6 mm thick using 0.3 mm nozzle and 0.4 mm thick using 0.2 mm nozzle. Test showed that 0.6 mm is the minimal usable wall thickness. It presented both a good quality and mechanical strength. Size 0.4 mm showed inconsistencies in the wall thickness and had small holes in the places where the retractions occurred.

Another aspect is the necessity to create support structure while printing a horizontal overhang. This implies the use of angled ribs in the wings and empennage. Maximum overhang angle that does not need support is equal to 45°. The ribs have

Figure 1 Surface quality at 0.2 mm layer height

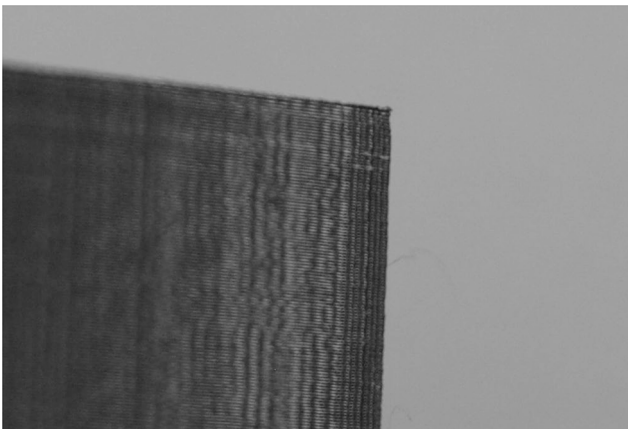


Figure 2 Thin wall cylinder test sample, 0.6 mm thickness



to be angled as removing supports from inside the wing would be impossible without damaging the covering.

Aircraft design process

Sizing and mass analysis

Several constraints were put on the aircraft:

- Motor-glider was chosen as the type of the aircraft because of its simple fuselage and lack of complicated landing gear.
- Another constraint is a maximum wingspan of 1.6 m. Aircraft should be detachable and easy to transport. 1.6 m span also allows the user to print the whole wing at once, since the wing consists of eight 0.2 m wide components, that easily fit into a standard size print volume of 200 × 200 × 200 mm.
- The maximum wingspan was set to 1.6 m, so that the aircraft was portable after dismounting. Aircraft should be detachable and easy to transport. Build height of the printing chamber is 200 mm, so it is optimal for the printing time to have a wingspan equal to 200 mm multiplied by an integer. Wingspan of 1.6 m results in eight 0.2 m segments that can fit in the build volume all at once, and the whole wing is printed together. Bigger wing e.g. 2 m with ten segments would not fit to the build volume at once. Maximum aspect ratio of the wing was set to 12 – higher aspect ratio would cause problems with torsional stiffness of the wing.
- V-tail type was chosen because of its durability – it is much less likely to be damaged during landing than a conventional empennage.
- Static thrust to weight ratio was set to 1 to achieve superior climb performance.

During mass analysis, weight of all components was approximated by their technical data sheets. The masses were then summed up, as shown in the Table II.

Weight of the 3D printed components has been calculated using a simple geometrical method. The area of each component was approximated using CAD software or analytical equations. After that weight was calculated by multiplying area by component thickness and material density. The weight of the

Table II Weight of the RC components

Component	Amount	Unit weight	Weight
Motor	1	60	60
ESC	1	22	22
Servo	4	6	24
Propeller	1	10	10
Spinner	1	15	15
Receiver	1	6	6
Battery	1	124	124
Wires	1	13	13
		Total	274

wing structure was divided into several components. The weight of each component is shown in the Table III.

The table clearly shows that covering is the heaviest element in the wing structure and is responsible for 61 per cent of its weight. It cannot be lighter because it is already at the smallest possible thin wall thickness of 0.6 mm. The weight of empennage and fuselage structural components is presented in Tables IV and V, respectively.

Fuselage is not fully 3D printed. Carbon fibre beam was used between the wing and empennage. 3D printing the beam would significantly move the centre of gravity backwards and preventing that by extending the nose would be difficult.

Table III Weight of the wing structure

Component	Weight (g)
Covering	277.6
Angled ribs	71.6
Connecting ribs	16.1
Spar cap	23.6
Spar web	11.1
Wing joiner	40.8
Wing joiner mount	13.8
Total	454.6

Table IV Weight of the empennage structure

Component	Weight (g)
Covering	41.7
Angled ribs	6.5
Connecting ribs	1.4
Wing spar	2.1
Wing joiner mount	10.2
Wing joiner	4.0
Total	65.9

Table V Weight of the fuselage structure

Component	Weight (g)
Plastic part	70.2
Carbon fibre beam	38.0
Total	108.2

As shown in the Table VI, weight of the wing structure is more than 50 per cent of total aircraft weight. Also, total structure weight is almost 70 per cent of the all-up-weight, which is not common in small RC aircraft.

Comparison to fibre reinforced polymer (FRP) technology

Surface quality and roughness of 3D printed aircraft has an influence on the boundary layer of air and changes aircraft aerodynamics. It is impossible to compare aerodynamic characteristics of 3D printed and composite aircraft without performing wind tunnel testing.

Weight is another factor that needs to be compared between different manufacturing technologies. Weight of composite structure was calculated. Types and thicknesses of composites are similar to those used in 2016 Micro class SAE Aerodesign WUT aircraft.

Wing

Outer wing structure consists of one layer of Carboline fibre with specific weight 25 g/m², separating material Rohacell 51 with 1 mm thickness and 51 g/m³ density and another layer of Carboline fibre.

Ribs are made of 1.5 mm thick balsa wood with 110 kg/m³ density, and they are located every 10 cm of wingspan. Wing spar cap is made of 4 mm thick balsa wood. It is assumed that the weight of wing spar web, wing joiner and wing joiner mount is identical in both manufacturing methods.

Fuselage

Structure of the front part of the fuselage consists of one layer of glass fibre with specific weight 50 g/m² and two layers of carbon fibre with specific weight 200 g/m². Weight of a carbon fibre beam is identical in both manufacturing techniques.

Empennage

Structure of the empennage is identical to the structure of the wing.

Weight comparison

After calculating the weight of the composite structure, it was compared to the 3D printed structure as shown in the Table VII.

Calculations show that composite structure is significantly lighter than 3D printed structure. In this case, the difference is equal to 58 per cent. This clearly shows that in the case of designing a professional RC aircraft of UAV, where weight savings are crucial for good performance, 3D printed structures are not a good choice. Weight that is saved by using 3D printed

Table VI Total aircraft weight

Component	Weight (g)
Wing	454.6
Empennage	65.9
Fuselage	108.2
Total	628.6
RC equipment	274
AUW	902.6

Table VII Comparison of composite and 3D printed structure

Part	Composite structure (g)	3D printed structure (g)
Wing	147.06	454.56
Empennage	25.29	64.30
Fuselage	90.66	108.20
Total	263.01	627.06

structure can be used for a bigger battery which increases flight endurance.

Cost comparison

Composite materials, especially carbon fibres, are expensive. Cost of materials was calculated, including carbon and glass fibres, Rohacell foam, balsa wood and resins. Total cost of materials required for manufacturing the aircrafts structure in FRP technology is equal to \$160, compared to \$30 in 3D printed technology. Another factor is manufacturing, which can cost up to several thousands of dollars, depending on the material used and cost of milling.

Choosing an airfoil

One of the biggest aspects that needed to be taken into consideration was surface roughness and selection of suitable airfoil for the main wing. A good software tool to analyse the airfoil is Xfoil (Drela, 1989) which can be used within the optimization process (Goetzendorf-Grabowski, 2017) as it was presented in MADO (Goetzendorf-Grabowski *et al.*, 2012). Finally, specialized software tool for airfoils optimization – Xoptfoil (Prosser, 2017) – was applied. It also uses Xfoil for aerodynamic analysis and particle-swarm optimization (PSO) method (Kennedy and Eberhart, 1995) to find the profile that meets the desired objective function.

Forced turbulent boundary layer transition point was set to 30 per cent chord. Other optimization parameters were:

$$C_{lopt} = 0,8$$

$$Re_{vopt} = 88500$$

$$Min\ thickness = 0,09$$

Several operating points with different weight ratios were put into the objective function to achieve optimal airfoil with smooth characteristics. Having not enough operating points while using Xoptfoil often results in a non-smooth polar due to Xfoil calculation errors and local laminar flow occurrences. The parameters of the objective function are listed in Table VIII:

Table VIII Objective function parameters

Oppoint	1	2	3	4	5
Specified Cl	0.4	0.8	0.85	1.25	1.39
Re	125,000	88,500	86,000	70,500	67,000
Optimization target	min-drag	min-drag	min-drag	min-drag	min-drag
Point weight	3	10	3	3	3

The result of this was an airfoil with lower C_d at desired values of C_l , compared to typical glider airfoils.

It is visible that the optimized airfoil has higher max camber than typical RC glider airfoils (Figure 3). Another thing that strongly distinguishes the optimized airfoil is low thickness in the second half of the chord.

Figures 4 and 5 clearly show that the optimized airfoil performs better than the airfoils it is compared to Cl goes up to 1.4 without any significant drag increase and boundary layer separation. Cl/Cd at the operating range of angles of attack between 5° and 8° is higher. Max Cl/Cd is 18.7 per cent higher than the one of SD7037 airfoil.

Measuring wing loads

There is no sufficient data regarding accelerations and loads generated on small aircraft of MTOW < 1 kg. Tests using an RC glider with 2 m wingspan and 800 g weight were performed to determine the loads.

Figure 3 Airfoil shape comparison

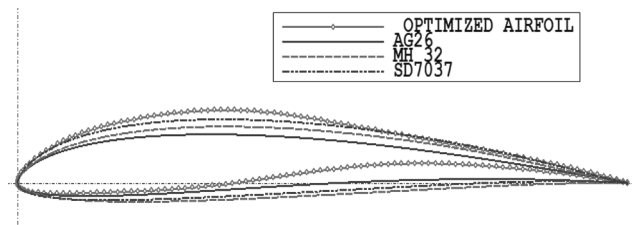


Figure 4 Airfoil polar comparison

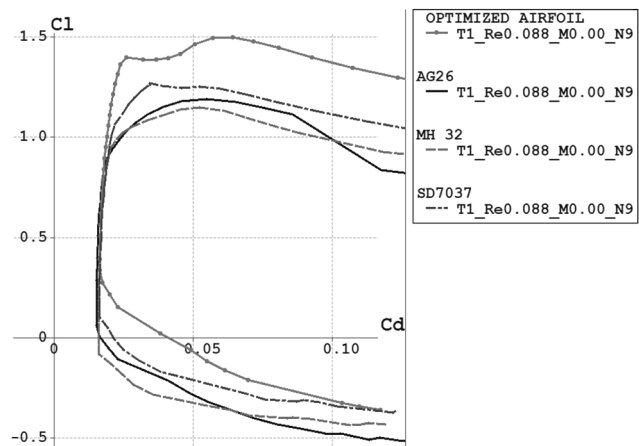
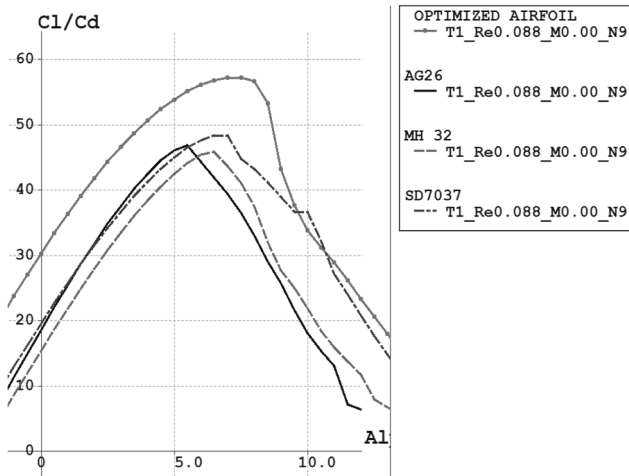


Figure 5 Airfoil L/D



Accelerations were measured in the z -axis. An Arduino with MPU6050 IMU was used to collect the data. Sensor was mounted at the centre of gravity of the aircraft. Initial five test flights were performed each one consisting of different maneuvers. The results are shown in Figures 6 and in 7. The first one shows a flight where the maximum generated G-load was the lowest. The second one shows a flight where the highest G-load was measured.

Tests show that during normal flight without aerobatic maneuvers G-forces do not exceed 3G. However, during aerobatic maneuvers, G-forces reached as high as 8G. These data were used during calculations of wing spar.

Wing design

Wing is a semi-elliptical design with 1.6° negative twist along the chord to improve stall characteristics. Wing has no dihedral. Each wing has been divided into four segments to fit inside the build volume of the printer. Aileron is printed separately with an integrated hinge. The tube joining the wings is a carbon fibre tube of 10 mm diameter. Wing spar cap is made of carbon fibre. Servo box is integrated in one of the wing segments. All of the wing structure is 0.6 mm thin. Figure 8 shows the location of different components of the wing structure on one segment of the wing.

Figure 6 Accelerations during normal flight

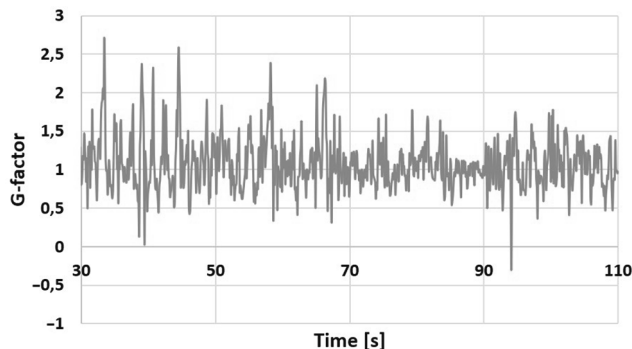


Figure 7 Accelerations during a dive

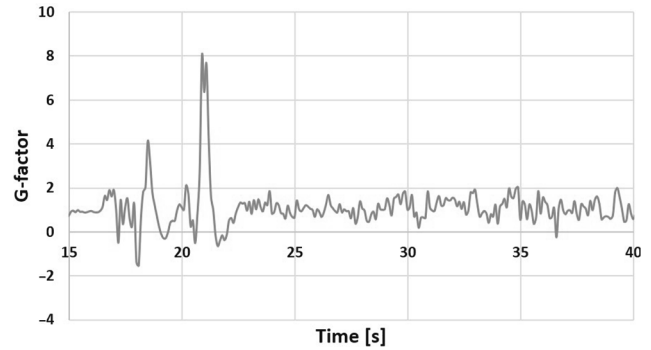
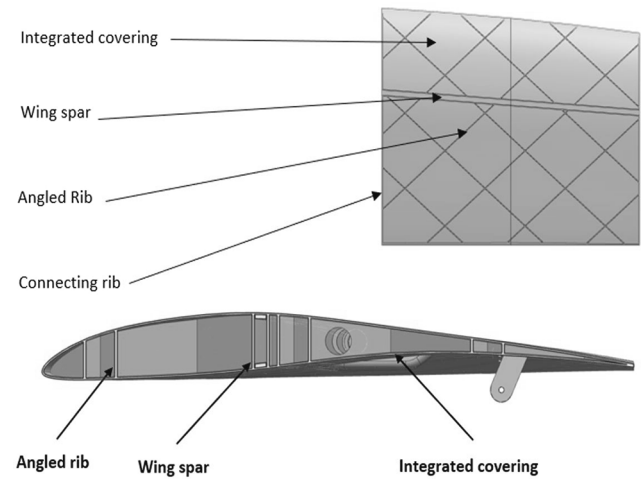


Figure 8 Wing segment structure



Maximum calculated L/D of the wing without empennage and fuselage is equal to 23, which is a good result for a 12 aspect ratio wing. Aircraft technical data is presented in the Table IX.

Empennage and fuselage design

Empennage is a V-Tail type. Angle between stabilizers is equal to 102 degrees. Horizontal tail volume $C_{HT} = 0.5$, Vertical tail

Table IX Aircraft technical data

Wingspan	1,600	mm
Length	1,170	mm
Wing Area	21.24	dm ²
MAC	144	mm
Wing twist	1.6	°
L/D max	20.5	
Optimal speed	9.5	m/s
Minimal speed	7.4	m/s
Cl max	1.25	
Angle of incidence	5	°
AUW	903	g
Wing loading	42,51,412	g/dm ²
C_{HT}	0.5	
C_{VT}	0.03	
Empennage angle of incidence	1	°

volume $C_{VT} = 0.03$. Empennage is mounted to the fuselage via a 6 mm tube. The airfoil is a symmetric NACA0009.

Main part of the fuselage (Figure 9) is 3D printed. It contains propulsion system, receiver and battery as well as servos for the v-tail. Tail boom is a carbon fiber tube. At the end of the tail boom, there is a 3D printed V-tail mount.

Manufacturing process

Aircraft has been printed on Prusa i3 MK2S printer with PET filament. Whole printing process took 65 machine-hours. Success ratio of prints averaged at 75 per cent. Man Labour includes slicing models in the slicing software, gluing the model with special CA glue and installing RC equipment. Assembling the aircraft took 10 man-hours. Aircraft assembly process is simple and involves CA glue and some pliers for removing support material. The built began with assembling the wings. Four parts of each wing were glued together (Figure 10). Small carbon rods inserted in designated holes helped with positioning of each segment.

Then, two aileron segments were glued together and the aileron installed in place with a carbon rod used as a hinge. After that, carbon wing spars were covered with a glue and inserted in place. In the end, aileron servos and pushrods were installed and servo wire was passed through a dedicated hole. Assembling the fuselage was simple. Three separate plastic parts were glued together and carbon fibre beam was mounted in place (Figure 11).

Next, the empennage mount was glued in place and stabilizers with elevators were mounted. The last step of the build was to mount the Bowden tubes for empennage pushrods

Figure 9 Fuselage assembly

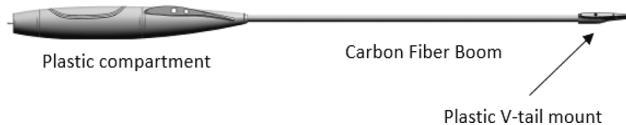


Figure 10 3D printed wing segment



Figure 11 Fuselage 3D printed part



and install the servos and a propulsion unit. The assembled aircraft is presented in Figure 12.

Cost of manufacturing the aircraft is fairly low. Filament cost is about \$15. Other materials including e.g. glues, carbon fibre tubes cost \$15. The cost of the RC equipment used for the project was about \$70. Total manufacturing cost is about \$100.

Test flight results

Several test flights were performed to determine aircraft's aerodynamic flight characteristics. Plane performs well in typical flight patterns such as thermal soaring or high-speed glide. There is a wide airspeed range available and stall characteristics are good and predictable, without tendencies for unexpected spins. The maximum deflection of the ailerons had to be reduced to reduce maneuverability and reach a comfortable flight.

There are two aspects that need further work:

- 1 Investigating a possibility of using ailerons as airbrakes for easier landing – aircraft with no airbrakes is difficult to land on a constrained area because of high L/D ratio.
- 2 Investigating ways of reducing the pitching-up effect at full throttle. Possibly a simple throttle to elevator mix would be enough to counteract the effect. Otherwise, motor angle of inclination would have to be altered.

Figure 12 Assembled aircraft



Conclusion

FDM 3D printing is a powerful manufacturing method which has performed big technological advancements over the last few years, and it is still developing today. Quality of the prints increases as well as reliability of the printing process. New materials with superior mechanical properties are being tested (Szczesniak *et al.*, 2018) and introduced. RC glider, which has been designed and built is proof that an aircraft made almost completely using 3D printing process can fly and perform well in terms of aerodynamic characteristics. Further developments in FDM technology may allow for easier printing with lighter and stronger materials. If it happens, creating 3D printed RC aircrafts and mini UAVs may not only be possible but also become a reasonable competition against composite materials, wood or foam. Design and building of the 3D printed RC motor-glider was a success, but further research needs to be done to improve the aircraft. Most important aspects that need to be investigated are influence of the rough 3D printed surface on Cl and Cd of the wing and advanced structural analysis that may allow for weight savings.

References

- 3Dlab Print (2015), available at: <https://3dlabprint.com> (accessed 6 July 2018).
- Banke, J. (2018), “3D printing offers multi-dimensional benefits to aviation”, available at: www.nasa.gov/aero/3D-printing-offers-multi-dimensional-benefits-to-aviation (accessed 30 September 2018).
- Drela, M. (1989), “XFOIL: an analysis and design system for low Reynolds number airfoils”, in Mueller, T.J. (Ed.), *Low Reynolds Number Aerodynamics*, Lecture Notes in Eng. 54.
- Ferro, C.G., Mazza, A., Belmonte, D., Secli, C. and Maggiore, P. (2017), “A comparison between 3D printing and milling process for a spar cap fitting (Wing-fuselage) of UAV aircraft”, *Procedia CIRP*, Vol. 62, pp. 487–493.
- Goetzendorf-Grabowski, T. (2017), “Multi-disciplinary optimization in aeronautical engineering”, *Proceedings of the Institution of Mechanical Engineers Part G: Journal of Aerospace Engineering*, Vol. 231 No. 12, pp. 2305–2313.
- Goetzendorf-Grabowski, T., Mieloszyk, J. and Mieszalski, D. (2012), “MADO – software package for high order multidisciplinary aircraft design and optimization”, *Proceedings of 28th International Congress of the Aeronautical Sciences, Brisbane*, pp. 481–490.
- Julien, M. (2016), “Airbus presents 3D-printed mini aircraft”, available at: <https://phys.org/news/2016-06-airbus-3d-printed-mini-aircraft.html> (accessed 6 July 2018).
- Kennedy, J. and Eberhart, R. (1995), “Particle swarm optimization”, *Proceedings of the IEEE International Conference on Neural Networks, Perth*, pp. 1942–1945.
- Mieloszyk, J., Tarnowski, A., Kowalik, M., Perz, R. and Rządkowski, W. (2018), “Preliminary design of 3D printed fittings for UAV”, *Aircraft Engineering and Aerospace Technology*, doi: 10.1108/AEAT-07-2018-0182.
- Prosser, D. (2017), “Airfoil optimization with Xfoil”, available at: <https://sourceforge.net/projects/xoptfoil> (accessed 6 July 2018).
- Stratasys (2018), “3D printing aircraft interiors”, available at: www.stratasysdirect.com/industries/aerospace/3d-printing-aircraft-interiors (accessed 30 September 2018).
- Szczesniak, R., Kowalik, M., Cader, M. and Pyrzanowski, P. (2018), “Parametric numerical model for predicting mechanical properties of structures made with FDM technology from polymeric materials”, *Polimery*, Vol. 63 No. 9, pp. 952–958, doi: 10.14314/polimery.2018.9.7.

Corresponding author

Igor Skawiński can be contacted at: igorskawinski@gmail.com

Identification of a degradation of aerodynamic characteristics of a paraglider due to its flexibility from flight test

Robert Kulháněk

Department of Aerodynamics Vyzkumny a Zkusebni Letecky Ustav, Prague, Czech Republic

Abstract

Purpose – Aerodynamics of paragliders is very complicated aeroelastic phenomena. The purpose of this work is to quantify the amount of aerodynamic drag related to the flexible nature of a paraglider wing.

Design/methodology/approach – The laboratory testing on scaled models can be very difficult because of problems in the elastic similitude of such a structure. Testing of full-scale models in a large facility with a large full-scale test section is very expensive. The degradation of aerodynamic characteristics is evaluated from flight tests of the paraglider speed polar. All aspects of the identification such as pilot and suspension lines drag and aerodynamics of spanwise chambered wings are discussed. The drag of a pilot in a harness was estimated by means of wind tunnel testing, computational fluid dynamics (CFD) solver was used to estimating smooth wing lift and drag characteristics.

Findings – The drag related to the flexible nature of the modern paraglider wing is within the range of 4-30 per cent of the total aerodynamic drag depending on the flight speed. From the results, it is evident that considering only the cell opening effect is sufficient at a low-speed flight. The stagnation point moves forwards towards the nose during the high speed flight. This causes more pronounced deformation of the leading edge and thus increased drag.

Practical implications – This paper deals with a detailed analysis of specific paraglider wing. Although the results are limited to the specific geometry, the findings help in the better understanding of the paraglider aerodynamics generally.

Originality/value – The data obtained in this paper are not affected by any scaling problems. There are only few experimental results in the field of paragliders on scaled models. Those results were made on simplified models at very low Reynolds number. The aerodynamic drag characteristics of the pilot in the harness with variable angles of incidence and Reynolds numbers have not yet been published.

Keywords Aerodynamic drag, Aerodynamic, Flight testing, Paraglider, Speed polar

Paper type Research paper

Nomenclature

S [m²] = Reference area;
 CL [1] = Lift coefficient = Lift/ qS ;
 Cl [1] = Section lift coefficient;
 CD [1] = Drag coefficient = Drag/ qS ;
 G [N] = Weight;
 q [Pa] = Dynamic pressure = $\frac{1}{2} \rho V \infty^2$;
 U [1] = Velocity unit vector;
 V [ms⁻¹] = Velocity; and
 k/d [1] = relative roughness (absolute roughness/line diameter).

Symbols

Γ [m²s⁻¹] = Circulation;
 θ [rad] = Glide angle;
 ρ [kgm⁻³] = Density; and
 λ [1] = Aspect ratio.

Subscripts

∞ = Related to infinity;
 $2D$ = CD related to wing section;
 w = CD related to wing;
 p = CD related to pilot and harness;
 f = CD related to flexibility of wing; and
 l = CD related to suspension.

Definitions, Acronyms and Abbreviations

NLLT = Nonlinear lifting line theory; and
VZLÚ = Czech Aerospace Research Centre.

Introduction

Paragliders are similar to ram air parachutes, at first sight, but they are intended more for flying instead of as a decelerator. Paragliders have a greater glide ratio (up to 12) and speed range (up to 70 kph) compared to parachutes. A number of cells of a modern paraglider can exceed 100 and suspension lines of

The current issue and full text archive of this journal is available on Emerald Insight at: www.emeraldinsight.com/1748-8842.htm



Aircraft Engineering and Aerospace Technology
91/6 (2019) 873–879
© Emerald Publishing Limited [ISSN 1748-8842]
[DOI 10.1108/AEAT-06-2018-0162]

This work was realized, thanks to the grant of the Ministry of Education, Youth and Sports of the Czech Republic nr. SGS16/070/OHK2/1T/12.

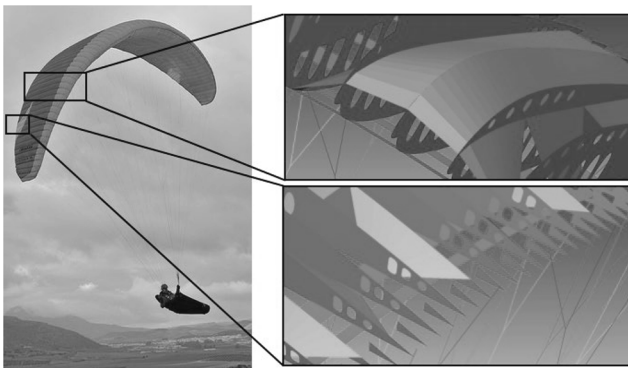
Received 8 June 2018
Revised 3 August 2018
Accepted 4 September 2018

paragliders are much thinner (less than 1 mm). Paragliders have no rigid structure and thus their shape is formed during a flight. Thus, any performance predictions can be very challenging. Typical paraglider and its inner structure can be seen in Figure 1. The ribs and the diagonal reinforcements from the front view are shown in the top right part. The trailing edge structure can be seen in the bottom part of the figure. Paragliders are filled by air through a cell opening. The cell openings are located on a pressure side of a wing very close to the leading edge.

Many experimental and theoretical results applicable to the ram air parachutes were published by various authors. For example, Lingard (1995) published the study about the aerodynamic design of modern parachutes. Geiger and Wailes (1990) performed full-scale wind tunnel testing of parachutes at different dynamic pressures. Matos *et al.* (1998) described the effect of the leading edge deformations while an angle of attack decreases at higher flight speed. Those experiments were made on the parachute wings with a very low aspect ratio (up to 3). Those results cannot be applied to an analysis of modern paraglider wings because parachutes have much larger cell opening, lower number of cells, much thicker suspension lines, much lower aspect ratio, etc.

A few experimental results related to the paraglider cell deformation can be found in the literature. An inflated cell shape and its inner pressure was measured by Uddin and Mashud (2010). Becker (2017) tested a flexible paraglider airfoil model to investigate its aerodynamic characteristics. Similar experiments on a series of flexible wing models were performed by Pohl (2011). He studied the effect of cell opening shapes and cells aspect ratio on the aerodynamic characteristics of paraglider wing sections. The experiments performed by Pohl are very valuable because they compared the flexible airfoil with the rigid one. The past three cited experiments were performed at very small Reynolds numbers on scaled models. Hanke and Schenk (2014) evaluated the flight shape of a full-scale paraglider wing using stereo-cameras. They evaluated only outer outlines, not the local deformation such as wrinkling. Boffadossi and Savorgnan (2015) performed the numerical and experimental study of a paraglider airfoil with the aim to optimize an airfoil inlet. A rigid model of an airfoil was used in their experiment. A pure numerical approach of authors Mittal *et al.* (2001), Mohammadi and Johari (2009) or

Figure 1 Typical paraglider with its inner structure (Credit: Axis Paragliders)



Ross (1993) does not include the effects of the paraglider flexibility in their studies. Their results are more focussed on parachute airfoils. Belloc *et al.* (2016) performed a computational study of a 2D pSaraglider airfoil with many combinations of cell openings to investigate the influence of their position and width. Babinsky (1999) published the extensive study of paraglider aerodynamics. His work consists of force, pressure distribution and deformation measurements on scaled flexible models in a low-speed wind tunnel.

The overall performance of paragliders depends on not only the aerodynamic characteristics of their wing. The suspension lines contribute to the overall drag significantly (up to 20 per cent). The pilot in the harness contributes to the overall drag in an amount similar to the suspension lines. Many types of paragliding harnesses exist. Some of them are partially covered to reduce drag. Virgílio (2004) published the drag coefficients (Drag/qS) of common types of paragliding harnesses. The aim of this paper is to identify the increment of the drag of a modern paraglider from flight test experiments.

Aerodynamics of the paraglider

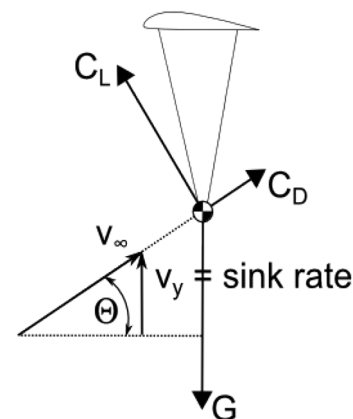
The model assumes a steady straightforward gliding flight with the following equilibrium in lift and drag directions, this situation can be seen in Figure 2.

$$C_{Lw}qS - G\cos\theta = 0 \quad (1)$$

$$\tan\theta = \frac{C_D}{C_{Lw}} = \frac{C_{Dw} + C_{Dp} + C_{Dl} + C_{Df}}{C_{Lw}} \quad (2)$$

Equations (1) and (2) are written in the aerodynamic axis system. The speed polar relates the glide angle θ to the airspeed V_∞ , as is illustrated in Figure 2. It is assumed that the lines and the pilot do not contribute to the overall lift. The line and pilot drag in equation (2) are denoted as C_{Dl} and C_{Dp} , respectively. The C_{Dw} stands for the drag coefficient of the smooth wing. The wing drag C_{Dw} can be directly assigned from the computed aerodynamic polar of the wing for known lift coefficient (Lift/qS) (C_{Lw}). The C_{Df} coefficient takes into account all the effects related to the flexible nature of the wing such as deformation of the leading edge, cell opening, skin

Figure 2 Equilibrium during gliding flight



wrinkling, airfoil and trailing edge thickening, etc. Those factors are the most unknown in the paraglider aerodynamics.

For the known value of the Θ , q and G , the wing Lift/ qS at each point of the speed polar can be easily computed. The estimation of the Drag/ qS of the lines, pilot and a smooth wing is discussed in the following sections.

Flight testing

The flight test data were acquired during many glide test flights. The well-known method “altimeter vs time” published by Johnson (1989) was used for speed polar measurements. The flight speed was measured with towed pitot-static tube, and the sink rate was evaluated from the change of an atmospheric pressure. The measured altitude change is the pressure altitude as defined by ICAO (2002) corrected to the non-standard temperature lapse rate. The flight tests were performed in temperature inversion conditions to minimize the effects of thermal convection on a steady flight. It was assumed that the measured temperature is the static air temperature because of the flight speed of the paraglider is slow (20 m/s maximum) and thus the ram rise is negligible. The effects of humidity in the atmosphere were not taken into account during the measurements. According to Guinn and Barry (2016), this can cause the error in glide angle up to 2 per cent maximally for the conditions during the testing.

Test case details

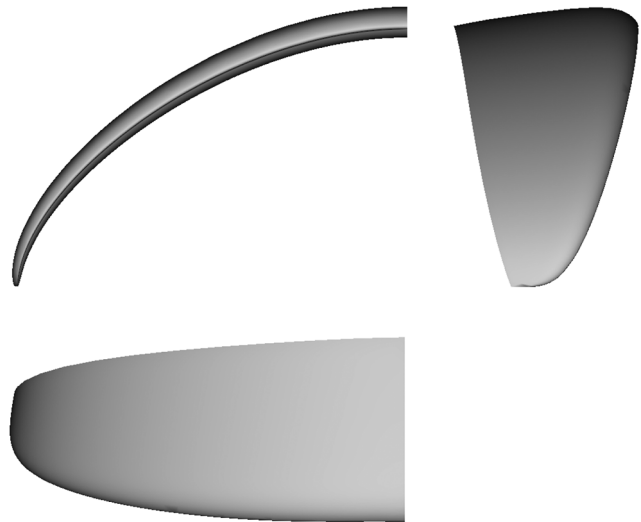
The tested paraglider is a high-performance model with the flat aspect ratio of 6.6 and the projected aspect ratio of 4.7. The wing consists of 66 cells. The diameter of the suspension lines ranges from 0.6 to 2 mm, an overall length of 250 m and the frontal area measuring 0.257 m². The three-component view of the smooth wing is visualized in Chyba! Nenalezen zdroj odkazů. The wing is equipped with turbulent airfoil with the maximum thickness of 17 per cent located at 23 per cent of the chord and maximum camber of 2 per cent located at 19 per cent of the chord. The wing has no aerodynamic or geometrical twist (Figure 3).

Aerodynamic characteristic of wings with spanwise camber (C_{Lw} , C_{Dw})

Paragliders are wings with high anhedral and relatively high aspect ratio. The numerical lifting line theory (NLLT) is a suitable model for fast analysis of this kind of a wing. The NLLT formulation of Phillips and Snyder (2000) was used in this study. The theory was tested on the appropriate experimental data at the first stage. Belloc (2015) tested a model of the rigid, smooth spanwise cambered wing in the low-speed wind tunnel. The Belloc reference wing with the flat aspect ratio of 6.35 was equipped with NACA 23015 airfoil. The ratio of the projected span to the arc height was 3.66. It represents the geometry of a modern paraglider very well. The NLLT algorithm requires a 2D airfoil data as input. All necessary airfoil characteristics were computed with the CFD solver OpenFOAM with assumption 2D incompressible turbulent flow (Spalart–Allmaras turbulence model).

The NLLT solves the circulation (Γ) distribution on the spatially curved lifting line of a wing. In general, the wing is discretized into a system of N horseshoe vortices. The

Figure 3 Three component view of the smooth wing



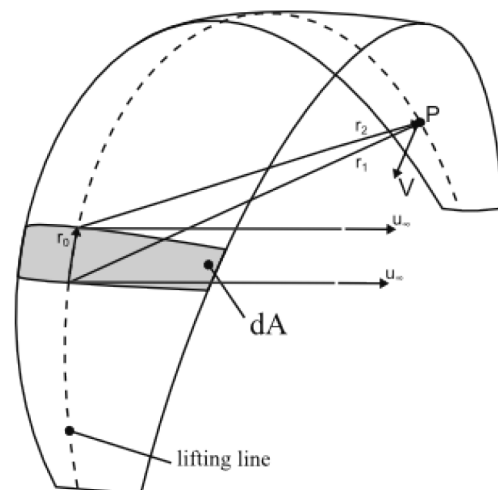
Notes: Front view – Upper left; Side view – Upper right; Top view – Lower left

equilibrium of forces on the bound part of the lifting line is described by equation (3). The local velocity (\vec{V}) is the sum of the freestream velocity and the total induced velocity by all vortices in the system as it is defined in equation (4). Induced velocity from one vortex is calculated by means of equation (5). The system of nonlinear equations (3)–(5) can be used to calculate the lift and drag of the spatially curved wing. The equations are evaluated in the midpoint of r_0 vector (Figure 4).

$$\frac{1}{2} \rho v_{\infty}^2 C_l dA = \Gamma \rho \left| \vec{V} \times \vec{dl} \right| \quad (3)$$

$$\vec{V} = \vec{V}_{\infty} + \sum_N \vec{V}_{ind} \quad (4)$$

Figure 4 Horseshoe vortex notation



$$\vec{V}_{ind} = \frac{\Gamma}{4\pi} \left[\frac{\vec{u}_{\infty} \times \vec{r}_2}{r_2(r_2 - \vec{u}_{\infty} \cdot \vec{r}_2)} + \frac{(r_1 + r_2)(\vec{r}_1 \times \vec{r}_2)}{r_1 r_2 (r_1 r_2 - \vec{r}_1 \cdot \vec{r}_2)} - \frac{\vec{u}_{\infty} \times \vec{r}_1}{r_1(r_1 - \vec{u}_{\infty} \cdot \vec{r}_1)} \right] \quad (5)$$

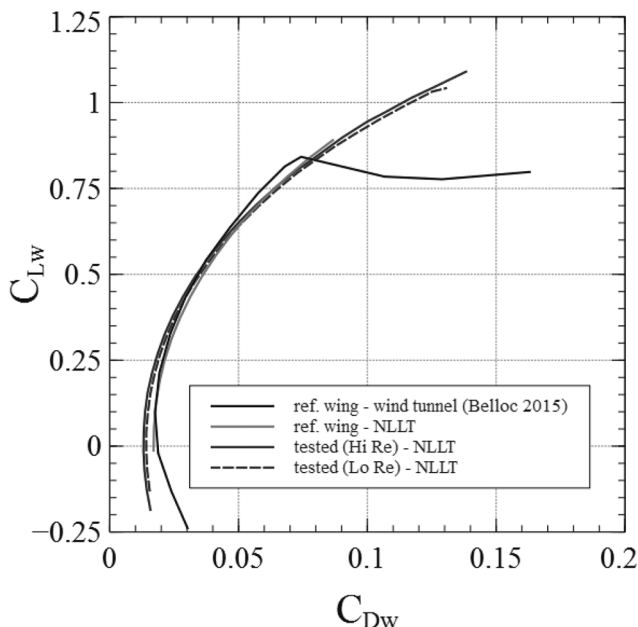
The comparison of the experimental and the numerical results is shown in Figure 5. The match of the results is evident, especially in the region of lower wing Lift/qS ($C_{Lw} < 0.6$). The induced drag can make up to 50 per cent of the overall drag in a slow-speed flight close to the maximal value of L/D and about 10 per cent in the high-speed flight. Therefore, the induced drag is a very important part, and thus, the span efficiency factors were compared. The λe factor is defined in equation (6). The derivative in the denominator was deduced from the linear part of $C_D = f(C_{Lw}^2)$ functions.

$$\lambda e = \frac{1}{\pi} \frac{dC_{Lw}^2}{dC_{Dw}} \quad (6)$$

The λe from the Belloc (2015) data is 4.1 and that from the NLLT computation is 4.0; thus, the difference is less than 3 per cent. Babinsky (1999) assumed traditional induced drag formulas for elliptically loaded wings derived from classical Prandtl lifting line theory with span efficiency $e = 1$. The tested paraglider has the span efficiency factor $e \approx 0.85$ according to the NLLT.

The blue lines in Figure 5 are the aerodynamic polars of the tested wings for the flight test Reynolds numbers (related to the mean aerodynamic chord). It has changed from 1.5 to 2.5 million during the flight test. The C_{Dw} in equation (2) was interpolated from those blue lines.

Figure 5 Aerodynamic polar of the wings



Note: NLLT stands for the result were obtained with numerical lifting line theory

Suspension lines

Suspension lines (C_{Dl}) create up to 20 per cent of the overall drag of a paraglider. The lines are made from Vectran and Dyneema materials. The total length of the lines of the evaluated paraglider is 250 m with diameters from 0.6 to 2 mm. The lines are not perfectly smooth; a relative roughness (k/d) of the lines is within the range 0.05–0.12. Figure 6, taken from Hoerner (1965), shows us the well-known Drag/qS of circular cylinders with the effect of roughness as a function of Reynolds number (related to cylinder diameter). The regime is subcritical even if we encounter the roughness effect, so the $C_D = 1$ for the individual line is convenient. The Drag/qS of the complete line set of the tested wing is $C_{Dl} = 0.98$ with the reference area equal to 0.257 m^2 . The influence of the inclined flow to the lines was evaluated as negligible.

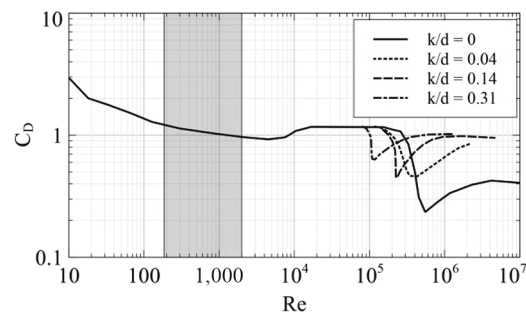
Harness and pilot

The drag contribution of a pilot in a harness (C_{Dp}) is a very important part of the paraglider performance. Virgilio (2004) published the measurement of basic types of paragliding harnesses available on the market. His study covers the open harness for beginners as well as the covered harnesses for competition pilots. The study was performed in only one Reynolds number and one angle of attack.

Aerodynamics characteristics of the paraglider harness with variable Reynolds number and angle of incidence was measured to increase the accuracy of the identification from the flight test. The test setup of the author in the harness in the low-speed atmospheric wind tunnel at VZLÚ (3mLSWT) can be seen in Figure 7. The four force transducers were attached to the wires (blue lines in Figure 7). The results were corrected to the support effects and blockage effect with methods published in AGARD (1998). The business name of the tested harness is Advance Lightness 2. From the results, the black lines plotted in Figure 7 show us the measured Drag/qS of the pilot in the harness with variable Reynolds numbers and angles of attack.

We assumed that the Drag/qS depends on the angle of incidence and Reynolds number linearly. The aerodynamic

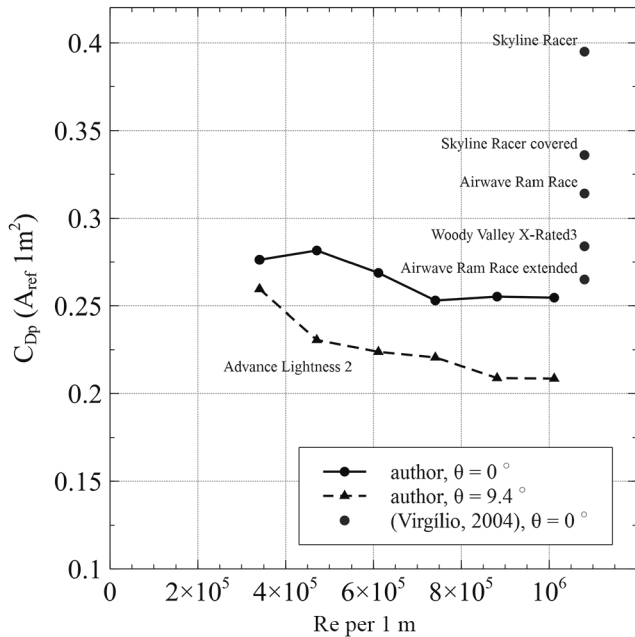
Figure 6 The Drag/qS of the smooth and rough cylinder



Note: Local Re of the lines during the flight test is marked with the red strip

Source: Adapted from Hoerner (1965)

Figure 7 Drag/ qS of the pilot in the harness



model of the paraglider pilot in harness is defined by equation (7).

$$C_{Dp} = C_{Dp0,0} + \frac{\partial C_{Dp}}{\partial \theta} \theta + \frac{\partial C_{Dp}}{\partial Re} Re \quad (7)$$

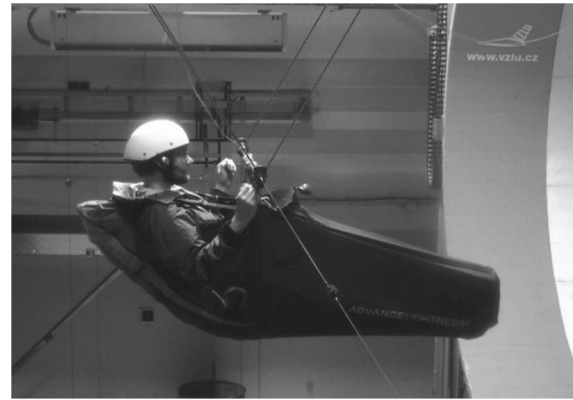
The $C_{Dp0,0}$ is the Drag/ qS of the pilot in the harness at zero θ and Re . The remaining terms are derivatives of the Drag/ qS with respect to the angle of attack and Reynolds number. For the tested harness, the coefficients and the derivatives are as follows: $C_{Dp0,0} = 2.94e^{-1}$, $\partial C_{Dp}/\partial \theta = -2.23e^{-1}$ and $\partial C_{Dp}/\partial Re = 4.84e^{-8}$ with the overall uncertainty of predicted C_{Dp} equal to $3.24e^{-2}$. The area used as the reference for the Drag/ qS of the harness with a pilot is 1 m^2 . The derivatives $\partial C_{Dp}/\partial \theta$ and $\partial C_{Dp}/\partial Re$ are valid in only reasonable limits of the angle of attack and Re , respectively (Figure 8).

Degradation of the aerodynamic characteristics due to flexibility (C_{Df})

The C_{Df} is defined as the increment in the profile Drag/ qS of a flexible wing with cell opening with respect to the theoretically smooth wing with surface created from the rib profiles. It is assumed that the wing flexibility does not influence the wing-induced drag. This assumption can be supported by the results of Babinsky (1999) and Pohl (2011), where they report no significant change in the lift curve slope of the flexible airfoils in the region of lower C_L (< 0.8). This leads to the same lift distribution at specified wing C_L . Thus, it leads to the identical induced drag.

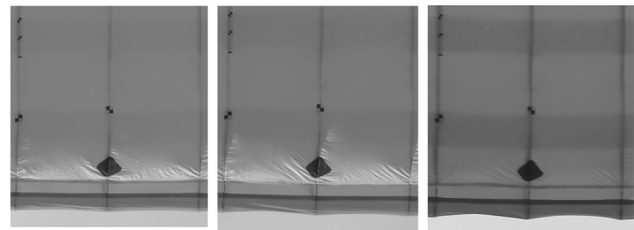
The photographs of the leading edge details during the flight at different speeds are shown in Figure 9. The

Figure 8 Test setup at 3mLSWT



Note: Author, $\theta = 0^\circ$

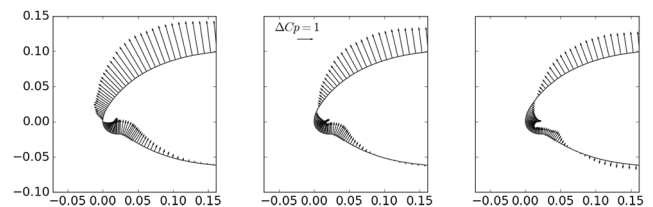
Figure 9 Deformation of the paraglider leading edge of the two central cells during flight at different speed



Note: From the left to the right $V_\infty \approx 10, 12, 14.5 \text{ m/s}$

deflection is caused by the increase in the dynamic pressure and the shift of the position of the stagnation point. The position of the stagnation point is visualized in Figure 10. The arrows denote the difference between the pressure coefficient inside the airfoil and the pressure coefficient on the theoretical airfoil surface. The pressure coefficient inside is taken as the average pressure in the position of the cell opening, thus it is assumed to be constant at specific flight condition. This approach was experimentally verified by Boffadossi and Savorgnan (2015). The deflection of the leading edge is about 10 mm at

Figure 10 ΔC_p computed using Xfoil



Notes: From left to right corresponds to the $V_\infty \approx 10, 12, 14.5$ and local $CL = 0.41, 0.61, 0.88$ (It represents conditions in symmetry plane of the wing). The short red line marks the cell opening. The airfoil surface is represented by the blue line

the maximum speed of the tested paraglider. The deflection of the leading edge is not the only one mode of a cell deformation. Wrinkles and cell contraction are also present. The cell contraction is about 5 mm (2 per cent of its width) at maximum speed.

The aerodynamic polars of all drag components are shown in Figure 11. The flexibility effect C_{Df} (denoted by the gray area) is more pronounced with the increase of the flight speed (reduction of the wing Lift/qS). This behavior is in agreement with the shift of the stagnation point toward the nose. The drag increment is about 4 per cent at slow speed to 30 per cent at high speed of the paraglider total drag.

As Figure 12 indicates, the C_{Df} grows linearly with respect to the airspeed. The error bars of the evaluated C_{Df} from the flight test represent the influence of an uncertainty in glide measurement about 1L/D point and 10 per cent of speed measurement. It covers the uncertainty of flight tests conservatively. The constant dash-dotted line is the cell opening effect measured by Boffadossi and Savorgnan (2015). Their experiment was performed on a rigid model of an airfoil with a cell opening size of 3.8 per cent of the chord. The tested paraglider has the cell opening with size about 2 per cent of the wing local cord. The identified C_{Df} is very close to the rigid airfoil results with the cell opening at low speed where the minimal deformations occur. The cell opening drag increment found by Babinsky (1999) is very close to the results of Boffadossi and Savorgnan (2015). Babinsky proposed that the drag increment due to the cell opening is a function of the opening size relative to the cord (h/c).

Pohl (2011) predicted the aerodynamic degradation of paraglider airfoils as a function of the cell aspect ratio (λ_c , the ratio of the cell cord to its width) and the profile drag of rigid smooth wing (C_{D2D}). His method is defined by equation (8), and the result is plotted as the dashed line in Figure 12.

Figure 11 Aerodynamic polar of each aspect of the aerodynamic drag of tested paraglider

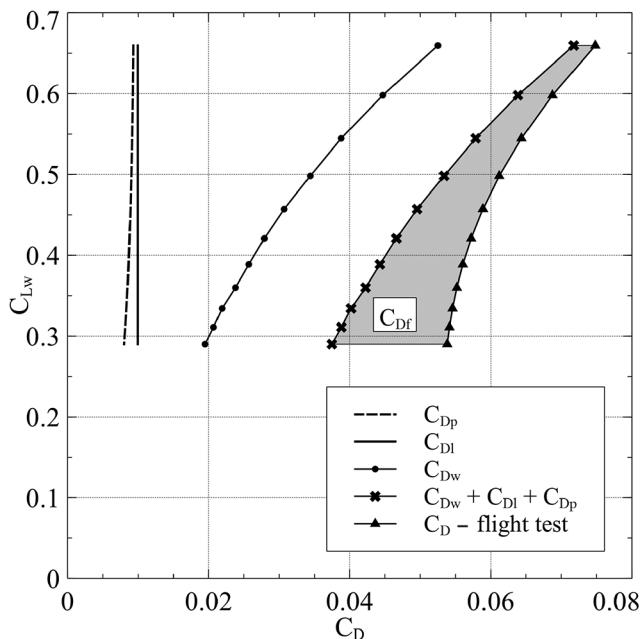
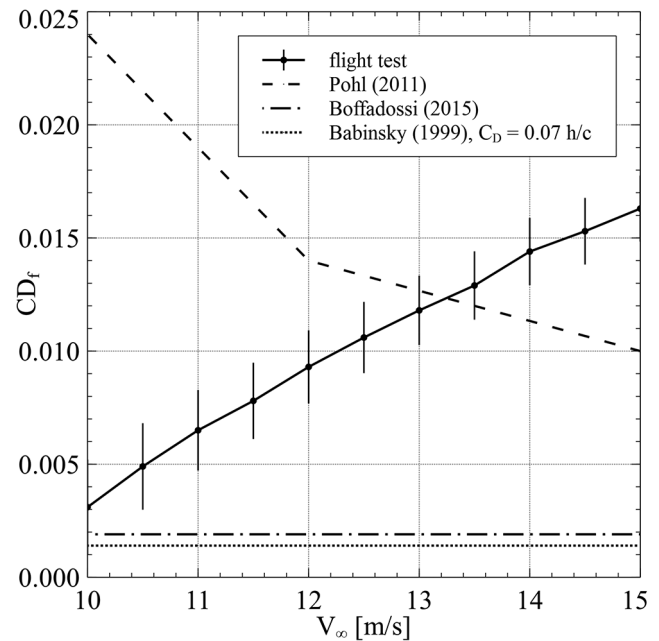


Figure 12 Effect of the flexibility on the Drag/qS during the flight

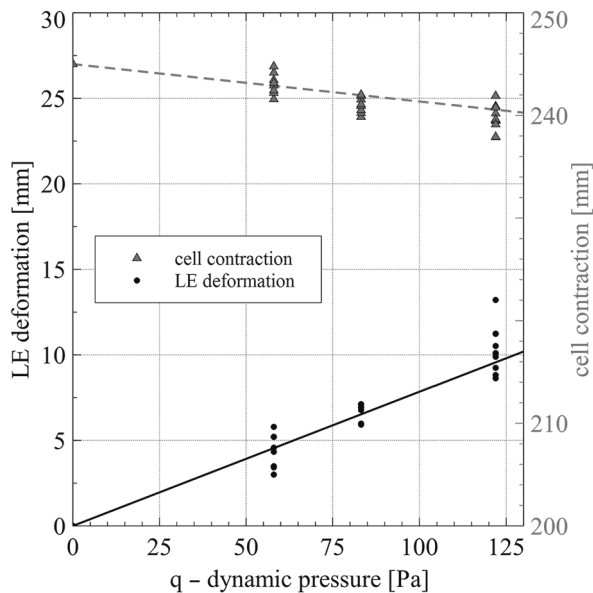


$$C_{Df} = C_{D2D} 4.45 \frac{1}{\lambda_c} \quad (8)$$

From the results, it is evident that considering only the cell opening effect is sufficient in the range of the low-speed flight. The Pohl (2011) method assumes that the C_{Df} depends on only the cell aspect ratio and the section drag of undeformed wing. The section Drag/qS (C_{D2D}) decreases with increasing flight speed because of the increasing Reynolds number. This can explain the difference in trend between Pohl's and flight test results in Figure 12. Babinsky (1999) analyzed paraglider aerodynamics by means of results of wind tunnel testing and theoretical calculations. According to his study, the profile drag ($C_{D2D} + C_{Df}$) increases with flight speed linearly from 38 per cent of overall drag at 10 m/s to the 43 per cent at 15 m/s. The profile drag of the tested paraglider in the present study has a more pronounced change with respect to the flight speed. It rises from 26 per cent to 53 per cent in the identical speed range.

Conclusions

The drag increment caused by the flexibility of the typical paraglider wing was discussed and identified from flight measurements. The greatest advantages of the flight measurements are the possibility to avoid the problems related to maintaining an elastic similitude of scaled models and that the realistic Reynolds number is automatically achieved. On the other hand, a flight test environment is not as friendly as a laboratory one. Even with considering very conservative sources of errors during the flight testing, the trend of the flexibility effect on the airfoil drag is different from the laboratory results of Pohl, as can be seen in Figure 12 (Figure 13). The flight test results include the effect of the stagnation point shift and the Reynolds number change during the flight. The stagnation point moves forward to the nose direction and causes more pronounced deformation of the leading edge, as can be seen in Figures 9 and 10. This effect

Figure 13 Leading-edge deformation and cell contraction during flight

Note: Results are taken from the photographs of two central cells

was not quantified in other studies related to paragliders. The present study shows that the effects related to the flexible nature of paraglider wings are an integral part of paraglider aerodynamics and give the values of the aerodynamic drag degradation of the modern paraglider.

References

- Babinsky, H. (1999), “The aerodynamic performance of paragliders”, *The Aeronautical Journal*, Vol. 103 No. 1027, pp. 421-428.
- Becker, S. (2017), *Experimental Study of Paraglider Aerodynamics*, Master of Science Thesis, Imperial College London.
- Belloc, H. (2015), “Wind tunnel investigation of a rigid paraglider reference wing”, in *Journal of Aircraft*, Vol. 52 No. 2, pp. 703-708.
- Belloc, H., Chapin, V., Manara, F., Sgarbossa, F. and Meyer, F., A. (2016), “Influence of the air inlet configuration on the performances of a paraglider open airfoil”, in *International Journal of Aerodynamics*, Vol. 5 No. 2.
- Boffadossi, S. and Savorgnan, F. (2015), “Analysis on aerodynamic characteristics of a paraglider airfoil”, in *Aerotecnica Missili & Spazio*, Vol. 95 No. 4, pp. 211-218.
- Geiger, R.H. and Wailes, W.K. (1990), “Advanced recovery systems wind tunnel test report”, *Nasa-CR-177563*, Washington, DC.
- Guinn, T.A. and Barry, R.J. (2016), “Quantifying the effects of humidity on density altitude calculations for professional aviation education”, in *international journal of aviation, Aeronautics, and Aerospace*, Vol. 3, available at: <https://doi.org/10.15394/ijaaa.2016.1124>
- Hanke, K. and Schenk, S. (2014), “Evaluating the geometric shape of a flying paraglider, in the international archives of photogrammetry”, *Remote Sensing and Spatial Information Sciences*, Vol. 40 No. 5, p. 265.
- Hoerner, S.F. (1965), “Fluid-dynamic drag: practical information on aerodynamic drag and hydrodynamic resistance”, *Hoerner Fluid Dynamics*, Brick Town, NJ.
- ICAO (2002), *Manual of the ICAO Standard Atmosphere Extended to 80 Kilometers (262 500 Feet)*, 3rd ed. Montreal. ISBN 9291940046.
- Johnson, R.H. (1989), “Sailplane Performance Flight Test Methods”, in *Soaring Magazine*, Soaring Society of America.
- Lingard, J.S. (1995), “Ram-Air parachute design”, presented in *13th AIAA Aerodynamic Decelerator Systems Technology Conference, Clearwater Beach*.
- Matos, C., Mahalingam, R., Ottinger, G., Klapper, J., Funk, R. and Komerath, N. (1998), “Wind tunnel measurements of parafoil geometry and aerodynamics”, in *AIAA Paper*, pp. Vol. 606.
- Mittal, S., Saxena, P. and Singh, A. (2001), “Computation of two-dimensional flows past ram-air parachutes”, *International Journal for Numerical Methods in Fluids*, Vol. 35 No. 6, pp. 643-667.
- Mohammadi, A. and Johari, H. (2009), “Computation of flow over a high performance parafoil”, in *20th AIAA Aerodynamic Decelerator Systems Technology Conference and Seminar*, p. 2979.
- Phillips, W.F. and Snyder, D.O. (2000), “Modern adaptation of prandtl’s classic lifting-line theory”, in *Journal of Aircraft*, Vol. 37 No. 4, pp. 662-670.
- Pohl, L. (2011), *Aerodynamic Research of the Airfoils for the Paragliders*, Doctoral dissertation, Czech Technical University in Prague.
- Ross, J.C. (1993), “Computational aerodynamics in the design and analysis of Ram-Air-Inflated wings”, in *AIAA Paper*, Vol. 1228, pp. 10-13.
- Uddin, M.N. and Mashud, M. (2010), “Wind tunnel test of a paraglider (flexible) wing canopy”, in *International Journal of Mechatronics Engineering IJMME-IJENS*, Vol. 10 No. 3, pp. 7-13.
- Virgilio, N.F.E. (2004), “Estudo da eficiência aerodinâmica de equipamento de voo livre”.

Further reading

- Burk, S.M., Jr and Ware, G.M. (1967), “Static aerodynamic characteristics of three ram-air-inflated low aspect ratio fabric wings”, *Nasa TN D-4182*, Washington, DC.
- Krynitzky, A., Ewald, B. and Voß, R. (1998), *AGARD-AG-336. Technical report, NATO Research and Technology Organisation, AGARD-AG Neuilly-sur-Seine Cedex, France*.

Corresponding author

Robert Kulhánek can be contacted at: kulhanek@vzlu.cz

For instructions on how to order reprints of this article, please visit our website:

www.emeraldgroupublishing.com/licensing/reprints.htm

Or contact us for further details: permissions@emeraldinsight.com

An automatic system for a helicopter autopilot performance evaluation

Antoni Kopyt, Sebastian Topczewski, Marcin Zugaj and Przemysław Bibik

Department of Automation and Aeronautical Systems, Warsaw University of Technology, Warsaw, Poland

Abstract

Purpose – The purpose of this paper is to elaborate and develop an automatic system for automatic flight control system (AFCS) performance evaluation. Consequently, the developed AFCS algorithm is implemented and tested in a virtual environment on one of the mission task elements (MTEs) described in Aeronautical Design Standard 33 (ADS-33) performance specification.

Design/methodology/approach – Control algorithm is based on the Linear Quadratic Regulator (LQR) which is adopted to work as a controller in this case. Developed controller allows for automatic flight of the helicopter via desired three-dimensional trajectory by calculating iteratively deviations between desired and actual helicopter position and multiplying it by gains obtained from the LQR methodology. For the AFCS algorithm validation, the objective data analysis is done based on specified task accomplishment requirements, reference trajectory and actual flight parameters.

Findings – In the paper, a description of an automatic flight control algorithm for small helicopter and its evaluation methodology is presented. Necessary information about helicopter dynamic model is included. The test and algorithm analysis are performed on a slalom maneuver, on which the handling qualities are calculated.

Practical implications – Developed automatic flight control algorithm can be adapted and used in autopilot for a small helicopter. Methodology of evaluation of an AFCS performance can be used in different applications and cases.

Originality/value – In the paper, an automatic flight control algorithm for small helicopter and solution for the validation of developed AFCS algorithms are presented.

Keywords Aeronautical design standard, Automatic flight control system, Helicopter dynamic model, Linear quadratic regulator, Mission task elements

Paper type Research paper

Introduction

The paper presents selected goals achieved in the HELIMARIS project (“Modification of an optionally piloted helicopter for maritime mission performance”) led by PZL Świdnik in cooperation with Warsaw University of Technology. The project is devoted to the development of additional features allowing maritime operations of a light, single-engine helicopter with introducing high level of automatization. In this paper, the authors focused on aspects of development and evaluation of an automatic flight control system (AFCS) algorithm for the specified type of helicopter.

For the automatic control algorithm design, a linear quadratic regulator (LQR) is used. LQR is an optimal regulator which acts as a controller in proposed approach, minimizing the values of a cost function – differences between desired and actual state variables values of the controlled object dynamic model. For the proper and satisfactory operation of the LQR, an accurate linear model of the controlled object dynamics is required. Here, the linear model was derived from reliable nonlinear helicopter model developed in the FLIGHTLAB

environment. The model was validated using flight test data. In the next step, evaluation procedure of the developed AFCS algorithms was selected and applied. In the final step, test case was established and evaluated. For the test case, a slalom flight maneuver was chosen. The maneuver was selected from the Aeronautical Design Standard 33 (Anonymous, 1994), a document that contains the requirements for the flying and ground handling qualities for various types of rotorcrafts.

Helicopter dynamic model

Comprehensiveness of modeling the helicopter dynamics depends on the purpose to which the model will be used (Padfield, 2008). For the project, a single turboshaft engine, classical configuration helicopter model is developed in Flightlab software. All elements of the helicopter, except the undercarriage, are modeled as rigid. The main and tail rotors are modeled in a similar way, using blade element approach

The research was conducted as part of the INNOLOT sector project (acronym HELIMARIS) entitled “Modification of an optionally piloted helicopter to maritime mission performance” coordinated by Wytwórnia Sprzętu Komunikacyjnego “PZL-Świdnik” Spółka Akcyjna, co-financed by the National Center for Research and Development under the Smart Growth Operational Program 2014-2020, 1. Priority Axis, Support for R&D activity of Enterprises; Action 1.2, Agreement No. POIR.01.02.00-00.0004/15.

Received 12 July 2018
Revised 19 September 2018
4 October 2018
Accepted 4 November 2018

The current issue and full text archive of this journal is available on Emerald Insight at: www.emeraldinsight.com/1748-8842.htm



Aircraft Engineering and Aerospace Technology
91/6 (2019) 880–885
© Emerald Publishing Limited [ISSN 1748-8842]
[DOI 10.1108/AEAT-07-2018-0190]

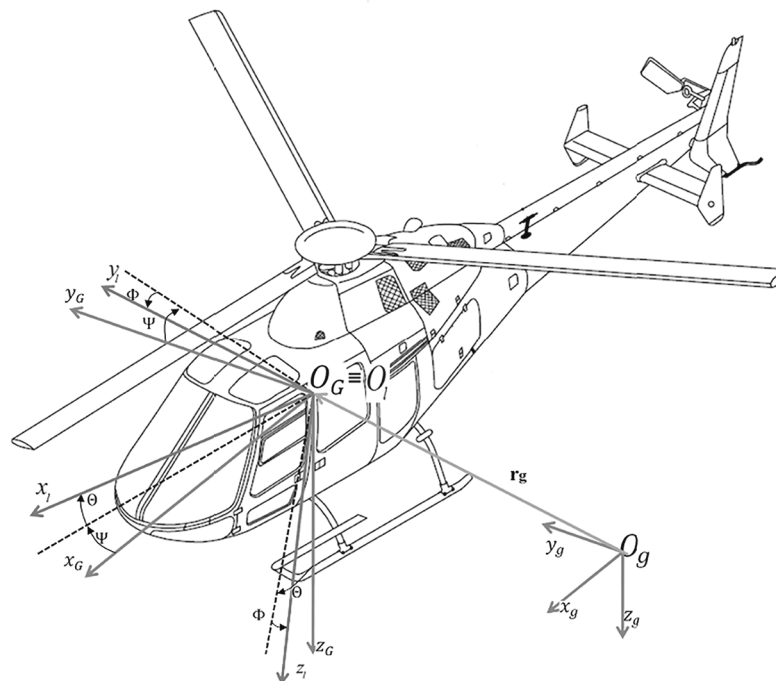
with flapping dynamics included. The main rotor is a three-bladed, articulated rotor; the tail rotor is a see-saw rotor. The aerodynamic model selected is a nonlinear unsteady one with stall delay, and Peters-He 6 state-induced velocity model with an empirical ground effect model. The interactions between rotors and fuselage are also included. The airframe model includes fuselage, empennage, sensors and a landing gear. The aerodynamic loads of the fuselage and empennage are modeled using empirical look-up tables. The engine model is based on Flightlab turboshaft engine model with detailed model of its dynamics and control systems.

The selected helicopter model control system does not include any stability augmentation system – there are only hydraulic boosters placed in the control lines between pilot sticks and the swashplate. The helicopter numerical model is validated using flight test data delivered by the helicopters' manufacturer. The validation covers both steady flight and dynamic response cases. Helicopter coordinate systems are presented in Figure 1.

As typical three, Cartesian, right-handed systems of coordinates were used:

- 1 Inertial, stationary system of coordinates $O_g x_g y_g z_g$, with the origin O_g located at an arbitrary point on the earth surface, the direction of the $O_g z_g$ axis is coincident with the orientation and sense of the earth acceleration vector, the $O_g x_g y_g$ plane is tangent to the earth surface, the $O_g x_g$ axis is directed toward the North with the $O_g y_g$ axis completing the right-hand system directed East.
- 2 Gravitational coordinate system $O_G x_G y_G z_G$ is fixed to the vehicle, with the system's origin O_G located at the helicopter arbitrary point. This coordinate system is translated in parallel, relative to the $O_g x_g y_g z_g$ inertial system, and senses of both systems' axes are matching.

Figure 1 Helicopter systems of coordinates



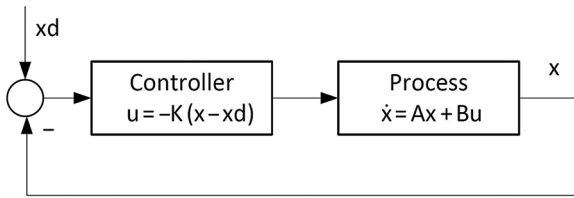
- 3 Body coordinate $O_1 x_1 y_1 z_1$ system is associated with the aircraft; origin of the system O_1 matches the origin of the gravitational system O_G , with the $O_1 x_1$ axis lying in the aircraft's plane of symmetry $O_1 x_1 z_1$ and is directed toward the front of the aircraft's fuselage; the $O_1 z_1$ axis is directed "down", with positive sense toward the aircraft's landing gear; and the $O_1 y_1$ axis completes the right-handed system and is directed toward the right side of the fuselage.

Automatic flight control system

Most of the helicopters because of a multi-axis coupling are low stable (mainly in hover) with strongly limited tendency of returning to trimmed attitude conditions. Thus, workload of the pilots can be very high, especially in degraded visual and environmental conditions like strong wind gusts and turbulence. Continuous action is required from the pilots to maintain the desired airspeed and helicopter orientation angles. AFCS can reduce workload of the pilots and improve flying qualities and safety of the helicopter operations. The fundamental functionalities of the AFCS are to stabilize and control the helicopter in automatic way. The idea of the AFCS was applied much earlier than the era of digitization has come – historical information can be found in Meyers *et al.* (1951), Prouty and Curtiss (2003), Sissingh (1948).

The basic AFCS consists of three main elements (presented in Figure 2):

- 1 sensors which are necessary to obtain the required information about actual helicopter state variables and navigation data;
- 2 computer with embedded automatic control algorithms which (based on information from sensors and desired values) determines control signals; and

Figure 2 Typical AFCS block diagram

- 3 dedicated, additional actuators (working in parallel to basic control actuators) to perform desired control signals.

AFCS (as a highest-level automatic control system) can be divided into autopilot (AP) and stability augmentation system (SAS) (Figure 2). SAS is a lower-level system whose main functionality is to stabilize the angular rates (and attitude) of the helicopter with limited authority – usually 10 per cent in three channels – yaw, pitch and roll (Anonymous, 2008). AP is a full-authority system with several functionalities to maintain or change flight state and conditions.

Here (for the evaluation of the developed AFCS algorithms), the authors focused on two selected functionalities of the AP:

- 1 body velocities hold; and
- 2 navigation mode – to control the helicopter via desired three-dimensional route.

It is assumed that all necessary navigation information is provided to the AFCS.

Linear quadratic regulator

For applying control laws, LQR was chosen. This is a linear control method requiring linear model of the controlled object dynamics. LQR works in a feedback loop (Figure 3). Using difference between actual and desired controlled system state variables, it calculates optimal gains holding the system in desired setpoint of work.

Practically, typical parameters which determine the correctness of work of the regulator, such as response speed and overshoot, depends here on specific weighting matrices values which should be selected regarding the assigned limitations and constraints. The most popular method of choosing the weighting matrices values (weighting matrices Q and R in most cases have diagonal character) is an iterative expert method. Values are changed till controlled system works within desired limits and with desired performance with balance which satisfies the responses of the state variables and control efforts (Luo and Lan, 1995). Except the iterative method, approach of algebraic selection of weighting matrices values can be applied, linking together boundary conditions of transient response and steady state (Kumar *et al.*, 2008).

To define the LQR working with infinite horizon and continuous time, specific assumptions have to be made:

- linear model of the controlled object is known and is set in equilibrium point;
- all system state variables are available and observable for the regulator;
- initial conditions for state variables are established and known; and

- the pair of state matrix A and control matrix B is stabilizable.

For the linear continuous state-space system written as:

$$\dot{x} = Ax + Bu, \quad (1)$$

where A is a state matrix with $n \times n$ dimensions, and B is a control matrix with $n \times m$ dimensions, where:

- n is the number of states (the number of states is related to the number of states in linear model used);
- m is the number of control effectors (longitudinal cyclic, lateral cyclic, collective, pedal);

with cost function defined as:

$$\mathcal{J} = \int_0^{\infty} (x^T Q x + u^T R u) dt, \quad (2)$$

Q is a symmetrical, positively semi-definite matrix with $n \times n$ dimensions, and R is a symmetrical, positively defined matrix with $m \times m$ dimensions, regulation in feedback, which minimizes the cost function, is defined as:

$$u = -K(x - x_{DES}), \quad (3)$$

where x_{DES} is a vector of desired state variables values, and K is the feedback gain with $m \times n$ dimensions, which minimizes the cost function \mathcal{J} , described as:

$$K = R^{-1} B^T P, \quad (4)$$

where P is the Riccati's equation matrix solution with $n \times n$ dimensions for the continuous time defined as:

$$A^T P + PA - PBR^{-1}B^T P + Q = 0. \quad (5)$$

Mission task elements

As the dedicated algorithm for AFCS was applied, the test case could be evaluated. As it was mentioned, the test task was one of the basic flight maneuvers defined in the ADS-33 report. The advantage of this basic mission task element (MTE) was its full description and assurance that trajectory is possible to perform. The MTE definition is presented in Figure 4, and in that form, it was implemented as a reference trajectory.

There was one slight change done comparing to the original MTE – the one curve more was added. However, this change does not impact on the general approach for the system test. According to the ADS-33 document, the set of requirements for the flight are not very complex. There are two main criteria: altitude and forward speed not higher than a certain level. However, the flight performance and the LQR algorithm for the flight control could be examined and assessed in more aspects. The method presented in the article extended the set of the criteria by the fuselage roll and yaw angles. The altitude and forward velocity requirements were also tightened. The last one additional requirement was to perform the turns as a coordinate turn. As thus, the reference values for each eight parameters could be evaluated.

Figure 3 LQR feedback loop

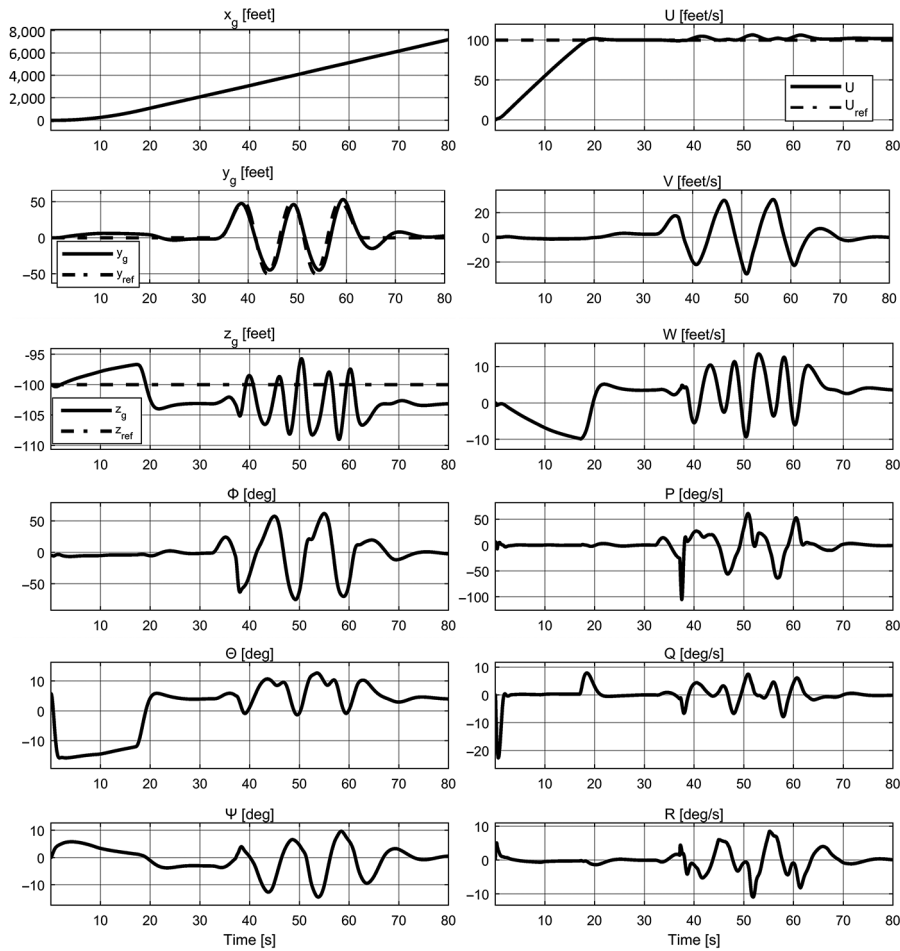
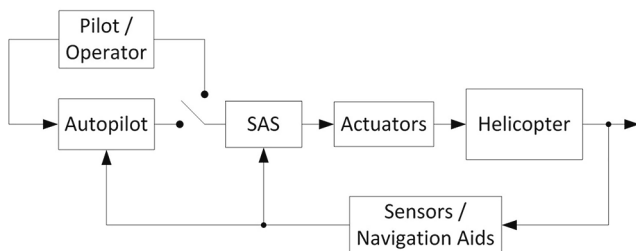


Figure 4 Slalom trajectory definition (Anonymous, 1994)



The reference matrix could be presented as in equation (6), where every single parameter is defined either as a constant value or as a function of position along the x_g axis (maneuver longitudinal axis). All the values from the M_{ref} are directly related to the function defining the trajectory $y_g = f(x_g)$. This is a basic function, and the rest of the function parameters base on this reference trajectory. The trajectory $y_g = f(x_g)$ is divided into three segments: entry to the slalom, exit from the slalom and internal part. The trajectory definition could be found in Kopyt *et al.* (2014) presented as sinewave or as polynomial described in Celi (2007). The difference between the functions is the shift phase and the amplitude:

$$y_g(x) = \begin{cases} A_{se} - A_{se} \times \cos(Lx_g) & \text{for } 500 < x_g < 2000 \\ A_{si} - A_{si} \times \cos(Lx_g) & \text{for } x_g > 500 > x_g > 2000, \end{cases} \quad (6)$$

where:

A_{si} – amplitude of the sinewave for entry and exit segment;
 A_{se} – amplitude of the sinewave for internal segment; and
 L – distance between pylons.

The helicopter fuselage pitch angle was assumed to be constant, as well as the lateral and vertical velocities. In the coordinated turn, both of them should be not only constant, but equal to zero value:

$$M_{ref} = \begin{bmatrix} \Theta_{ref}(x) \\ \Phi_{ref}(x) \\ \Psi_{ref}(x) \\ U_{ref}(x) \\ V_{ref}(x) \\ W_{ref}(x) \\ y_{ref}(x) \\ z_{ref}(x) \end{bmatrix} \quad (7)$$

The roll angle function is presented in following form:

$$\Phi_{ref}(x_g) = \arctg\left(\frac{U_{ref}^2(x_g)|y''(x_g)|}{g(1+y'(x_g))^{3/2}}\right) = \arctg\left(\frac{U_{ref}^2(x_g)A_{si}L^2\cos(Lx_g)}{g(1+A_{si}L\sin(Lx_g))^{3/2}}\right). \quad (8)$$

And, the yaw angle presents as follows:

$$\Psi_{ref}(x_g) = \arctg(A_{si}L\sin(Lx_g)). \quad (9)$$

The method to assess the algorithm/system performance could be expressed as the criterion commonly used in automation:

$$\mathcal{J} = \int_{x_p}^{x_k} e^2(x_g) dx, \quad (10)$$

where x_p and x_k were the coordinates of the start and end of the slalom, respectively. The e is the error value – the difference between the reference and actual value for each x value, e.g. for lateral translation, the error is defined as:

$$e_y^2(x_g) = (y_{ref}(x_g) - y_{real}(x_g))^2. \quad (11)$$

Thus, the final assessment value is presented as a value that has no physical representation. However, the \mathcal{J} value provides information about how close to the original, reference trajectory was the performance in individual parameter:

$$\mathcal{J}_{total} = \begin{bmatrix} \mathcal{J}_\theta \\ \mathcal{J}_\Phi \\ \mathcal{J}_\Psi \\ \mathcal{J}_U \\ \mathcal{J}_V \\ \mathcal{J}_W \\ \mathcal{J}_y \\ \mathcal{J}_z \end{bmatrix}. \quad (12)$$

Test case

In this paper, test case for evaluation of AFCS algorithm performance is presented, based on slalom maneuver presented in ADS-33 document.

In test, it is required that:

- helicopter maintains constant forward speed of 100 ft/s;

- helicopter maintains constant altitude of 100 ft; and
- helicopter follows desired route (slalom) – in the test case slalom starting point described by equation (6) is shifted by 2,500 (ft) because of the forward speed acquiring (start of the test from hover position).

For adequate realization of these requirements, LQR weighting matrices (Q and R) values were selected. Selection of the Q and R matrices values was made with respect to the limitations of the control efforts. LQR gains were calculated using THE reduced linear model – only insignificant states from dynamic point of view were reduced. Simulation was performed using a full nonlinear dynamic model with the developed LQR controller.

The test is divided to four phases:

- 1 100 ft/s forward speed acquiring (starting from hover);
- 2 trajectory interception and tracking – straight flight;
- 3 trajectory tracking – slalom maneuver; and
- 4 trajectory tracking – straight flight.

Test results are presented in Figure 5 (actual y_g trajectory vs desired y_{ref} trajectory in relation to x_g position), and in Figure 6, here, 12 model state variables are shown – x_g, y_g, z_g (position), Φ, θ, Ψ (attitude – roll, pitch, yaw), U, V, W (body velocities), P, Q, R (angular rates – roll, pitch, yaw). Desired values of parameters y_{ref} (slalom), z_{ref} (altitude) and U_{ref} (forward speed) are marked by the dotted line. Test was started from trimmed hover – position ($x_g = 0, y_g = 0, z_g = -100$ [ft]), attitude ($\Phi = -2.68, \theta = 2.89, \Psi = 0$ [deg]), linear velocities ($U = 0, V = 0, W = 0$ [ft/s]), angular velocities ($P = 0, Q = 0, R = 0$ [deg/s]). Total time of the simulation is 80 (s).

The \mathcal{J} values for each parameter form the M_{ref} matrix are presented below. The \mathcal{J} value was calculated only for the x_g range between 3,000 and 5,000 ft:

$$\mathcal{J}_{total} = \begin{bmatrix} 15463 \\ 32502 \\ 12049 \\ 2453 \\ 15735 \\ 25042 \\ 6794 \\ 42882 \end{bmatrix}. \quad (13)$$

The values from \mathcal{J}_{total} present eight different \mathcal{J} values for each parameter. The \mathcal{J} values from M_{ref} matrix are not comparable between each other due to various ranges of amplitudes and units. However, the interpretation of vector \mathcal{J}_{total} is as follows:

Figure 5 Slalom maneuver – $y_g - x_g$ results

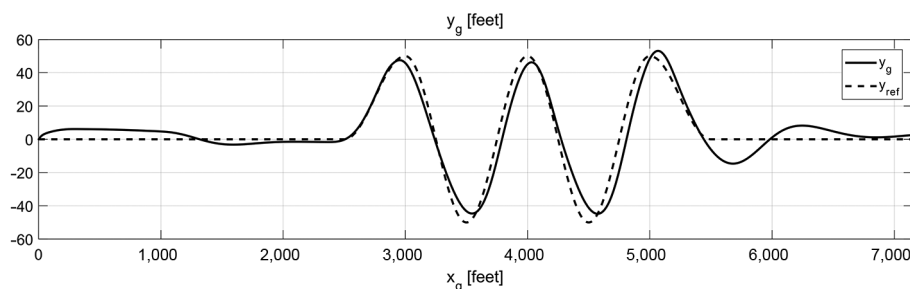
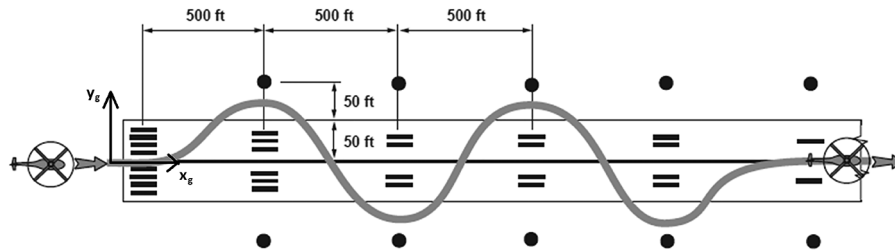


Figure 6 Slalom maneuver – full results in time

closer the number is to zero value, the parameter assessment is better. From Figure 6 and from equation (13), it can be seen that the \mathcal{J}_y is not significantly big – thus, the position trajectory was performed positive. The altitude value was not kept as it was desired, and clearly, it can be seen on the \mathcal{J}_z value. Both side and vertical velocities were not constant as they should be, which can be easily noticed from Figure 6. The methodology for performance assessment clearly presents and confirms the data presented in Figure 6. This method could be used in further research to assess the various configurations of the autopilot or various algorithms tested on the similar MTE.

Conclusion

In this paper, the methodology of a helicopter AFCS functionalities (ground speed hold and navigation mode) realization by the LQR algorithm is presented. Basic information about the principle of operation of an AFCS was provided and the LQR algorithm was described. For evaluation of the LQR algorithm performance, a specified test case was applied, and a developed methodology of performance evaluation was presented. Test was performed using a small helicopter dynamic model developed in Flightlab software and consisted of performing slalom maneuver via desired trajectory, with constant velocity and altitude. Based on the presented performance evaluation method, the proper configuration of the regulator may be derived. The presented assessment method may also be used to provide a quick, brief information about the autopilot performance evaluating other MTEs. The same method and tools may also be used for pilots' performance analysis to increase his/her performance and pilotage technique.

References

- Anonymous (1994), *Aeronautical Design Standard ADS-33D, Handling Qualities Requirements for Military Rotorcraft*, US Army Aviation and Troop Command, St. Louis, MO.
- Anonymous (2008), *UH-60A Automatic Flight Control System (AFCS)*, United States Army Aviation Warfighting Center, Fort Rucker, AL.
- Celi, R. (2007), *Optimization-Based Inverse Simulation of a Helicopter Slalom Manoeuvre*, Department of Aerospace Engineering University of MD, College Park, MD 20742, USA.
- Kopyt, A., Biernacki, M. and Piotrowski, M. (2014), "The study on the mental stress impact on pilots on the PZL SW-4 flight simulator", *Transactions of the Institute of Aviation*, Vol. 3 No. 32, pp. 26-34.
- Kumar, M., Sampath, P., Suresh, S., Omkar, S. and Ganguli, R. (2008), "Design of a stability augmentation system for a helicopter using LQR control and ADS-33 handling qualities specifications", *Aircraft Engineering and Aerospace Technology*, Vol. 80 No. 2, pp. 111-123.
- Luo, J. and Lan, C. (1995), "Determination of weighting matrices of a linear quadratic regulator", *Journal of Guidance, Control, and Dynamics*, Vol. 18 No. 6, pp. 1462-1463.
- Meyers, D., Vanderlip, E. and Halpert, P. (1951), "A tested solution of the problem of helicopter stability and automatic control", *Aeronautical Engineering Review*, Vol. 10 No. 7, pp. 27-32.
- Padfield, G. (2008), *Helicopter Flight Dynamics: The Theory and Application of Flying Qualities and Simulation Modelling*, Blackwell Publishing.
- Prouty, R. and Curtiss, H. (2003), "Helicopter control systems: a history", *Journal of Guidance Control and Dynamics*, Vol. 26 No. 1, pp. 12-18.
- Sissingh, G. (1948), "Automatic stabilization of helicopters", *Journal of the Helicopter Association of Great Britain*, Vol. 2 No. 2, pp. 4-25.

Corresponding author

Antoni Kopyt can be contacted at: akopyt@meil.pw.edu.pl

Conceptual design of an aircraft for Mars mission

Agnieszka Kwiek

School of Computing, Engineering and Mathematics, University of Brighton, Brighton, UK

Abstract

Purpose – The purpose of this paper is to present the results of a conceptual design of Martian aircraft. This study focuses on the aerodynamic and longitudinal dynamic stability analysis. The main research questions are as follows: Does a tailless aircraft configuration can be used for Martian aircraft? How to the short period characteristic can be improved by side plates modification?

Design/methodology/approach – Because of a conceptual design stage of this Martian aircraft, aerodynamic characteristics were computed by the Panukl package by using the potential flow model. The longitudinal dynamic stability was computed by MATLAB code, and the derivatives computed by the SDSA software were used as the input data. Different aircraft configurations have been studied, including different wing's aerofoils and configurations of the side plate.

Findings – This paper presents results of aerodynamic characteristics computations and longitudinal dynamic stability analysis. This paper shows that tailless aircraft configuration has potential to be used as Martian aircraft. Moreover, the study of the impact of side plates' configurations on the longitudinal dynamic stability is presented. This investigation reveals that the most effective method to improve the short period damping ratio is to change the height of the bottom plate.

Practical implications – The presented result might be useful in case of further design of the aircrafts for the Mars mission and designing the aircrafts in a tailless configuration.

Social implications – It is considered by the human expedition that Mars is the most probable planet to explore. This paper presents the conceptual study of aircraft which can be used to take the high-resolution pictures of the surface of Mars, which can be crucial to find the right place to establish a potential Martian base.

Originality/value – Most of aircrafts proposed for the Mars mission are designed in a configuration with a classic tail; this paper shows a preliminary calculation of the tailless Martian aircraft. Moreover, this paper shows the results of a dynamic stability analysis, where similar papers about aircrafts for the Mars mission do not show such outcomes, especially in the case of the tailless configuration. Moreover, this paper presents the results of the dynamic stability analysis of tailless aircraft with different configurations of the side plates.

Keywords CFD, Stability analysis, Aircraft for mars mission

Paper type Research paper

Nomenclature

Symbols

b	= wingspan [m];
C_D	= drag coefficient;
C_L	= lift coefficient;
CM	= pitching moment coefficient;
DR	= damping ratio;
g	= gravity acceleration [m/s^2];
I_y	= moment of inertia respect in a body axis system [$kg\ m^2$];
m	= mass [kg];
q	= angular velocities around y axis [rad/s];
S	= reference area [m^2];
T	= period [s];
$T_{1/2}$	= time to half damping [s];
U_{freq}	= undamped frequency; and
δe	= elevons (elevator) deflection [deg.].

Definitions, acronyms and abbreviations

MAC	= mean aerodynamic chord [m];
SDSA	= simulation and dynamic stability analysis; and
UAV	= unnamed aerial vehicle.

Introduction

So far, Mars exploration has been done using orbiters, landers and rovers. However, rovers' range is restricted, therefore only the area close to a landing point can be photographing by rovers. On the other hand, orbiters observe Mars from orbits, which are far from the surface. In 2018, NASA (2018) launched on the Atlas V 401 rocket the InSight project. This mission's payload includes not only the lander but also two 6U CubeSats, which is the first attempt to use a CubeSat in a deep space [NASA webs site]. In case of a more extensive Mars exploration, including a preparation for the first manned mission, collecting more information about a potential place for a Martian base is required. A small UAV could fly close to the ground surface and collect high-resolution pictures. An example of a project which is

The current issue and full text archive of this journal is available on Emerald Insight at: www.emeraldinsight.com/1748-8842.htm



Aircraft Engineering and Aerospace Technology
91/6 (2019) 886–892
© Emerald Publishing Limited [ISSN 1748-8842]
[DOI 10.1108/AEAT-08-2018-0231]

Received 16 August 2018
Revised 16 September 2018
19 November 2018
Accepted 8 December 2018

developing a rocket for a human Mars mission is SpaceX BFR project.

A few projects of aircraft for Mars are developing but none of those designs have been launched on Mars yet. A few different concepts have been investigated, for example, the NASA project (Guynn *et al.*, 2003) for ARES mission, a solar aircraft (Noth *et al.*, 2004) and rotorcraft (Young *et al.*, 2005). Moreover, the study on Martian aircraft aerodynamic (Anyoji *et al.*, 2017; Naoya Fujioka *et al.*, 2014) is also conducted. All listed aircraft concepts are assuming designing the aircraft in classic configuration. This paper presents the results of the conceptual design of Martian aircraft in a tailless configuration. The presented aircraft concept can be used as a platform for Martian surface photographing.

Mars atmosphere

The Martian atmosphere has a lower density than the atmosphere of Earth; the density at the altitude close to Mars ground surface corresponds to the density of the atmosphere of Earth at the altitude of 33 km. On the other hand, the gravity acceleration on Mars is lower than on Earth and is equal to 3.8 m/s^2 . Figure 1 presents the lift coefficient of Martian aircraft versus true airspeed; those results have been plotted for different altitudes. The presented data were calculated for the aircraft mass equal to 6.0 kg and wing area equal to 0.906 m^2 . Figure 2 presents Reynolds number and Mach number versus

Figure 1 Lift coefficient versus true airspeed for different altitudes

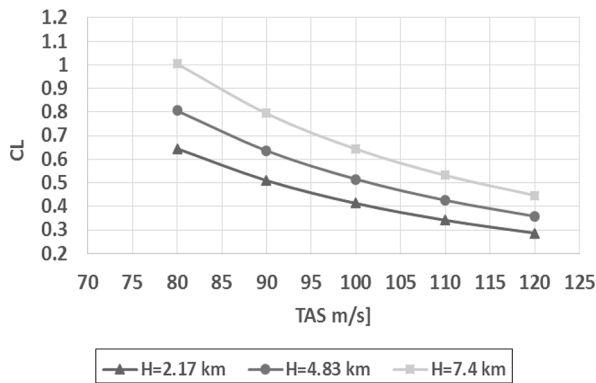
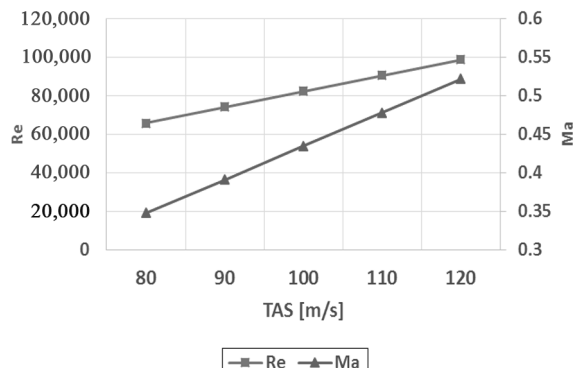


Figure 2 Reynolds and Mach number versus true airspeed in case of Martian aircraft flying at 2.17 km



true airspeed; those results correspond to flying on the altitude equal to 2.17 km. A speed of the sound on Mars is lower than on Earth and is equal to 230 m/s, which means that the compressible effect occurs for a lower speed than on Earth. The Reynolds number is lower than the typical values used in case of an aircraft design for flights in the atmosphere of Earth. Moreover, properties of the atmosphere of Mars are not uniform and might depend on a longitude and latitude. In this paper, the Mars Global Reference Atmospheric Model 2005 was used in all calculations; this model is presented in Justus and Johnson (2001). The Martian atmosphere has also a different air composition and consists of 0.13 per cent of oxygen only; therefore, the best type of engine will be the rocket engine.

Mission definition

According to the mission assumptions, the Martian aircraft can be transporting on Mars using the Atlas V rocket. The weight of aircraft's payload is about 1 kilogram, the cruising speed range is 110–120 m/s, and the maximum weight of the aircraft should be less than 6.5 kg. Because of the air composition of the atmosphere of Mars, the aircraft will be equipped with the rocket engine.

Aircraft geometry

The tailless configuration was selected for this Martian aircraft. Such a configuration is more compact compared to a configuration with a classic tail; therefore, the aircraft does not require to be foldable during the transportation between Earth and Mars. The delta wing was selected as a wing platform, such configuration can be useful if aircraft would be dropped during the atmosphere entry, because the delta wing can generate a lift vortex which can be used to decrease a sink rate; moreover, the delta wing is good in terms of flying in stall conditions (Figat *et al.*, 2012; Galiński *et al.*, 2007). The pitch channel will be controlled by elevons or by rotating all moving plates (in unsymmetrical deflection) (Figat *et al.*, 2012; Galiński *et al.*, 2007; Kwiek and Figat, 2016). The elevons cover 30 per cent of a local chord, and the span of elevons covers 20 to 89 per cent of the wingspan. The roll channel will be controlled by elevons and the yaw channel will be controlled by rotating of all moving plates (in symmetrical deflection). A few different configurations of the aircraft were investigated; the basic geometrical data are presented in Table I. Figure 3 shows the definition of the side plates' geometrical parameters. Figure 4 is presenting the layout of one of the analysed configurations of the aircraft – Model v7.

Aerodynamic characteristics

This paper presents only a preliminary investigation into the Martian aircraft. Because of the preliminary stage of the design, the aerodynamic characteristics were computed by Panukl package (Panukl, 2018). This software using a low order potential method; moreover, the impact of compressible effect was included by Karman–Tsien correction. Because of the very low Reynolds number when the viscosity effect is significant the Panukl, drag coefficient results were modified by using the empirical equation for a friction drag estimation. The aerodynamic forces and moment coefficients are presented

Table I Martian aircraft geometrical parameters

Parameters	Model v1,2,3	Model v4,5	Model v6	Model v7,8,9	Model v10,11
Wing area [m ²]	0.906	0.906	0.906	0.906	0.906
Wing Span [m]	1	1	1	1	1
Aerofoil	A18 A18/CJ6 A18/E374	A18/CJ6 A18/E374	A18/CJ6	A18/CJ6 A18/E374 A18	A18/CJ6 A18
H _{top} [m]	0.2	0.25	0.25	0.25	0.25
H _{bottom} [m]	0.12	0.18	0.18	0.15	0.12
θ _{top} [deg.]	63.43	59	59	59	59
θ _{bottom} [deg.]	90	65	90	90	90
Span with tail plates [m]	1.2	1.3	1.3	1.3	1.3
MAC [m]	0.957	0.957	0.957	0.957	0.957
XCG [%MAC]	27.64%	27.38%	27.38%	33.41%	33.26%
I _y [kg·m ²]	0.614	0.654	0.655	0.643	0.636
Mass [kg]	6	6.16	6.16	6.11	6.09

Figure 3 Definition of the side plate geometrical parameters

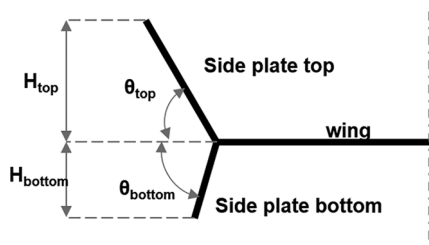
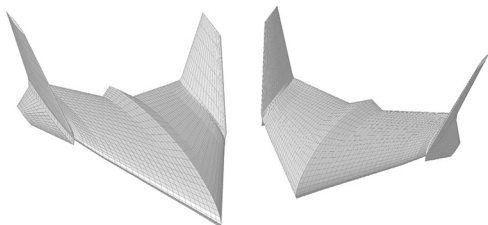


Figure 4 Geometry of the Martian aircraft



in Figures 5–7 because the data were computed by the panel method only a linear part of the lift coefficient was taken into consideration (Figure 8).

Longitudinal stability

Static stability

The dynamic stability was computed by SDSA package (Goetzendorf-Grabowski *et al.*, 2011; SDSA, 2018) based on the Panukl package results. Figure 9 presents the static stability margin versus angle of attack for the case of Model v1 and Model v11. The aircraft is statically stable for the whole analysed range of angles of attack.

Dynamic stability

The most popular way to solve equations of motion is linearization around the trim point using stability derivatives,

Figure 5 Drag coefficient versus angle of attack, Model v11

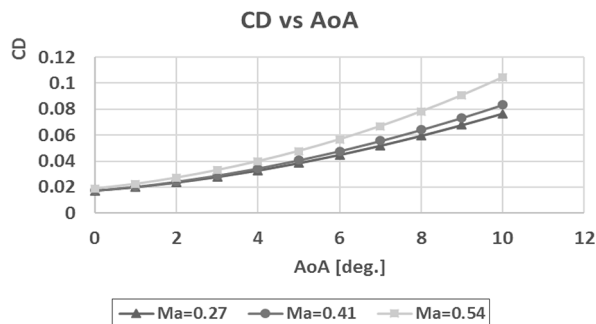
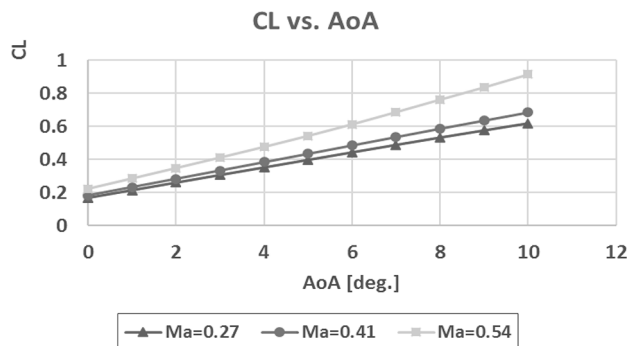


Figure 6 Lift coefficient versus angle of attack, Model v11



this approach is described in the literature (Cook, 2007; Etkin and Reid, 1996; Nelson, 1998). The dynamic stability was computed by SDSA software and MATLAB code. The SDSA software was used for the stability derivatives calculation (Cook, 2007; Etkin and Reid, 1996). The MATLAB code was used to solve the aircraft equation of motion in a state space form, which can be expressed by equations (1)–(4) (Cook, 2007); those equations presenting only the longitudinal model of the dynamic stability with assumption that equations of motion can be decoupling (Cook, 2007). The MATLAB code solves the eigenvalue problem described by equations (5)–(6)

Figure 7 Pitching moment coefficient for the reference point of 25 per cent of MAC versus angle of attack, Model v11

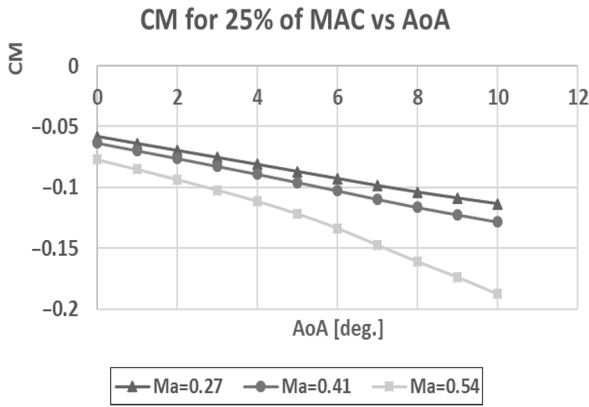


Figure 8 Pressure distribution for Model v11 and AoA = 5°, Ma = 0.41

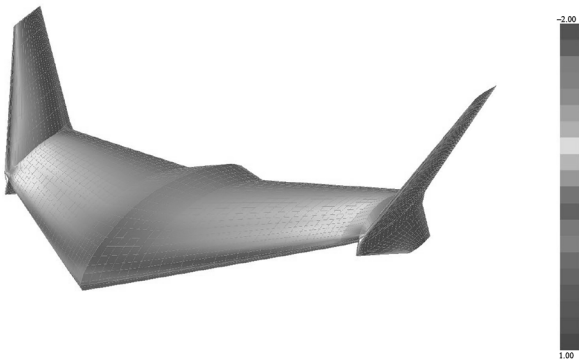
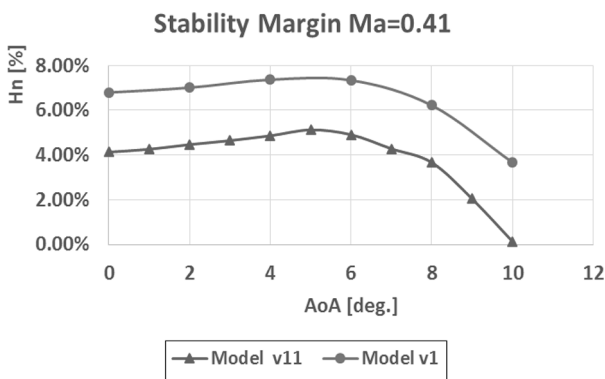


Figure 9 Aircraft static stability margin in case of the Model v1 and v11 for Ma = 0.41



and the solution is expressed by equation (7). A damping ratio, undamped frequency, period and halftime to damping can be expressed by equations (8)-(11), respectively:

$$\dot{x} = Ax + Bc \tag{1}$$

$$x = [u \quad w \quad q \quad \theta]^T \tag{2}$$

$$A = M^{-1}A' \tag{3}$$

$$A = \begin{bmatrix} x_u & x_w & x_q & x_\theta \\ z_u & z_w & z_q & z_\theta \\ m_u & m_w & m_q & m_\theta \\ 0 & 0 & 1 & 0 \end{bmatrix} \tag{4}$$

$$x(t) = x_0 e^{\lambda t} \tag{5}$$

$$(A - \lambda I)x_0 = 0 \tag{6}$$

$$\lambda = \xi + i\eta \tag{7}$$

$$\zeta_d = -\frac{\xi}{\sqrt{\xi^2 + \eta^2}} \tag{8}$$

$$\omega_{nd} = \sqrt{\xi^2 + \eta^2} \tag{9}$$

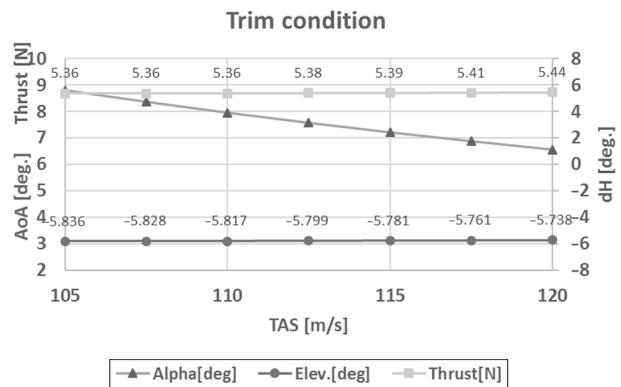
$$T = \frac{2\pi}{\eta} \tag{10}$$

$$T_{1/2} = -\frac{\ln 2}{\xi} \tag{11}$$

The trim conditions were computed by SDSA; this software has only data about the atmosphere of Earth. The trim calculations were done at the altitude equal to 33,900 m; this condition corresponds to the Martian air density at 2.17 km. Because of different gravity acceleration, the mass of the aircraft in SDSA was decreased to simulate the condition on Mars; the results are presented in Figure 10.

The results of the dynamic stability were computed by the MATLAB based on the trim conditions and derivatives computed by the SDSA. This research focuses on the dynamic stability analysis of different configurations of the aircraft. First, different wing's aerofoils were tested A18 (Model v1), A18 & CJ6 (Model v2) and A18 and E374

Figure 10 Trim condition – Model v11



(Model v3). The results of the short period and phugoid computations are presented in Figures 11 and 12. The aircraft is damping the longitudinal oscillation for the whole range of the speed. However, according to MIL-F-8785C (1980) regulation, to achieve level 3 of the dynamic stability, the damping ratio of the short period should be at least 0.15. Figure 11 shows that the strongest damping ratio occurs for the Model v1, but all the presented models achieve the damping ratio smaller than 0.15.

The next geometrical parameter which was investigated is the angle of the bottom plate. Figures 13 and 14 present the damping ratio for the short period and phugoid mode of Model v4 and Model v6. The aircraft in configuration v6 ($\theta_{\text{bottom}} = 90 \text{ deg.}$) has a stronger damping ratio for the short period, but still, according to MIL-F-8785C regulation, the damping ratio is too small. In terms of phugoid mode, the Model v4 ($\theta_{\text{bottom}} = 65 \text{ deg.}$) has a stronger damping ratio, according to MIL-F-8785C regulation, both models of the aircraft are stable.

The last investigated parameter was the height of the bottom plate; Figures 15 and 16 show results for Model v9 and Model v11. In terms of the short period, the Model v11 (with the smaller height) has damping ratio bigger than 0.15 for low speed (about 105 m/s), moreover, this damping ratio is stronger than the damping ratio of Model v4. The phugoid

Figure 11 Damping ratio of the short period mode, the same tail configuration but different aerofoil

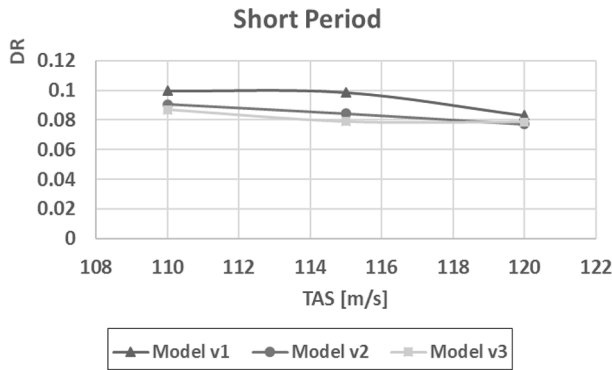


Figure 12 Damping ratio for the phugoid mode, the same tail configuration but different aerofoil

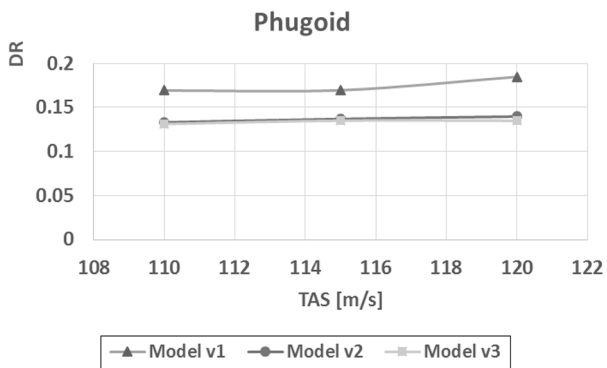


Figure 13 Damping ratio for the short period mode, the same size of side plates but different θ_{bottom}

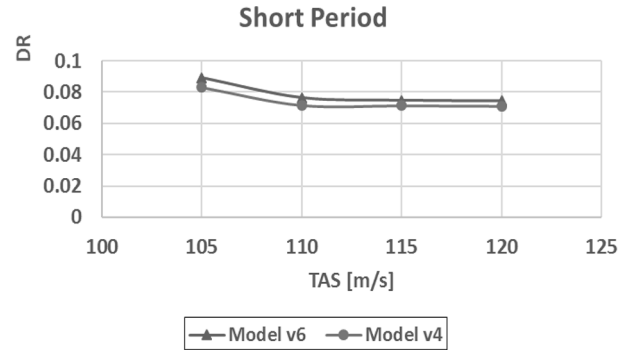


Figure 14 Damping ratio for the phugoid mode, the same size of side plates but different θ_{bottom}

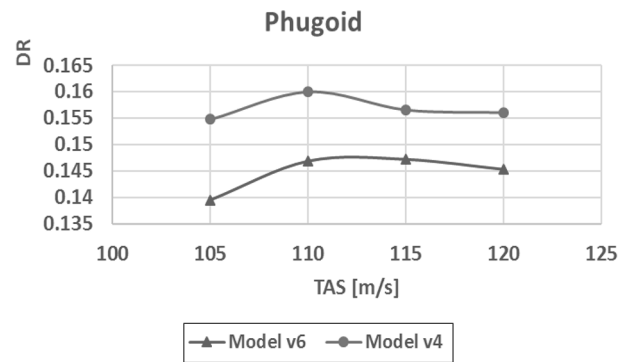
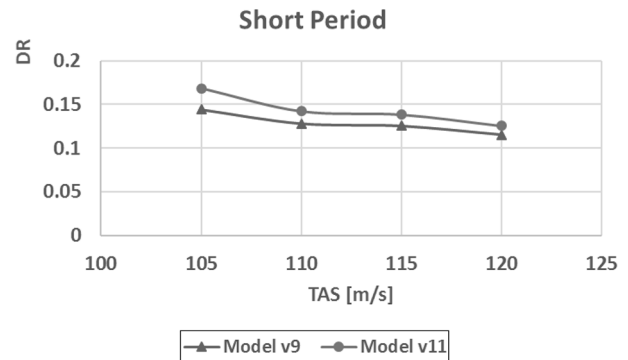


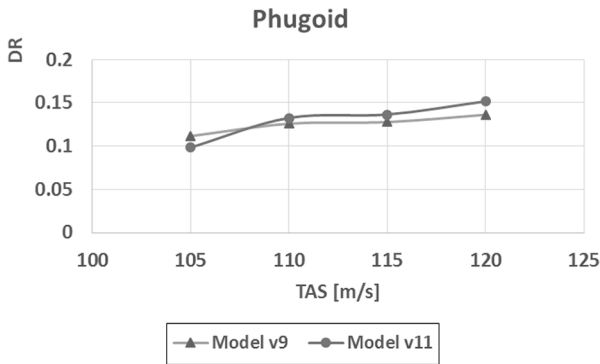
Figure 15 Damping ratio for the short period mode, the same size of side plates but different H_{bottom}



damping ratios are very similar for both models and fulfil the MIL-F-8785C regulation.

According to MIL-F-8785C regulation, the phugoid mode is stable for all considered models; the damping ratios classified the results for level 1. In case of the short period, according to MIL-F-8785C regulation, only Model v11 is stable but only for low airspeed. The damping ratio of the rest of the analysed model is lower than 0.15. The most effective way to improve the short period damping ratio is changing the height of the bottom plate, this effect

Figure 16 Damping ratio for the phugoid mode, the same size of side plates but different H_{bottom}



is not only related to the aerodynamic characteristics but also to the position of the CG and to the moment of inertia. In further analysis, the short period characteristics need to be improved. Model v11 complete results of the longitudinal dynamic stability are presented in Figures 17-20.

Figure 17 Results of the period and time to half damping for the short period mode, Model v11

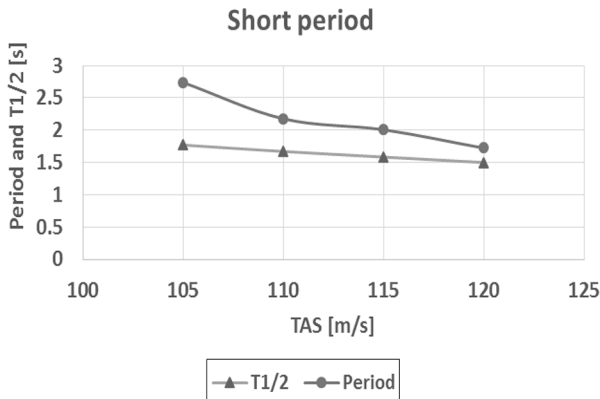


Figure 18 Results of the undamped frequency for the short period mode, Model v11

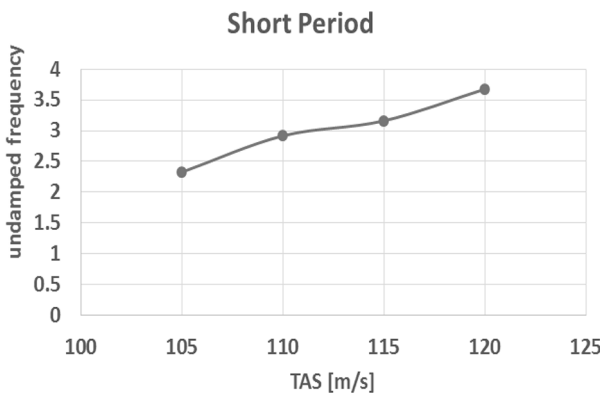


Figure 19 Results of the period and time to half damping for the phugoid mode, Model v11

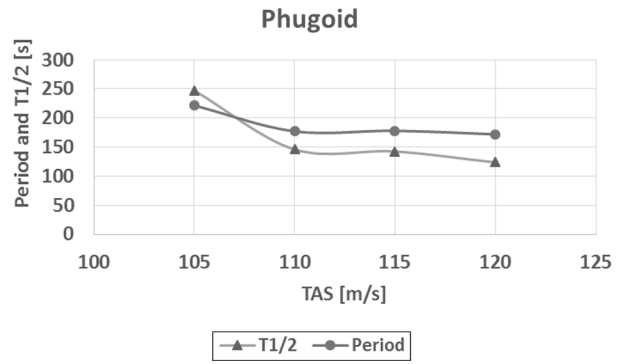
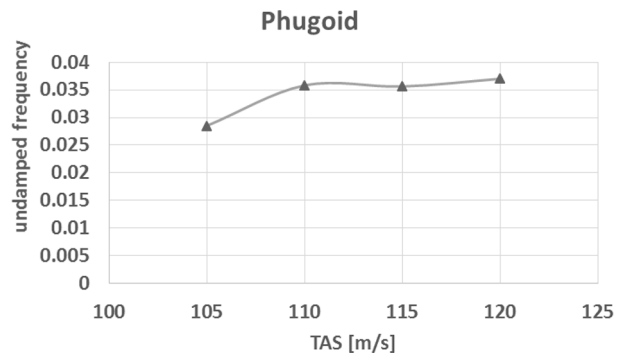


Figure 20 Results of the undamped frequency for the phugoid mode, Model v11



Conclusion

Preliminary results of the aerodynamic analysis and dynamic stability analysis were presented. Because of a low density of the atmosphere of Mars, it is challenging to design the aircraft, but it is possible. However, it is recommended that aircraft fly with high speed because of the problem with a low Reynolds number. A few different configurations of the aircraft were analysed, including different aerofoils, the angle of the side plate, and the height of the bottom plate. All presented models have been designed in the tailless configuration, and all fulfil the MIL-F-8785C criteria for the phugoid mode; however, the short period mode required improvements. Only for the Model v11 the short period damping ratio is bigger than 0.15. This investigation reveals that the most effective method to improve this damping ratio was changing the height of the bottom plate.

Based on the presented results, it can be concluded that tailless aircraft has the potential to be the Martian aircraft, but the concept needs some further work. Because of the compact structure, the tailless aircraft can be transported without foldable elements, what improves the reliability of the aircraft. The aerodynamic characteristics need to be validated by more advanced software and the high angles of attack need to be also analysed to make sure that aircraft can be also released during the atmospheric entry.

Further work

The problem of the lateral and directional stability will be analysed in a next step, and improvement in the damping ratio in case of the short period oscillation is also required.

References

- Anyoji, M., Okamoto, M., Fujita, K., Nagai, H. and Oyama, A. (2017), "Evaluation of aerodynamic performance of mars airplane in scientific balloon experiment", *Fluid Mechanics Research International Journal*, Vol. 1 No. 3.
- Cook, M.V. (2007), *Flight Dynamics Principles*, Elsevier, Oxford.
- Etkin, B. and Reid, L.D. (1996), *Dynamics of Flight. Stability and Control*, John Wiley & Sons, New York, NY.
- Figat, M., Galiński, C. and Kwiek, A. (2012), "Modular aeroplane system: a concept and initial investigation", *Proceedings of ICAS 2012 Conference*, 23–28 September, Brisbane.
- Galiński, C., Goetzendorf-Grabowski, T., Mieszalski, D. and Stefanek, Ł. (2007), "A concept of two-staged spaceplane for suborbital tourism", *Transactions of the Institute of Aviation*, Vol. 191 No. 4, pp. 33–42.
- Goetzendorf-Grabowski, T., Mieszalski, D. and Marcinkiewicz, E. (2011), "Stability analysis using SDSA tool, progress in aerospace sciences", Vol. 47 No. 8, November, pp. 636–646.
- Gynn, M.D., Croom, M.A., Smith, S.C., Parks, R.W. and Gelhausen, P.A. (2003), "Evolution of a mars airplane concept for the ARES mars scout mission", *2nd AIAA "Unmanned Unlimited" Systems, Technologies and Operations – Aerospace*, 15–18 September, AIAA, San Diego, CA, pp. 2003–6578.
- Justus, C.G. and Johnson, D.L. (2001), "Mars global reference atmospheric model 2001 version (Mars-GRAM 2001): users guide", NASA Report TM-2001-210961.
- Kwiek, A. and Figat, M. (2016), "LEX and wing tip plates' interaction on the rocket plane in tailless configuration", *The Aeronautical Journal*, Vol. 120 Issue No. 1224, pp. 255–270.
- MIL-F-8785C (1980), "MIL-F-8785C military specification flying qualities of piloted airplanes", 5 November 1980.
- NASA (2018), available at: <https://mars.nasa.gov/insight/mission/overview/>
- Naoya, F., Taku, N., Akira, O., Makoto, Y. and Kozo, F. (2014), "Computational analysis of aerodynamic performance of mars airplane", *Transactions of the Japan Society for Aeronautical and Space Sciences, Aerospace Technology Japan*, Vol. 12 No. 29, pp. Tk_1-Tk_5.
- Nelson, R. (1998), *Flight Stability and Automatic Control*, McGraw-Hill, New York, NY.
- Noth, A., Bouabdallah, S., Michaud, S., Siegwart, R. and Engel, W. (2004), "SKY-SAILOR design of an autonomous solar powered martian airplane", *Proceedings of the 8th ESA Workshop on Advanced Space Technologies for Robotics, (ASTRA 2004)*, Noordwijk.
- Panukl (2018), available at: www.meil.pw.edu.pl/add/ADD/Teaching/Software/PANUKL
- SDSA (2018), available at: www.meil.pw.edu.pl/add/ADD/Teaching/Software/SDSA
- Young, L.A., Aiken, E., Lee, P. and Briggs, G. (2005), "Mars rotorcraft: possibilities, limitations and implications for human/robotic exploration", *2005 IEEE Aerospace Conference*, ISBN: 0-7803-8870-4.

Corresponding author

Agnieszka Kwiek can be contacted at: A.Kwiek@brighton.ac.uk

Fast high fidelity CFD/CSM fluid structure interaction using RBF mesh morphing and modal superposition method

Corrado Groth and Ubaldo Cella

Department of Enterprise Engineering "Mario Lucertini", School of Engineering,
Universita degli Studi di Roma Tor Vergata, Roma, Italy

Emiliano Costa

D'Appolonia SpA, Rome, Italy, and

Marco Evangelos Biancolini

Department of Enterprise Engineering "Mario Lucertini", School of Engineering,
Universita degli Studi di Roma Tor Vergata, Roma, Italy

Abstract

Purpose – This paper aims to present a fast and effective approach to tackle complex fluid structure interaction problems that are relevant for the aeronautical design.

Design/methodology/approach – High fidelity computer-aided engineering models (computational fluid dynamics [CFD] and computational structural mechanics) are coupled by embedding modal shapes into the CFD solver using RBF mesh morphing.

Findings – The theoretical framework is first explained and its use is then demonstrated with a review of applications including both steady and unsteady cases. Different flow and structural solvers are considered to showcase the portability of the concept.

Practical implications – The method is flexible and can be used for the simulation of complex scenarios, including components vibrations induced by external devices, as in the case of flapping wings.

Originality/value – The computation mesh of the CFD model becomes parametric with respect to the modal shape and, so, capable to self-adapt to the loads exerted by the surrounding fluid both for steady and transient numerical studies.

Keywords Fluid structure interaction, Radial basis functions, Mesh morphing, Modal superposition

Paper type Technical paper

Nomenclature

Symbols

β	= weights of the polynomial corrector vector;
γ	= RBF coefficients vector;
η	= vector of modal coordinates η_m ;
s	= damping factor;
φ	= radial function;
ω	= natural frequency;
F	= vector of modal forces F_m ;
g	= known values of displacement;
h	= RBF correction polynomial;
K	= structural stiffness matrix;
x	= position of a 3d point;
x_k	= vector of source points x_{k_i} ;
M	= structural mass matrix;
P	= constraint matrix used for RBF fit;

r	= euclidean distance between two points;
q	= generic polynomial;
Q	= nodal loads;
s	= RBF interpolant;
Δu	= matrix of eigenvectors Δu_m ;
u	= vector of structural displacements;
U	= interpolation matrix used for RBF fit;
X_{CFD}	= mesh nodes position; and
X_{CFD_0}	= mesh nodes in the undeformed position.

Definitions, acronyms and abbreviations

AePW	= aeroelastic prediction workshop;
CAE	= computer-aided engineering;
CFD	= computational fluid dynamics;
CSM	= computational structural mechanics;
DLM	= doublet lattice method;
FFD	= free-form deformation;
FEM	= finite element model;
FRF	= frequency response functions;
FSI	= Fluid structure interaction;
GAF	= generalised aerodynamic force;

The current issue and full text archive of this journal is available on Emerald Insight at: www.emeraldinsight.com/1748-8842.htm



Aircraft Engineering and Aerospace Technology
91/6 (2019) 893–904
© Emerald Publishing Limited [ISSN 1748-8842]
[DOI 10.1108/AEAT-09-2018-0246]

Received 18 September 2018

Revised 27 November 2018

Accepted 9 December 2018

RBF = radial basis functions;
 ROM = reduced order model; and
 SMM = standard mortar method.

Introduction

Fluid structure interaction (FSI) is an important phenomenon that, in most engineering applications, cannot be neglected. The numerical solution of the FSI mechanism is a difficult task that requires to account both structural and fluid dynamic solution in a common environment. Structural behaviour is, in fact, a troublesome boundary condition for the computational fluid dynamics (CFD) domain and, for this reason, in the past CFD analysts preferred to neglect the elastic deformation under load assuming boundaries as rigid, and deferring the verification of the aeroelastic performance to a post design phase. On the other hand, lots of computational structural mechanics (CSM) analysts commonly chose to assume the fluid inside or outside a structure to be merely generating a constant pressure on the walls.

The need to face multi-physics problems is growing more and more in many industrial fields and, during the last decades, a significant effort was spent on the development of FSI analysis tools. Today many commercial codes are able to offer CFD-CSM coupling capabilities, but the setup of accurate and efficient FSI simulations is still a complex and difficult task.

Several examples and methods have been proposed during the years and are available in literature. Notable reviews on FSI methods were written by Morand and Ohayon (1995), Dowell and Hall (2001), Mittal and Iaccarino (2005), Benra *et al.* (2011), Hou *et al.* (2012) to name a few. A first categorisation of the implemented methods can be done according to two main groups, namely monolithic and partitioned approaches. In the former (Hubner *et al.*, 2004) a single system composed of both structural and fluid dynamics equations is assembled and solved in the same numerical framework, whereas in the latter CFD and CSM problems are independently managed by different codes. Both approaches have their peculiar pros and cons. In general, the monolithic approach is more computationally demanding and requires effort and expertise to be developed, but it is more stable even if maintainability and implementation may be problematic. On the other hand, the partitioned approach, also called two-way method, (Degroote, 2013) can exploit known and well-established software to solve separately fluid and structural domains, but it requires expensive and complex data transfer between solvers. Moreover, in most cases CFD and CSM meshes are non-matching, meaning that numerical grid elements, nodes, data location and connectivity are not coincident at boundaries, thus requiring an interpolation method to consistently transfer data back and forth between solvers. To this end, several load mapping methods (Wang *et al.*, 2016; Franke, 1982; Biancolini *et al.*, 2018), such as the Standard Mortar Method (SMM) (Cebal and Löhner, 1997) and the Force Reaction Method (Hou and Satyanarayana, 2000), have been developed in the past, but the implemented models need to be synchronised in terms of displacements by updating the CFD grid with the results achieved by means of the CSM simulation. Remeshing the CFD domain at each iteration can be viable, but it is computationally expensive and problems related to numerical

noise and meshing errors may arise. A significant step forward for boosting the efficiency and simplifying FSI analyses was provided by the introduction of *mesh morphing* technologies. Such a technique allows to update the numerical grid by deforming the computational domain in a cost efficient manner, enabling the restart of the simulation after the geometrical change thanks to the preservation of mesh topology characterising mesh morphing. Several methods to handle this task were proposed by both researchers and commercial codes, and they are mainly based on the free-form deformation (Rousseau *et al.*, 2007) and elastic model (Masud *et al.*, 2007).

An advanced mesh morphing tool based on radial basis functions (RBF) is *RBF MorphTM* (www.rbf-morph.com). The software was born as an Add-On of the CFD solver *ANSYS® Fluent®* and currently it is also available as a stand-alone module compatible with most structural and fluid dynamic codes present in the market. In addition to a traditional two-way coupling between CFD and CSM solutions, *RBF Morph* offers the possibility to setup FSI analyses by a modal approach embedding the structural modes in the CFD setup thus making the analysis extremely efficient and flexible. In fact, this strategy renders the fluid numerical domain intrinsically aeroelastic and such to be able to reshape the deformable components during the progress of the computation depending on the applied loads.

It is well known that structural modes, and related frequency signature, represent the basic nature of the dynamic behaviour of a structure. Facing FSI analyses with the modal approach offers the possibility to exploit several advantages related to its simplified numerical environment, which permits to study static and dynamic aeroelastic mechanism more easily but with the restriction of a validity limited to linear structural problems. The working principle consists of importing a certain number of modes (the higher the number of modes introduced the lower the related truncation error), computed by a preliminary structural modal analysis, into the CFD solver. This operation makes the CFD domain parametric with respect to modal shapes that are opportunely combined and amplified according to the modal loads computed from the actual fluid dynamic solution. The main advantage is that the information exchange, that is required for two-way FSI, is no more required and the mesh update is very fast, automatic and accomplished during the progress of the run.

As it will be detailed in the sections of this paper, the embedded modes can be used for three classes of industrial applications: transient FSI with movement prescribed in advance, steady FSI to have the structural deformation modelled on the CFD mesh and full coupled transient FSI.

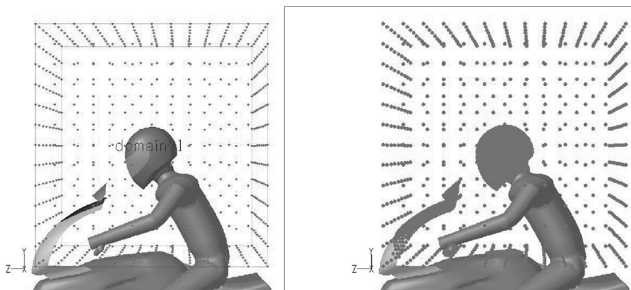
Advanced modal FSI functionalities are efficiently embedded in *ANSYS® Fluent®* by adopting the Add On version of *RBF MorphTM*; in this case the strong integration with the mesh deformation algorithms of the CFD solver allows to face both steady and transient simulations adopting the modal shapes coming from the structural solver of choice. The *RBF4AERO* platform (www.rbf4aero.eu) enables to extend such approach (at the moment only for steady cases) to a wider family of fluid and structural solvers; the *Morpher Tool* adopted in the platform is the Stand Alone version of the *RBF MorphTM* mesh morphing software. In this paper, we review a collection of successful industrial and research applications in

several fields of engineering that are based on the concepts and on the aforementioned technologies. The contents of the paper are arranged as follows: an overview of the modal approach toward FSI is first given in the *Introduction*, the basic concepts to enable a fast and parametric mesh deformation adopting RBF are given in the section *Radial Basis Functions Mesh Deformation*, basic principles of modal theory are recalled in the section *Modal analysis and mode superposition*, the FSI workflows enabled by the proposed method are then explained in the section *Setup of modal FSI analysis* and a collection of practical examples is finally given in the section *Industrial applications of FSI modal approach*.

Radial basis functions mesh deformation

RBF mesh deformation is the technology the FSI modal method here described is based on. It consists in the smooth propagation of a deformation field, defined by a certain number of points in the space (source points), to the surrounding nodes of the volume mesh. In the implementation of the FSI modal method a set of RBF solutions is defined (one per modal shapes) to constitute a parametric mesh formulation to be used to adapt the fluid dynamic domain according to the structural deformation. The final volume mesh is obtained combining, and opportunely amplifying, the modal base of RBF solutions. The smoothing action is controlled by placing a distribution of control points (sources) within the mesh domain. It is common to have sources at the wetted surfaces, at a set of fixed surfaces and, optionally, at special entities border (cylinders or boxes) that are used to wrap and limit the extent of the morphing domain to a large enough region around the deformable part. It is worth to notice that the RBF mesh morphing approach here presented can be used for various applications ranging from shape optimisation to advanced multi-physics workflow. Figure 1 (Biancolini, 2009) demonstrates a typical arrangement of source points: the CFD meshes adapted to a new position of the driver by assigning a new position to the helmet, setting as fixed the surfaces of the motorbike and leaving the body of the driver free to deform. The surrounding box region allows to limit the action of the mesh deformation around the updated surfaces.

Figure 1 Example of an RBF morph set up to change the a motorbike driver attitude



Notes: The morphing action is limited within a box region (left). The motion of the surfaces inside the encapsulation domain (right) is imposed to the points on the windshield (fixed), the fairing (fixed) and the helmet (moving)

Radial basis functions background theory

From mathematical point of view, the solution of the RBF problem consists of the calculation of the coefficients of a linear system of order equal to the number source points (De Boer *et al.*, 2007), by means of which the displacement of an arbitrary mesh's node (target) can be expressed, and then imposed, as the summation of the radial contribution of each controlled node (source). In such a way, mesh smoothing can be rapidly applied by maintaining mesh topology in terms of total number and type of elements.

In particular, the RBF Morph tool utilises the RBF interpolant s composed by a radial function containing the RBF φ and a multivariate polynomial corrector vector h of order $m - 1$, where m is said to be the order of φ , introduced with the aim to assure the uniqueness of the RBF solution and the compatibility for rigid motions. Specifically, if N is the total number of source points, the formulation of the RBF interpolant is:

$$s(\mathbf{x}) = \sum_{i=1}^N \gamma_i \varphi(\|\mathbf{x} - \mathbf{x}_{k_i}\|) + h(\mathbf{x}) \quad (1)$$

where \mathbf{x} is the vector identifying the position of a generic node belonging to the surface and/or volume mesh \mathbf{x}_{k_i} is the i^{th} source node position vector and $\|\cdot\|$ is the Euclidean norm.

The RBF fitting solution exists in case the RBF coefficients vector γ_i and the weights of the polynomial corrector vector β_i can be found such that, at source points, the interpolant function possesses the specified (known) values of displacement \mathbf{g}_i , whilst the polynomial terms give a null contribution, namely the following relations are simultaneously verified:

$$s(\mathbf{x}_{k_i}) = \mathbf{g}_i \quad 1 \leq i \leq N \quad (2)$$

$$\sum_{i=1}^N \gamma_i q(\mathbf{x}_{k_i}) = 0 \quad (3)$$

for all polynomials q with a degree less than or equal to that of polynomial h (Beckert and Wendland, 2001). The minimal degree of polynomial h depends on the choice of the RBF type. It can be demonstrated that a unique RBF interpolant exists if the RBF is conditionally positive definite (Van Zuijlen *et al.*, 2007). In the case that this latter condition is established and if the order is less than or equal to 2 (Jin *et al.*, 2001), a linear polynomial applies:

$$h(\mathbf{x}) = \beta_1 + \beta_2 x + \beta_3 y + \beta_4 z \quad (4)$$

enabling to exactly recover rigid body translations.

In the event such assumptions are verified, the interpolant has the form:

$$s(\mathbf{x}) = \sum_{i=1}^N \gamma_i \varphi(\|\mathbf{x} - \mathbf{x}_{k_i}\|) + \beta_1 + \beta_2 x + \beta_3 y + \beta_4 z \quad (5)$$

and γ_i and β_i values can be obtained by solving the system:

$$\begin{pmatrix} \mathbf{U} & \mathbf{P} \\ \mathbf{P}^T & 0 \end{pmatrix} \begin{pmatrix} \boldsymbol{\gamma} \\ \boldsymbol{\beta} \end{pmatrix} = \begin{pmatrix} \mathbf{g} \\ 0 \end{pmatrix} \quad (6)$$

where \mathbf{U} is the interpolation matrix having the elements derived by calculating all the radial interactions between source points as follows:

$$U_{ij} = \varphi(\|\mathbf{x}_{ki} - \mathbf{x}_{kj}\|) \quad 1 \leq i \leq N, \quad 1 \leq j \leq N \quad (7)$$

and \mathbf{P} is a constraint matrix that arises balancing the polynomial contribution, that is:

$$\mathbf{P} = \begin{pmatrix} 1 & x_{k1} & y_{k1} & z_{k1} \\ 1 & x_{k2} & y_{k2} & z_{k2} \\ \vdots & \vdots & \vdots & \vdots \\ 1 & x_{kN} & y_{kN} & z_{kN} \end{pmatrix} \quad (8)$$

assuming that source points are not contained in the same plane (otherwise the interpolation matrix would be singular).

For what described, by satisfying the displacement field prescribed at source points, RBF Morph operates the smoothing of mesh nodes using the following formulation of the interpolant:

$$\begin{cases} s_x(\mathbf{x}) = \sum_{i=1}^N \gamma_i^x \varphi(\|\mathbf{x} - \mathbf{x}_{ki}\|) + \beta_1^x + \beta_2^x x + \beta_3^x y + \beta_4^x z \\ s_y(\mathbf{x}) = \sum_{i=1}^N \gamma_i^y \varphi(\|\mathbf{x} - \mathbf{x}_{ki}\|) + \beta_1^y + \beta_2^y x + \beta_3^y y + \beta_4^y z \\ s_z(\mathbf{x}) = \sum_{i=1}^N \gamma_i^z \varphi(\|\mathbf{x} - \mathbf{x}_{ki}\|) + \beta_1^z + \beta_2^z x + \beta_3^z y + \beta_4^z z \end{cases} \quad (9)$$

A great flexibility using RBF can be achieved acting on the radial functions that can be compactly or globally supported. Common options are summarised in Table I. *RBF Morph*

Table I Typical radial basis functions

Radial basis functions (RBF) with global support	$\varphi(r)$
Spline type (Rn)	$r^n, n \text{ odd}$
Thin plate spline (TPSn)	$r^n \log(r), n \text{ even}$
Multiquadric (MQ)	$\sqrt{1+r^2}$
Inverse multiquadric (IMQ)	$\frac{1}{\sqrt{1+r^2}}$
Inverse quadratic (IQ)	$\frac{1}{1+r^2}$
Gaussian (GS)	e^{-r^2}
Radial Basis Functions (RBF) with compact support	$\varphi(r) = f(\xi), \quad \xi \leq 1, \xi = \frac{r}{R_{sup}}$
Wendland C0 (C0)	$(1-\xi)^2$
Wendland C2 (C2)	$(1-\xi)^4(4\xi+1)$
Wendland C4 (C4)	$(1-\xi)^6\left(\frac{35}{3}\xi^2+6\xi+1\right)$

allows to use various radial functions. The distance function (global supported and bi-harmonic in 3D) is used by default and performs very well in volume morphing as it allows to get very good quality and it is accelerated so that it can handle RBF problem beyond 1 million of centres (source points). Wendland functions (C0, C2 and C4) are available for surface sculpting as the high level of continuity can be used to control a surface using just a few control points.

Parametric mesh formulation

According to equation (9), the new position of each node of the volume mesh to be morphed by the RBF field can be computed in a meshless fashion using as input just its original position and the RBF expansion:

$$\mathbf{x}_{node_{new}} = \mathbf{x}_{node} + \begin{bmatrix} s_x(\mathbf{x}_{node}) \\ s_y(\mathbf{x}_{node}) \\ s_z(\mathbf{x}_{node}) \end{bmatrix} \quad (10)$$

The core of the modal implementation is the parametric mesh formulation, by modal coordinates computed during the computation, and its inclusion within the CFD environment. As explained in equation (15) of the next section, the full deformed shape of the structure can be represented by linearly combine each structural mode using as weight the companion modal coordinate η_m . The RBF mesh deformation approach allows to have the full CFD mesh parametric with respect to the modes. As the modal theory is linear, there is no need to use the costly RBF formula (10) at each mesh update and the linear combination:

$$\mathbf{X}_{CFD} = \mathbf{X}_{CFD_0} + \sum_{m=1}^n \eta_m \Delta \mathbf{u}_m \quad (11)$$

is preferred, where \mathbf{X}_{CFD} are the updated positions of the grid nodes, \mathbf{X}_{CFD_0} are the positions of the nodes of the undeformed baseline mesh, η_m are the updated modal coordinates and $\Delta \mathbf{u}_m$ are the modal displacements of the mth mode precomputed in advance adopting equation (10). The vectors $\Delta \mathbf{u}_m$ (usually of the same size of the full CFD mesh) could be stored on the disk or in memory for a faster access depending on the implementation; transient analyses presented in this paper requires to be stored in memory to guarantee that the time required for the updating of the mesh at each time step is lower (usually a small fraction) than the one needed for the CFD solution update.

Modal analysis and mode superposition

Modal analysis is a well-established and known theory of structural mechanics. A briefly theoretical introduction on it is provided in this section to quickly put the reader in the position to better understand the proposed FSI approach. Modal analysis consists in the calculation of the undamped free vibration modes of a mechanical system, each characterised by a natural shape and frequency. In FEM modelling, where the behaviour of continuum systems is simulated by operating with their discrete representation, the modal analysis enables to determine the structural static and dynamic response in

linearity conditions. If the damping is null nodal amplitudes (modes) \mathbf{u} and natural frequencies of a structure can be computed by solving the eigenvalue problem mathematically identified by the system:

$$\mathbf{K}\mathbf{u} = \omega^2 \mathbf{M}\mathbf{u} \quad (12)$$

where \mathbf{K} is the stiffness matrix, ω^2 is an eigenvalue, ω is a natural frequency, and \mathbf{M} is the mass matrix of the system, stating that a vibration mode is a configuration in which a balance between elastic resistance and inertial loads occurs (Cook et al., 2002).

Mechanical systems are characteristically low-pass; the lowest frequency modes have the highest energy levels and are physically prominent. The complete solution of the eigenvalue problem can be approximated retaining only a limited number of its lowest modes with a favourable reduction of DOF that need to be treated. Moreover, since the solution of the eigenvalue problem is a subspace of eigenvectors problem, the sign and the entity of each eigenvector may change depending on the algorithm adopted for the solution achievement (Meirovitch, 2010). For solution purposes, a convenient normalisation is performed by imposing for each m^{th} mode $\Delta \mathbf{u}_m$ a unit modal mass so as to obtain:

$$\Delta \mathbf{u}_m^T \mathbf{M} \Delta \mathbf{u}_m = 1 \quad (13)$$

and then:

$$\Delta \mathbf{u}_m^T \mathbf{K} \Delta \mathbf{u}_m = \omega_m^2 \quad (14)$$

One of most important aspects of modal analysis is the spectral decomposition, which means that modes are orthogonal and form a basis in the modal coordinates (or displacements) η . In this case, the dynamic response of a mechanical system can be approximated by the truncated summation of the response of each mode:

$$\mathbf{u} = \sum_{m=1}^n \Delta \mathbf{u}_m \eta_m = \Delta \mathbf{u} \boldsymbol{\eta} \quad (15)$$

where η_m is the value of the modal coordinate of the retained mode and $\Delta \mathbf{u}_m$ is its modal shape and n is the number of retained modes.

As a matter of fact, because of the orthogonality of the basis, each mode acts as a single DOF dynamic system (i.e. mass and stiffness matrixes become diagonal) and then the following system relationship is valid:

$$\ddot{\eta}_m + \omega_m^2 \eta_m = \frac{F_m}{M_{mm}} \quad m = 1, 2, \dots, n \quad (16)$$

being $\ddot{\eta}_m$ and η_m , respectively, the acceleration and displacement of the modal coordinate, and F_m the load value for the m^{th} mode. The modal mass M_{mm} results to be the unity if mass normalisation is imposed.

Modal superposition for static analysis

Even if this is not a common practice in structural analysis, the modal approach can be usefully employed for approximating a

static solution by superposing modes assuming the linear behaviour of the analysed system. In this specific scenario, equation (16) simplifies as follows:

$$\omega_m^2 \eta_m = \frac{F_m}{M_{mm}} \quad (17)$$

The modal forces F_m are obtained, according to equation (21), from the external loads over the entire structure related to pressure and shear stresses. Once η_m are computed from equation (17) it is possible to get the new position of the structure in natural coordinates according to equation (15).

Formulation for unsteady modal analysis

If the physical FSI phenomenon cannot be considered as static, each modal coordinate evolves according to the expression (Meirovitch, 2010):

$$\eta(t) = e^{-\varsigma \omega_n t} \left[\eta_0 \cos(\omega_d t) + \frac{\dot{\eta}_0 + \varsigma \omega_n \eta_0}{\omega_d} \sin(\omega_d t) \right] + e^{-\varsigma \omega_n t} \left\{ \frac{1}{m \omega_d} \int_0^t e^{-\frac{\varsigma \omega_n (t-\tau)}{2m}} f(\tau) \sin[\omega_d (t-\tau)] dx \right\} \quad (18)$$

where η_0 and $\dot{\eta}_0$ are respectively the modal coordinate and the modal velocity at the initial instant of computation. ς is the damping factor and ω_d are the damped circular frequencies of the system having the following expression:

$$\omega_d = \omega_n \sqrt{1 - \varsigma^2} \quad (19)$$

The integral formulation within the curly brackets in the equation (18) is known as *Duhamel integral* and states that the reaction of a linear system subjected to a force $f(t)$ can be expressed by summing all the differential responses developed during the loading history (i.e. equal to the sum of the reactions of the system to the single impulses constituting the total force time evolution). This formulation cannot be applied to a generic numerical analysis. However, if the acting force is assumed to be constant within a single time step, the equation (18) is still valid considering as η_0 and $\dot{\eta}_0$ the values at the beginning of the time step and can be used to update modal coordinates at the end of each time step:

$$\eta(t + \Delta t) = e^{-\varsigma \omega_n \Delta t} \left[\eta(t) \cos(\omega_d \Delta t) + \frac{\dot{\eta}(t) + \varsigma \omega_n \eta(t)}{\omega_d} \sin(\omega_d \Delta t) \right] + e^{-\varsigma \omega_n \Delta t} \left\{ \frac{F(t)}{\omega_d} \left[\frac{4 \omega_d}{\varsigma^2 \omega_n^2 + 4 \omega_d^2} - e^{-\varsigma \omega_n \Delta t} \frac{2 \varsigma \omega_n \sin(\omega_d \Delta t) + 4 \omega_d \cos(\omega_d \Delta t)}{\varsigma^2 \omega_n^2 + 4 \omega_d^2} \right] \right\} \quad (20)$$

providing a suitable and stable tool for a time marching algorithm. Similarly to the steady case, the whole deformation of the structure in unsteady state conditions can be determined by linearly combining a certain number of modes (retained modes) using their time dependent modal coordinates as

weights. In the specific, once η_m are computed from (20), it is possible to get the new position of the structure in natural coordinates according to equation (15).

Setup of modal fluid structure interaction analysis

The RBF mesh morphing concepts presented in section “Radial Basis Functions Mesh Deformation” can be combined to the modal theory presented in the section *Modal analysis and mode superposition* to put in place a straightforward and effective approach toward the solution of industrial FSI problems. The modal FSI implementation is based on a preliminary FEM modal analysis from which a number of natural modes is selected to be used in the creation of a parametric fluid dynamic domain. In a strict sense, modal shapes could result from experiments or other numerical/theoretical approach; for instance, the beam theory can be an excellent tool for the computation of natural modes of simple structures. However, in this paper we assume the modal shape to be computed by FEM. It is important to point out that usually FSI coupling requires an accurate representation of the wetted surfaces both on the structure and the fluid sides; an interpolation across non-matching mesh is usually required, as the spacing of FEA and CFD meshes is usually different because of different solvers requirements. For the implementation of the proposed modal approach such level of detail is not mandatory. The RBF interpolation allows in fact to have modal shapes properly represented on the CFD mesh even if just a poor representation is available on the structure. This means that simple beam or mixed beam/shell FEM models can be adopted making the FSI study possible in situations where a standard two-way approach is not applicable.

The CFD grid is made parametric on modal coordinates and updated by mesh morphing during the progress of the fluid dynamic computation. Modal coordinates are used as weights for the morphing action of each modal shape and are related to the modal forces extracted by integrating the pressure and friction forces on the wall boundaries. They represent the “interface” between the fluid dynamic and the structural solution. The usage of such interface depends on the kind of FSI scheme adopted, but in any case, the evaluation of modal loads is required. As already anticipated, the modal load is a scalar quantity that results from integrating and projecting the actions known at physical coordinates onto the modal shape. In the proposed method, we compute the fluid loads at the nodal position of the wetted surface on the CFD mesh side. The dot product between the CFD nodal force and the nodal displacement of the mode is accumulated for all the CFD nodes that belong to the wetted surface:

$$F_m = \sum_{i=1}^{n_{nodes}} \Delta u_{mi} \cdot F_{CFDi} \quad m = 1, 2, \dots, n \quad (21)$$

The numerical integration of the modal load is performed accounting for both pressure and shear loads, a special care is required to get the correct resultant loads at CFD nodes because usually pressure loads are known at the centroids of the surface mesh cells; in the case of parallel partitioned CFD

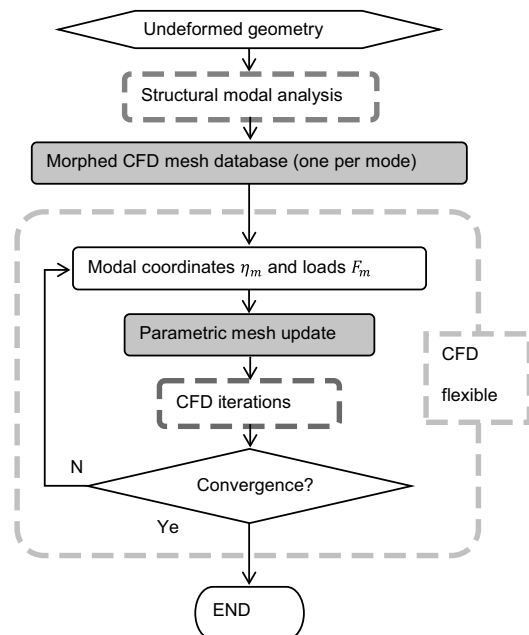
meshes the summation needs a further attention so that overlapping cells at partition interfaces are not summed twice.

The complete workflow of the modal FSI analysis is described in Figure 2. Once available, the modal FEM shapes are used to generate an RBF solution for each one of the selected modes. The solutions are stored to constitute the database of the parametric mesh model (this action has to be performed only once for every structural configuration). The last step consists in implementing, within the CFD solver, the execution of the RBF based mesh update. The structural response can now be evaluated directly in the modal space. The analysis begins with the initialisation of the dynamic mesh morpher with the stored RBF solutions and the modal forces calculation module to be available for recall during the computation.

Mode embedding within the CFD solver allows to tackle different FSI problems. Among them we can consider three classes:

- 1 Transient FSI with movement prescribed in advance. This include flapping devices undergoing a complex motion computed using FEA and multi body solvers or acquired experimentally. Structural modes acceleration in the CFD model can be used to set-up reduced order models (ROM) suitable for non-linear flutter analysis.
- 2 Steady FSI to have the structural deformation modelled on the CFD mesh. This can be used for aeronautical and motorsport applications (wing deformation) and allows to steer shape optimisation accounting for the coupled response. The deflection of the structure can affect strongly the surrounding flow field.
- 3 Full coupled transient FSI. In this case, a time marching solution allows to capture the interaction between the fluid flow and the structural vibration.

Figure 2 Workflow of a modal FSI analysis



For all the three options, the simulation evolves according to modal coordinates and modal forces updating with some differences. In the first case specific time law are decided in advance and assigned to the deformable part; the mode embedding approach allows to get the desired evolution of the shape and to evaluate the modal forces related to the enforced motion. The second and third approaches are similar because in both cases the deformed shape is not known in advance but is a result of the simulation. On the implementation side (even if such functionalities are available as out of the box adopting the proposed software tools), it must be said that there is a major complexity because of the fact that the structural coordinate evolution needs to be handled with specific (and new) functions within the CFD solver environment.

The updating of the steady case is straightforward; considering in fact that a mass normalisation criterion was defined for modes extraction, from equation (17) the modal coordinates are expressed as:

$$\eta_m = \frac{F_m}{\omega_m^2} \quad (22)$$

The final expression of the parametric mesh formulation becomes:

$$\mathbf{X}_{CFD} = \mathbf{X}_{CFD_0} + \sum_{m=1}^n \frac{F_m}{\omega_m^2} \Delta u_m \quad (23)$$

and the update of the mesh is triggered after a certain number of CFD solver iterations (for wings, for instance, it's typical to have less than ten shape updates during a complete steady run); usually the converged results of the rigid case are used as the starting condition for the FSI calculation.

In the case of a transient simulation, such direct expression is not available and new variables are required to store the modal coordinates and their derivatives. Modal coordinates are updated adopting equation (20) according to the evolving modal loads that are considered constant at each time step, the update of the mesh, that is usually triggered at the end of each time step, results from equation (11).

Some doubts about the generality of the modal approach, especially in the application for static FSI analysis, concern the optimal choice of the number of modes to be adopted (Ritter, 2012). It was however demonstrated that when a new configuration has to be studied, and the opportune number of modes to be adopted cannot be estimated on the basis of previous experience, uncertainty can be reduced by a modal base qualification procedure. The procedure consists in the extraction of a large enough modal base, in a preliminary CFD analysis of the rigid model (from which to extract loads and modal coordinates) and in the comparison of the modal amplified solution with the deformation computed by a static FEM analysis (using the same model adopted for the eigenvalues analysis) of the baseline geometry using the loads estimated by the rigid CFD model. The ability of the modal base to correctly replicate the FEM estimated displacement shape is then investigated by examining the vector field obtained subtracting the displacement of the modal approximation (using a candidate number of retained modes) from those coming from the static FEM analysis. The resulting

vector field represents the modal truncation error. It can be used to decide how many modes to retain and to confirm if the guess base is large enough.

Compared to other approaches, as the ones mentioned in the literature review in the introduction, the modal approach has both advantages and disadvantages. For the modal approach, the eigenvalue solution can be seen as a pre-processing stage, being solved only before the FSI iterations are carried, with the advantage of extracting once both modal shapes and frequencies, being them suitable also if there is a change in the boundary conditions. From this point of view, compared to other methods such as the 2-way, the structural evaluations are reduced to a minimum accelerating the whole simulation. The modal approach has also the big advantage of not having all the bottlenecks related to the expensive task of data transfer and load/displacement interpolation from and to the structural solver. Employing a mesh morphing method, the FSI is further accelerated by not needing an expensive remeshing to accommodate the new shape of the fluid dynamic domain. This feature is particularly felt for transient FSI simulations, in which a comparison with ANSYS System Coupling highlight a mesh deterioration because of remeshing and a higher computational cost mostly caused by mapping, being up to 10 times slower compared to modal superposition. All this advantages however come at the cost of the big drawback of the modal superposition method, being it limited only to linear problems for which is valid the eigenvalue problem.

Industrial applications of fluid structure interaction modal approach

The modal approach based on RBF mesh morphing was applied in many industrial applications in several fields of engineering. In this section a set of examples are provided briefly describing the problems and the results obtained. The presented cases are divided in three subsections according to the category of problems that can be faced. Results are collected from literature and a comprehensive description is not herein given. For each reviewed application, the source is cited so that the interested reader can deepen the individual case.

Transient fluid structure interaction with prescribed deformation examples

There are many applications where a known time history needs to be prescribed at the moving walls of a system interacting with a flow. An example of systems requiring this kind of interaction and that can be tackled by employing the modal superposition method are flapping devices, which generate a thrust according to the moving law applied (Ortega-Casanova and Fernandez-Feria, 2016), but also applications in which a given modal shape must be excited to catch the dynamic response of the system, for instance to obtain the frequency response functions (FRF) as shown by Chwalowski *et al.* (2013). To validate the numerical grids available for the HIRENASD wing in the framework of the First Aeroelastic Prediction Workshop (AIAA, 2012), several meshes and solvers were compared to experiments performed by exciting the wing in structural eigenmodes using piezoelectric stacks. The FRF of pressure because of displacements was obtained by carrying first a static FSI analysis and then by sinusoidally amplifying each structural mode displacement in

transient simulations to collect the pressure time histories. A similar approach was followed by Castronovo *et al.* (2017) on the well-known three-dimensional aeroelastic wing AGARD 445.6. With the aim of obtaining a ROM of linearised aeroelastic analyses around non-linear steady solutions, a transient FSI with prescribed deformation was employed to calculate the generalised aerodynamic force matrix. An impulsive gaussian-like function was used to enforce in turn the amplification of each of the first four modes, shown in Figure 3, collecting the history of pressure coefficients projected along each excited mode. By employing this method authors satisfactorily reproduced the transonic dip with errors lower than 1 per cent with respect to experimental results, while low-fidelity linear methods, based on doublet lattice method for aerodynamics, reach errors of about 30 per cent., Figure 3 shows the flutter velocities achieved with the proposed method and compares them with both literature values and those achieved employing a linear method.

Steady fluid structure interaction examples

To demonstrate the quality of the static modal superposition method, in Biancolini *et al.* (2016) the steady aerodynamic response of the transonic wind tunnel model of the PIXX, a Piaggio Aerospace business jet class aircraft, was studied and compared to the one obtained using the 2-way method and to experimental data. Only the wing was assumed as deformable, as shown in Figure 4 left, where the RBF points used to map the FEA computed displacements (green points) onto the CFD mesh are shown. To reduce the morphing action accelerating

the calculation, only the volume elements inside the cylindrical region highlighted by the red points were involved by mesh deformation. The modal superposition method was carried increasing the number of modes employed, demonstrating that a very good result can be achieved using the first two modes only, obtaining a maximum difference with respect to the 2-way method of 0.03 mm, equal to 3.1 per cent of the displacement. The comparison of polar solutions for experimental, 2-way and modal approach is shown in Figure 4 right.

A similar study was conducted on the well-known HIRENASD test case (Chwalowski *et al.*, 2011) available on the database of the NASA Aeroelastic Prediction Workshop (AePW). The aim of this study was to demonstrate the feasibility of the modal method also when a discrepancy between structural and fluid dynamic models is present. In this case the structural model of the wing shown in Figure 5 right, available from the NASA database, was tuned to reproduce the behaviour of the wing tunnel model, in which the fuselage fairing is mechanically

Figure 5 Left: setup for the HIRENASD wing. Right: FEM model of the wing



Figure 3 Left: flutter velocity results for the AGARD 445.6 case. Right: first four AGARD 445.6 modal shapes

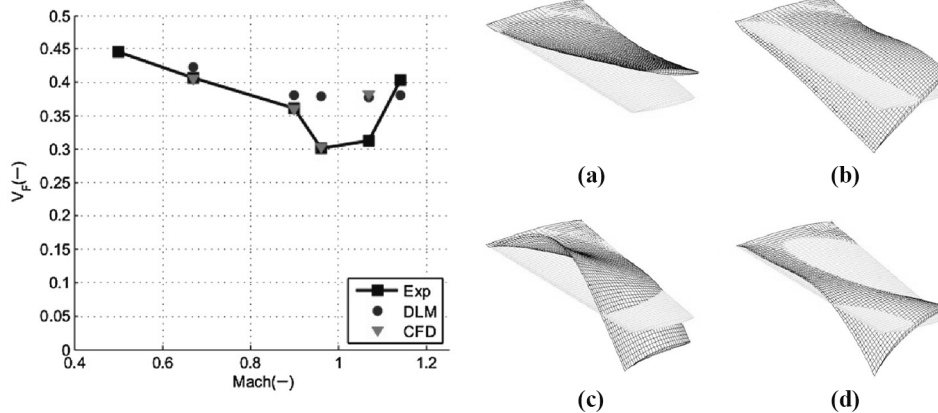
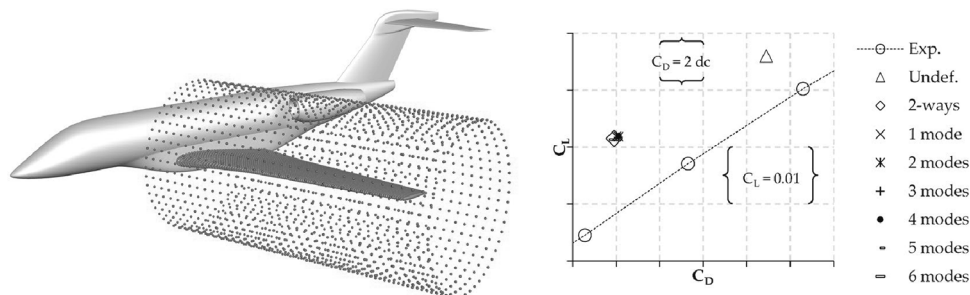


Figure 4 Left: RBF setup for P1XX model. Right: polar results comparison



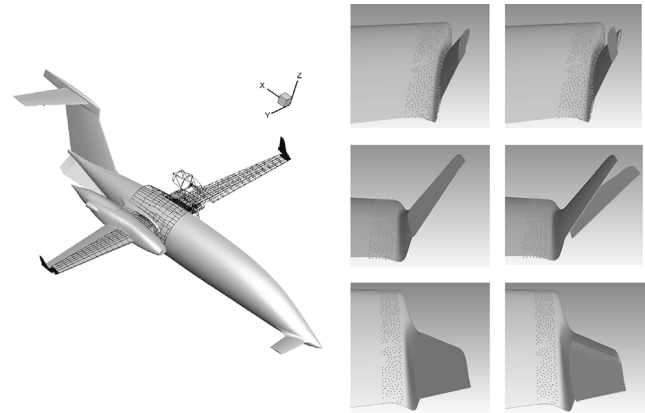
uncoupled from the wing and a slight motion of the wing root is allowed. For this reason, modal shapes were imported as usual and applied to the wetted surfaces, but a small portion of the fuselage around the wing of the CFD model was left free to deform using a buffer region to absorb the required motion, as shown in Figure 5 left, in which the cylinder containing the buffer zone is shown in the case of the second modal shape.

Results in terms of maximum displacements at the tip were compared to the ones obtained using the two-way method, increasing the number of modes employed. The comparison, shown in Figure 6 left, demonstrates that the discrepancy does not reduce further adopting more than four modes, obtaining a very good agreement with respect to experimental data, depicted in Figure 6 right.

The modal superposition approach using RBF can be efficiently employed also for the shape optimisation of structures in which the geometrical variation has a limited influence on the structural behaviour but is relevant from a fluid dynamic perspective. An example of this application was performed within the EU FORTISSIMO 2 project (Costa *et al.*, 2018) on the Piaggio Aerospace Avanti EVO aircraft, adopting the *rbf4aeroFSI* solver based on the modal superposition method, implemented in the RBF4AERO optimisation platform (Bernaschi *et al.*, 2016). With the goal of improving the efficiency of the aircraft, three shape parameters focussing on the winglet geometry were employed, namely the cant, sweep and twist angles, as shown in Figure 7 right. For each design point, seeded employing a genetic algorithm, the baseline CFD mesh was first morphed according to the shape parameters, and then the FSI study was conducted with the modal superposition method. The modal shapes and frequencies employed were the one of the baseline CSM mesh, thus underestimating the influence of the shape parameters in the structural response and drastically accelerating the calculation, being the eigenvalue analysis needed only once. RBF allowed the use of a simplified CSM model, exploiting its extrapolation capabilities in the non-overlapping areas, as shown in Figure 7 left, where the CSM and CFD models were overlapped.

Figure 8 left shows the comparison between the baseline (bottom-grey) and the deformed configuration (coloured with the pressure coefficient map) of the aircraft wing, while on the right side the output parameters of the optimisation are shown. As visible, the FSI optimisation confirms that there is room for

Figure 7 Left: P180 CSM and CFD models. Right: RBF setup for the P180 shape parameters

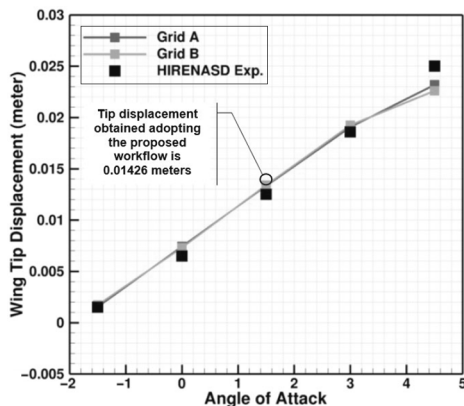


effectively optimise the winglet in cruise conditions. A similar multi-physic workflow has been implemented for the optimisation of the propeller of the Pipistrel's electric aircraft WATTsUP (Andrejašič *et al.*, 2016), obtaining an increase of the weighted sum of efficiencies at two different flight regimes equal to 4.0 per cent.

Transient fluid structure interaction examples

The efficiency of the modal superposition method employing RBF, in terms of computational requirements and flexibility, is particularly evident when dealing with transient FSI cases. In Di Domenico *et al.* (2018) authors reproduced the test case shown in Ausoni (2009), consisting in a NACA0009 Hydrofoil submerged in water. The aim of the work was to reproduce, adopting the boundary conditions shown in Figure 9 and at different flow velocities, the vortex shedding induced vibrations and the lock-in/lock-off frequencies for which experimental data is available in literature. Simulations were carried out importing the first six modal shapes at two different velocities of the flow, 16m/s and 22m/s, extracting the displacements in time of a chosen point near the trailing edge and studying the behaviour in the frequency domain. Results, shown in Figure 9 right, compare very good with experimental data, exhibiting lock-in and lock-off frequencies of 909.91 Hz and 1202.9 Hz.

Figure 6 Left: displacements compared to experimental results. Right: comparison to two-way method



	Tip displacement (mm)	Relative discrepancy (%)
2-way	14.44	-
1 mode	15.26	-5.64
2 modes	14.18	1.81
3 modes	14.18	1.80
4 modes	14.26	1.29
5 modes	14.26	1.29
6 modes	14.26	1.29

Figure 8 Left: deformed and not deformed configurations. Right: design space main results

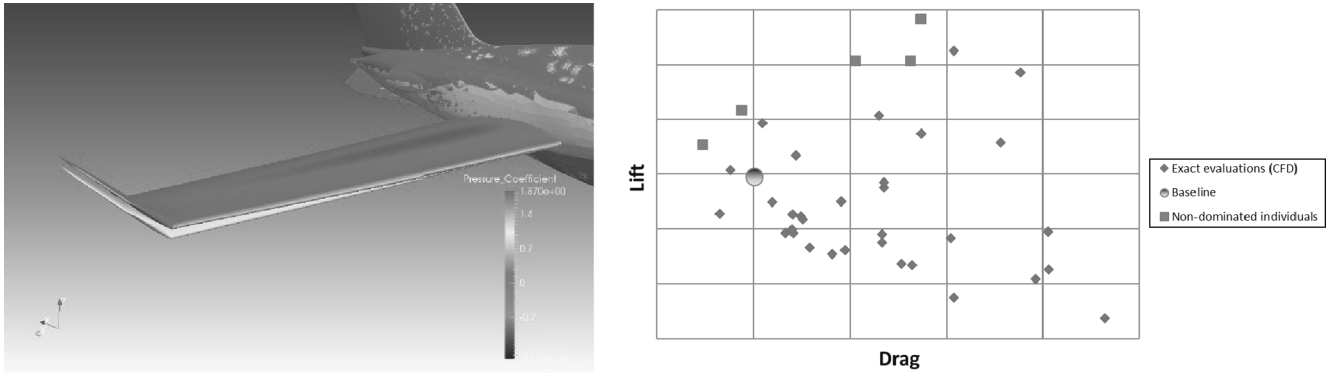


Figure 9 Left: boundary conditions for the NACA0009 hydrofoil. Right: results compared to experiments

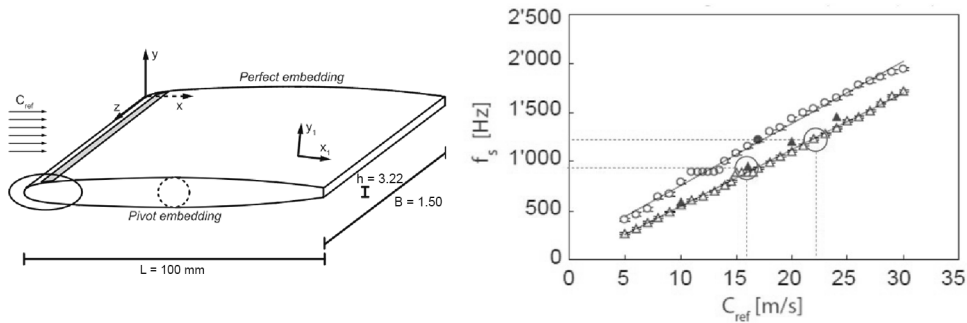
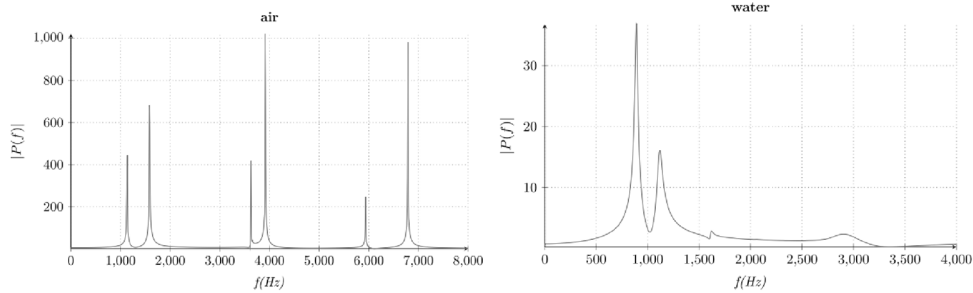


Figure 10 Spectral analysis for 16 m/s and 22 m/s



With a 16 m/s flow the hydrofoil is interested by resonance at 909.91 Hz, a lower value compared to the frequency obtained by the eigenvalue analysis in air, for which the first mode had a frequency of 1133.8 Hz. To extract the natural frequencies of the hydrofoil in water another transient FSI analysis was carried, this time imposing a zero velocity of the flow and applying an amplification for all the modal shapes (obtained in air) at $t = 0$, later removed. The same simulation was carried replacing the water with air. Displacements in time were converted in the frequency domain and the spectral analysis is shown in Figure 10. Results in air (left) match perfectly, as expected, those obtained by the eigenvalue analysis, while the simulation in calm water shows that the first natural frequency of the submerged hydrofoil is equal to 891.9 Hz. This value matches perfectly experimental data and validates the lock-in resonant frequency obtained with the

Figure 11 Numerical grid for the heat exchanger case and the first three modal shapes for each tube

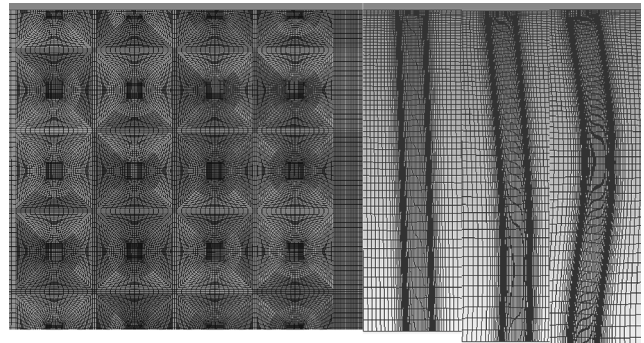
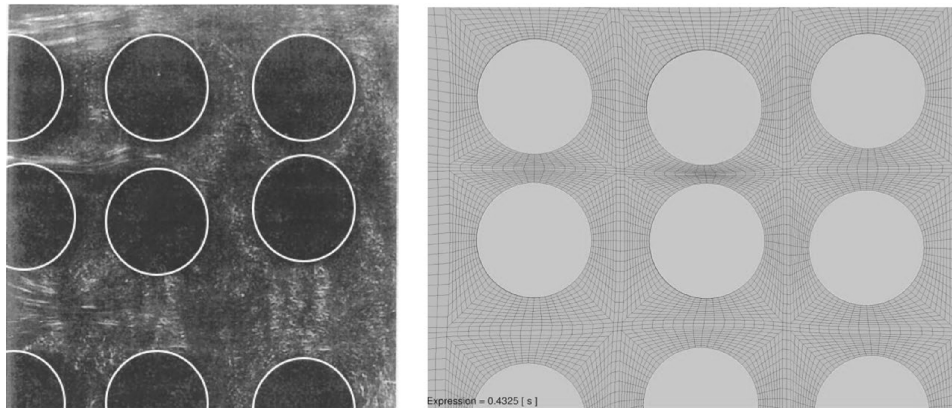


Figure 12 Left: experimental deformation at 0.44 m/s. Right: numerical deformations for the same velocity



simulation at 16 m/s. Imposing prescribed deformations or loads is very easy using the modal superposition method, since those boundary conditions can be introduced in the calculation as modal coordinates, as done in the hydrofoil case, or as modal forces in equation (21). This last strategy was employed to simulate the weight of a store by Reina *et al.* (2014), adding at each FSI cycle the modal force introduced by the store to the one computed on the wetted surfaces and later removed to simulate store separation.

Transient modal superposition allows also to deal with cases in which multiple different flexible objects are interacting each other's, as in the case shown by Costa *et al.* (2017), in which the aim was to study the vortex shedding in an in-line cross-flow heat exchanger composed by a 3X4 array of tubes and to compare results to the literature values found in (Ali Abd-rabbo, 1984). A single eigenvalue problem was solved to obtain modal shapes and frequencies, being the same for all tubes. The RBF problem was replicated for each tube by translating the source points to overlap with the geometry. In Figure 11, a portion of the numerical grid and the side view for the first three modal shapes is shown.

The FSI transient simulation was carried out at different velocities of the flow starting from 0.32 m/s, obtaining at first small vibrations but causing instabilities at 0.37 m/s. Induced vortices disturb the flow also for downstream tubes, triggering resonance. This phenomenon is more evident raising the flow velocity at 0.44 m/s as shown in Figure 12, where numerical and experimental deformations are depicted. Numerical results compare well with experimental ones, in which the critical velocity is 0.35 m/s.

Conclusions

In this paper, a fast and effective approach to tackle complex fluid structure interactions problems was presented. CFD and CSM models are coupled by making the CFD grid elastic embedding the structural modes using RBF mesh morphing. After a theoretical explanation of the method, the feasibility and applicability of this method for industrial problems and employing different solvers is showcased with several examples including static FSI, dynamical transient problems and cases in which the vibration is prescribed or excited by external devices.

References

- Aeroelastic Prediction Workshop (AIAA) (2012), available at: https://c3.nasa.gov/dashlink/static/media/other/AEPW_legacy.htm, (accessed 13 September 2018).
- Ali Abd-rabbo, A. (1984), "Flow visualization and dynamics of heat exchanger tube arrays in water cross-flow", PhD thesis, McMaster University, July 1984.
- Andrejasić, M., Erzen, D., Costa, E., Porziani, S., Biancolini, M. and Groth, C. (2016), "A mesh morphing based FSI method used in aeronautical optimization applications", *Proceedings of the VII European Congress on Computational Methods in Applied Sciences and Engineering. Institute of Structural Analysis and Antiseismic Research School of Civil Engineering National Technical University of Athens (NTUA) Greece*, ISBN: 9786188284401.
- Ausoni, P. (2009), "Turbulent vortex shedding from a blunt trailing edge hydrofoil", PhD thesis. STI, Lausanne.
- Beckert, A. and Wendland, H. (2001), "Multivariate interpolation for fluid-structure-interaction problems using radial basis functions", *Aerospace Science and Technology*, Vol. 5 No. 2, pp. 125-134.
- Benra, F.K., Dohmen, H.J., Pei, J., Schuster, S. and Wan, B. (2011), "A comparison of one-way and two-way coupling methods for numerical analysis of fluid-structure interactions", *Journal of Applied Mathematics*, Vol. 2011, available at: <https://doi.org/10.1155/2011/853560>
- Bernaschi, M., Sabellico, A., Urso, G., Costa, E., Porziani, S., Lagasco, F., Groth, C., Cella, U., Biancolini, M.E., Kapsoulis, D.H., Asouti, V.G. and Giannakoglou, K.C. (2016), "The RBF4AERO benchmark technology platform", *7th ECCOMAS Congress 2016, Crete Island*, 5-10 June.
- Biancolini, M.E., Cella, U., Groth, C. and Genta, M. (2016), "Static aeroelastic analysis of an aircraft wind-Tunnel model by means of modal RBF mesh updating", *ASCE's Journal of Aerospace Engineering*, Vol. 29 No. 6.
- Biancolini, M.E., Biancolini, C., Costa, E., Gattamelata, D. and Valentini, P.P. (2009), "Industrial application of the meshless morpher RBF morph to a motorbike windshield optimisation", *EASC 2009 Proceedings of the 4th European Automotive Simulation Conference, Munich*, 6-7 July 2009.
- Biancolini, M.E., Chiappa, A., Giorgetti, F., Groth, C., Cella, U. and Salvini, P. (2018), "A balanced load mapping method based on radial basis functions and fuzzy sets", *International*

- Journal for Numerical Methods in Engineering*, available at: <https://doi.org/10.1002/nme.5850>
- Castronovo, P., Mastroddi, F., Stella, F. and Biancolini, M.E. (2017), “Assessment and development of a ROM for linearized aeroelastic analyses of aerospace vehicles”, *CEAS Aeronautical Journal*, Vol. 8 No. 2, pp. 353–369.
- Cebral, J.R. and Löhner, R. (1997), “Conservative load projection and tracking for fluid-structure problems”, *AIAA Journal*, Vol. 35 No. 4, pp. 687–692, doi: 10.2514/2.158.
- Chwalowski, P., Florance, J.P., Heeg, J., Wieseman, C.D. and Perry, B. (2011), Preliminary computational analysis of the HIRENASD configuration in preparation for the aeroelastic prediction workshop, IFASD-2011-108, pp. 1–21.
- Chwalowski, P., Heeg, J., Dalenbring, M., Jirasek, A., Ritter, M. and Hansen, T. (2013), Collaborative hirenasd analyses to eliminate variations in computational results, IFASD-2013-1D.
- Cook, R.D., Malkus, D.S., Plesha, M.E. and Witt, R.J. (2002), “*Concepts and Applications of Finite Element Analysis*, 4th ed., John Wiley & Sons.
- Costa, E., Biancolini, M.E., Groth, C., Caridi, D., Lavedrine, J. and Dupain, G. (2017), “Unsteady FSI analysis of a square array of tubes in water crossflow”, *Flexible Engineering*, in press.
- Costa, E., Groth, C., Biancolini, M.E., Asouti, V., Giannakoglou, K., Spisso, I., Arlandini, C., Sabellico, A., Bernaschi, M., Travostino, G., Morasso, R. and Cozzolino, A. (2018), “FSI optimization of industrial airplanes: the P180 Avanti EVO study”, *Proceedings of the International CAE Conference 2018, 7th-8th October, Vicenza*.
- De Boer, A., van der Schoot, M.S. and Bijl, H. (2007), “Mesh deformation based on radial basis function interpolation”, *Computers & Structures*, Vol. 85 Nos 11/14, pp. 784–795.
- Degroote, J. (2013), “Partitioned simulation of Fluid-Structure interaction”, *Archives of Computational Methods in Engineering*, Vol. 20 No. 3, pp. 185–238, available at: <https://doi.org/10.1007/s11831-013-9085-5>
- Di Domenico, N., Groth, C., Wade, A., Berg, T. and Biancolini, M.E. (2018), “Fluid structure interaction analysis: vortex shedding induced vibrations”, *Procedia Structural Integrity*, Vol. 8, pp. 422–432.
- Dowell, E.H. and Hall, K.C. (2001), “Modeling of fluid-structure interaction”, *Annual Review of Fluid Mechanics*, Vol. 33 No. 1, pp. 445–490.
- Franke, R. (1982), “Scattered data interpolation: tests of some method”, *Mathematics of Computation*, Vol. 38 No. 157, pp. 181–200, doi: 10.2307/2007474.
- Hou, G. and Satyanarayana, A. (2000), “Analytical sensitivity analysis of a static aeroelastic wing”, in 8th Symposium on Multidisciplinary Analysis and Optimization, American Institute of Aeronautics and Astronautics, Reston, available at: <https://doi.org/10.2514/6.2000-4824>
- Hou, G., Wang, J. and Layton, A. (2012), “Numerical methods for fluid-structure interaction – a review”, *Communications in Computational Physics*, Vol. 12 No. 2, pp. 337–377, available at: <https://doi.org/10.4208/cicp.291210.290411s>
- Hubner, B., Walhorn, E. and Dinkler, D. (2004), “A monolithic approach to fluid-structure interaction using space-time finite elements”, *Computer Methods in Applied Mechanics and Engineering*, Vol. 193, pp. 2087–2104.
- Jin, R., Chen, W. and Simpson, T.W. (2001), “Comparative studies of metamodelling techniques under multiple modelling criteria”, *Structural and Multidisciplinary Optimization*, Vol. 23 No. 1, pp. 1–13.
- Masud, A., Bhanabhagwanwala, M. and Khurram, R.A. (2007), “An adaptive mesh rezoning scheme for moving boundary flows and fluid-structure interaction”, *Computers & Fluids*, Vol. 36 No. 1, pp. 77–91.
- Meirovitch, L. (2010), *Fundamentals of Vibrations*, Reissue edition, Waveland Press Inc.
- Mittal, R. and Iaccarino, G. (2005), “Immersed boundary methods”, *Annual Review of Fluid Mechanics*, Vol. 37 No. 1, pp. 239–261.
- Morand, H.J.-P. and Ohayon, R. (1995), *Fluid-Structure Interaction: Applied Numerical Methods*, Wiley.
- Ortega-Casanova, J. and Fernandez-Feria, R. (2016), “Analysis of the aerodynamic interaction between two plunging plates in tandem at low Reynolds number for maximum propulsive efficiency”, *Journal of Fluids and Structures*, Vol. 63, pp. 351–373.
- Reina, G., Della Sala, A., Biancolini, M.E., Groth, C. and Caridi, D. (2014), “Store separation: theoretical investigation of wing aeroelastic response”, Paper presented at Aircraft structural design conference, Belfast.
- Ritter, M. (2012), “Static and forced motion aeroelastic simulations of the HIRENASD wind tunnel model”, *53rd AIAA/ASME/ASCE/AHS/ASC Structures, Structural Dynamics and Materials Conference*, number 1633, Honolulu, HI, 23–26 April.
- Rousseau, Y., Men'shov, I. and Nakamura, Y. (2007), “Morphing-based shape optimization in computational fluid dynamics”, *Transactions of the Japan Society for Aeronautical and Space Sciences*, Vol. 50 No. 167, pp. 41–47.
- Van Zuijlen, A.H., De Boer, A. and Bijl, H. (2007), “Higher-order time integration through smooth mesh deformation for 3D fluid-structure interaction simulations”, *Journal of Computational Physics*, Vol. 224 No. 1, pp. 414–430.
- Wang, T., Wüchner, R., Sicklinger, S. and Bletzinger, K.U. (2016), “Assessment and improvement of mapping algorithms for non-matching meshes and geometries in computational FSI”, *Computational Mechanics*, Vol. 57 No. 5, pp. 793–816, doi: 10.1007/s00466-016-1262-6.

Further reading

- Cella, U. (2017), “Setup and validation of high fidelity aeroelastic analysis methods based on RBF mesh morphing”, PhD thesis, University of Rome “Tor Vergata”.
RBF Morph (2018), available at: www.rbf-morph.com/

Corresponding author

Marco Evangelos Biancolini can be contacted at: biancolini@ing.uniroma2.it

For instructions on how to order reprints of this article, please visit our website:

www.emeraldgroupublishing.com/licensing/reprints.htm

Or contact us for further details: permissions@emeraldinsight.com

Multidisciplinary wing design of a light long endurance UAV

Wojciech Grendysa

Faculty of Power and Aeronautical Engineering, Warsaw University of Technology, Warszawa, Poland

Abstract

Purpose – The purpose of this paper is finding the optimal geometric parameters and developing of a method for optimizing a light unmanned aerial vehicle (UAV) wing, maximizing, at the same time, its endurance with the assumed parameters of aircraft mission.

Design/methodology/approach – The research is based on the experience gained by the author's contribution to the project of building medium-altitude, long-endurance class, light UAV called "Samonit". The author was responsible for the structure design, wind tunnel tests and flight tests of the "Samonit" aircraft. Based on the experience, the author was able to develop an optimization process considering various disciplines involved in the whole aircraft design topics such as aerodynamics, flight mechanics, structural stiffness and weight, aircraft stability and maneuverability. The presented methodology has a multidisciplinary nature, as in the process of optimization both aerodynamic aspects and the influence of wing geometric parameters on the wing structure and weight and the aircraft payload were taken into account. The optimal wing configuration was obtained using the genetic algorithms.

Findings – As a result, a set of wing geometrical parameters has been obtained that allowed for achieving twice as long endurance as compared with the initial one.

Practical implications – Using the methodology presented in the paper, an aircraft designer can easily find the optimum wing configuration of a designed aircraft, satisfying the mission requirements in a best way.

Originality/value – An original procedure has been developed, based on the actual design, wind tunnel tests and numerical calculations of "Samonit" aircraft, enabling the determination of optimum wing configuration for a small unmanned aircraft.

Keywords UAV, Multidisciplinary, Aircraft design, Optimization, Endurance, Range

Paper type Research paper

Introduction

The unmanned aerial vehicle (UAV) applications in military strategic and tactical reconnaissance have been known for many years in developed countries. Less common is the use of UAV in civil missions, for the following two reasons: i.e. a relatively high price of a UAV system and the lack of regulations for legitimate UAV operation.

More than ten-fold reduction in the weight of forward-looking infrared (FLIR) cameras or synthetic aperture radar (SAR) device without any loss in image quality has resulted in the fact that the reconnaissance tasks performed so far by the medium-altitude, long-endurance class aircraft (take-off weight of 1,500 kg) have been now performed by unmanned mini-planes with a mass of up to 100 kg and a span of only 4-5 m (instead of 12 m). Miniaturization of image recognition and transmission devices and the possibility of using a mini-plane as a carrier allowed for significant reduction of the whole system price. It is also much easier to find legal solutions for low take-off mass aircraft (similar to the radio-controlled models) (Goraj *et al.*, 2010). For these reasons, manufacturing light unmanned airplanes is becoming more and more justified, and that is why

in 2007 the project of manufacturing a light unmanned airplane called "Samonit" was launched at Warsaw University of Technology (Figure 1).

At an early stage of the aircraft design process, the main designer should decide how general the new aircraft must be. When increasing the aircraft applicability, one often loses the ability to maximize the flight performance matched to the target mission (Steinbuch *et al.*, 2003; Steinbuch and Shepshelovich, 2004).

The use of a small aircraft as a base for an unmanned aerial vehicle system gives the possibility of better matching of this system to the requirements of the mission in comparison to the use of a larger aircraft. This is because using a small aircraft makes it easy to prepare new, special components (e.g. wing) optimized for the requirements of the new mission. One can imagine a production company offering an unmanned aircraft built of a standard fuselage and a wing strictly matched to the requirements set by the customer. It is now possible to generate a numeric document of the wing structure in such a way that after changing the geometric parameters of the wing, the structure automatically adapts to the new geometry. Using numerical machining technology, it is possible to quickly and easily prepare production tools (a molded set for composite manufacturing) for the new structure. Because of this capability, it is particularly important to create a tool that allows

The current issue and full text archive of this journal is available on Emerald Insight at: www.emeraldinsight.com/1748-8842.htm



Aircraft Engineering and Aerospace Technology
91/6 (2019) 905-914
© Emerald Publishing Limited [ISSN 1748-8842]
[DOI 10.1108/AEAT-09-2018-0256]

Received 27 September 2018
Revised 26 November 2018
19 December 2018
Accepted 21 December 2018

Figure 1 "Samonit" in flight



quick optimization of the wing configuration for the given mission parameters (Jameson *et al.*, 2007).

The use of unmanned mini-planes for various missions gives the designer some extra possibilities. As a small aircraft can be easily modified, its parameters can be more suited to the given mission. The greater susceptibility for modifications of such aircraft results from its small size and from the fact that the production of prototype or a small production batch needs lower financial and time contribution. Using composite materials for structure, computer-aided design and numerical machining tools, one can build a mini UAV in a small workshop in a short time and with a relatively small financial contribution. Based on the "Samonit" project, it is estimated that the cost of preparing the production of a small series of aircrafts, including the tools necessary to produce parts of the structure and subassemblies, but excluding the technical labor, would not exceed €10,000.

Automation of the design process and simplicity of arrangement aspects allow for perfect matching of the aircraft to its mission (Yakinthos, 2018). Additionally, when new requirements appear, the design can be easily modified or redesigned. Computer-aided design systems allow for partial automation of the aircraft structure design process, but there are no tools for straightforward optimization of the designed aircraft configuration to meet specific mission requirements (Mieloszyk, 2017). This referenced article presents the framework for the optimization process used to determine an optimal wing configuration of the designed aircraft with respect to the mission requirements imposed.

The following process is based on the experience gained from the development of "Samonit" project. The results obtained from tests of the "Samonit" aircraft together with its components are also taken into account. The results of wind tunnel tests were used to determine the aerodynamic drag of the whole aircraft and to verify the results of numerical calculations of the wing flow. Data from the weight of the wing structure allowed for building an analytical model that relates geometric parameters of the wing to the weight of its structure. The thrust-specific fuel consumption of the aircraft engines was also measured. This is a particularly important parameter, necessary for the correct calculation of the aircraft performance (Goraj *et al.*, 2012).

During the "Samonit" project, three different wing configurations of the aircraft were built and tested. In this number, there was one classic configuration and two tailless configurations. The final configuration is tailless. This paper focuses on the multidisciplinary design optimization (MDO) of

the wing geometry parameters of tailless aircraft similar to the "Samonit" is shown in Figure 2.

This paper consists of two parts. The first part presents a simplified multidisciplinary analytical model allowing one to optimize the wing aspect ratio, maximizing the endurance. Moreover, the mathematical analytical model offers the possibility to trace the relationship of aerodynamic and structural parameters to the aircraft performance and helps to understand how the numerical model works (Gudmundsson, 2014). The framework and results of the numerical procedure searching for the optimal wing configuration to maximize the aircraft endurance are described in a "multidisciplinary wing design" section (Martins and Lambe, 2013).

Analytical approach

The following chapter presents the analytical, multidisciplinary mathematical model of the wing taking into account the effect of wing aspect ratio on endurance through changing aerodynamic properties and weight of the wing structure. This model illustrates the effects of interactions between aerodynamic forces and weight that a designer can use in a preliminary analysis of optimal wing parameters.

The aircraft endurance can be described by the formula:

$$E = - \int_{W_1}^{W_2} \frac{1}{c_t D} \frac{dW_f}{W} \quad (1)$$

And for the propeller-driven aircraft:

$$E = - \int_{W_1}^{W_2} \frac{\eta_{pr} C_L}{c V_\infty C_D} \frac{dW}{W} \quad (2)$$

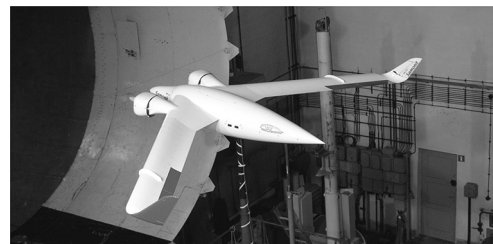
It can be assumed that during the flight parameters η_{pr} , c , ρ_∞ and $C_L^{3/2}/C_D$ remain constant, thus:

$$E = \frac{\eta_{pr}}{c} \frac{C_L^{3/2}}{C_D} \sqrt{2 \rho_\infty S} \left(\frac{1}{\sqrt{W_2}} - \frac{1}{\sqrt{W_1}} \right) \quad (3)$$

where:

- E = endurance [s];
- η_{PR} = propeller efficiency;
- c = specific fuel consumption [N/(N*m/s)*1/s] = [1/m];
- C_L = lift force coefficient;
- C_D = drag force coefficient;
- ρ = air density [kg/m³];

Figure 2 "Samonit" in a wind tunnel



S = wing area (reference area) [m²];
 W, W_1, W_2 = weight (current, take-off, landing) [N]; and
 $\frac{C_L^{3/2}}{C_D}$ = endurance coefficient.

From equation (3), it follows that the endurance depends on aerodynamic parameters, specific fuel consumption (engine performance) and weight of the spent fuel (relation between the aircraft weights with full and empty fuel tanks, respectively). The maximum take-off weight is a basic parameter of the aircraft; therefore, it should be considered as a constant. Similarly, the propulsion performance for a specific engine and propeller model, specific fuel consumption and propeller efficiency remain constant. Therefore, it follows that the endurance-affecting parameters are essentially the endurance coefficient and the landing weight. To search effectively for the optimal wing configuration that maximizes the endurance, it is necessary to consider the influence of wing geometric parameters on aerodynamic coefficients and on the aircraft structure and stiffness and, as a result, on the wing weight. As one can see, the optimization task defined in this way is a multidisciplinary problem.

Wing structure influence

Hereinafter, we concentrate on the determination of wing weight as a function of its aspect ratio, A . We assume that the reference surface of the wing remains unchanged, so that the wingspan is as follows: $b = \sqrt{S} * \sqrt{A}$ and the chord (assuming that the wing taper ratio is equal to 1) has the value of $c = \sqrt{S}/\sqrt{A}$.

It is assumed that bending loads are carried only by the wing spar. Another assumption is that the spar has a C cross-section, although the method of modeling is exactly the same for an H-beam or a box shape. Looking for the influence of aspect ratio on the wing weight, a rectangular shape of the wing can be assumed, so the wing thickness and height of the spar remain constant along the span. The experience gained in the ‘‘Samonit’’ project shows that the spar weight is about 20 per cent of the wing structure weight.

The aspect ratio affects both the bending moment distribution and moment of inertia of the spar cross-section. These relations should also be taken into account, using the equation that represents the maximum stress of the wing spar caps:

$$\sigma_{max} = \frac{M_g * z_{max}}{I_y} \leq \sigma_{lim} \quad (4)$$

where:

$I_y = \frac{d * h^2 * t}{4}$ = moment of inertia of the wing and spar;
 M_g = bending moment; and
 z_{max} = half of the spar height.

As the wing aspect ratio increases, the bending moment increases proportionally to the concentrated force arm, and thus proportionally to the wingspan. The spar height decreases proportionally to the chord (because the relative thickness of the profile remains constant), while the spar caps thickness should increase proportionally to square of the wingspan. These relations can be represented by the following set of equations:

$$\frac{h}{h_0} = \frac{b_0}{b} \Rightarrow h = h_0 \frac{b_0}{b} = h_0 \frac{\sqrt{A_0 * S}}{\sqrt{A * S}} = h_0 \frac{\sqrt{A_0}}{\sqrt{A}} \quad (5)$$

thus:

$$\frac{t}{t_0} = \frac{b^2}{b_0^2} = \frac{h_0^2}{h^2} \xrightarrow{I_y=const} t = t_0 \frac{b^2}{b_0^2} = t_0 \frac{A * S}{A_0 * S} = t_0 \frac{A}{A_0} \quad (6)$$

$$\frac{M_g}{M_{g0}} = \frac{b}{b_0} \Rightarrow M_g = M_{g0} \frac{b}{b_0} = M_{g0} \frac{\sqrt{A * S}}{\sqrt{A_0 * S}} = M_{g0} \frac{\sqrt{A}}{\sqrt{A_0}} \quad (7)$$

where:

A = aspect ratio;
 b = half of span;
 h = height of the spar;
 t = spar cap thickness; and
 $A_0, b_0, h_0, t_0, M_{g0}$ = reference value of parameter from the Samonit.

The total mass increase is proportional to the thickness increase (as a result of a change in geometry and for $I_y=const$) and from the bending moment increase, so the total increase in the mass of the spar caps is:

$$\begin{aligned} \Delta m_{caps} &= M_{g0} \frac{\sqrt{A}}{\sqrt{A_0}} * t_0 \frac{A}{A_0} = C * \frac{\sqrt{A}}{\sqrt{A_0}} * \frac{\sqrt{A}}{\sqrt{A_0}} * \frac{\sqrt{A}}{\sqrt{A_0}} \\ &= C * \left(\frac{A}{A_0}\right)^{3/2} \end{aligned} \quad (8)$$

where C is a proportional constant and it can be determined from the boundary conditions.

The landing weight W_2 in equation (1) is lower than the initial weight W_1 by the weight of spent fuel and depends on the wing aspect ratio A . An increase in the aspect ratio increases the spar weight and consequently reduces the fuel weight, a decrease in the aspect ratio causes a decrease in the spar weight and an increase in the weight of available fuel. For the endurance optimization we assume that, according to equation (8), the spar weight is proportional to the aspect ratio A with the exponent of (3/2), and therefore, we assume the following functional relation:

$$W_2 = W_{20} + K \left(\frac{A}{A_0}\right)^{3/2} \quad (9)$$

where:

W_{20} = aircraft weight with no spar and fuel;
 A_0 = Samonit wing aspect ratio; and
 K = Samonit spar weight, for $A = A_0 = 10$.

Aerodynamics

Consider again equation (3). A propeller driven aircraft flight is calculated. A flight is performed at the minimum required power and hence at the maximum endurance coefficient $C_L^{3/2}/C_D$.

The required power can be written as follows:

$$P_R = D * V = W * \frac{C_D}{C_L} * \sqrt{\frac{2W}{\rho * S * C_L}} = \sqrt{\frac{2W^3}{\rho * S}} * \frac{C_D}{C_L^{3/2}} \quad (10)$$

In most cases, it can be assumed that the polar curve is symmetrical; hence, the following can be written:

$$C_D = C_{D0} + \frac{1}{\pi A} C_L^2 \quad (11)$$

where:

C_{D0} = minimal drag coefficient.

Using equation (10) for the required power and assuming a symmetrical polar curve and best flight conditions, we obtain the relation between the endurance coefficient and wing aspect ratio:

$$\frac{C_L^{3/2}}{C_D} = \frac{(3\pi A)^{3/4} * C_{D0}^{-1/4}}{4} \quad (12)$$

Results

Now the relation between the endurance and aspect ratio can finally be found. Equations (9) and (12) are based on equation (3) and result in the following:

$$E = \frac{\eta_{pr}}{c} * \frac{(3\pi A)^{3/4} * C_{D0}^{-1/4}}{4} * \sqrt{2\rho_\infty S} * \left(\frac{1}{\sqrt{W_{20} + K\left(\frac{A}{A_0}\right)^{3/2}}} - \frac{1}{\sqrt{W_1}} \right) \quad (13)$$

As one can see, equation (13) shows a direct relation describing the effect of aspect ratio on flight endurance. The wing aspect ratio influences both aerodynamic parameters and the maximum fuel amount, therefore, the aforementioned approach can be considered as a multidisciplinary one. Figure 3 shows the defined function:

From Figure 3, it can be seen that the relationship between the endurance and aspect ratio has a clear maximum:

$$E_{max}(A = 32.8) = 26.67[h]$$

The limitations imposed by the simplified approach used should be taken into account. When increasing the aspect ratio, one reduces the wing chord, and therefore, changes the Reynolds (Re)

number. A high aspect ratio can yield such a small Re number that the nature of the wing flow changes. Another limitation is imposed by the wing structure. In this study, the C-beam cross-section was assumed. Increasing the aspect ratio leads to a reduction in the wing chord and spar height. A low spar height may bring about the cross-section change from C to a rectangle and it may be impossible to achieve the required strength.

The most important conclusion resulting from this simplified analysis is that the relationship between the endurance and aspect ratio has a clear maximum appearing for an aspect ratio greater than the value used in the “Samonit” project.

The approach presented is based on several simplifications, i.e. rectangular load distribution, symmetrical polar curve, the constant thickness of the spar caps and lack of the wing tapering. The study should be treated as an estimation of the relation between endurance and aspect ratio. A more detailed analysis, based on numerical calculations and optimization, taking into account the aspect ratio, taper ratio and wing twist angle, respectively, is presented below.

Multidisciplinary wing design

The framework and results of the numerical procedure searching for the optimal wing configuration that maximizes the aircraft endurance, are presented below. The considered aircraft in the flying wing configuration agrees with the assumptions accepted for the “Samonit” project (Table I).

The presented procedure aims at searching for optimal values of three independent variables maximizing the objective function. The aspect ratio, taper ratio and twist of the wing were taken as independent variables (or decision variables). A flowchart of the optimization process is shown in Figure 4.

The objective function value is determined by the formula:

$$E = \frac{\eta_{pr}}{c} \sqrt{2\rho_\infty S} \frac{C_L^{3/2}}{C_D} \left(\frac{1}{\sqrt{W_2}} - \frac{1}{\sqrt{W_1}} \right) = const \frac{C_L^{3/2}}{C_D} \left(\frac{1}{\sqrt{W_2}} - \frac{1}{\sqrt{W_1}} \right) \quad (14)$$

Figure 3 Relation between the endurance and aspect ratio

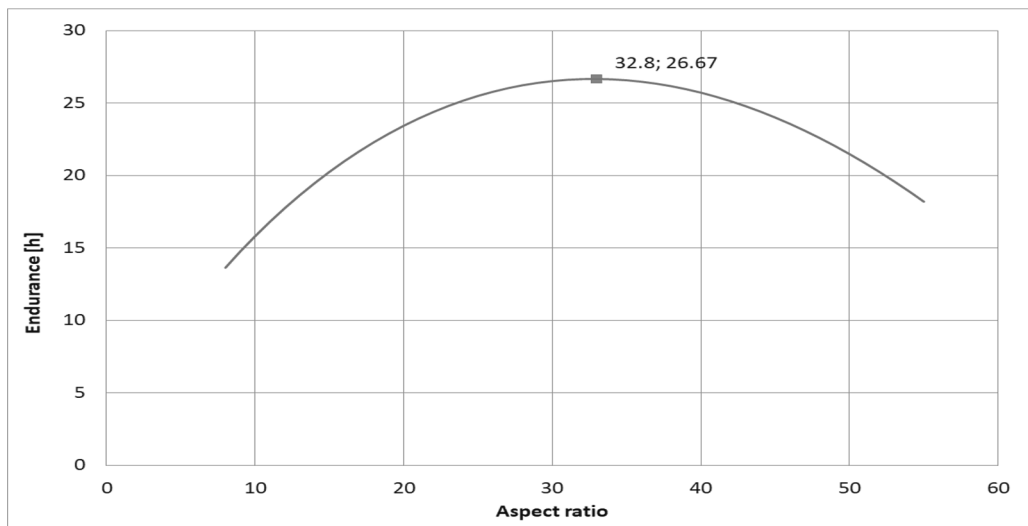
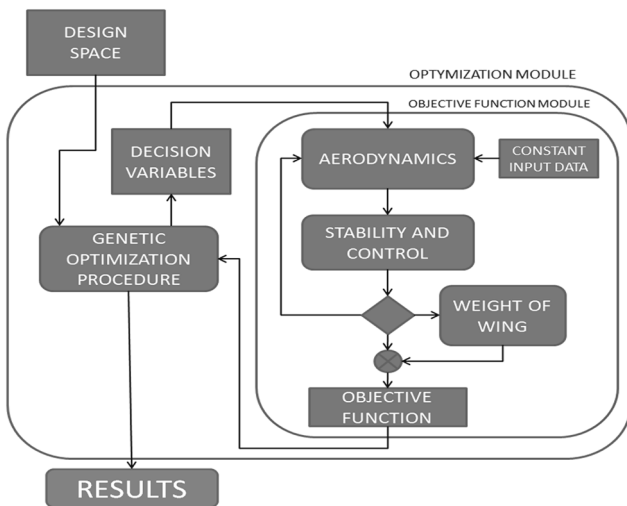


Table I Technical data

Medium-altitude, long-endurance class, light and unmanned aerial vehicle		
Parameter	Value	Unit
Maximum take-off weight	79	kg
Payload	16.6	kg
Empty weight	29	kg
Fuel	33.4	kg
Fuel reserve	3.34	kg
Stall speed	20.8	m/s
Operating speed	27	m/s
Maximum speed	70	m/s
Maximum load factor (79 kg)	6	–
Operating level	200	m

Figure 4 Optimization procedure flowchart



The first part of the equation (14) represents the aircraft and assumed mission parameters. Since these parameters are constant they, therefore, do not have any impact on the solution and have been neglected in the process of optimization. As a result, the target function is described by equation (15):

$$F(A, \lambda, t) = \frac{C_L^{3/2}}{C_D} \left(\frac{1}{\sqrt{W_2}} - \frac{1}{\sqrt{W_1}} \right) \quad (15)$$

As can be seen from equation (15), the objective function value is determined by:

- $C_L^{3/2}/C_D$ = endurance coefficient;
- W_1 = take-off weight; and
- W_2 = landing weight of the aircraft.

The aerodynamic coefficients were a result from numerical aerodynamic calculations and wind tunnel tests. A detailed description of the process can be found in the sub-section Aerodynamics.

The maximum take-off weight of the considered aircraft is known from the “Samonit” project. The values of W_2 and W_1 differ by the fuel weight spent during the flight. The landing weight (W_2) consists of: the weight of the structure, aircraft

equipment, mission equipment and fuel reserve. The aspect ratio, taper ratio and twist, respectively, of the wing as independent variables, affect the aircraft landing weight in terms of the wing structure weight. If a fixed take-off weight is assumed, a change in the wing structure weight affects the amount of available fuel. The influence of variables on the wing structure was determined based on the wing load distribution resulting from aerodynamic calculations (Gadomski *et al.*, 2006; Goetzendorf-Grabowski *et al.*, 2006; Goetzendorf-Grabowski and Mieloszyk, 2017; Kontogiannis *et al.*, 2016; Panagiotou *et al.*, 2014; Panagiotou *et al.*, 2018).

The calculations were performed in the Matlab environment. In the first step, an objective function module (OFM) has been programmed. OFM uses the external program AVL to determine the aerodynamic coefficients of a new aircraft configuration. The AVL uses an extended vortex lattice method for modeling lifting surfaces, together with a slender-body model for fuselages and nacelles. The results of AVL calculations are verified in terms of the neutral point position with respect to the center of gravity. If the center of gravity is situated within the assumed range, the procedure is continued by activating the module responsible for wing weight calculation in the new configuration. Based on the load distribution resulting from AVL calculations, the wing weight function determines the local thickness of the spar caps, the weight of the entire spar and weight of the entire wing. Knowing the wing structure weight, it is possible to determine a fuel weight in the new aircraft configuration and, as a result, to determine the objective function. Finally, the objective function module, with three independent variables used as the input, yields the objective function value. The OFM can then be optimized. For that purpose, a tool available in the Matlab environment called the “optimization tool” was used. To find the optimal solution, a genetic optimization algorithm was used.

Design space

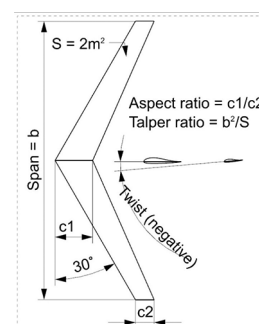
The design space is defined by a choice of independent variables and their ranges. In our case, Table II shows three decision variables have been chosen with different ranges.

Where the parameters in Table II are defined as it is shown on Figure 5.

Table II Design space

18 <	Aspect ratio “A”	>40
0.1 <	Taper ratio “λ”	>1
–10 <	Twist “t”	>5

Figure 5 Design space definition



Genetic optimization

The genetic algorithms (GA) methods have been developed since the 1960s and the pioneer in this field was John Henry Holland, American scientist, Professor of psychology and Professor of electrical engineering and computer science at the University of Michigan. Professor Holland (1975) wrote the ground-breaking book on genetic algorithms, *Adaptation in Natural and Artificial Systems*. GA is an optimization method based on natural selection mechanisms. The knowledge of evolutionary strategies (Rechenberg, 1994; Schwefel, 1993), allows for programming effective numerical procedures (Koza, 1998) enabling one to find the optimal solution even in discontinuous space of variables. The presented calculations were performed in the Matlab environment and for optimization purposes the provided “optimization tool” was used, allowing for genetic optimization. The GA parameters in Table III were adopted for the optimization process.

Aerodynamics

The AVL program was used to determine aerodynamic coefficients. The “Samonit” wing geometry was taken as the starting point for the aforementioned calculations. To speed up calculations, only the wing model with a winglet is examined in the AVL, additional drag of other parts of the aircraft was supplied based on the wind tunnel test results. The geometry of next configuration results from three independent variables and a series of constants presented in the Table IV.

The geometry described in Table IV is shown in Figure 6.

The AVL uses the extended vortex lattice method for modeling the lifting surfaces combined with a slender-body model for fuselages and nacelles. From such an approach it is

Table III GA parameters

Population	
Population type	Double vector
Population size	20
Creation function	Constraint dependent
Scaling function	Rank
Selection	Stochastic uniform
Reproduction	
Elite count	2
Crossover fraction	0.8
Mutation function	Constraint dependent
Crossover function	Scattered

Table IV Aerodynamic model parameters

Wing area (reference area)	2	m ²
Single trapezoidal wing contour		
Leading edge sweep angle	30	deg
Dihedral angle	0	deg
Winglet height	0.5	m
Aileron surface	2 × 0.03	m ²

not possible to extract information about the friction drag. At that stage, the wind tunnel test results proved helpful. Comparison between the AVL calculations results for the “Samonit” configuration and wind tunnel test results made it possible to find the total drag. However, the induced drag considered as a component of the total drag, results from the AVL calculations.

For the optimization process in the AVL calculations, a steady horizontal flight with zero slip angle is considered. The angle of attack is adjusted so as to obtain a load factor $n = 1$ for a specified aircraft mass, speed and flight altitude, respectively. The elevon deflections are controlled by the program in the way to ensure a balanced horizontal flight with the flight parameters given in Table V.

The results of aerodynamic analysis important to the optimization process comprise the drag and lift force coefficients determined for the new aircraft geometry and the corresponding wing load distribution (Figure 7).

Weight of the wing

Based on the wing load distribution for the current aircraft configuration (resulting from the AVL calculations), the “weight of wing” module calculates the cross-section area of spar caps along the wingspan, and then the weights of the spar and the entire wing (Figure 8). These calculations are made on the following assumptions:

- the maximum stress is equal to: $\sigma_{max} = \frac{\sigma_{UGS}}{1.5} = 476 \text{ MPa}$;
- the spar height in consecutive sections is equal to the maximum thickness of the local profile (13 per cent of the chord);
- the wing skin weight is constant (because the wing surface is constant); and
- the weights of wing internal structure elements are proportional to the spar weight.

The wing weight in the new configuration is determined by the formula:

$$W_{WING} = W_{SPAR} + W_{SKIN} + W_{Internal\ structure} \\ = 3.99 + 2.68 * W_{SPAR} \quad (16)$$

If the wing structure weight is known, the weight of available fuel for the new aircraft configuration can be found and the objective function value can be determined.

The analysis yields the information that the optimal wing configuration is described by the following parameters:

$$\text{Aspect ratio } A = 20.96;$$

$$\text{Taper ratio } \lambda = 0.21;$$

$$\text{Twist angle } t = -0.8$$

The optimal wing configuration for the UAV is shown in Figure 9.

Figure 6 AVL aerodynamic model

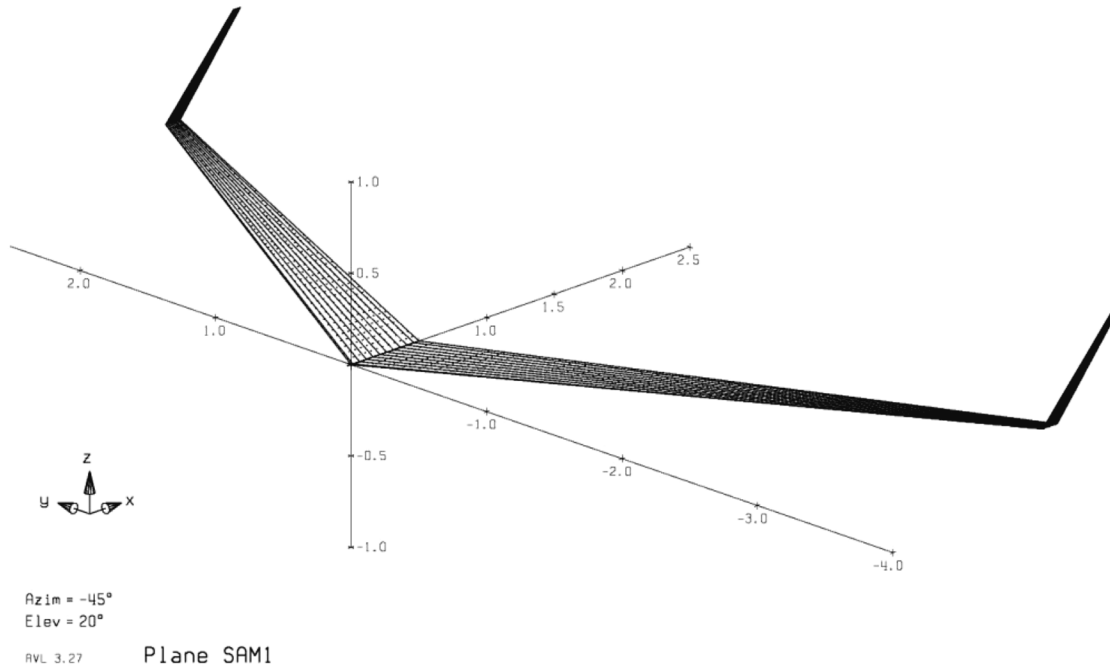
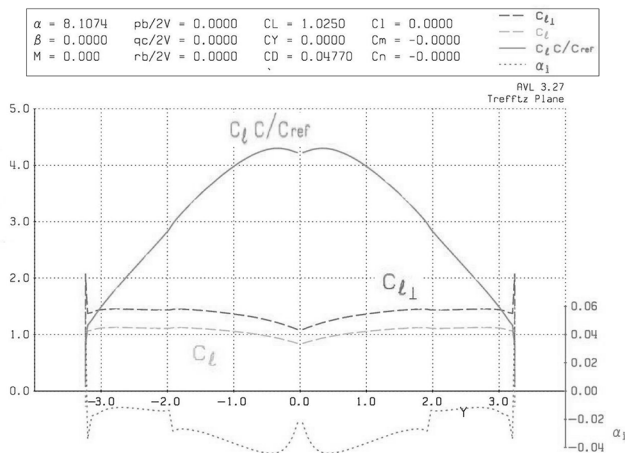


Table V Aerodynamic model parameters

Flight speed	25.09	m/s
Flight altitude	200	m
Lift force coefficient	1.025	
Zero-lift drag force coefficient	0.034	m

Figure 7 Wing load distribution



The objective function value representing the calculated optimal point of variable space is equal to:

$$F(A, \lambda, t) = 0.22876$$

In addition, after applying equation (15), the endurance equals:

$$E = 29h$$

The optimal configuration resulting from the above analysis is unquestionable. The calculations prove that the wing configuration, which maximizes the UAV endurance is similar to a typical glider wing configuration.

In the optimization process, 24 iterations were performed. Each population had 20 individuals, yielding, after addition of a few mutated individuals, about 500 points of the variable space with defined objective function values. As the function has three independent variables, it is difficult to present it on a plane diagram. Three perpendicular projections of the variable space, with the calculation points marked, are shown in Figures 10–12.

The objective function values resulting from the optimization procedure are presented in Figures 10–12. The Figures show all measurement points, therefore, for a specified variable value one can see several values of the target function. These points have different values of the other two variables. The envelope of maximum values in the above graphs may represent the relation between the endurance and a given variable. However, it should be emphasized that this is a relation between the objective function and a given variable, on the assumption that the other two variables achieve their optimal values.

Conclusion

The numerical procedure presented here is an effective and efficient tool for finding the optimum configuration of the UAV wing. In the optimization process, the objective function values were determined for about 500 points of the variable space. It took about 40 min for a middle-class PC to do this. This may not be very fast, but it is an acceptable time for a given application.

Figure 8 Bending moment and spar cap cross-section area distribution

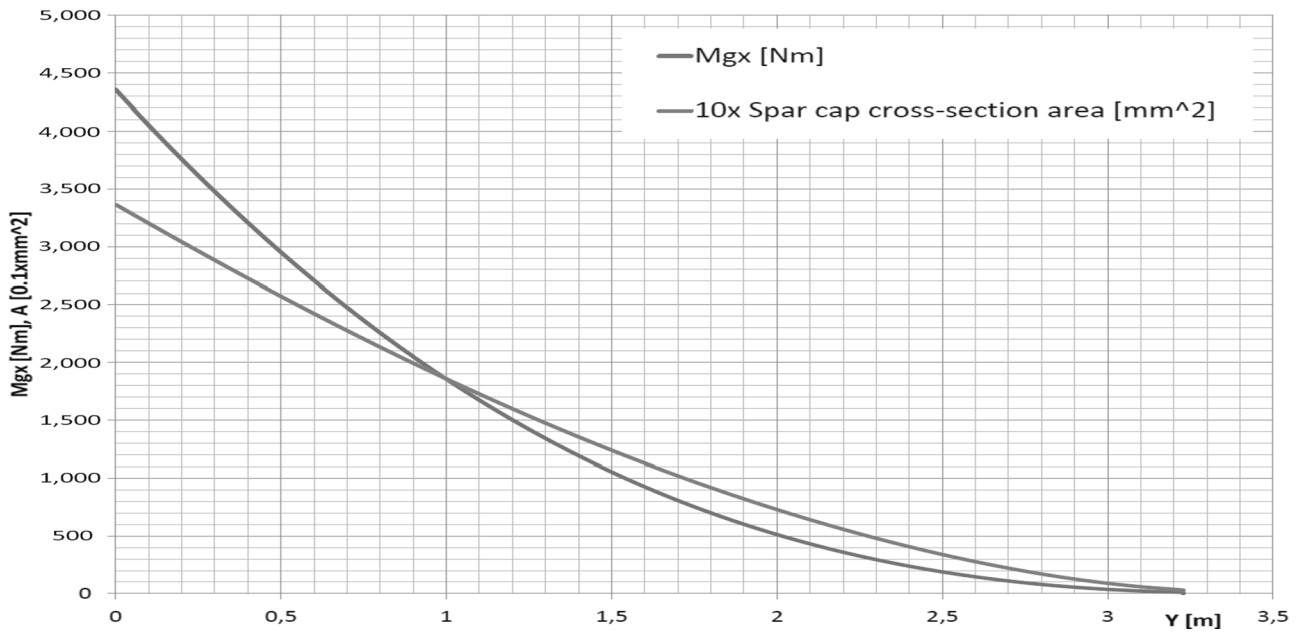


Figure 9 Optimal wing configuration

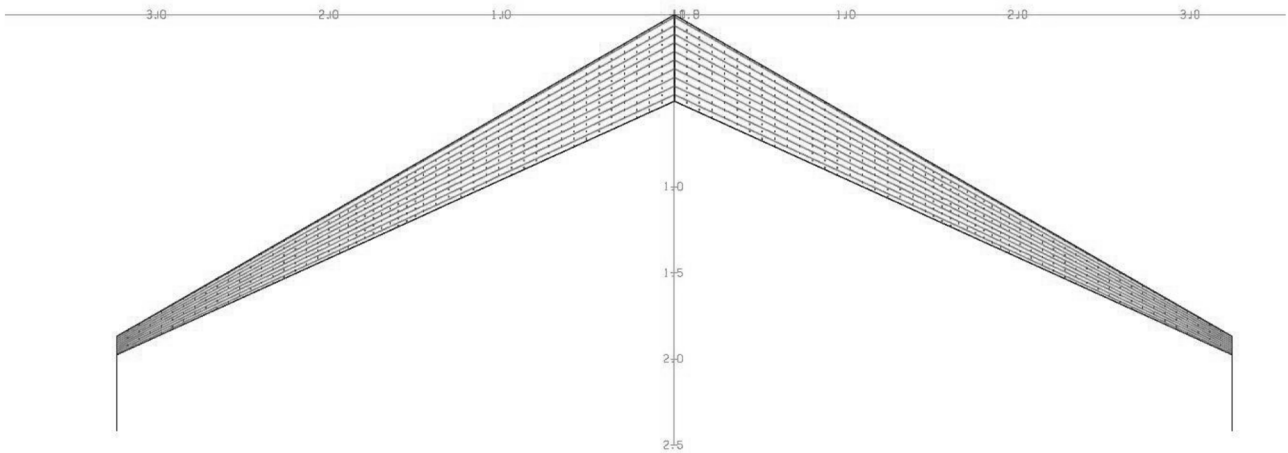


Figure 10 Results, aspect ratio vs the endurance (plane view)

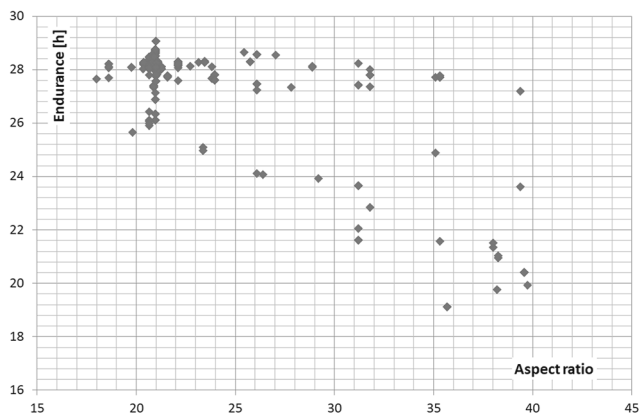


Figure 11 Results, taper ratio vs the endurance (plane view)

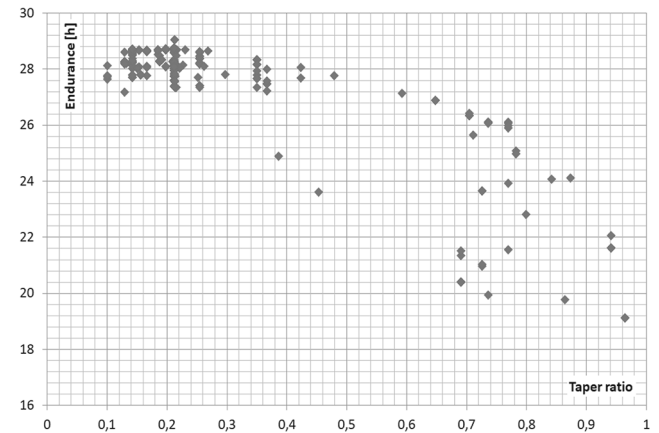
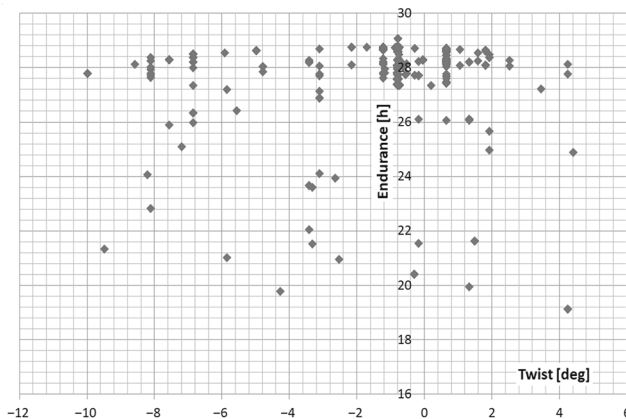


Figure 12 Results, wing twist vs the endurance (plane view)

GA is a good tool for the multidisciplinary optimization task described above. The GA allows discontinuities in the objective function due to, for example, numerical errors in aerodynamic calculation results. In that case, the optimization module assigns a low score to such an individual, and thus, the individual leaves the population in the selection process. Moreover, the GA also determines local extremes and that information can be very helpful for a designer in the determination of a new aircraft configuration (Nosratollahi *et al.*, 2010).

As a result of the analysis, one can find parameters of the optimum configuration; the aspect ratio equals 21, taper ratio equals 0.21 and a small negative twist of the wing equals -0.8° . These results are sensible and mean that the best solution for a Samonit-type aircraft is a wing configuration similar to typical glider wings.

As one can see, the wing aspect ratio greater than the optimum value, results in a slight decrease in endurance. It may suggest that this is also a good solution. It should be emphasized that increasing the aspect ratio causes additional technological or functional problems, and thus, such a solution is not recommended.

Further work

The procedure above-presented analyses the target function value for a specified configuration, taking into account that for each new configuration the gravity center lies in front of the aerodynamic neutral point. This is a simple condition for ensuring the longitudinal stability of the analyzed configuration. However, this condition is not sufficient to avoid all types of instability that may occur, especially in view of the fact that a flying wing configuration is analyzed. In the aforementioned analysis, only the resulting configuration has been examined for its stability and controllability (Goraj, 2014). The stability and controllability analysis is not part of the optimization process. In further work, it would be justified to include the stability and controllability analysis into the optimization process. It will make this procedure more versatile and allow one, for example, to examine the effect of changing the wing sweep angle on the objective function value.

References

- Gadomski, J., Hernik, B. and Goraj, Z. (2006), "Analysis and optimisation of a male UAV loaded structure", *Aircraft Engineering and Aerospace Technology*, Vol. 78 No. 2, pp. 120-131.
- Goetzendorf-Grabowski, T. and Mieloszyk, J. (2017), "Common computational model for coupling panel method with finite element method", *Aircraft Engineering and Aerospace Technology*, Vol. 89 No. 5, pp. 654-662.
- Goetzendorf-Grabowski, T., Frydrychewicz, A., Goraj, Z. and Suchodolski, S. (2006), "Male UAV design of an increased reliability level", *Aircraft Engineering and Aerospace Technology*, Vol. 78 No. 3, pp. 226-235.
- Goraj, Z. (2014), "Flight dynamics models used in different national and international projects", *Aircraft Engineering and Aerospace Technology*, Vol. 86 No. 3, pp. 166-178.
- Goraj, Z., Nowakowski, M. and Hajduk, J. (2010), "Long term influence of UAVNET/USICO/CAPECON projects on polish UAS activities (research/design/testing/production/education etc)", UAVNET WORKSHOP No. 18, Tel Aviv, 20-21 Oct. 2010, available at: www.uavnet.org (accessed 20 November 2011).
- Goraj, Z., Rodzewicz, M., Grendysa, W. and Jonas, M. (2012), "Design and configuration layouts of an advanced long endurance UAV-lessons learnt after flight testing", *Proc. of 28th International Congress of the Aeronautical Sciences, Sept. 2012, Paper. 763, Brisbane*.
- Gudmundsson, S. (2014), *General Aviation Aircraft Design Applied Methods and Procedures*, Butterworth-Heinemann, Waltham.
- Holland, J. (1975), *Adaptation in Natural and Artificial Systems*, The University of MI Press, Ann Arbor, MI.
- Jameson, A., Leoviriyakit, K. and Shankaran, S. (2007), "Multi-point aero-structural optimization of wings including planform variations", *45th AIAA Aerospace Sciences Meeting and Exhibit, Aerospace Sciences Meetings, Reno, NV*.
- Kontogiannis, S.G., Mazarakos, D.E. and Kostopoulos, V. (2016), "ATLAS IV wing aerodynamic design: from conceptual approach to detailed optimization", *Aerospace Science and Technology*, Vol. 56, pp. 135-147.
- Koza, J.R. (1998), *Genetic Programming*, MIT press, Cambridge, MA.
- Martins, J.R.R.A. and Lambe, A.B. (2013), "Multidisciplinary design optimization: a survey of architectures", *AIAA Journal*, Vol. 51 No. 9, pp. 2049-2075.
- Mieloszyk, J. (2017), "Practical problems of numerical optimization in aerospace sciences", *Aircraft Engineering and Aerospace Technology*, Vol. 89 No. 4, pp. 570-578.
- Nosratollahi, M., Mortazavi, M., Adami, A. and Hosseini, M. (2010), "Multidisciplinary design optimization of a reentry vehicle using genetic algorithm", *Aircraft Engineering and Aerospace Technology*, Vol. 82 No. 3, pp. 194-203.
- Panagiotou, P., Fotiadis-Karras, S. and Yakinthos, K. (2018), "Conceptual design of a blended wing body MALE UAV", *Aerospace Science and Technology*, Vol. 73, pp. 32-47.
- Panagiotou, P., Kaparos, P. and Yakinthos, K. (2014), "Winglet design and optimization for a MALE UAV using CFD", *Aerospace Science and Technology*, Vol. 39, pp. 190-205.

- Rechenberg, I. (1994), *Evolution Strategies*, Frommann-Holzboog, Stuttgart.
- Schwefel, H.P. (1993), *Evolution and Optimum Seeking*, Wiley, New York, NY.
- Steinbuch, M. and Shepshelovich, M. (2004), "Development of high altitude long endurance airfoils", *42ND AIAA Conference, AIAA 2004-1052, Reno, NV*.
- Steinbuch, M., Marcus, B. and Shepshelovich, M. (2003), "Development of UAV wings-subsonic designs", *41st*

- Aerospace Sciences Meeting and Exhibit, AIAA Conference, AIAA, Reno, NV*.
- Yakinthos, K. (2018), "Aerodynamic and structural design for the development of a MALE UAV", *Aircraft Engineering and Aerospace Technology*, Vol. 90 No. 7, pp. 1077-1087.

Corresponding author

Wojciech Grendysa can be contacted at: wgrendysa@meil.pw.edu.pl



eJournal Collections

A leading library of management research

Over 160,000 articles from more than 300 journals by end of 2017, Emerald eJournals combine research rigour with practical relevance to showcase the most relevant topics from the leading thinkers within their field.

Visit emeraldinsight.com

**Get eJournal
Collections for your library**

Recommend eJournals to your librarian today.

Find out more: emeraldpublishing.com/eJournalcollections



Backfiles Collections

Preserving over 100 years of management research online

A lifetime investment for your institution, Emerald Backfiles will significantly enhance your library's offering by providing access to over 125,000 articles from more than 260 journals dating back to 1898.

Visit emeraldinsight.com

**Get Backfiles
Collections for your library**

Recommend Backfiles to your librarian today.

Find out more: emeraldpublishing.com/backfilescollections